Device Modelling of Perovskite Solar Cells

Daniel Anthony Jacobs

A thesis submitted for the degree
Doctor of Philosophy of
The Australian National University

College of Engineering and Computer Science
The Australian National University

May 2018

Statement of Originality

The work in this thesis is my own and original except where stated otherwise. Detailed contribution statements for each chapter are given in sec. 1.5. I credit my colleagues Heping Shen, Yiliang Wu and The Duong for their contribution of cells, and for taking most of the measurements referenced in Chapter 2.

23/05/18

Acknowledgements

A significant trial in every PhD's journey is the search for a "vein" both rich and accessible enough to mine a thesis out of. To some such a vein will be revealed at the outset, but in research (as in mining I suppose) these are always liable to be less deep and less approachable than first appearances might suggest. Being one whose choice of initial projects uncovered only dust and nuggets – no veins – I was lucky to have colleagues who could set me straight. I must credit Yiliang Wu and Heping Shen in particular for their prospective digging on the issue of I-V hysteresis and for involving me on this topic, which proved ideal for a worker with my tools (a rather general physics background), and a desire to contribute somewhere in the area of perovskite solar cells.

Further progress would not have been possible without the tireless help of Heping Shen, always willing to accommodate my need for cells into her own schedule, and if not to make a new schedule! I thank her also for frequently involving me in the capacity of the "theory guy" in several investigations that form a significant fraction of this thesis (the latter halves of Chapter 2 and 4 in particular). It is no understatement to say that no thesis would have materialized (in so short a time at least) without her involvement.

The material herein would seem to me hopelessly niche and recherché were it not for the continued interest and encouragement of my colleagues in the PV group. Our weekly meetings were an important motivator to put ideas in order and useful as an all-around training-ground in presentation and listening. I'm grateful to the previous names as well as to Thomas White, Klaus Weber, Fiona Beck, Daniel Walter, Chog Baerhujin, and Niraj Lal for stimulating discussions and helpful suggestions. I acknowledge all of the above for their stamina in proof-reading my manuscripts, particularly those tortuous first drafts. Thanks also to my other colleagues in the PV group who provided cells and various forms of experimental assistance over the years, including Jun Peng, The Duong and Xiao Fu.

Special thanks are due to my supervisor Kylie Catchpole, whose contributions can only be given summary credit here. First, for being top of the list in terms of providing helpful suggestions and encouraging feedback at our weekly meetings. Also for a generous attitude which emphasised taking the time necessary to find a suitable vein. Much of what I take away from this experience stems from that process of trying, and at first failing, to find a fruitful problem. In addition to supervisory patience this also entails the wisdom of not withholding the opinion that certain approaches and problems are simply not worthwhile, and knowing when it is better to simply move on (a non-trivial lesson for students like myself to whom almost every self-generated idea seemed exciting). On a separate matter Kylie's presentations and papers are exemplary in their clarity. I hope I can truthfully say that my academic writing has benefited from her tutelage and example, the only concrete evidence in favour of this being that both the extent and number of her corrections has diminished over time!

I'm continually grateful to Fiona Beck for her trust in allowing essentially free reign over her freshly purchased lab equipment. This enabled much of the work in Chapter 3, and was an ideal experience in running (albeit simple) experiments from the ground up. It was also simply great fun.

Finally, to my partner Vicky whose love and companionship has been a wellspring of resilience. Even the darkest days have yielded a spot of sunshine in her presence, to say nothing of the finer weather.

Abstract

This thesis is primarily concerned with the electrical characterization and modelling of perovskite solar cells. Perovskite cells are a new player in the photovoltaic arena with several intriguing properties. One of these is the presence of intrinsic mobile ions which make these semiconductors simultaneously ionic conductors at room temperature. The presence of mobile ions is significant in that it leads to a number of transient behaviours in optoelectronic measurements, including nominally simple current-voltage measurements where the phenomena are broadly labelled as aspects of "I-V hysteresis". The first two-thirds of this thesis describes our work on extended drift-diffusion models which incorporate the presence of mobile ions into the conventional equations of semiconductor physics. These allow us to uncover mechanistic explanations for a variety of transient behaviours which are broadly caused by coupling between electronic and ion dynamics. The first third (Chapter 2) deals with hysteresis in the form of rate-dependent I-V sweeps: a selection of unusual measurements of this type is presented including a temporary enhancement in open-circuit voltage following prolonged periods of negative bias, dramatically S-shaped current-voltage sweeps, decreased current extraction following positive biasing or "inverted hysteresis", and non-monotonic transient behaviours in the dark and the light. This initial study is supplemented with a more in-depth investigation of inverted hysteresis and its correlation with band-alignment. The second third (Chapter 3) delves deeper into electrical characterization with a first-principles study of electrical impedance spectroscopy. We focus on accounting for features in the measured capacitance spectrum (sufficient for a full account of the total impedance due to the Kramers-Kronig relations) of standard-structure (non-inverted) perovskite cells. Here our models make clear the necessity of distinguishing fundamental contributions to the measured capacitance due to charging, from those due to currents delayed by slow processes such as ion migration. With this distinction clearly established we provide a detailed account of all the major features observed in impedance measurements of these cells, including the exotic and previously puzzling appearance of giant photo-induced capacitance, loop features and negative capacitance.

The final part of this thesis in Chapter 4 concerns the integration of perovskite cells into tandem arrangements with a partner such as the crystalline silicon cell. Of relevance to any thin-film solar cell, and to 4-terminal tandem cells in particular, is the specifications of its transparent conductor layers. We analyze transparent conductor requirements under different regimes of metallization (the addition of metallic bus-bars or fingers). Here a key parameter is the minimal achievable wire width, which dictates the necessary trade-off between transparency and conductivity in the underlying transparent conductor. We identify 30 µm as a critical width below which many emerging transparent conducting layers such as carbon nanotubes and graphene become competitive with state-of-the-art transparent conductive oxides such as ITO for a stand-alone perovskite cell. We also discuss a novel strategy for integrating perovskite and Si cells into a single monolithic structure without the need for a tunnel junction or recombination layer. This is identified as being possible due to the presence of interfacial sub-gap states which can facilitate high-conductivity ohmic contact between TiO_2 and p-type Si, and has significant advantages in terms of reducing optical losses and processing steps.

Contents

1 Introduction **7**
1.1 Motivation: Innovation beyond Si . . . 7
1.2 Perovskite Photovoltaics . . . 9
1.3 The Role of Modeling . . . 14
1.4 Chapter Outlines . . . 15
1.5 Chapter Papers . . . 16

2 I-V Hysteresis **23**
2.1 Introduction . . . 23
2.2 Modelling Ionic Semiconductors . . . 24
2.2.1 Drift-Diffusion of Holes and Electrons . . . 24
2.2.2 Drift-Diffusion for Ions . . . 26
2.2.3 SCAPS Model . . . 27
2.2.4 COMSOL Implementation . . . 29
2.3 Experimental . . . 29
2.3.1 Rapid-scan characterization . . . 30
2.4 The Many and Varied Effects of Ion Accumulation . . . 31
2.4.1 Surface versus bulk recombination . . . 32
2.4.2 S-shaped I-V scans at high forward bias . . . 35
2.4.3 Effect of positive accumulation . . . 36
2.4.4 Simulations with dynamic accumulation . . . 39
2.4.5 Enhancement of transient photovoltage by ionic accumulation . . . 41
2.4.6 Accumulation Widths in the Fixed-Layer Model . . . 42
2.4.7 Surface Recombination and S-shapes . . . 44
2.4.8 Forward Scan Shapes . . . 45
2.4.9 Non-monotonic dark current as evidence for trap-saturation . . . 45
2.5 Inverted Hysteresis . . . 45
2.5.1 Rate-dependent I-V Scans . . . 49
2.5.2 Role of Band Alignment . . . 52
2.5.3 Wavelength Dependence . . . 56
2.5.4 XPS Measurements . . . 59
2.5.5 Relation to Tress et al. 2016 . . . 60
2.6 Summary and Conclusions . . . 62

3 Electrical Impedance Spectroscopy **69**
3.1 Introduction . . . 69
3.2 Outline . . . 70
3.3 A Conflicted Literature . . . 70
3.4 EIS: Basic Theory . . . 72
3.4.1 Displacement current . . . 73
3.4.2 Impedance of a uniform semiconductor . . . 73
3.4.3 Carrier relaxation . . . 74

3.4.4 Heuristic model of a diode with mobile ions . . . 75
3.4.5 Capacitance from Continuity . . . 78
3.4.6 C_Q: Geometric, Accumulation and Chemical Capacitances . . . 80
3.5 Antiphase Recombination in Capacitance Measurements . . . 85
3.5.1 Experimental Methods . . . 87
3.5.2 Photo-induced Capacitance . . . 87
3.5.3 Loop Features and Ion Diffusion . . . 92
3.5.4 Negative Capacitance . . . 96
3.6 C-V Measurements . . . 97
3.7 Ion-Electrode Capacitance . . . 101
3.8 Quantifying Hysteresis with EIS . . . 102
3.8.1 The effect of passivation . . . 106
3.8.2 Susceptance versus Voltage and Illumination . . . 108
3.8.3 Temperature dependence . . . 109
3.9 Summary and Conclusions . . . 110

4 Tandem Cell Integration 120
4.1 Transparent Conductor Requirements . . . 121
4.1.1 Transparent Conductor Requirements with Metallization . . . 123
4.1.2 Figures of Merit for Solar Cells . . . 128
4.1.3 4-T Tandem Electrodes . . . 131
4.2 Direct Integration of a Monolithic (2-T) Tandem . . . 133
4.2.1 Interconnect-Free Tandem Design . . . 134
4.2.2 Characterization of the Titania-Silicon Contact . . . 136
4.2.3 Role of Defects & the Titania-Silicon Band-Offset . . . 138
4.2.4 Role of Mesoporous Titania – Maintaining the Built-in Voltage . . . 141
4.3 Summary and Conclusions . . . 142

5 Closing Remarks and Future Directions 150

A Continuity and the Admittance 154

B Analysis of SRH Contact Resistivity 156

Chapter 1

Introduction

What is the goal of photovoltaic research today? In 2016, a mid-point in the author's PhD, worldwide installations of new photovoltaic (PV) capacity overtook that of all other electricity sources [1]. Projections indicate that PV is on the path to become, if not a primary electricity source, then a very substantial player in the world's energy mix [1, 2]. This tends to provoke one of two possible reactions: on the one hand it may seem that the technology has already *made it*, signalling a "game over" situation for PV research.[1] Is there much need for blue-skies thinking about a technology with such formidable industrial momentum? Perhaps one's efforts would be better spent elsewhere. The other reaction sees the present situation as a stimulus: now more than ever is the time when incremental improvements stand to have tangible real-world consequences. Indeed, despite being one of the cheapest sources of electricity in several worldwide locations (alongside wind) [3], in many other places PV still lags behind non-renewable sources due to regional variability in yield and installation costs. Even in the most competitive locations the cost advantage of PV tends to disappear at levels that require storage [4]. It follows that reductions in the cost of PV electricity still have a large role to play in the technologies' adoption, and therefore in the world's commitment to renewable energy. Both the optimistic and pessimistic lines of thinking hit on partial truths however and deserve our attention. In the following we will discuss aspects of a new player in the PV arena: the perovskite solar cell. The rapidly-shifting terrain of industrial feasibility, market forces and fast-moving science makes this a risky but exciting domain of research.

1.1 Motivation: Innovation beyond Si

Forecasts concerning PV adoption are generally sunny: the direct conversion of sunlight to electricity is already one of the cheapest ways to generate energy in many regions of the world, and is nearing the threshold in many others [1, 2, 3]. To date the massive growth in PV adoption has been driven largely by impressive cost reductions in the c-Si module ($> 90\%$ of the current PV market-share [5]) with some help from local policy incentives [1]. Further cost reductions can be

[1] Every worker in the field has surely encountered this "gauntlet throw" at least once, whether from the mouths of another (in the authors case) or simply as a challenge to themselves.

expected to continue into the near future as industrial production catches up with advancements made in the lab. Manufacturers will have to contend with the technologies' intrinsic efficiency limit in the longer term however. If unsurpassed, this efficiency limit will constrain improvements in the levelized cost of electricity for silicon photovoltaics due to balance-of-systems costs, which arise from relatively mature products (racking, inverters, wiring etc.), and are comparably difficult to reduce. Motivated by such factors, a projection of PV development to the year 2050 [3] has considered the situation in which single-junction Si cells continue to dominate the market by 2050 a "conservative" base case. A more likely, "average" scenario is one in which the incentives for higher-efficiency have shifted production to dual-junction ("tandem") cells by 2050 with a module efficiency of 30%, surpassing the 24% base case (close to the realistic limit for Si module efficiencies, estimated to be 25% [3]) with 35% triple-junction modules coming to dominate by the same time in an optimistic scenario.

Among the many third-generation proposals for circumventing the thermodynamic efficiency limit of single-junction cells, multi-junction cells are widely regarded as being both the most practical and economically viable strategy [6]. This last point hinges on the existence of low-cost sub-cells that satisfy matching criteria with respect to their band-gaps. In addition to being commercially established, Si has a highly favourable band-gap for use as a bottom-cell in tandem or multi-junction arrangements. Unfortunately, no comparably established wide-bandgap cell exists as a partner for Si at present. Furthermore, the list of candidate technologies in development with the necessary high band gaps was both short and unpromising until recently (see e.g. [7]). Good band-gap pairings can be achieved with III-V semiconductors, but the considerable materials and processing cost of these [8], far outweighing that of silicon, hampers the commercial viability of such designs for terrestrial non-concentrating applications. Silicon quantum dots were pursued for a while as another alternative [9], but appear to have lost favour recently, possibly due to the stringent processing requirements needed to compromise between quantum confinement and adequate conductivity. Recently the shortlist admitted a new and more promising entry in the halide perovskites, which with their well-matched band gaps and low materials cost have emerged as promising tandem partners for Si. Whilst not without its challenges, the possibility of boosting the efficiency of Si cells with a perovskite top-cell has attracted the attention of many researchers from the domains of semiconductor engineering, to materials science and chemistry, and is now the leading strategy for bringing perovskite photovoltaics to market [10].

1.2 Perovskite Photovoltaics

Halide perovskites exploded onto the photovoltaic scene in the period 2012-2014, becoming the focus of many research groups previously devoted to organic and dye-sensitized cells. Despite their historical relation, state-of-the-art perovskite cells have more in common with other inorganic thin-film technologies due to their long diffusion lengths and low exciton binding energies. These result in mostly free carriers under 1 sun illumination that can be put to work using the familiar concept of a carrier-selective heterojunction [11]. The perovskite cell therefore represents an evolution rather than a revolution in photovoltaics, although there are still uncertainties as to which key physical properties have enabled their rapid climb to prominence. In addition to providing nearly ideal band-gaps for tandem pairings with Si, many have touted perovskite cells as being competitive in their own right. Optimists consider the latent advantages of low-cost roll-to-roll processing, and the possibility of making flexible cells, as enabling future cost-reductions relative to the Si cell. Such claims remain controversial, and one certain consideration is that economies of scale, which have worked so strongly in the Si cell's favour, present a high barrier-to-entry for competitive technologies lacking truly breakthrough advantages. Many therefore believe that a more likely path to commercialization sees perovskite cells being adopted by Si manufacturers as a means to boost the efficiency of their product, and thus gain competitive advantage [12]. This may eventually lead to spin-off perovskite products after industrial-scale learning has made the technology more competitive. Of course, any commercial application in photovoltaics will require a solution to the stability problem [13], which is serious but largely outside the scope of this thesis.

On top of their commercial prospects, photovoltaic perovskites exhibit a number of unusual physical properties that have attracted significant scientific attention. Their unique properties, ranging from controversial to well-established, include complex electronic structures featuring "dynamical" band gaps, hints of ferroelectric ordering, and large intrinsic ionic conductivities. To provide a sense of these and the excitement they have generated, a selection of interesting results will be reviewed in the section below. Whilst of only indirect relevance to the remainder of this thesis, these materials properties may have much to do with what makes perovskite photovoltaics worthwhile. It is also important for us to consider these and their possible impact on device behaviour given our focus on modelling.

A vital and curious aspect of the photovoltaic perovskites is their remarkably long charge carrier lifetimes when prepared in polycrystalline thin-films (typically 10-1000 ns [14, 15]) and single-crystal form (1-10 µs [16]). These indicate low rates of defect-mediated non-radiative recombination, a particularly surprising property for solution-processed thin-films that cannot withstand high temperature annealing, and are therefore significantly disordered. Given the soft

character of these materials (small lattice binding energies [17]), it is practically certain that crystallographic defects are present in high numbers, from which it follows that the majority of these must be relatively benign. The reason for this "defect tolerance" has yet to be confidently identified, but many creative and intriguing suggestions have been put forward. Low rates of bi-molecular radiative recombination have also been observed [18] and may follow from the same or related mechanisms.

Sub-gap Defects

Although far from the only possibility, the simplest mechanism to explain long lifetimes would be a relative absence of recombination-active defects in the photovoltaic perovskites. Indeed, several ab initio calculations have indicated that most point-defects in $CH_3NH_3PbI_3$ ($MAPbI_3$) form only shallow levels inside the band gap [19, 20] whereas those defects that do form deep levels have a fortuitously high formation energy [19]. Although direct confirmation for this property is apparently still lacking, it has been pointed out that the unusual "inverted" band-structure of $MAPbI_3$, characterized by anti-bonding orbitals in the valence band and bonding conduction-band orbitals, could partially account for this phenomenon [21]. In particular, the dangling bonds at vacancy sites and grain boundaries are predicted to yield shallow or band-resonant energy levels, making both relatively benign. Unfortunately this elegant and unusual property is unlikely to represent the full story, as several other candidate PV materials have been identified by using inverted band structures as a screening criterion, but none of these have achieved comparable lifetimes [22].

Ferroelectric Highways

The possibility of ferroelectricity has been extensively discussed with reference to $MAPbI_3$ and related materials due to its prevalence in inorganic perovskites, particularly the peroskite oxides [23]. Certain types of ferroelectric ordering could provide internal carrier separation along "ferroelectric highways" and thereby explain the long observed lifetimes [24, 25, 26]. Several studies have reported direct evidence for the existence of polarized nanoscale domains, apparently of the kind needed to aid charge separation, using piezoresponse force microscopy on $MAPbI_3$ films [27, 28]. The fact that similar measurements by other groups have failed to obtain such evidence [29] is suggestive of strong preparation dependence however. Notably for the correlation with lifetimes, Vorpahl et al. have shown that the domains apparent in the piezoresponse disappear upon heating above the cubic phase transition [30]. Although heating above room temperature generally has an adverse effect on $MAPbI_3$ cell performance, a dramatic change at the tetragonal to cubic transition is not observed [31, 32], contrary to the sudden disappearance of ferroelectric

ordering. The role that ferroelectricity plays in the photovoltaic operation of perovskite cells therefore remains unclear.

Polaronic Carriers

Within conventional band theory lattice distortions act to reduce the strength of electrostatic interactions between internal charges, including carriers and charged defects. Correspondingly, dielectric polarization is most often considered in terms of its effect on properties such as the exciton binding energy and capture cross sections. Measurements of the static dielectric constant (carefully excluding the ionic contribution) indicate very large values in the range of $\epsilon_{\text{stat}} \approx 60$ for $MAPbI_3$ [33], a factor which could account for the ready breakup of excitons [34], and reduced rates of defect capture [33]. The back-action of lattice polarization on the carriers themselves is a distinct effect of dielectric polarization, less relevant in covalent semiconductors such as Si, but potentially crucial in ionic materials. Several authors have suggested that these "polaronic" effects could be vital to a proper description of carriers in $MAPbI_3$ [35, 34, 36, 37, 38, 33, 39]. The interaction between carriers and the lattice polarization has two primary effects of relevance to device operation, namely a reduction in mobility and reduced recombination rates. Values of $100\,\text{cm}^2\,\text{V}^{-1}\,\text{s}$ to $200\,\text{cm}^2\,\text{V}^{-1}\,\text{s}$ have been derived for the electron and hole mobilities from theories of polaron transport [40, 41], which agree well with the highest values obtained from single-crystal measurements [16]. These figures represent an upper limit for single-crystals, and will be further reduced by impurity and defect scattering in polycrystalline films. Perhaps of greater interest is the possible effect of lattice polarization on reducing recombination rates beyond the simple prediction of Langevin's theory [42]. Localization of carriers should reduce recombination rates, whether due to random potential fluctuations [43] or the coordinated polarization involved in polaron formation, with one estimate putting the size of this effect at two orders of magnitude in terms of rate reduction [44]. Signatures have been observed in transient infrared absorption which appear to support the polaron theory [45]. Another very tentative indication in favour is a thermally activated recombination rate [33], which would follow if carriers must first be thermally excited out of their self-induced polarization-well before recombining. Thermally activated recombination has indeed been reported in measurements [46, 47] but attributed to a mechanism invoking the indirect band gaps discussed below.

Direct-Indirect Band Gap

$MAPbI_3$ and its relatives have mostly been labelled as direct band-gap semiconductors due to their strong absorption features, but several lines of evidence now point to a more nuanced picture. A number of computational studies [48, 49, 50, 51, 52], and recent experimental evidence

[47] indicate the formation of a slightly indirect gap in $MAPbI_3$ due to spin-orbit coupling. A necessary condition for a spin-split band gap is broken inversion symmetry, as can be seen by noting that the momentum separation Δk and spin σ of two spin-split extrema define a pseudovector $\Delta k \times \sigma$, which must vanish whenever inversion symmetry is present. In $MAPbI_3$ both the polar organic molecule and distortions of the inorganic sublattice break inversion symmetry "dynamically" (as both are disordered at room temperature), and the heavy Pb atom contributes relativistic electrons to result in a spin-split band gap [48]. Importantly, the splitting is small enough to only slightly shift the energy required for direct transitions, so the strong absorption implied by a direct gap is retained. It has been estimated that the indirect character contributes to a 350-fold reduction in direct recombination rates compared to the case with no spin-splitting [52]. The experimental evidence in favour of this theory is a thermally activated recombination rate [47], which might alternatively arise from the polaron mechanism described above. Nonetheless, the possible importance of spin-orbit coupling is both intriguing and well demonstrated theoretically, with important implications for compositional design (in particular, the heavy Pb atom may be practically irreplaceable if this is the key property of photovoltaic perovskites).

Ionic Conductivity

Several inorganic perovskites (both oxides and halides) are known to be good ion conductors [53], perhaps explaining why ionic conduction was quick to emerge as an explanation for slow transient behaviour in perovskite cells. The first mention of ion conduction in the perovskite photovoltaic literature appears to be work by Dualeh et al. [54] which noted significant low-frequency features in impedance spectroscopy measurements. Subsequent studies focusing on EIS were not unanimous in this attribution however, with others opting for an explanation in terms of dielectric relaxation [55, 56]. Shortly thereafter, a switchable photovoltaic effect was found in devices with non-selective contacts and explained in terms of ion migration [57], with a key piece of evidence being material changes observed under poling that would not be expected if ferroelectricity or traps were responsible. The finding that films of $MAPbX_3$ (X=Cl, Br, I) could be inter-converted via anion exchange provided the first unambiguous evidence that the halides in these films are mobile, with dipping conversion occurring on a timescale of seconds to minutes [58]. The analogous effect of cation exchange between $MAPbI_3$ and $FAPbI_3$ was also observed with a timescale on the order of 10 minutes [59]. Meanwhile computational studies predicted highly facile formation [60] and diffusion [61] of iodine vacancies in $MAPbI_3$, with the latter study even concluding that iodide diffusion is too fast (activation energy 0.08 eV) to account for the commonly observed transient phenomena, proposing motion of the less mobile MA vacancies instead. Another computational study found a significantly higher activation

energy for V_I diffusion (0.58 eV) and good agreement between this value and temperature-dependent transient measurements [62].

There are now several studies which have provided spatial information about the nature of ion migration in $MAPbI_3$. Photothermal induced resonance microscopy (an atomic force microscopy technique) was used to map the distribution of MA^+ ions after electrically biasing a lateral $MAPbI_3$ structure for $100 - 200$s [63]. The large ($\approx 10\,\mu$m) accumulation zones were found to undergo a work function change following biasing, supporting the picture that mobile ions act as a dynamic doping profile. Localized illumination was also observed to cause a migration of ions (this time I^-), possibly due to photo-charging induced by a significant density of carrier traps [64]. Another significant finding concerns the role of grain-boundaries: local I-V measurements were performed using conductive atomic force microscopy to reveal that hysteresis is apparently strongest at grain boundaries in $MAPbI_3$ [65]. This suggests that ion migration may occur primarily along isolated pathways at the grain boundaries rather than through the bulk, although bulk migration is still necessary to account for the interconversion experiments. Migration of iodine along grain boundaries was detected directly using energy-dispersive X-ray spectroscopy in the same study, but was only detectable at slightly elevated temperatures of 330 K [65]. At the same time no observable motion of the lead element was detected, consistent with predictions of a higher activation energy for migration for this species [61].

More recently it has been discovered that in addition to intrinsic ion migration in $MAPbI_3$, extrinsic species such as Li^+, Na^+ and H^+ are also mobile in the material [66]. These extrinsic ions originate primarily from the contact layers, and could explain some of the observed sensitivity of hysteresis behaviour to the choice of contacts (including different activation energies for relaxation [67, 68]). The occurrence of a material with high intrinsic (and extrinsic) ionic conductivity represents a first in the space of high-performing solar absorbers, and is relatively novel in the context of semiconductor physics as well. Standard characterization methods must therefore be used with caution on the halide perovskites and conventional device models must be re-examined.

This concludes our brief survey of the physical properties which make the photovoltaic perovskites scientifically interesting. As already mentioned, it is still unclear how many of these properties are essential for a proper description of perovskite devices. In the face of this uncertainty, it is worth taking some time to consider the role of device modelling, which constitutes the major focus of this thesis.

1.3 The Role of Modeling

The trajectory of perovskite efficiencies over the 4-7 year period to date provides an interesting opportunity to reflect on the factors at play in photovoltaic R&D. In its early stages one can discern that great leaps were made in perovskite cell design by intuitive reckoning, based mostly on experience and basic observation: the key moves from liquid to solid electrolytes (motivated by stability issues) and from the sensitized to thin-film architecture (on the basis of long lifetimes) are prime examples. Significant advances in more recent times continue to be made via simply-motivated (but seldom simply-executed) processing improvements, directed for example at producing more uniform films with larger grain sizes. Prior experience from other photovoltaic technologies also plays a role in motivating approaches such as interface passivation and band-alignment tuning. Clearly such progress requires little input from advanced cell characterization or device modelling. This tight-looped "direct" approach, largely guess-and-try (although seldom reported as such), can be contrasted with the more involved process of making advancements in a mature technology such as the Si cell. Here progress is heavily reliant on a detailed understanding of the semiconductor and materials physics relevant to device operation. Well-vetted models underpin a sizable arsenal of characterization techniques and simulation packages that are used routinely in guiding cell and process design. In part this can be attributed to the multitude of steps involved in Si cell fabrication, which can be separately optimized given the right tools. Clearly the technology's maturity is also a factor, as it is hard to imagine the intuitive approach characteristic of perovskite research today making much headway on record Si efficiencies. Due to strong process interactions it is hard to apply compartmentalized optimization to perovskite cells, and it is anyway rather quicker to simply finish a cell and check its efficiency. The most useful kind of model for perovskites would therefore be those applicable to completed devices and capable of pinpointing their major failings.

A clear sense of what a useful model needs to accomplish can be gained by considering the workhorse diode models of Si cell analysis. These capture quantitative information about device performance in just a few effective parameters (e.g. series resistance and saturation currents), which generally relate to a combination of microscopic quantities. This compromise (a "lumped approximation") is an acceptable and even desirable one, as for the purpose of guiding fabrication it is enough that each effective parameter should relate to a strict subset of the processing steps. For example, if the series resistance can be confidently related to the contact materials or metallization, and not to other cell properties such as passivation, its determination provides useful input into the development feedback loop. Clearly such models should be physically well-motivated, as no clear correspondence between effective parameters and processing steps can be expected to occur "for free". As yet, no models with the reliability and utility of the

conventional diode models have been established for perovskite solar ells. Instead, a large part of the work in this thesis concerns the preliminary step of correctly identifying the relevant device physics (a process that crucially distinguishes modelling from straightforward fitting).

1.4 Chapter Outlines

What physics? (Chapter 2)

The primary focus of this thesis is on the device modelling of perovskite cells, both singly and in tandem arrangements with Si. In light of the observations above, our main task lies in identifying the physics relevant for a proper description of these devices. Several of the unusual physical properties described above call for a re-examination of the basic assumptions entrenched in conventional photovoltaic thinking, and contraindicate the incautious use of established characterization methods. Questions arise as to whether certain exotic physical properties are essential to an understanding of perovskite devices, or whether they can incorporated with a business-as-usual approach using modified material constants. It is here that modelling in an exploratory way can play a vital role in terms of sharpening thinking about these issues and identifying gaps in our understanding.

Since the first suggestions that ionic conductivity might be significant in the halide perovskites, it seemed clear that (if true) this fact would have a vital impact on the way we conceptualize cell operation, and on the business of characterization. This is less true for the other exotic properties mentioned in sections 1.3-1.6, for example: defect tolerance, indirect band gaps and polaronic effects should be felt mostly in reduced recombination rates (and mobility in the latter case), and are therefore accommodated by a "business-as-usual" approach to semiconductor device modelling. Ferroelectricity is anticipated to have more complex consequences depending on the size of the effect, but there have been several indications that it is not a primary factor in transient behaviour (although it may play a microscopic role in aiding charge separation, c.f. the ferroelectric highways concept). By contrast, the evidence for ion migration is now practically irrefutable, and there have been several highly suggestive links between it and transient device behaviour. The primary evidence for ion migration was reviewed above and the links to cell behaviour will be covered in Chapter 2. Subsequently we describe an approach for incorporating mobile ions into a standard p-i-n model, which is then used to address a series of curious features seen in I-V measurements of our own group's $MAPbI_3$ cells (2.4). This is followed by an in-depth study of so-called "inverted hysteresis" (sec. 2.5).

Ions and EIS (Chapter 3)

Having successfully established the mobile ions suffice to explain much (if not all) of the qualitative behaviour seen in I-V measurements, we proceed to test these models against EIS measurements in Chapter 3. Although not far removed from an I-V measurement, EIS allows for probing cell behaviours over a large range of timescales (up to 9 decades) in a single measurement, and therefore provides a more stringent test of a model's transient component. Once again we find that the ionic cell models are remarkably adept at accounting for these measurements, and are able to provide rigorous explanations for a number of previous puzzling phenomena.

Tandem Modelling (Chapter 4)

Several aspects of cell design have little to do with the details of the perovskite absorber, particularly when it comes to making tandems. These include the design of transparent electrodes, paramount in 4-terminal tandem design, and interconnection layers for monolithic 2-terminal cells. Chapter 4 deals with both of these aspects of tandem cell design, addressed specifically at perovskite/Si devices.

To construct a 4-terminal tandem from its component subcells the only modification needed is removal of the top cell's reflective back contact, and its replacement with a transparent conductor. The choice of transparent conductor is therefore a key step in 4-terminal tandem design, and can have a significant impact on the resulting performance. We begin Chapter 4 by reviewing the standard requirements for transparent conductors, before considering in detail how these are affected by the inclusion of metal bus-bars or fingers.

In 2-terminal monolithic tandems, the top cell's reflective back contact is conventionally replaced by a transparent interconnection layer to carry current between the two subcells. We report on a collaborative project which resulted in proof-of-concept tandem cells with no interconnection layer, entailing conductive direct contact between the two subcells. The author's involvement in this project concerned the physical mechanisms responsible for enabling this design, which appear to be sub-gap defects in the amorphous interfacial region. We present the device modelling and observations in favour of this theory, and a discussion of how these fed back into the design process.

1.5 Chapter Papers

This thesis is largely a compilation of publications by the author. These are listed below:

Chapter 2

Chapter 2 is based on first-authored publication [1] listed below and a co-first authored publication [2] with minor modifications to figures and text. Our contributions to [2] included writing of (the entire) manuscript, preparation of all figures, development of the theory and execution of the modelling. H. Shen contributed experimental design, characterization and fabrication of the cells, as well as initiating the study.

[1] Jacobs, D. A.; Wu, Y.; Shen, H.; Barugkin, C.; Beck, F. J.; White, T. P.; Weber, K.; Catchpole, K. R. Hysteresis Phenomena in Perovskite Solar Cells: the Many and Varied Effects of Ionic Accumulation. *Physical Chemistry Chemical Physics* **2017**, *19*, 3094-3103.

[2] Shen*, H.; Jacobs*, D. A.; Wu, Y.; Duong, T.; Peng, J.; Wen, X.; Fu, X.; Karuturi, S. K.; White, T. P.; Weber, K.; et al. Inverted Hysteresis in $CH_3NH_3PbI_3$ Solar Cells: Role of Stoichiometry and Band Alignment. *The Journal of Physical Chemistry Letters* **2017**, *8*, 2672-2680. *Co-first authors.

Chapter 3

Chapter 3 is based on the first-authored publication listed below, currently under review, with some minor modifications to figures and text, plus additional content:

[1] Jacobs, D. A.; Shen, H.; Pfeffer, F.; Peng, J.; White, T. P.; Beck, F. J.; Catchpole, K. R. Capacitance Measurements of Perovskite Solar Cells: Antiphase Recombination is Vital. *Under Review* **2018**.

Chapter 4

Chapter 4 is based on the first-authored publication [1] and a co-first authored manuscript [2] which is presently under review. Our contribution to [2] included: significant writing of the manuscript and the entirety of the theory and modelling section, analysis and interpretation of results, and the preparation of Figs. 4.10, 4.11 and 4.13. The experimental design, fabrication and characterization was carried out primarily by H. Shen and the other co-authors, who also initiated the study.

[1] Jacobs, D. A.; Catchpole, K. R.; Beck, F. J.; White, T. P. A Re-Evaluation of Transparent Conductor Requirements for Thin-Film Solar Cells. *Journal of Materials Chemistry A* **2016**, *4*, 4490-4496.

[2] Shen H.*, Omelchenko S. T.*, Jacobs D. A.*, S. Yalamanchili*, Wan Y., Wu Y., Phang P., Duong T., Peng J., Yin Y., Yan D., Samundsett C., Wu N., White T. P., Andersson

G. G., Lewis N. S., Catchpole K. R. Ohmic p-Si/titania contact enables high efficiency, interconnect-free monolithic perovskite/silicon tandem solar cells *Submitted*, **2018**. *Co-first authors.

Bibliography

[1] REN21, R. Global Status Report, REN21 Secretariat, Paris, France. Technical report, ISBN 978–3–9818107–6–9 **2017**.

[2] Finkel, A.; Moses, K.; Munro, C.; Effeney, T.; O'Kane, M. Independent review into the future security of the National Electricity Market: Blueprint for the future. *Canberra: Commonwealth of Australia* **2017**.

[3] Mayer, J. N.; Simon, P.; Philipps, N. S. H.; Schlegl, T.; Senkpiel, C. Current and future cost of photovoltaics. *Long-term scenarios for market development, system prices and LCOE of utility-scale PV systems* **2015**.

[4] Lazard Lazard's Levelized Cost of Energy Analysis 11.0. `https://www.lazard.com/perspective/levelized-cost-of-energy-2017/`, Accessed: May 2018.

[5] Group, I.; et al. International Technology Roadmap for Photovoltaic (ITRPV) 2017 Results. *SEMI, Berlin, Germany* **2017**.

[6] Peters, I.; Sofia, S.; Mailoa, J.; Buonassisi, T. Techno-economic analysis of tandem photovoltaic systems. *RSC Advances* **2016**, *6*, 66911–66923.

[7] White, T. P.; Lal, N. N.; Catchpole, K. R. Tandem solar cells based on high-efficiency c-Si bottom cells: top cell requirements for¿ 30% efficiency. *IEEE Journal of Photovoltaics* **2014**, *4*, 208–214.

[8] Bosi, M.; Pelosi, C. The potential of III-V semiconductors as terrestrial photovoltaic devices. *Progress in Photovoltaics: Research and Applications* **2007**, *15*, 51–68.

[9] Conibeer, G.; Green, M.; Cho, E.-C.; König, D.; Cho, Y.-H.; Fangsuwannarak, T.; Scardera, G.; Pink, E.; Huang, Y.; Puzzer, T.; et al. Silicon quantum dot nanostructures for tandem photovoltaic cells. *Thin Solid Films* **2008**, *516*, 6748–6756.

[10] Oxford PV collaborates with HZB to move perovskite solar cells closer to commercialisation. `https://www.oxfordpv.com/News` Accessed : May 2018.

[11] Würfel, P. Physics of solar cells, volume 1. Wiley-vch Weinheim **2005**.

[12] Graydon, O. View from... PSCO 2016: The race for tandems. *Nature Photonics* **2016**, *10*, 754.

[13] Deretzis, I.; Smecca, E.; Mannino, G.; La Magna, A.; Miyasaka, T.; Alberti, A. Stability and Degradation in Hybrid Perovskites: Is the Glass Half-Empty or Half-Full? *The journal of physical chemistry letters* **2018**.

[14] Stranks, S. D.; Eperon, G. E.; Grancini, G.; Menelaou, C.; Alcocer, M. J.; Leijtens, T.; Herz, L. M.; Petrozza, A.; Snaith, H. J. Electron-hole diffusion lengths exceeding 1 micrometer in an organometal trihalide perovskite absorber. *Science* **2013**, *342*, 341–344.

[15] Zhou, H.; Chen, Q.; Li, G.; Luo, S.; Song, T.-b.; Duan, H.-S.; Hong, Z.; You, J.; Liu, Y.; Yang, Y. Interface engineering of highly efficient perovskite solar cells. *Science* **2014**, *345*, 542–546.

[16] Dong, Q.; Fang, Y.; Shao, Y.; Mulligan, P.; Qiu, J.; Cao, L.; Huang, J. Electron-hole diffusion lengths¿ 175 μm in solution-grown CH3NH3PbI3 single crystals. *Science* **2015**, *347*, 967–970.

[17] Walsh, A. Principles of chemical bonding and band gap engineering in hybrid organic–inorganic halide perovskites. *The Journal of Physical Chemistry C* **2015**, *119*, 5755–5760.

[18] Wehrenfennig, C.; Liu, M.; Snaith, H. J.; Johnston, M. B.; Herz, L. M. Charge-carrier dynamics in vapour-deposited films of the organolead halide perovskite CH 3 NH 3 PbI 3- x Cl x. *Energy & Environmental Science* **2014**, *7*, 2269–2275.

[19] Yin, W.-J.; Shi, T.; Yan, Y. Unusual defect physics in CH3NH3PbI3 perovskite solar cell absorber. *Applied Physics Letters* **2014**, *104*, 063903.

[20] Kim, J.; Lee, S.-H.; Lee, J. H.; Hong, K.-H. The role of intrinsic defects in methylammonium lead iodide perovskite. *The journal of physical chemistry letters* **2014**, *5*, 1312–1317.

[21] Zakutayev, A.; Caskey, C. M.; Fioretti, A. N.; Ginley, D. S.; Vidal, J.; Stevanovic, V.; Tea, E.; Lany, S. Defect tolerant semiconductors for solar energy conversion. *The journal of physical chemistry letters* **2014**, *5*, 1117–1125.

[22] Brandt, R. E.; Poindexter, J. R.; Gorai, P.; Kurchin, R. C.; Hoye, R. L.; Nienhaus, L.; Wilson, M. W.; Polizzotti, J. A.; Sereika, R.; Zaltauskas, R.; et al. Searching for "defect-tolerant" photovoltaic materials: combined theoretical and experimental screening. *Chemistry of Materials* **2017**, *29*, 4667–4674.

[23] Abrahams, S. C.; Keve, E. T. Structural basis of ferroelectricity and ferroelastcity. *Ferroelectrics* **1971**, *2*, 129–154.

[24] Frost, J. M.; Butler, K. T.; Brivio, F.; Hendon, C. H.; Van Schilfgaarde, M.; Walsh, A. Atomistic origins of high-performance in hybrid halide perovskite solar cells. *Nano letters* **2014**, *14*, 2584–2590.

[25] Liu, S.; Zheng, F.; Koocher, N. Z.; Takenaka, H.; Wang, F.; Rappe, A. M. Ferroelectric domain wall induced band gap reduction and charge separation in organometal halide perovskites. *The journal of physical chemistry letters* **2015**, *6*, 693–699.

[26] Sherkar, T. S.; Koster, L. J. A. Can ferroelectric polarization explain the high performance of hybrid halide perovskite solar cells? *Physical Chemistry Chemical Physics* **2016**, *18*, 331–338.

[27] Hermes, I. M.; Bretschneider, S. A.; Bergmann, V. W.; Li, D.; Klasen, A.; Mars, J.; Tremel, W.; Laquai, F.; Butt, H.-J.; Mezger, M.; et al. Ferroelastic fingerprints in methylammonium lead iodide perovskite. *The Journal of Physical Chemistry C* **2016**, *120*, 5724–5731.

[28] Röhm, H.; Leonhard, T.; Hoffmann, M. J.; Colsmann, A. Ferroelectric domains in methylammonium lead iodide perovskite thin-films. *Energy & Environmental Science* **2017**, *10*, 950–955.

[29] Fan, Z.; Xiao, J.; Sun, K.; Chen, L.; Hu, Y.; Ouyang, J.; Ong, K. P.; Zeng, K.; Wang, J. Ferroelectricity of CH3NH3PbI3 perovskite. *The journal of physical chemistry letters* **2015**, *6*, 1155–1161.

[30] Vorpahl, S. M.; Giridharagopal, R.; Eperon, G. E.; Hermes, I. M.; Weber, S. A.; Ginger, D. S. Orientation of ferroelectric domains and disappearance upon heating methylammonium lead triiodide perovskite from tetragonal to cubic phase. *ACS Applied Energy Materials* **2018**.

[31] Zhang, H.; Qiao, X.; Shen, Y.; Moehl, T.; Zakeeruddin, S. M.; Grätzel, M.; Wang, M. Photovoltaic behaviour of lead methylammonium triiodide perovskite solar cells down to 80 K. *Journal of Materials Chemistry A* **2015**, *3*, 11762–11767.

[32] Quarti, C.; Mosconi, E.; Ball, J. M.; D'Innocenzo, V.; Tao, C.; Pathak, S.; Snaith, H. J.; Petrozza, A.; De Angelis, F. Structural and optical properties of methylammonium lead iodide across the tetragonal to cubic phase transition: implications for perovskite solar cells. *Energy & Environmental Science* **2016**, *9*, 155–163.

[33] Anusca, I.; Balčiūnas, S.; Gemeiner, P.; Svirskas, Š.; Sanlialp, M.; Lackner, G.; Fettkenhauer, C.; Belovickis, J.; Samulionis, V.; Ivanov, M.; et al. Dielectric response: Answer to many questions in the methylammonium lead halide solar cell absorbers. *Advanced Energy Materials* **2017**, *7*.

[34] Soufiani, A. M.; Huang, F.; Reece, P.; Sheng, R.; Ho-Baillie, A.; Green, M. A. Polaronic exciton binding energy in iodide and bromide organic-inorganic lead halide perovskites. *Applied Physics Letters* **2015**, *107*, 231902.

[35] Brivio, F.; Frost, J. M.; Skelton, J. M.; Jackson, A. J.; Weber, O. J.; Weller, M. T.; Goni, A. R.; Leguy, A. M.; Barnes, P. R.; Walsh, A. Lattice dynamics and vibrational spectra of the orthorhombic, tetragonal, and cubic phases of methylammonium lead iodide. *Physical Review B* **2015**, *92*, 144308.

[36] Zhu, X.-Y.; Podzorov, V. Charge carriers in hybrid organic–inorganic lead halide perovskites might be protected as large polarons **2015**.

[37] Chen, Y.; Yi, H.; Wu, X.; Haroldson, R.; Gartstein, Y.; Rodionov, Y.; Tikhonov, K.; Zakhidov, A.; Zhu, X.-Y.; Podzorov, V. Extended carrier lifetimes and diffusion in hybrid perovskites revealed by Hall effect and photoconductivity measurements. *Nature communications* **2016**, *7*, 12253.

[38] Neukirch, A. J.; Nie, W.; Blancon, J.-C.; Appavoo, K.; Tsai, H.; Sfeir, M. Y.; Katan, C.; Pedesseau, L.; Even, J.; Crochet, J. J.; et al. Polaron stabilization by cooperative lattice distortion and cation rotations in hybrid perovskite materials. *Nano letters* **2016**, *16*, 3809–3816.

[39] Miyata, K.; Meggiolaro, D.; Trinh, M. T.; Joshi, P. P.; Mosconi, E.; Jones, S. C.; De Angelis, F.; Zhu, X.-Y. Large polarons in lead halide perovskites. *Science advances* **2017**, *3*, e1701217.

[40] Sendner, M.; Nayak, P. K.; Egger, D. A.; Beck, S.; Müller, C.; Epding, B.; Kowalsky, W.; Kronik, L.; Snaith, H. J.; Pucci, A.; et al. Optical phonons in methylammonium lead halide perovskites and implications for charge transport. *Materials Horizons* **2016**, *3*, 613–620.

[41] Frost, J. M. Calculating polaron mobility in halide perovskites. *Physical Review B* **2017**, *96*, 195202.

[42] Wehrenfennig, C.; Eperon, G. E.; Johnston, M. B.; Snaith, H. J.; Herz, L. M. High charge carrier mobilities and lifetimes in organolead trihalide perovskites. *Advanced materials* **2014**, *26*, 1584–1589.

[43] Ma, J.; Wang, L.-W. Nanoscale charge localization induced by random orientations of organic molecules in hybrid perovskite CH3NH3PbI3. *Nano letters* **2014**, *15*, 248–253.

[44] Ambrosio, F.; Wiktor, J.; De Angelis, F.; Pasquarello, A. Origin of low electron–hole recombination rate in metal halide perovskites. *Energy & Environmental Science* **2018**, *11*, 101–105.

[45] Ivanovska, T.; Dionigi, C.; Mosconi, E.; De Angelis, F.; Liscio, F.; Morandi, V.; Ruani, G. Long-lived photoinduced polarons in organohalide perovskites. *The Journal of Physical Chemistry Letters* **2017**, *8*, 3081–3086.

[46] Savenije, T. J.; Ponseca Jr, C. S.; Kunneman, L.; Abdellah, M.; Zheng, K.; Tian, Y.; Zhu, Q.; Canton, S. E.; Scheblykin, I. G.; Pullerits, T.; et al. Thermally activated exciton dissociation and recombination control the carrier dynamics in organometal halide perovskite. *The journal of physical chemistry letters* **2014**, *5*, 2189–2194.

[47] Hutter, E. M.; Gélvez-Rueda, M. C.; Osherov, A.; Bulović, V.; Grozema, F. C.; Stranks, S. D.; Savenije, T. J. Direct–indirect character of the bandgap in methylammonium lead iodide perovskite. *Nature materials* **2017**, *16*, 115.

[48] Brivio, F.; Butler, K. T.; Walsh, A.; Van Schilfgaarde, M. Relativistic quasiparticle self-consistent electronic structure of hybrid halide perovskite photovoltaic absorbers. *Physical Review B* **2014**, *89*, 155204.

[49] Motta, C.; El-Mellouhi, F.; Kais, S.; Tabet, N.; Alharbi, F.; Sanvito, S. Revealing the role of organic cations in hybrid halide perovskite CH 3 NH 3 PbI 3. *Nature communications* **2015**, *6*, 7026.

[50] Zheng, F.; Tan, L. Z.; Liu, S.; Rappe, A. M. Rashba spin–orbit coupling enhanced carrier lifetime in CH3NH3PbI3. *Nano letters* **2015**, *15*, 7794–7800.

[51] Etienne, T.; Mosconi, E.; De Angelis, F. Dynamical origin of the rashba effect in organohalide lead perovskites: A key to suppressed carrier recombination in perovskite solar cells? *The journal of physical chemistry letters* **2016**, *7*, 1638–1645.

[52] Azarhoosh, P.; McKechnie, S.; Frost, J. M.; Walsh, A.; Van Schilfgaarde, M. Research Update: Relativistic origin of slow electron-hole recombination in hybrid halide perovskite solar cells. *APL Materials* **2016**, *4*, 091501.

[53] Mizusaki, J.; Arai, K.; Fueki, K. Ionic conduction of the perovskite-type halides. *Solid State Ionics* **1983**, *11*, 203–211.

[54] Dualeh, A.; Moehl, T.; Tétreault, N.; Teuscher, J.; Gao, P.; Nazeeruddin, M. K.; Grätzel, M. Impedance spectroscopic analysis of lead iodide perovskite-sensitized solid-state solar cells. *ACS Nano* **2014**, *8*, 362–73.

[55] Bisquert, J.; Bertoluzzi, L.; Ivan, M.; Germa, G. Theory of Impedance and Capacitance Spectroscopy of Solar Cells with Dielectric Relaxation, Drift-Diffusion Transport, and Recombination. *J Phys Chem C* **2014**, *118*, 18983–18991.

[56] Sanchez, R. S.; Victoria, G.; Lee, J.; Park, N.; Kang, Y.; Ivan, M.; Bisquert, J. Slow Dynamic Processes in Lead Halide Perovskite Solar Cells. Characteristic Times and Hysteresis. *J Phys Chem Lett* **2014**, *5*, 2357–2363.

[57] Xiao, Z.; Yuan, Y.; Shao, Y.; Wang, Q.; Dong, Q.; Bi, C.; Sharma, P.; Gruverman, A.; Huang, J. Giant switchable photovoltaic effect in organometal trihalide perovskite devices **2015**, *14*, 193–198.

[58] Pellet, N.; Teuscher, J.; Maier, J.; Gratzel, M. Transforming Hybrid Organic Inorganic Perovskites by Rapid Halide Exchange **0**, *27*, 2181–2188.

[59] Eperon, G. E.; Beck, C. E.; Snaith, H. J. Cation exchange for thin film lead iodide perovskite interconversion **2015**, *3*, 63–71.

[60] Walsh, A.; Scanlon, D.; Chen, S.; Gong, X. Self-Regulation Mechanism for Charged Point Defects in Hybrid Halide Perovskites. *Angewandte ...* **2015**.

[61] Azpiroz, J. M.; Mosconi, E.; Bisquert, J.; Angelis, F. Defect migration in methylammonium lead iodide and its role in perovskite solar cell operation **2015**, *8*, 2118–2127.

[62] Eames, C.; Frost, J. M.; Barnes, P. R.; C, O. B.; Walsh, A.; Islam, S. M. Ionic transport in hybrid lead iodide perovskite solar cells. *Nat Commun* **2015**, *6*, 7497.

[63] Yuan, Y.; Chae, J.; Shao, Y.; Wang, Q.; Xiao, Z.; Centrone, A.; Huang, J. Photovoltaic Switching Mechanism in Lateral Structure Hybrid Perovskite Solar Cells **2015**, *5*, 1500615.

[64] W, d. D.; Zhang, W.; Burlakov, V. M.; Graham, D. J.; Leijtens, T.; Osherov, A.; Bulović, V.; Snaith, H. J.; Ginger, D. S.; Stranks, S. D. Photo-induced halide redistribution in organic-inorganic perovskite films. *Nat Commun* **2016**, *7*, 11683.

[65] Shao, Y.; Fang, Y.; Li, T.; Wang, Q.; Dong, Q.; Deng, Y.; Yuan, Y.; Wei, H.; Wang, M.; Gruverman, A.; et al. Grain boundary dominated ion migration in polycrystalline organic–inorganic halide perovskite films. *Energy Environ Sci* **2016**, *9*, 1752–1759.

[66] Li, Z.; Xiao, C.; Yang, Y.; Harvey, S. P.; Kim, D.; Christians, J. A.; Yang, M.; Schulz, P.; Nanayakkara, S. U.; Jiang, C.; et al. Extrinsic ion migration in perovskite solar cells. *Energy Environ Sci* **2017**.

[67] Kim, H. S.; Jang, I. H.; Ahn, N.; Choi, M.; Guerrero, A.; Bisquert, J.; Park, N. G. Control of I-V Hysteresis in $CH_3NH_3PbI_3$ Perovskite Solar Cell. *J. Phys. Chem. Lett.* **2015**, *6*, 4633–4639.

[68] Zhang, Y.; Liu, M.; Eperon, G. E.; Leijtens, T. C.; McMeekin, D.; Saliba, M.; Zhang, W.; de Bastiani, M.; Petrozza, A.; Herz, L. M.; et al. Charge selective contacts, mobile ions and anomalous hysteresis in organic-inorganic perovskite solar cells. *Mater. Horiz.* **2015**, *1*, 96.

Chapter 2

I-V Hysteresis

2.1 Introduction

With reference to perovskite solar cells (PSCs) the term "hysteresis" is used to describe any rate or preconditioning dependence in an (opto-)electronic measurement.[1] Large hysteresis effects render the traditional diode models of photovoltaic analysis ineffective, and thereby complicate the process of device design and characterization. The most common form of hysteresis occurs in I-V measurements, where it manifests as a sensitivity to sweep rate, direction and pre-conditioning (the recent history of applied voltage and illumination levels). I-V hysteresis is not unique to perovskite cells: it was studied some time ago in dye-sensitized solar cells where it presented similar problems for reliable characterization [1]. There the phenomenon was associated with a slow diffusion of ions in the cell's electrolyte [2], just as the present understanding of perovskite hysteresis emphasizes the role of solid-state ion diffusion.

The issue of hysteresis in perovskite cells was first given due recognition in a paper from H. Snaith's group in early 2014 [3] (i.e. some time after the field's foundational papers which gave it no mention). The hysteresis in this early work was referred to as "anomalous" since the slow relaxation upon voltage shifts (significant after hundreds of seconds) was long enough to give the appearance of increasing hysteresis at lower scan rates, contrary to the trend expected with capacitive hysteresis. A low-frequency response had already been observed prior to this in impedance spectroscopy [4], although at that time the implications for I-V characterization were not discussed. Ref. [3] pointed out the now well known fact that the I-V curves of perovskite cells can be strongly influenced by factors such as scan-rate, direction and preconditioning, as well being one of the first to suggest that ionic conduction could be responsible. Other hypotheses included a ferroelectric response and the influence of slow trapping/de-trapping due to defects in the perovskite bulk or interfaces. For some time afterward the three mechanisms of ion conduction, ferroelectricity and slow trapping were treated on almost equal footing as viable explanations for I-V hysteresis. In the intervening years however the evidence that halide

[1] "Relaxation" would be a more suitable term due to the transience of these effects, but we will adhere to using simply "hysteresis" throughout. Sometimes "rate-dependent hysteresis" is used in the literature to acknowledge the discrepancy with the words' usual meaning in physics, which does not imply any time-dependence.

perovskites (in particular $MAPbI_3$) are facile ion conductors has become practically indisputable [5, 6, 7, 8] (see also section 1.2), whilst the evidence in favour of ferroelectric effects is still hotly contested. Carrier trapping and de-trapping have yet to be proven sufficient to describe I-V hysteresis, although a certain degree of trapping-induced transience is strongly implicated by observations of slow responses in bare titania films, and by capacitance measurements (see Chapter 3, in particular sec. 3.7).

Whether ionic disorder is simply a temporary nuisance in halide perovskites, or whether it is more deeply associated with some of the materials more desirable properties is as yet unclear. It is certainly tempting to speculate that the several unique peroperties of these materials (ionic conductivity included) may be related to one another rather than present by a coincidence. One possible link concerns the materials soft character: this simultaneously contributes to its strong polarizability, suggested to enable long carrier lifetimes (section 1.2), and also to the ready formation and diffusion of ionic defects. It is therefore uncertain whether future generations of perovskite cells will inherit the peculiar features of the cells today which make them so challenging to characterize. For the present hysteresis effects are still manifest in even high performing cells (although typically at somewhat faster timescales, see sec. 3.8), and remain an obstacle to rigorous characterization. We remark that some of the slow performance variations on the timescale of hours under operating conditions have also been attributed to ion migration [9].

Two studies on the topic of modelling I-V hysteresis with a drift-diffusion treatment of ion migration were published prior to ours [10, 11], and were crucial as inspiration. These were primarily concerned with explaining the sweep-rate and pre-conditioning dependence of standard I-V measurements. Their success in explaining the basic qualitative features of I-V measurements motivated the author to apply a similar approach to explaining some of the measurements generated by the perovskite cell-makers at ANU. These data sets exhibited a considerable variety of effects not seen in the literature, which promised to thoroughly test the ionic theories' adequacy. Sections 2.4 and 2.5 describe the methods and outcomes of this investigation, with joint conclusions given in sec. 2.6, all of which argue resoundingly in favour of the ionic hypothesis.

2.2 Modelling Ionic Semiconductors

2.2.1 Drift-Diffusion of Holes and Electrons

Most analyses of semiconductor devices are made on the basis of the semi-classical drift-diffusion equations for carrier transport. To arrive at these from the starting point of many-body quantum theory involves several stages of approximation, first to the single-particle Schrödinger equation,

then to its semi-classical approximation, and then to Boltzmann's transport equation, which finally has the drift-diffusion equations as one of its limits [12]. We will not attempt to outline all the required assumptions here (see [12] for an in-depth treatment and extensive references). We remark on only one of these which is necessary to move from the Boltzmann transport equations to drift-diffusion: that is that the device dimensions are large compared to the carrier mean free path (clearly necessary for the description of carriers using position-dependent quasi-fermi levels). The mean free path is estimated very roughly by the relation $l_p \sim m^* \mu v_{th}/e$, which yields a value of approximately 30 nm for a mobility of $\mu = 10\,\mathrm{cm^2\,V^{-1}\,s^{-1}}$ and $m^* \sim 0.5$. This value is somewhat lower than the ∼300 nm predicted for tetragonal $MAPbI_3$ by a combined density-functional and transport theory calculation [13], but we note that this study derives mobility values ($\sim 1000\,\mathrm{cm^2\,V^{-1}\,s^{-1}}$) an order of magnitude larger than any measurement we are aware of, and similarly in excess of the mobility calculated on the basis of polaron theory [14]. The polaron value ($\sim 100\,\mathrm{cm^2\,V^{-1}\,s}$ in the absence of impurity scattering) also yields $l_p \sim 300$ nm using the estimate based on mobility. The scatter of these values clearly overlaps squarely with the typical length scales (thicknesses) in a perovskite solar cell, and it can therefore be expected that non-equilibrium corrections to transport may be significant in these devices (see [15] for a corrected treatment in the context of short-base diodes). Several further approximations are implicit in the use of 1D drift-diffusion models, such as the neglect of 2 dimensions (and therefore effects related to inter-grain coupling and mesoporous or rough interfaces) and lateral disorder.

As is often the case in physics, the seemingly indulgent number of approximations required to derive the drift-diffusion equations does not greatly compromise their utility. Indeed, the drift-diffusion approach is considered foundational in most treatments of semiconductor device physics [16], and has been used to good effect in the analysis of thin-film devices (including polycrystalline and amorphous solar cells) for decades (see [17, 18] and references therein). As a further example of this the drift-diffusion simulator SCAPS has been extensively used in modelling CdTe and CIGS thin-film cells (see references in [19] and its citations). Empirically this suggests that the required assumptions are not too serious despite appearing mathematically doubtful. Since our purpose in the following two chapters is mostly to obtain qualitative insight using the drift-diffusion equations these issues will not be of great concern to us hereafter. A few more assumptions are implicit in the use of our numerical modelling tools, SCAPS and the COMSOL Multiphysics® semiconductor module, which we state for completeness. These mainly concern the boundary conditions: in SCAPS, transport at a heterojunction is assumed to follow the thermionic emission mechanism [20], whereas our COMSOL models implemented the condition of continuous quasi-fermi levels. The thermionic model imposes what is effectively a (nonlinear) contact resistance whereas the assumption of continuous fermi-levels implies lossless transmission. These models therefore coincide except under conditions of high current, or abrupt

band discontinuities. It is clear that any interfacial resistance arising from the heterojunctions in perovskite cells must be either comparable to or less than the parasitic resistance from its other components (e.g. transparent contacts), otherwise the cells would be drastically limited by series resistance. We therefore consider that the effect of band-offsets and thermionic emission is not too significant at a qualitative level. Another assumption in both models concerns the generation profile: in SCAPS we have used the option of AM1.5G illumination using the in-built absorption coefficient model based on the band-gap (this yields approximately the correct short-circuit current with a profile extending significantly into the device – sufficient conditions for our purposes), whereas in COMSOL a single exponential generation profile was employed (with absorption depths of $\sim 100\,\mathrm{nm}$).

2.2.2 Drift-Diffusion for Ions

The models of ion migration used in this thesis are also based on a series of simplifying assumptions. These are partly based on the best available evidence concerning ionic conductivity in $MAPbI_3$, and partly on the need to integrate ion migration into the conventional drift-diffusion models which address electronic transport. The latter need in particular is satisfied by modelling ion migration itself with a drift-diffusion equation, making for easy integration with the finite-element solvers used in conventional semiconductor modelling. Physically, the time-dependence predicted by the use of drift-diffusion equation is seldom observed in ionic conductors [21], as it entails simple (single timescale) exponential relaxation in response to small perturbations. To the contrary, most ionic conductors exhibit "non-Debye" relaxation characterized by a wide distribution of timescales [21]. Whether there is a universal set of mechanisms responsible for this behaviour in ionic conductors is a question that is still under debate, but likely contributions in polycrystalline films include disorder and cooperative effects (i.e. interactions between ions). It is expected for example that ions will diffuse more easily along grain boundaries and other crystallographic defects than through the crystal bulk (c.f. evidence of grain-boundary migration in $MAPbI_3$ [22]) and individual grains may host a variable density of ions. The use of drift-diffusion equations to model ion migration is therefore not expected to give accurate results concerning dynamic (transient) observations. However, we can still inquire as to the effects of ion migration and accumulation within perovskite cells without demanding accuracy in their time dependence. This is the approach taken throughout this thesis. Indeed, the qualitative error involved is straightforward to anticipate: whereever single-exponential transients are predicted by drift-diffusion models, broadened transients (resembling stretched exponentials or power-law decays) can be expected to occur in real measurements. Likewise in the frequency-domain study of Chapter 3, Debye-type peaks and plateaus in the frequency spectra are expected to be broadened. To mitigate these considerations as much as possible, the prelimary invesigations in sec.

2.3.1 below employed the method of rapid-scan I-V sweeps for comparisons between theory and experiment, which factor out much of the time-dependence.

It is also necessary to make assumptions about how many ionic species are active (mobile at room or slightly elevated temperatures), and how these are compensated. The simplest assumption to make is that only a single ionic species is relevant, e.g. the iodine vacancy in $MAPbI_3$, and that these ions are compensated by a uniform, stationary background of counterions, such as lead vacancies. The situation just described is appropriate for modelling Schottky disorder, e.g. $3V_I' + V_{Pb}^{\bullet\bullet} + V_{MA}^{\bullet} \leftrightharpoons nil.$[2] under the assumption that the defects are homogeneously distributed throughout the bulk. Other formation mechanisms and compensation schemes, such as $V_I' + I_{surf.}^{-} \leftrightharpoons nil.$ (exchange between bulk and surface sites) are also conceivable but will not be addressed here.[3] The formation energies of such Schottky pairs and triplets is predicted to be small in $MAPb_3$ [24], leaving a high density of mobile iodine vacancies of order $\sim 1 \cdot 10^{19}\,\mathrm{cm}^{-3}$. By contrast the formation of vacancy-interstitial pairs (Frenkel) disorder is predicted to be less facile, as is the case in many other perovskite compounds [24]. The computationally predicted density of $\sim 1 \cdot 10^{19}\,\mathrm{cm}^{-3}$ is used as a starting point, but not adhered to strictly due to uncertainty about this figure and the likelihood of sample dependence. We note that this density puts the concentration of ionic defects somewhat beyond the dilute-solute limit, above which (at around 0.1 atomic %) the formation of defect complexes and ionic interactions are expected to be significant [25]. For modelling purposes the mobile species is specified by its charge, diffusion constant, and density. Since iodine diffusion has been observed directly and seems to be the fastest process we generally assume a +1 elementary charge for the mobile species. Diffusion constants have also been measured and predicted with significant spread, so we allow ourselves the liberty of varying these within the measured and predicted range. Parameter choices for each figure are given in the tables at the end of the chapter.

2.2.3 SCAPS Model

As a first approach to modelling perovskite cells with mobile ions we developed device models using SCAPS [19]. In these models the perovskite solar cell (apart from its mobile ions) is envisaged as an n-i-p heterojunction device governed by the usual drift-diffusion equations of semiconductor physics. This entails some simplification, particularly since the cells fabricated for our experiments all incorporate mesoporous a TiO_2 scaffold on the n-type contact. Nevertheless, we obtain good qualitative agreement by using only a single planar n-type contact layer

[2] This equilibrium represents a balance between vacancy formation and the perfect crystal. The vacancies are represented in Kröger-Vink notation [23] with V representing the species (vacancies in this case), the subscript its location (lattice site) and superscripts the relative charge ($^{\bullet}$ and $'$ for positive and negative resp.).

[3] This reaction in particular would be sensitive to interface properties such as the choice of contact material, and may have something to do with the observed sensitivity of hysteresis on these.

in the models. Recombination is taken to be predominately trap-mediated (SRH type) with contributions from both bulk defects as well as surface states at the Spiro-OMeTAD/$MAPbI_3$ (HTL/ABS) and $MAPbI_3/TiO_2$ (ABS/ETL) interfaces. The interfacial defects allow for holes in the HTL to recombine directly with electrons in the perovskite (along with the analogous process at the ABS/ETL interface), which proves to be an important feature referred to hereafter as "surface recombination". The main model parameters are given in table 2.6.

Ions were input as doping concentrations localized within narrow layers adjacent to the two perovskite interfaces, with concentration determined by an equilibrium condition at the pre-bias voltage. This is distinct from the drift-diffusion models applied later in this chapter (sec. 2.5), and in Chapter 3. The perovskite layer is assumed to be intrinsic on average, meaning that the mobile ions are compensated by an equal number of homogeneously distributed stationary defects of opposite charge, as in Schottky disorder [24]. The net doping which arises in the accumulation regions therefore corresponds to an accumulation of ions on one side and a depletion of ions on the other (Fig. 2.2). For simplicity the widths of the accumulation and depletion zones (hereafter "accumulation zones"), which are likely to differ in reality [11], are set equal, making the model agnostic about the charge of the mobile species.

The condition we use for equilibrium at a given bias voltage is that the bulk electric field within the perovskite (outside the accumulation zones) should be fully screened when the ions reach their resting positions, which assumes that the density of mobile ions is high enough for full screening to occur. Applied to the motion of ions a drift-diffusion balance implies that higher ionic densities will form narrower accumulation zones at equilibrium [11]. Our calculations suggest that densities above approximately $10^{17}\,\mathrm{cm}^{-3}$ result in full screening and accumulation in zones less than 50nm wide (Fig. 2.8). We note that mobile vacancy concentrations above $10^{19}\,\mathrm{cm}^{-3}$ have been predicted for $MAPbI_3$ [24]. At smaller concentrations ($< 10^{17}\,\mathrm{cm}^{-3}$) these regions spread outwards into the bulk and the concept of an accumulation zone loses its meaning. Once determined by the equilibrium condition, the distribution of ions is held fixed over a full I-V scan. This is meant to simulate measuring the cell over a time interval shorter than that of ionic relaxation. Because SCAPS calculates equilibrium properties at each bias voltage, the contribution of capacitive currents [31] is neglected in the I-V results presented herein. We have performed calculations comparing the total charge stored within cells under different conditions of accumulation which suggest that these capacitive corrections to the current are negligible within our assumptions. Chapter 3 treats the topic of capacitive currents in greater detail and provides the ultimate justification for this approach (see in particular sections 3.7 and 3.8).

2.2.4 COMSOL Implementation

Subsequent to our development of the SCAPS models, which approximate the distribution of ions with the inclusion of two narrow accumulation/depletion layers, more sophisticated transient models were developed in COMSOL Multiphysics that solved the fully coupled drift-diffusion equations for electrons, holes, and ions. These models were used in the study of section 2.5 and exclusively relied upon for the EIS simulations in Chapter 3. Parameters for the COMSOL models used in this chapter are given in tables 2.6 and 2.6.

2.3 Experimental

The measurements reported in Figs. 2.1, 2.4, 2.5, 2.6, and 2.7 of this chapter were performed on cells with a mesoporous structure (FTO/compact-TiO2/ mesoporous-TiO_2/$CH_3NH_3PbI_3$/spiro-OMeTAD/Au). The PSCs were fabricated on FTO glass substrates (TEC7, DYESOL, with sheet resistance of 7 Ω/sq), which were cleaned separately in acetone, isopropanol, and ethanol for 30 min each in an ultrasonic bath, and then dried in nitrogen gas. Compact layers were prepared by either a spin-coating processes or via atomic layer deposition (ALD). For the solution-deposited compact layer 50 nm of TiO2 was deposited on the substrates via spin coating at 2000 rpm for 45 s from a precursor solution consisting of (350 µl) titanium isopropoxide and HCl (35 µl, 350 mol) in anhydrous Et-OH (5 ml). Alternatively a $TiCl_4$ source was used to run atomic layer deposition at 250 °C to achieve a compact layer with the same (50 nm) thickness. The substrates with compact layer were then sintered in the furnace in air for 30 min at 500 deg °C. To develop the ≈250 nm thick mesoporous layer a TiO_2 paste (30 NR-D, Dyesol) with an average particle size of 30 nm diluted in anhydrous Et-OH (1:5 by weight) was spin coated for 40 s at 5000 rpm with a ramp of 500 rpm s^{-1}. After spin coating, the samples were immediately dried at 100 deg °C for 10 min on a hotplate and sintered in the furnace at 500 deg °C for 30 min in air. All the following processes were performed inside a glovebox. CH3NH3PbI3 was prepared using the halide precursors (PbI_2 1 M and CH_3NH_3I 1 M, Sigma-Aldrich) dissolved in mixed solvent of N,N- dimethylformamide (0.7 mL, DMF, Sigma-Aldrich) and dimethylsulfoxide (0.3 mL, DMSO, Sigma-Aldrich). The perovskite precursor was then spin coated onto the substrate at 5000 rpm for 60 s. During the spin-coating, chlorobenzene (50 µl, Sigma-Aldrich) was dropped onto the center of the substrate after spinning started for 10 s. The spin- coated film was annealed at 100 deg °C for 15 min on the hotplate and then left to cool in the Petri dish. The spiro-OMeTAD solution was spin-coated at 4000 rpm for 40 s onto the perovskite film to form the HTL. The spiro-OMeTAD precursor solution and film preparation were prepared as described in ref. 11. Finally, a 100 nm gold contact layer was thermally evaporated onto the rear of the device.

The measurements presented here represent a collection of what we believe are interesting

results spanning several batches, and in each case were chosen to best exhibit the effect in question. Apart from batch-to-batch variation, the only major difference between cells concerns the preparation of the compact titania layer: cells in Figs. 2.1, 2.4, 2.7 incorporated a solution-processed layer whereas those in Figs. 2.5, 2.6 were made via atomic layer deposition (ALD). The full implications of this difference in preparation are beyond the scope of this paper and form the subject of an ongoing investigation. Although we focus on cells made with pure $MAPbI_3$, the approach and mechanisms considered here are general and should apply equally to cells with mixed and inorganic compositions, provided they retain the essential feature of possessing slow mobile ions at a sufficient density to influence cell behaviour.

2.3.1 Rapid-scan characterization

In order to simplify comparisons between experiment and simulation, we begin by describing a non-standard measuring protocol suggested by ref. [26]. I-V hysteresis in PSCs is typically characterized by measuring forward and reverse scans after pre-biasing periods near open-circuit [27, 28] (authors differ in their choice of whether to perform the forward scan immediately after the reverse scan or following an additional biasing period, but this is of little concern here). The splitting between the forward and reverse I-V curves is used to gauge the severity of hysteresis, sometimes quantitatively with the use of an index [29, 30]. Whilst informative, such measurements suffer from the drawback that the scanning rate determines the degree to which a cell is able to equilibrate at each bias voltage, and can give misleading results if chosen either too high or too low. The response is effectively frozen in a scan which is too fast, whereas in a slow scan the cell comes close to reaching equilibrium at each bias voltage, with both cases leading to reduced or even negligible splitting of the forward and reverse I-V curves. At some intermediate scanning rate the difference between forward and reverse scans should reach a maximum, but the task of finding this maximal scan rate may require a large number of measurements. In any case the dependence on scan rate complicates the process of assessing the degree of hysteresis in a given cell.

An alternative procedure that mostly avoids the scan-rate dependence involves allowing the cell to equilibrate at two distinct "pre-bias" voltages (0 V and the stabilized open-circuit voltage make natural choices), instead of a single one, before performing rapid I-V scans over the range of interest. The hope is that the ions will be effectively frozen in their initial positions if these I-V scans are performed rapidly enough, so that the resulting data represents the cell's performance under two distinct static distributions of ions, instead of a time-varying distribution which evolves over the course of the measurement. A comparison of the more common "forward-reverse sweep" with rapid-scan measurements made on our mesoporous $TiO_2/MAPbI_3$/Spiro-OMeTAD cells shows that the latter method is indeed far more effective at manifesting the hysteretic

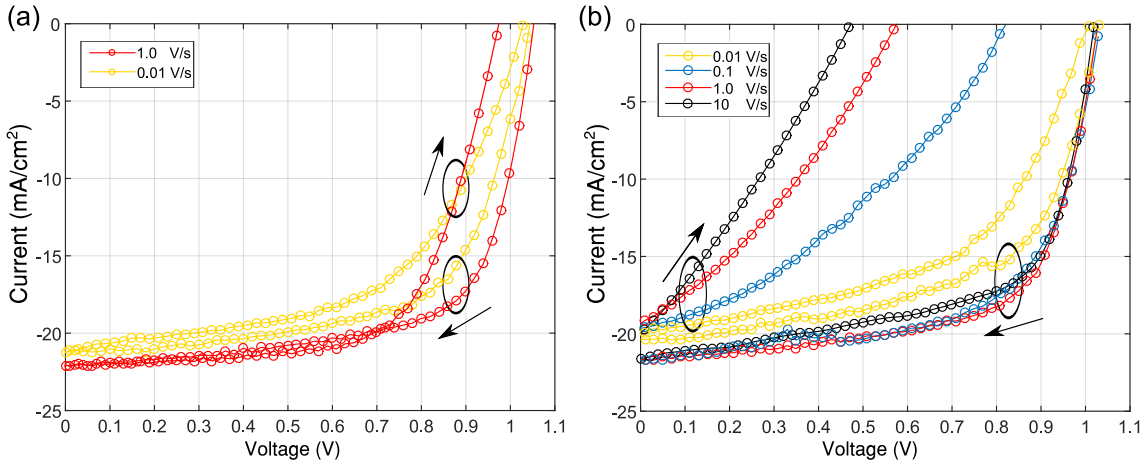

Figure 2.1: (a) I-V sweeps showing typical signatures of hysteresis, taken following periods of open-circuit biasing before each scan. Here the optimal scan rate is ambiguous, complicating comparisons between cells. (b) Rapid scan current-voltage measurements taken after pre-biasing at short-circuit (forward scan) and the stabilized open-circuit voltage (reverse scan). The trends with increasing scan rate are clearer, and appear to approach a limit representing cell performance under static accumulation.

behaviour (Fig. 2.1(a,b)). The large splitting between forward and reverse scans taken at a rapid speed demonstrates that these cells are profoundly affected by the pre-biasing conditions, and manifests qualitative features which beg for explanation (for instance, dramatically diminished voltages on the forward scan which we address shortly). The rapid-scan measurements also simplify the process of interpretation and comparison with simulation, as it is only necessary to compute two ionic distributions rather than performing fully transient simulations. The cells used in these experiments were relatively slow to stabilize, with typical settling times in the range of 10-100 s, and as a result scan rates of around $10\,\mathrm{V\,s^{-1}}$ were found to be sufficient for the rapid-scan characterization.

2.4 The Many and Varied Effects of Ion Accumulation

The modelling studies [10, 11] mentioned in our introduction were primarily concerned with explaining observations concerning the sweep-rate and pre-conditioning dependence of standard I-V measurements, emphasizing the impact of ion accumulation on the cell's internal electric field. In the "compensated field" picture [26] the primary effect of ion migration is to screen the electric field within the perovskite layer by accumulating at its interfaces, dramatically affecting carrier distributions and hence the photovoltaic current. Since their equilibration is slow, mobile ions will be accumulated at the interfaces to different degrees depending on the cell's

biasing history. As a starting point, the concept of a compensated electric field caused by ion accumulation accounts for the fundamental experimental observation of transiently lower current extraction following biasing periods at negative potential [27, 28] (i.e. $V < V_{\text{built-in}} \approx 1\,\text{V}$). Yet there remain a number of phenomena for which a basic understanding in terms of the compensated electric field proves insufficient, and it is necessary to consider in detail the effect of ion migration on carrier injection, accumulation and recombination. In the sections below we provide experimental evidence that a number of such phenomena occur in TiO_2/$MAPbI_3$/Spiro-OMeTAD solar cells. These are given mechanistic explanations based on numerical device modelling, demonstrating that the ionic theory can account for a variety of unusual electrical measurements beyond the standard rate-dependant I-V sweeps.

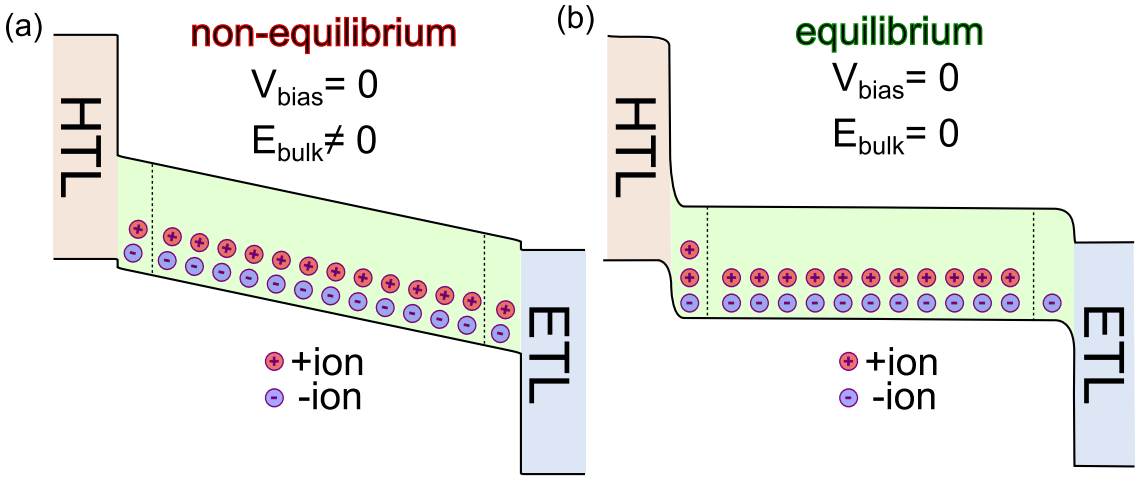

Figure 2.2: Schematic band diagram of the perovskite solar cell depicting how the motion of a single mobile species (positive here) leads to the accumulation of net positive and negative doping concentrations at the two interfaces, whilst the perovskite remains an intrinsic semiconductor in its bulk. In (a) the ions are shown in non-equilibrium positions with respect to the internal field whereas in (b) the internal field is screened after accumulation in layers of fixed width, and equilibrium is reached.

2.4.1 Surface versus bulk recombination

To begin our analysis we address the suggestion that hysteresis in PSCs cannot be attributed to mobile ions alone, but is due to a specific combination of mobile ions and interfacial traps or recombination centres [10]. In that study it was argued that whilst purely bulk recombination is capable of accounting for standard hysteresis behaviour, the required rate constants are unphysically high. We also find that surface recombination is an apparently necessary feature, but for different reasons which play an essential role in the results to follow.

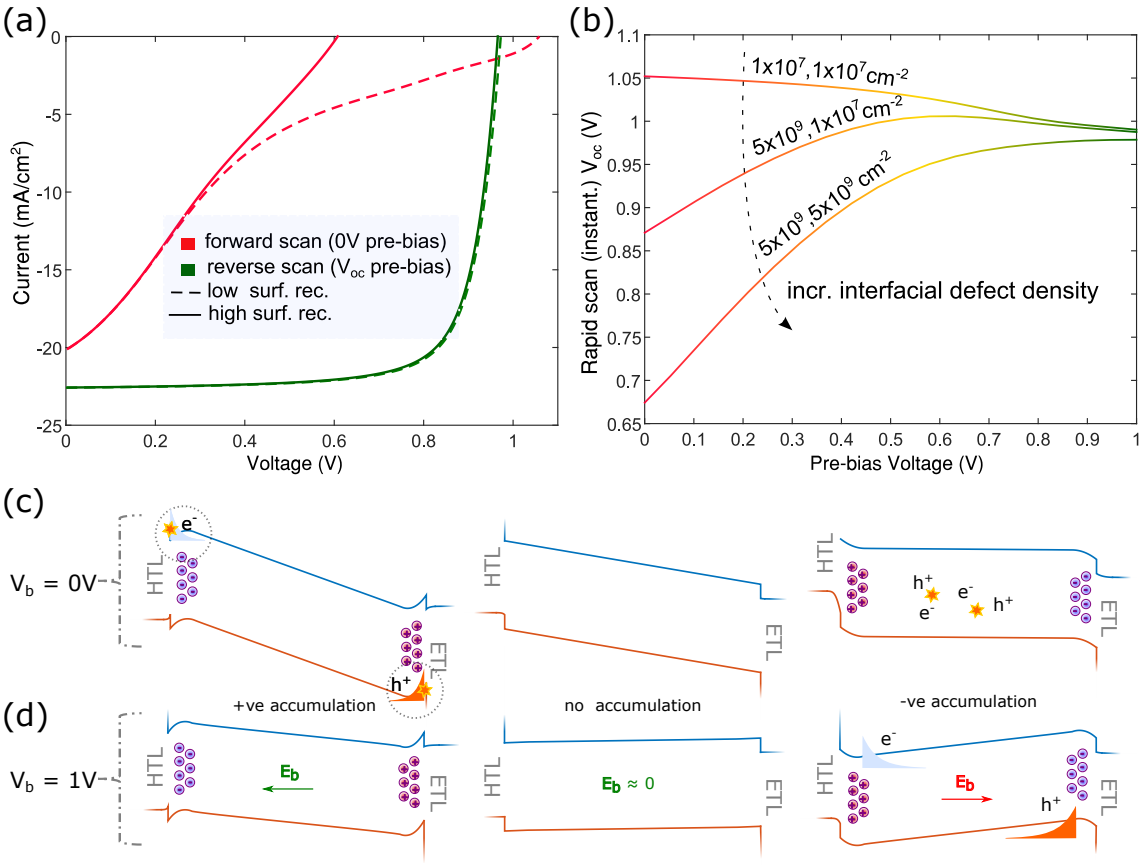

Figure 2.3: (a) Simulated rapid-scan characteristics (at instantaneous speed) for cells with high (solid) and low (dotted) rates of surface recombination corresponding to different pre-biasing voltages (equivalently degrees of negative ionic accumulation). The effect of surface recombination is most obvious in the forward scan open-circuit voltage which may be either enhanced or diminished compared to the reverse scan depending on the interfacial defect density. (b) Simulated trends in instantaneous open-circuit voltage versus pre-bias voltage showing qualitatively different behaviour depending on the interface defect density (labels correspond to defect densities at the HTL/ABS and ABS/ETL interfaces respectively). (c,d) Simulated band diagrams at 0 V (c) and 1V (d) bias demonstrating the effects of positive (left) and negative (right) ionic accumulation, as compared with no accumulation (middle). Negative accumulation (right) induces an unfavourable electric field that increases bulk SRH recombination at low bias voltages, but can lower it above the built-in voltage (e.g. near open-circuit) due to a reduced overlap in the carrier profiles relative to unaccumulated case (compare the middle and right panels in (d)). This effect explains the increased open-circuit voltage under negative accumulation seen in models with predominantly bulk-recombination (e.g. the topmost line in (b)). In (c,d,left), regions of reversed electric field or unfavourable band bending trap carriers near the wrong interface, causing increased surface recombination and hence reduced J_{sc} under positive accumulation.

Examples of simulated rapid-scan I-V measurements are shown in Fig. 2.3a subject to different degrees of surface recombination. From these results it is clear that surface recombination has a strong influence on the forward scan at high forward bias, and particularly affects its intercept or open-circuit voltage (V_{oc}). Without surface recombination the predicted forward scan voltage often exceeds that of the reverse scan, as shown in Fig. 2.3a (dotted lines), which contradicts the experimental trend represented in Fig. 2.1a. With added surface recombination (solid lines) the correct trends result, particularly in terms of the voltage, which is then drastically diminished in rapid scans following negative pre-biasing, as in experiment. The discrepancy between experiment and our simulated result with only bulk recombination in Fig. 2.3a suggests that the effect of surface recombination is apparently vital. In the following we will rationalize this observation by arguing that there are two competing effects of ion accumulation which influence the instantaneous open-circuit voltage: enhanced surface recombination due to the compensated field, and suppressed bulk recombination. Under certain circumstances this competition can lead to higher open-circuit voltages under ionic accumulation, a somewhat surprising prediction which we confirm in our transient V_{oc} measurements discussed later (Fig. 2.7).

For the remainder of this chapter it is helpful to introduce some terminology: here and in the following "negative ionic accumulation" is used to denote the state in which ions are distributed with positive ions located on the HTL side and negative ions on the ETL side of the absorber layer (we delay considering the opposite state of positive accumulation until sec. 2.4.3). Negative accumulation is to be expected if a cell is left to equilibrate at negative "internal bias" $(V - V_{\mathrm{built-in}}) < 0$.[4] Since a good cell should have $V_{\mathrm{built-in}} \approx 1\,\mathrm{V}$, most bias voltages in the power-generating quadrant of the I-V plane will cause negative ionic accumulation at equilibrium. Negative accumulation usually has a negative impact on cell performance, manifesting as instantaneously lower current extraction for cells pre-biased at 0 V as compared to those pre-biased at V_{oc} (e.g. Fig. 2.1a). This comes about because ions in negative accumulation screen the built-in field that would normally sweep photo-generated carriers out of the cell (compare Figs. 2.3(c,middle) and 2.3(c,right)). However, there are also circumstances under which negative accumulation can act to reduce recombination. Pertinent to the current discussion is the situation where a cell is measured above its built-in voltage, for instance at V_{oc}: here the electric field induced by ions under negative accumulation can instead act to reduce SRH recombination in the bulk. This occurs because the ion-induced field acts to reduce the overlap between the density of electrons and holes (Figs. 2.3(c,d)), thereby reducing the SRH recombination rate relative to homogeneous electron/hole distributions with an equal np product. This effect ex-

[4] as V refers to the potential difference across the perovskite layer the contribution of series resistances occurring elsewhere in the cell is not included.

plains why the model in Fig. 2.3a, having only bulk SRH recombination, fails to show a reduced open-circuit voltage under negative accumulation despite having reduced current over the rest of the I-V curve (which is below the built-in voltage).

Different instances of the competition between surface and bulk recombination under negative accumulation are demonstrated in Fig. 2.3b which shows the rapid-scan or instantaneous V_{oc} versus pre-bias voltage for cells with varying interfacial defect densities. These calculations show explicitly that without a significant density of interfacial defects there is a increasing trend in instantaneous open-circuit voltage with decreasing pre-bias voltage (equivalent to increasing negative ionic accumulation), whereas with high defect densities the trend is reversed. Interestingly, at intermediate densities a non-monotonic trend emerges which can be invoked to explain our measurement of non-monotonic transient open-circuit voltage (Fig. 2.7) discussed below. In summary, the inclusion of surface recombination seems indeed necessary to reproduce our experimental I-V curves, however, for a different reason than that stated in ref. [**?**] which simply invoked the relative sensitivity of recombination to bulk versus interfacial defects.

2.4.2 S-shaped I-V scans at high forward bias

We now turn to a separate but closely related rapid-scan measurement. By extending the range of our rapid-scan protocol beyond V_{oc} we obtained clear evidence that negative accumulation acts to increase the severity of surface recombination in our cells. The rapid-scan measurements of Fig. 2.4a manifest S-shaped[1] current-voltage characteristics for cells pre-biased at voltages less than 0.8 V. The location of the saturation features at approximately $J = +J_{\mathrm{sc}}$ (using the sign convention that $J(0\,\mathrm{V}) = -J_{\mathrm{sc}}$) strongly suggests that the cell's photocurrent is flowing in the forward instead of the reverse direction at high forward bias. This alone indicates significant surface recombination at both interfaces, without which it would be impossible for photocurrent to flow in the forward direction due to the large interface band offsets. The fact that the current increases only very slowly above $J = +J_{\mathrm{sc}}$ after pre-biasing at low voltages further indicates that there must be high barriers to injection which inhibit the forward current from growing further. We were able to simulate this phenomenon (Fig. 2.4b) in cells given a significant density of surface states at both interfaces (recombination velocity $\geqslant 10\,\mathrm{cm\,s^{-1}}$). This is apparently vital to reproducing the effect: only cells with both accumulated ions and surface recombination at both interfaces exhibit a forward current which saturates at $J = +J_{\mathrm{sc}}$. Cells with high interfacial defect densities but without accumulated ions retain their built-in field, which prevents the flow of photocurrent in the forward direction. On the other hand cells with high ion accumulation but a low density of interfacial defects can only drive a forward current via the injection pathway,

[1] The sense in which these are 'S-shaped' differs somewhat from previous usage: here the curves extend to high forward bias and the "levelling off" occurs at positive rather than zero current [26].

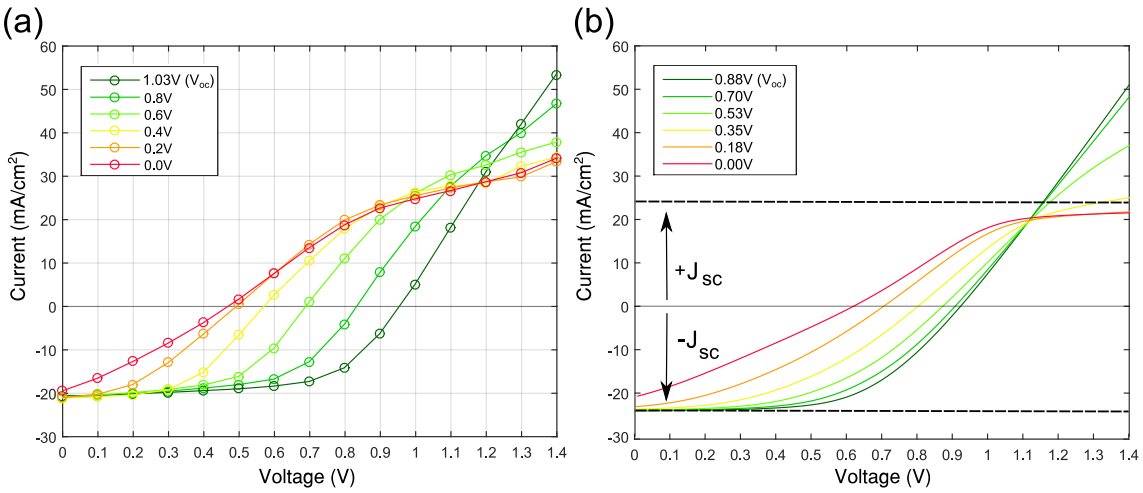

Figure 2.4: (a) Rapid ($20\,\mathrm{V\,s^{-1}}$) forward scan measurements taken after equilibration at different pre-bias voltages, showing S-shaped saturation features at high forward bias. (b) Simulated I-V curves under different conditions of ionic accumulation corresponding to pre-bias voltages shown in the legend. In this model a series resistance of 8Ω cm^2 was added to approximate the slope of the experimental curves at large bias.

and therefore there is also no S-shaped feature (Fig. 2.9). The measurement of Fig. 2.4a can therefore be regarded as simultaneous evidence for ionic accumulation and significant surface recombination at both perovskite interfaces.

2.4.3 Effect of positive accumulation

So far we have only considered negative ionic accumulation, which should occur when a PSC with mobile ions is left to equilibrate at bias voltages less than the cell's built-in potential ($V < V_{\mathrm{built-in}}$). Negative accumulation tends to reduce fill factors, J_{sc} and V_{oc}, and is therefore harmful to cell efficiency, although simulations indicate that it may lead to marginally higher open-circuit voltages under certain conditions as discussed above. The opposite state of positive accumulation may also come about if the cell is allowed to rest at positive pre-bias voltages satisfying $V > V_{\mathrm{built-in}}$. Positive accumulation is generally expected to improve cell performance according to the observation that reverse scans usually exhibit instantaneously higher currents, voltages and fill factors in PSCs (e.g. Fig. 2.1b). In Fig. 2.5a we show a set of measurements that partially violate this expectation by exhibiting lower J_{sc} in the rapid scans following forward pre-biasing, despite having higher open-circuit voltages. For this cell the effect is quite pronounced; another measurement showing a more subtle version of the same effect on a different cell is given in the SI of ref. [33] (Fig. S3†). The simulations accompanying this measurement are given in Fig. 2.5b, which shows similar fast-sweep current-voltage curves

under different degrees of both positive and negative ionic accumulation. We note that in this simulation a drastic reduction in J_{sc} under positive accumulation only emerges under high ion densities corresponding to equilibrium at approximately 1.5 V rather than the lower value of $V_{oc} \approx 1$ V as in the measurement, although there are signs of the same effect at lower densities (1.3 V pre-bias in the figure).[4] The discrepancy in pre-bias voltages between measurement and simulation could have a number of causes, but points to a deficiency in the equilibrium condition used for determining the ionic accumulation (which could be altered by the presence of additional contributions to the internal field such as that of trapped or accumulated carriers at the interface). Any other effect which would act to enhance the detrimental effect of positive accumulation could also be responsible.

Lowered current extraction (otherwise referred to as collection probability or IQE) following positive biasing has been reported recently under the name of "inverted hysteresis" [34], in which the authors invoke a reversed band-ordering at one of the interfaces to explain the phenomenon. The simulations presented here use the usual band ordering as in Fig. 2.2 and therefore preclude this explanation at least for our simulated result; instead the phenomenon can be understood directly by observing the simulated band diagrams under different conditions of accumulation as shown in Figs. 2.3(c,d,left). These simulated band diagrams show that extraction barriers at the perovskite interfaces can develop under high degrees of positive accumulation. These regions of reversed electric field or unfavourable band bending trap carriers near the wrong interface, causing increased surface recombination and hence reduced J_{sc}. The degree of the band bending is strongly affected by parameters such as the perovskite's dielectric constant and the band offsets, providing at least two examples of parameters which could influence the outcome of positive accumulation. Naturally we find that the effect is much reduced in models with a lower density of surface states (see Fig. 2.9b†). The same accumulation responsible for the loss in current causes an enhancement of the bulk electric field however (Fig. 2.2(d)), which contributes to a simultaneous improvement in open-circuit voltage. Indeed, our simulations for a small excess of positive accumulation tend to show higher conversion efficiencies than cells with either negative or no accumulation (Fig. 2.5b, labels) due to improvements in V_{oc} and fill factor. Despite their slightly higher power conversion efficiencies, the cells under positive accumulation shown in Fig. 2.5b would not be at ionic equilibrium at their maximum power points. Depending on the cell parameters our models can predict both positive and negative accumulation at the stabilized maximum power point, leading respectively to slightly enhanced and reduced conversion efficiencies, and an ambiguous answer as to how ions affect the stabilized

[4]This accounts for why the effect does not appear the in the simulation of Fig. 2.4b which extends to a maximum pre-bias voltage of only 0.88 V. We cannot at present say why the measurements of Fig. 2.4a failed to show the same effect, but this may be related to a preparation difference in the compact titania layer (solution-processed versus ALD, see the ESI†).

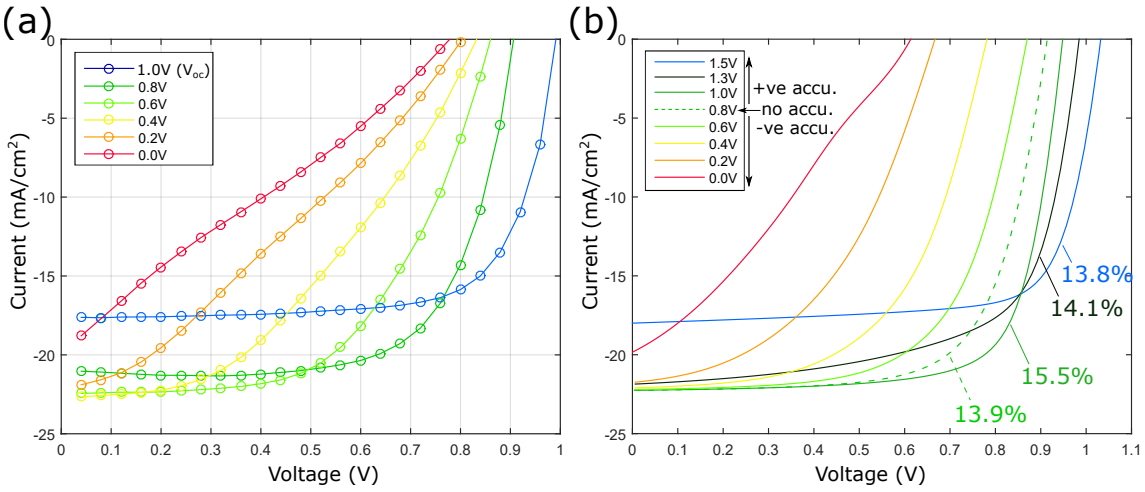

Figure 2.5: (a) Rapid forward scan measurements ($20\,\mathrm{V\,s^{-1}}$) taken after equilibration at different bias voltages given in the legend. These results exhibit reduced J_{sc} after forward biasing, or "inverse hysteresis". (b) Simulated forward scans showing the joint effects of positive and negative ion accumulation: negative accumulation reduces V_{oc} and J_{sc}, whilst positive accumulation enhances V_{oc}, but at the cost of J_{sc} under extreme positive accumulation (1.5V pre-bias in our model). Power conversion efficiencies for some of the curves are shown in the labels. (c,d) Simulated band diagrams at 0 V (c) and 1V (d) bias demonstrating the effects of positive (left) and negative (right) ionic accumulation, as compared with no accumulation (middle). Surface recombination caused by unfavourable band-bending (circled) reduces J_{sc} under severe positive accumulation, whilst the screened electric field under negative accumulation causes a similar reduction due to increased bulk recombination. At high forward bias the cell under positive accumulation enjoys the benefit of an enhanced bulk electric field (E_b) which enlarges the voltage as compared cells under no or negative accumulation.

efficiency of PSCs.

If it is correct to attribute the reduction in J_{sc} seen in the fast scan measurements of Fig. 2.5a to positive ionic accumulation, then it is noteworthy that the cell measured in Fig. 2.5a shows reduced J_{sc} after pre-biasing at only 0.8 V. This suggests that positive accumulation is already occurring at 0.8 V, and therefore that $V_{built-in} < 0.8\,V$ (by comparison the simulated cell of Fig. 2.5b has a built-in voltage of 0.82 V). If true this would imply that significant positive accumulation is occuring at the stabilized $V_{oc} \approx 1\,V$, which could therefore be considerably enhanced over its "bare value" by the presence of accumulated ions, as suggested by the trend that higher cell voltages occur in cells under positive accumulation (Fig. 2.5b). This leads us to speculate that positive ionic accumulation could be a contributor to the high open-circuit voltages of some PSCs. Although the difference between the open-circuit voltage without ions (914 mV) and in equilibrium with ions (933 mV, not shown) is hardly appreciable in the model of Fig. 2.5b, it must be noted that this model apparently underestimates the effects of positive accumulation quite significantly (given the discrepancy in pre-bias voltages noted earlier), implying the potential for larger enhancements in real cells.

2.4.4 Simulations with dynamic accumulation

Further insight into the consequences of ionic accumluation can be gained by measuring cells at a fixed bias, over time, following pre-biasing periods under different conditions. Here we report on two such measurements: one is a measurement of the dark current evolution in a cell pre-biased into negative accumulation, and another is a measurement of the photo-voltage transient following the onset of illumination. The former confirms our prediction that negative accumulation can suppress carrier injection into the cell, whilst the latter provides an explicit demonstration of the voltage enhancement under mild negative accumulation discussed earlier. These simulations were carried out by using MATLAB to perform successive SCAPS simulations using a time-varying ionic charge according to $\mathrm{d}N_{ion}/\mathrm{d}t \propto E_{bulk}$ where E_{bulk} represents a typical electric field in the perovskite layer. The timescale was left arbitrary to reflect our uncertainty about the ionic mobility, as well as other possible influences on the slow charging such as the role of the contact layers [35].

Fig. 2.6a shows the dark current evolution for two different cells measured at a fixed forward bias (1 V) after equilibration at 0 V in the dark. Under these conditions the ions are expected to begin in a state of negative accumulation before relaxing towards either a state of positive accumulation or approximate neutrality. In both cells the dark current is observed to increase dramatically over the course of this relaxation, supporting the idea that negatively accumulated ions inhibit carrier injection into the perovskite layer, and consistent with previous results [36]. However, an unexpected feature emerged which is that cells prepared with different compact

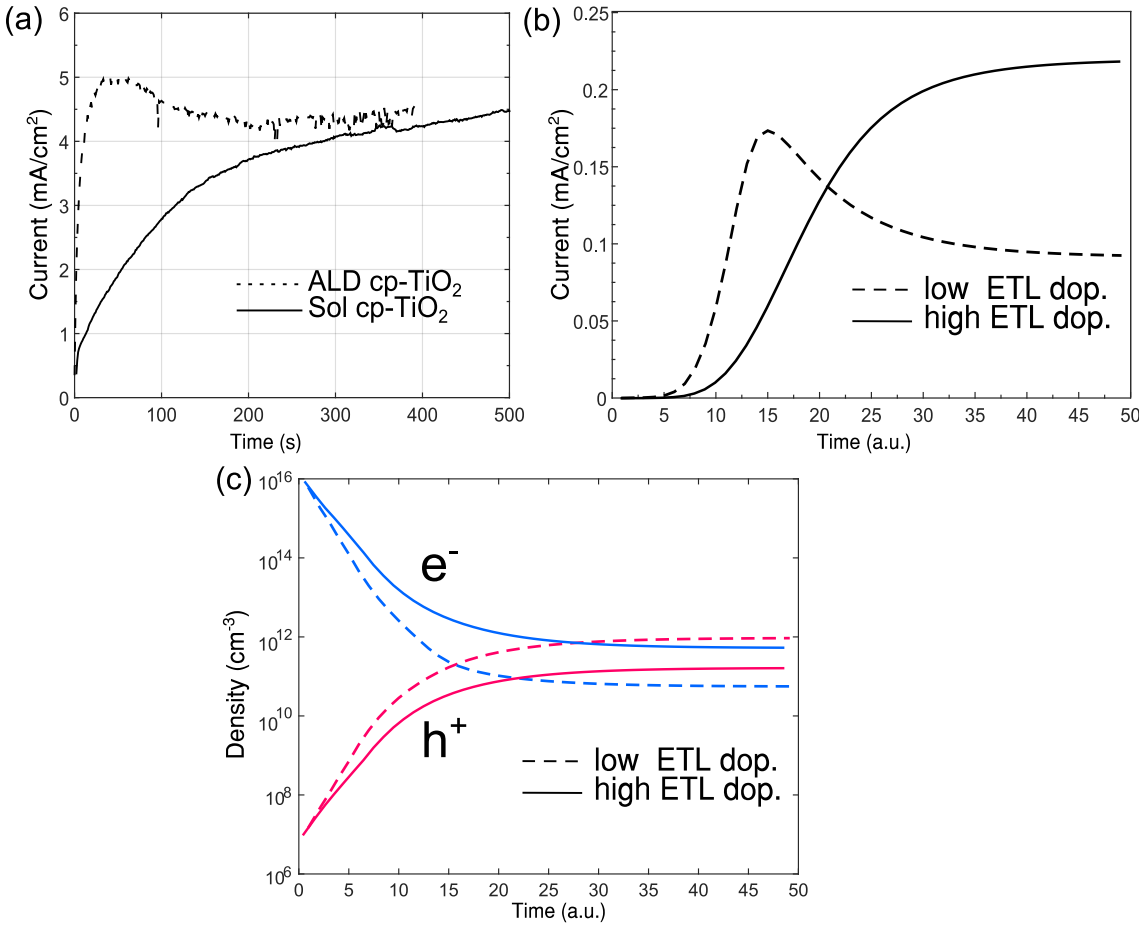

Figure 2.6: (a) Transient measurement of the dark current for cells pre-biased at 0 V, measured at 1 V. (b) Simulated dark current transients for the same biasing procedure (measured at 0.6 V due to numerical instability) predicting the non-monotonic trend in cells with low ETL doping. (c) Simulated electron and hole densities at the HTL/Perovskite interface. The electron densities are measured on the perovskite side and holes on the HTL side, making these the relevant carrier densities for surface recombination as defined earlier.

TiO_2 layers repeatedly exhibited different qualitative trends: while cells prepared with atomic layer deposition (ALD) compact (cp-) TiO_2 layers were found to respond faster and with a non-monotonic transient (Fig. 2.6a, dotted line), cells with a spin-coated cp-TiO_2 layer responded more slowly and monotonically (Fig. 2.6a, solid line). The difference in cp-TiO_2 layer preparation was determined to affect the compact layer's n-type doping level, which motivated a search for cell parameters that could account for both behaviours under a simple change in ETL doping. Such models were found, and the results from one of these are shown in Fig. 2.6b. We find that the non-monotonic behaviour can be attributed to trap-filling in cells with predomi-

nantly SRH-type non-radiative recombination. This is supported by the observation that cells simulated with purely radiative recombination always show monotonic trends under ionic accumulation (Fig. 2.11). In the model of Fig. 2.6b we include only one SRH recombination source for clarity, which is chosen to lie at the HTL/ABS interface. In this case the non-monotonic current evolution for the cell with low ETL doping can be traced to a switch-over in the limiting carrier for surface recombination from holes in the HTL to electrons in the absorber. A detailed explanation is given below.

In their initial state of negative accumulation, the ions cause a build-up of electrons at the HTL/ABS interface and a depletion of holes in the HTL layer, making holes the limiting species for recombination (Fig. 2.6c: $t = 0$). As the ions relax, the depletion decreases and more holes become available for recombination, initially enhancing the dark current in both cells (Fig. 2.6c: $0 < t < 15$). Meanwhile the surplus of electrons at the HTL interface decreases with time following the restoration of the cell's built-in field. In the cell with low ETL doping this decrease in electron density at the HTL interface eventually becomes the bottleneck for recombination, causing a gradual decrease in the dark current (Fig. 2.6c: $t > 15$). The cell with higher ETL doping injects relatively more electrons into the absorber layer however, so that holes remain the bottleneck carrier throughout the evolution and there is no switch-over. The non-monotonic behaviour therefore results once again from a competition between ionic effects on the internal electric field (which influenced the electron concentration at the interface in this example) and the injection of carriers into the absorber. In supplementary section 2.4.9 (Fig. 2.11) we show that a non-monotonic dependence on ion accumulation also appears in models with bulk rather than surface SRH recombination, but not in those with purely radiative recombination for which there is no concept of a limiting carrier.

2.4.5 Enhancement of transient photovoltage by ionic accumulation

Recording the evolution of a cell's open-circuit voltage after switching from dark to illuminated conditions often results in a monotonic increase in V_{oc} over time, which follows expectations based on the compensated field caused by negative ionic accumulation in the dark: namely, that this accumulation causes initially enhanced recombination and therefore lowered voltage until the ions relax under the influence of the forward bias $V = V_{\mathrm{oc}}$. Somewhat contrary to this expectation, we find that certain cells exhibit an increase in voltage followed by subsequent decay as shown in Fig. 2.7a. Such non-monotonic voltage transients have also been reported in other recent work [34, 37] and represent repeatable, genuine transient behaviour rather than evidence of permanent degradation. It is worth mentioning that these non-monotonic voltage transients have been observed in both pure as well as mixed halide perovskite cells in our lab. Simulations voltage transients were carried out to explore possible causes for this behaviour, one an example

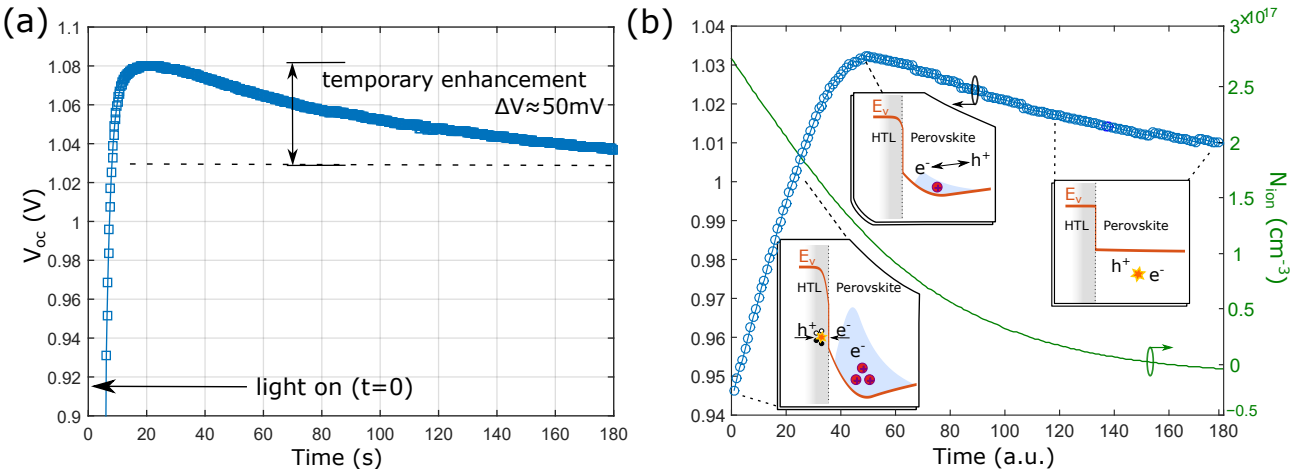

Figure 2.7: (a) Measurement of V_{oc} evolution after switching on illumination at t=0 (part of the fast initial rise for $t < 5\,\mathrm{s}$ is omitted). We interpret the maximum value as a temporary enhancement over the stabilized voltage caused by negative ionic accumulation. (b) Simulated V_{oc} (blue circles) showing non-monotonic behaviour despite the monotonically decreasing ionic charge (green line). For this cell $V_{\mathrm{built-in}} \approx 1V$, causing the ionic charge to settle to approximate neutrality ($V_{\mathrm{built-in}} - V_{\mathrm{oc}} \approx 0$). Insets illustrate the competition between surface and bulk recombination responsible for the temporary enhancement.

of which is given in Fig. 2.7b. These results exhibit a non-monotonic trend in the open-circuit voltage resembling that seen in the experimental data, despite the ions moving in only one direction from a state of negative to more positive accumulation. Indeed, the non-monotonic behaviour mirrors that shown in Fig. 2.2b for the cell with an intermediate level of surface recombination. The simulated result can be explained by noting that at $t = 0$ the cell begins in a state of high negative accumulation, leading to severe surface recombination and therefore reduced voltage. However, in their state of negative accumulation the ions act to suppress bulk SRH recombination, as seen in Fig. 2.2b, because the electrical field induced by them acts to separate electrons and holes (despite being in the "wrong direction", this separation actually has the effect of reducing the total SRH recombination rate). After an initial relaxation stage the surface recombination is reduced, and the remaining ions act to suppress bulk recombination, causing a temporary enhancement in open-circuit voltage lasting until the ions fully relax to equilibrium.

2.4.6 Accumulation Widths in the Fixed-Layer Model

To produce the simulations presented in the previous sections the ionic accumulation was assumed to occur in homogenous accumulation zones of fixed width. Since it is still uncertain

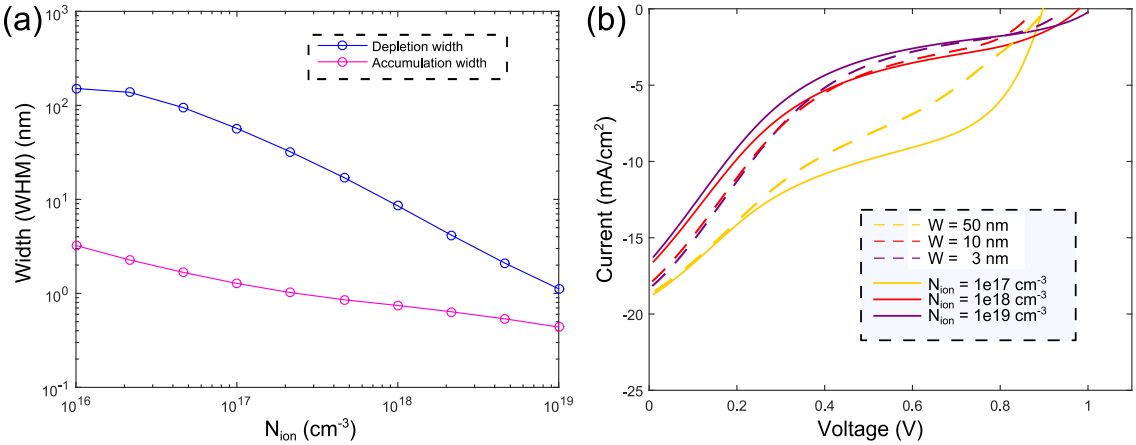

Figure 2.8: Comparing different models of ion accumulation: (a) Widths of the ionic space charge regions at each perovskite interface using the drift-diffusion equation for ion migration (with a single species one side is depleted of ions and the other sees accumulation). (b) Simulated rapid scans under negative accumulation (0 V equilibrium), showing the comparison between the drift-diffusion (solid lines) and fixed-accumulation width model (dashed lines) for a selection of ion densities and accumulation widths. There is a qualitative correspondence between the drift-diffusion results for high ion density and those of the fixed width model for small W, as expected from the trend in (a).

which ions are the dominant movers in $MAPbI_3$, and along which pathways they diffuse through the material, we believe that this simplification is justified. Here for completeness we compare the predictions of this simplified model with that of the drift-diffusion approach used in other recent work [10, 11].

The drift-diffusion equation predicts sharp accumulation zones and wider depletion zones which grow with the mobile ion density as shown in Fig. 2.8a. Whether accumulation occurs on one side of the cell or the other depends on the charge of the mobile species. To remove the complication of this asymmetry we consider accumulation and depletion within zones of equal width. As in Fig. 2.2a, Fig. 2.8b shows rapid-forward scan IV curves simulated after equilibrating the cell at 0 V, using both the drift-diffusion and homogeneous layer approximations. These results indicate that qualitative characteristics of the forward scan are mostly unaffected by the choice of accumulation model. Note that the ion density quoted in the figure corresponds to an average concentration, and that higher concentrations therefore correspond to narrower accumulation widths. It can be seen in the figure that the characteristics for the highest density using drift-diffusion qualitatively correspond to those of the narrowest width using the fixed-width approximation, and vice versa.

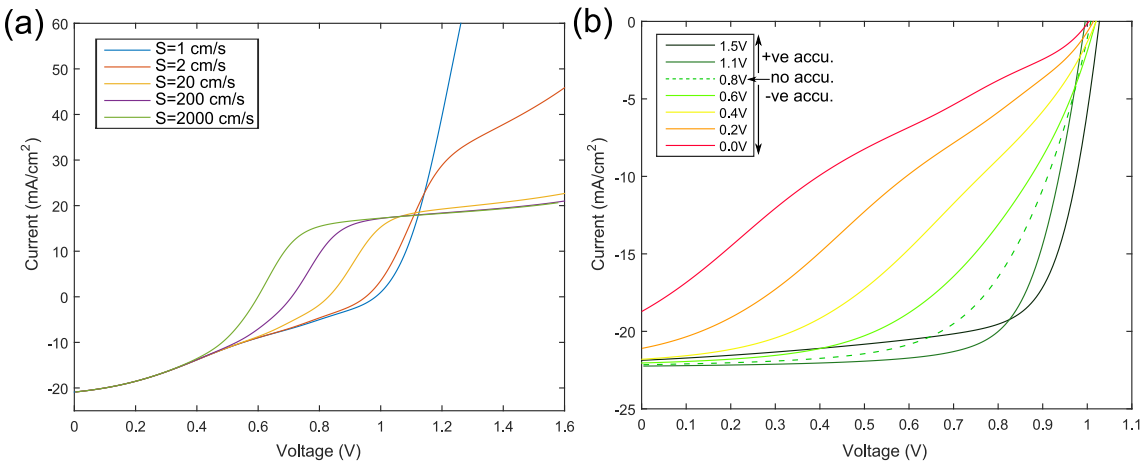

Figure 2.9: (a) Simulated rapid scans up to high forward bias as in Fig. 2.4, but this time under constant ionic accumulation (0 V pre-bias) but varying levels of surface recombination (set equal at both interfaces). The results indicate that significant surface recombination is necessary to see the S-feature. (b) Simulated rapid scans as in Fig. 2.5, but with reduced surface recombination, showing a smaller reduction in sc following forward-biasing (reduced inverse hysteresis) and less impact on the open-circuit voltages under negative accumulation.

2.4.7 Surface Recombination and S-shapes

In section 2.4.2 we discussed how surface recombination at both interfaces combines with ionic accumulation to result in the S-shaped rapid scans reported in Fig 2.4. The simulated results in Fig. 2.4b demonstrate that the negative accumulation resulting from pre-bias voltages near 0 V is one necessary feature. In Fig. 2.9a we show that high surface recombination is also necessary by calculating the same curves with fixed ion accumulation and varying interfacial recombination velocities. Given our story that the ion accumulation present in these simulations acts to suppress the injected current, it appears surprising that the curves with low surface recombination (e.g. $S = 1\,\mathrm{cm\,s^{-1}}$) exhibit large injected currents at forward bias. This is an effect of carrier accumulation within the cell, which acts to completely nullify the ionic accumulation when it reaches sufficiently large levels. In the simulations with low recombination velocities carriers accumulate to very high densities, cancelling the blocking effect of ions and allowing an injected current to flow at forward bias. Surface recombination plays an almost equally important role in the inverse hysteresis effect as illustrated in Fig. 2.9b and as discussed later in section 2.5.

It is worth noting that the S-shaped I-V curves considered here are similar to but distinct from the more familiar kind associated with rectifying or semi-rectifying contacts. These produce I-V curves which level off at $J = 0$ under illumination due to the high barrier towards current

flow in the forward direction. Ions in a condition of negative accumulation provide a similar barrier, but it is surface recombination which allows the photocurrent to flow in the forward direction, causing the level-off at $J = J_{sc}$.

2.4.8 Forward Scan Shapes

As in Fig. 2.10a, the forward scans (following 0 V pre-bias) are found to exhibit unusual shapes for some parameter choices, evoking two distinct fill factors. Some cells exhibit these shapes in experiment, although it is not clear at this stage why others display a more linear trend as in Fig. 2.1a. In our model these unusual rapid scans can be traced to the effect of extreme carrier build-up at forward bias caused by negative ionic accumulation. Becoming more severe at forward bias, the build-up of carriers eventually reaches the point where carrier-screening of the applied bias occurs. Beyond this point the applied potential drops over the interface layers rather than the perovskite itself (Fig. 2.10b). This can be verified by observing that the effect vanishes at lower illumination intensities under which carrier densities are smaller and the expected linear increase of electric field with applied bias re-emerges (Fig. 2.10c). The appearance of two separate fill factors in these curves can therefore be understood as indicating that the applied bias is dropping in different regions of the cell, first within the absorber bulk and then over the interface heterojunctions as the bias voltage is increased.

2.4.9 Non-monotonic dark current as evidence for trap-saturation

As discussed in section 2.4.4 we found that some cells exhibited non-monotonic transient behaviour when subjected to a change in bias voltage in the dark. This was attributed to the effect of trap-filling and a switch-over in the limiting carrier for SRH recombination. Figure 2.11 shows the simulated dark current (measured at 800 mV) at different levels of ionic accumulation for cells with different interface layers and subject to either SRH or purely radiative recombination. In the transient measurements and simulations of Fig. 2.7 the ions begin in the state labelled as 0 V and relax to the position labelled 0.8 V over the course of the measurement. It can be seen that only cells with SRH recombination exhibit non-monotonic behaviour, supporting our hypothesis that this comes about due to the existence of a limiting carrier for recombination which switches from holes to electrons (or vice versa) as a function of accumulation.

2.5 Inverted Hysteresis

The investigation described in section 2.4 turned up a number of curious features to do with simple I-V measurements, including the phenomenon of “inverted hysteresis”. Our explanation

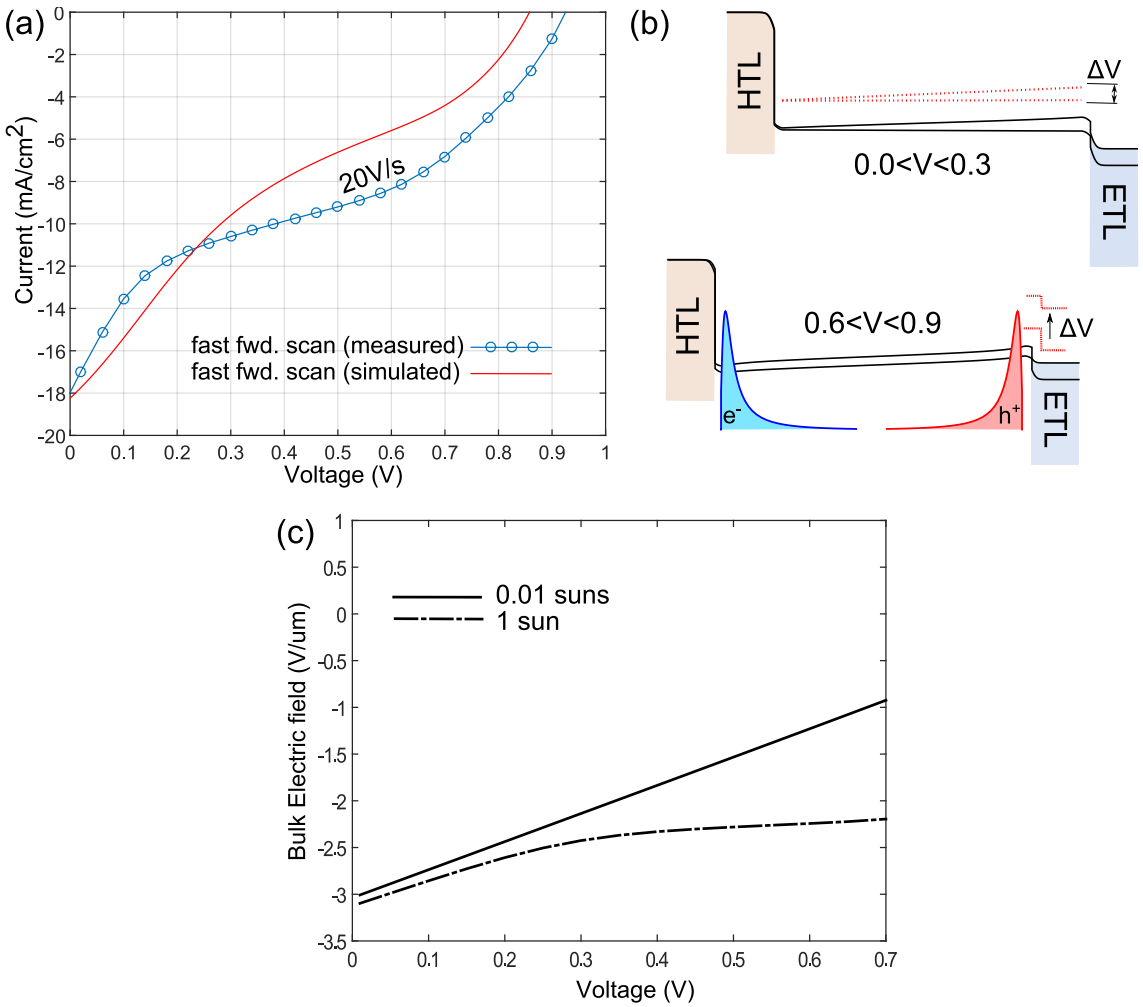

Figure 2.10: (a) Measured and simulated fast forward scans after 0 V pre-bias exhibiting unusually shaped IV curves which evoke two distinct fill factors. (b) Band diagrams (with only conduction band shown for clarity) taken from a SCAPS simulation, illustrating that the applied potential drops over different regions of the cell at different bias voltages due to the carrier build-up caused by negative ionic accumulation. (c) Bulk electric field versus bias voltage in a cell with negative ionic accumulation under low and standard illumination, providing further evidence that carrier build-up is responsible for screening the applied potential.

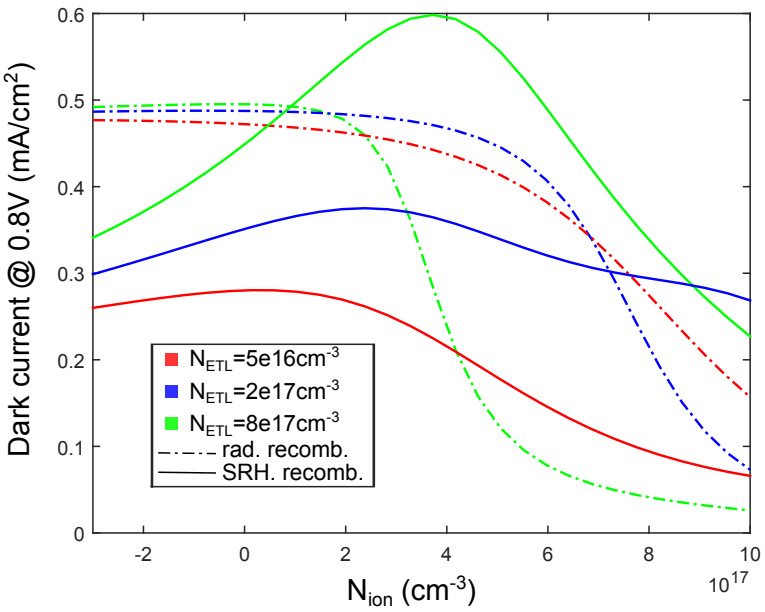

Figure 2.11: Simulated dark current at a bias of 0.8 V for cells with different modes of recombination: bulk SRH (solid line) and radiative (dotted line), indicating that non-monotonic dependence occurs only with SRH recombination. Differing trends for different values of the ETL doping show that details of interface layers may determine whether or not a non-monotonic current dependence occurs in a given cell. Here W was set to 30nm.

for this effect, provided by simulations which reproduced its main features, invoked increased surface recombination due to the ion accumulation resulting from forward-biasing a cell prior to measurement. This was somewhat at odds with a previous study (the first report of "inverted hysteresis", and the one that coined the term) [34], which instead emphasized a beneficial effect of negative accumulation in reducing an extraction barrier. Both explanations would appear to account for the basic feature of inverted hysteresis which is reduced current extraction following forward-biasing. It seemed clear however that these theories should differ somewhere in their detailed predictions. The following section describes a more focused investigation into inverted hysteresis, based on the observation that this effect appeared to emerge preferentially in cells fabricated according to certain proceedures. We uncovered one likely reason for such sensitivity by linking the stoichiometry in pure $MAPbI_3$ perovskite cells with the character of their hysteresis behaviour through the influence of internal band offsets. This study required extending the fixed-width accumulation-layer models of section 2.4 to fully-fledged drift-diffusion simulations of electrons, holes and ions (the COMSOL implementation). These were used to propose and analyze an additional mechanism leading to inverted hysteresis, distinct from the one discussed in 2.4.3, invoking accumulation of excess ionic charge in the perovskite bulk. Below we recap

some of the basic observations and concepts relevant to this study.

Typically, perovskite cells biased near their open-circuit voltage $\approx 1\,\mathrm{V}$ are granted temporarily enhanced performance as indicated by open-circuit voltage (V_{oc}), fill factor, and short-circuit current (J_{sc}) compared with those pre-biased at lower (more negative) voltages. This can be understood in terms of ionic accumulation occurring at the perovskite interfaces [26, 10, 11]: cells biased at lower voltages suffer from an accumulation of positive ions at the hole transport layer (HTL) interface and negative ions at the electron transport layer (ETL) interface which screen the cell's built-in field, hindering charge extraction. By stabilizing cells at forward bias this "negative" accumulation is averted, and instead the opposite effect of "positive" accumulation may occur, which is liable to improve photovoltaic performance by enhancing internal drift fields over most of the cell width (section 2.4). Indeed, the widely observed tendency is for perovskite cells to exhibit higher-performing J-V curves on reverse scans after biasing at open-circuit than on their forward scans [27, 38]. These expectations constitute the background to a surprising recent report that mixed ($FA_xMA_{1-x}PbI_yBr_{3-y}$) perovskite cells exhibit contrary behaviour in the form of *reduced* current extraction following forward biasing, termed "inverted hysteresis" [34]. The authors argue that this may come about when the band ordering at one of the contact interfaces (here the TiO_2 ETL) is reversed, presenting an extraction barrier for carriers moving out of the perovskite layer.

Here we identify the appearance of inverted hysteresis in pure $MAPbI_3$ cells. In light of the explanation outlined above for mixed perovskite cells this observation is surprising, since the common cell structure we employ (cp-TiO_2/mp-TiO_2/ $MAPbI_3$/Spiro-OMeTAD) is expected to feature normal band ordering at the $MAPbI_3$-TiO_2 interface [39]. To explain this phenomenon we consider two semiconductor models that attempt to account for ion accumulation, one based on the inclusion of simple doping layers (considered in 2.4.3) and the other on a drift diffusion equation for ion motion [10, 11]. Each model brings its own explanation of inverted hysteresis, one based on band bending and the other on corrections to the standard picture of ion accumulation. We use spectrally filtered J-V measurements to discriminate between these two contributions and conclude that band bending appears to be the dominant effect in our cells, although the mechanism of bulk ion accumulation could also account for inverted hysteresis in cells with unfavourable band offsets. With positive mobile charge of a relatively low density ($\approx 7 \cdot 10^{17}\,\mathrm{cm}^{-}3$) we show that significant band occurs in the drift-diffusion models, and are able to reproduce the qualitative trends of our J-V measurements in simulation. Finally, we show that the strength of the inverted hysteresis can be tuned by varying the perovskite precursor ratios, which is interpreted in terms of variations in the perovskite electron affinity [40] and the resulting effect on band offsets.

2.5.1 Rate-dependent I-V Scans

The motivating findings of this study are contained in Fig. 2.12, which displays the J-V scans of two different $MAPbI_3$ cell types taken with scan rates in the range of 0.01-10 $V\,s^{-1}$. The two cell types were fabricated via either a one- or two-step method (detail available in the ESI of ref. [**?**]) with an otherwise identical structure of FTO/cp-TiO_2/mp-TiO_2/$MAPbI_3$/Spiro-OMeTAD/Au. Crucially, the J-V scans were obtained after holding cells near open-circuit at a forward bias of 1.2 V for at least 20 s before each measurement. For both cell types, the consecutive reverse-forward scans (Fig. 2.12(a,b)) are found to exhibit normal ordering for low scan rates (0.01-0.1 $V\,s^{-1}$) in the sense that the forward scan lies below the reverse scan, and partly inverted behaviour at the higher scan rates (1-10 $V\,s^{-1}$) with crossings between the two curves. Although this trend of going from normal to inverted hysteresis with increasing scan rate is common to both cell types, the degree of inversion is consistently more pronounced in our two-step cells, as seen in Fig. 2.12b. To demonstrate that this is not necessarily an indication that the two-step procedure is simply inferior, Figs. 2.12c and 2.12d show measurements from a separate batch of cells in which both types exhibit highly comparable performance as measured at the slow speed of 10mV/s. Restricting attention to the reverse scans, Figs. 2.12(c,d) reveals that the maximum current (J_{sc}) is steadily reduced at higher scan rates, especially for the two-step cells (see insets in Figs. 2.12(c,d)). Measurements taken over several batches consistently show a larger J_{sc} reduction at higher scan rates in two-step cells, although the effect is often measurable in one-step cells as well. The reduction in J_{sc} and its scan rate dependence in Fig. 2.12d strongly suggest a penalty induced by biasing the cells at the large pre-conditioning bias of $V = 1.2$ V, one which relaxes over the course of the measurement and is therefore most pronounced at rapid scanning speeds. Such a penalty represents the central finding of these measurements, since it could easily account for the appearance of inversions in the current-voltage curves of Fig. 2.12(a,b). In detail, these inversions could be explained by increased recombination immediately following forward biasing at $V = 1.2$ V which would naturally manifest most strongly on the initial reverse scan. Whilst the scan is in progress the ions are able to relax away from their initial positions, so that by the time the forward scan is performed the accumulation causing increased recombination has diminished. At slow scan speeds the cell has more time to relax away from the forward biasing voltage, causing a reversion from inverted to normal hysteresis behaviour. Finding an explanation for the reduction in J_{sc} following forward biasing will therefore be the initial focus of our discussion.

In fact the observations of reduced current following forward biasing, as well as the characteristically linear line-shapes in Fig. 2.12d (1-10 $V\,s^{-1}$), have been noted previously (section 2.4.3) and were shown to emerge from simple models accounting for ion accumulation. These models, hereafter referred to as "doping layer" models (DLMs) for brevity, assume that ion

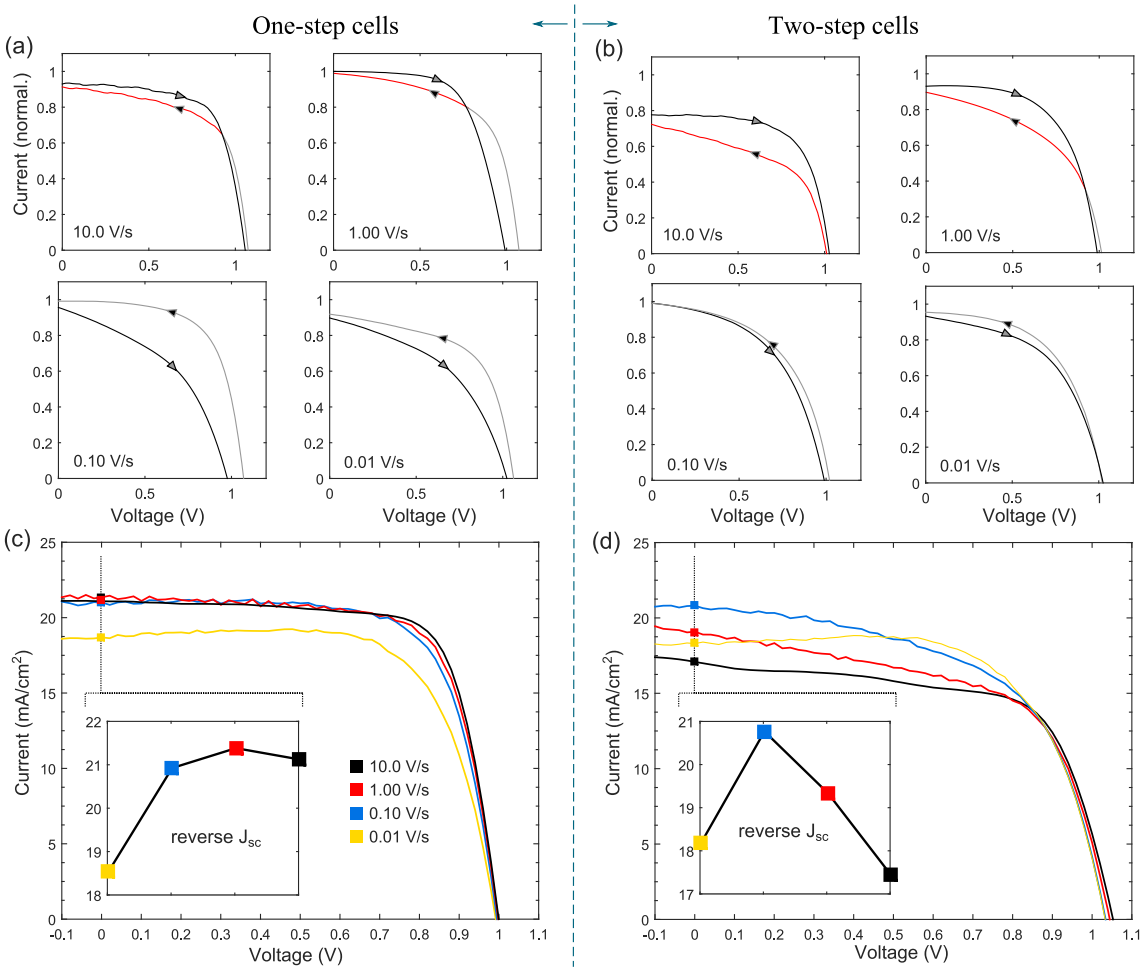

Figure 2.12: (a,b) Consecutive loop J-V scans of (a) a stoichiometric one-step cell and (b) an MAI enriched two-step cell exhibiting points of inversion (where the reverse scan lies under the forward scan, highlighted in red) at higher scan rates. The measurements were taken with endpoints at 1.2V and -0.1V after spending 20 s at the starting point of 1.2V before each loop scan. For (a) and (b) an LED illumination of 430nm wavelength and intensity $\approx$ 2 sun was used to bring out the qualitative trends (see Fig. 2.16 and associated discussion on the wavelength dependence) and to remove some of the noise generated by our solar simulator. Current is normalized with respect to its maximum value over all scan rates. In (c,d) we show just the reverse J-V sweeps taken under 1 sun illumination (AM1.5G spectrum) of a one (a) and two-step (b) cell selected from a batch where the performance of both cell types was highly similar on the slow 0.01 V s^{-1} scan. Insets show the J_{sc} values obtained from these curves versus scan rate. The measurements in (d) reveal a marked reduction in current at higher scan rates for the two-step cell, which suggests enhanced recombination induced by the forward biasing at 1.2V before each scan.

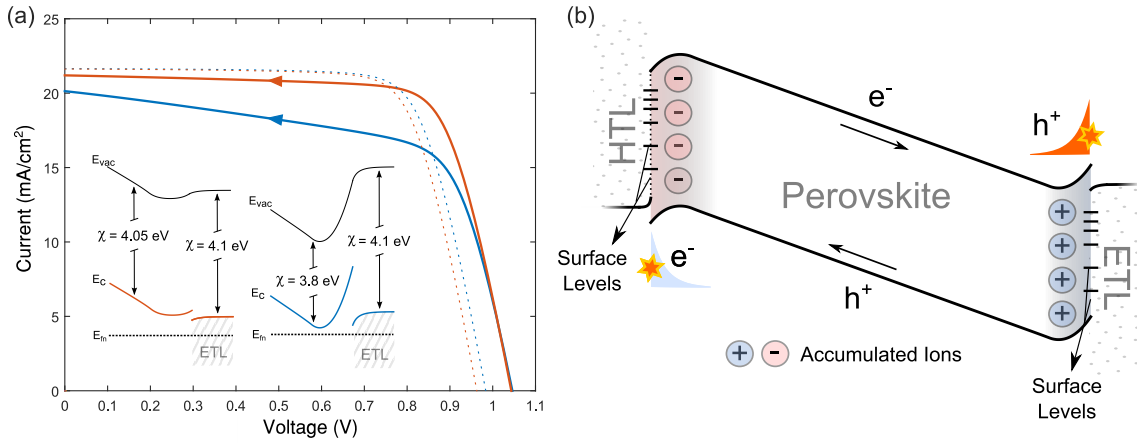

Figure 2.13: (a) Simulated reverse-scan J-V curves using the doping layer model. Ion accumulation is set to a value approximating 1.2V biasing (solid curves) and 0.6V (dotted curves). Two values of the perovskite electron affinity are used to indicate the effect of changing band offsets (colours correspond to the insets). The unfavourable band bending responsible for the current loss in this model is more significant in cells with a higher band offset (in the sense of larger $\chi_{TiO_2} - \chi_{MAPbI_3}$). (b) Band diagram from SCAPS DLM simulations showing energy levels at short circuit following equilibration (ion accumulation) at $\approx 1.2\,V$. The accumulated ions may enhance the internal drift field in the bulk but lead to unfavourable regions of reversed electric field at the interfaces, which trap carriers that subsequently recombine through surface levels.

accumulation is a process which occurs through an exchange between narrow layers located at the two perovskite interfaces, leaving the bulk perovskite free of accumulated ionic charge. This picture assumes that the mobile ionic species is charge-compensated by equal numbers of an opposing defect, a situation generally referred to as stoichiometric polarization [41]. The basic consequences of the DLM under stoichiometric polarization are easily determined with a numerical approach using thin-film solar cell simulators such as SCAPS [19]. In this approach narrow highly doped accumulation layers are first added to the interfaces of a p-i-n device model. Then, with the accumulation layer widths set to a small fraction of the total absorber width (constrained by recent measurements [42], but otherwise arbitrary), the doping/ion concentrations are uniquely determined by two key assumptions: the first being that the total ionic charge at each interface is equal and opposite, and the second that the magnitude of accumulated charge should produce flat bands (a screened electric field) in the bulk at the preconditioning voltage (1.2 V for the measurements of Fig. 2.12). Since the preconditioning voltage of 1.2 V is well above the measured built-in voltage of our cells ($\phi_{Spiro} - \phi_{TiO_2} = 5.08\,V - 4.22\,V \approx 0.9V$, see Fig. S6 in [33]), the sign of ionic accumulation is set such that positive ions are accumulated at the ETL interface.

We have used the DLM model to simulate the J-V curves shown in Fig. 2.13a, which were performed with fixed ion accumulation and therefore approximate taking measurements at fast scan rates. Notably, the reduced current and linear lineshape of the simulated blue curve in Fig. 2.13a strongly resemble the rapid reverse scan measurements of Figs. 1d. Analysing the model we find that the mechanism causing increased recombination following forward biasing is as illustrated in the band diagram of Fig. 2.13b. It is found that the ion accumulation corresponding to stabilization at 1.2 V causes band bending in the heavily doped ionic layers in the sense expected for an isotype heterojunction (note that the perovskite/ETL interface is locally n^+/n and the HTL/perovskite interface p/p^+ under forward-biased ionic accumulation). These regions of reversed electric field trap carriers generated within or near the layers at the 'wrong' interface. A large number of these carriers are then lost via recombination through surface levels, manifesting as the reduced current seen in Fig. 2.13a (solid curves) relative to the current measured after pre-biasing at a lower voltage (0.6V in dotted curves). The size of the current loss therefore depends crucially on the width of the ionic accumulation regions (primarily the region on the front side of the cell since this experiences a higher rate of generation) as well as the recombination probability within them. The 30 nm width used in the simulations of Fig. 2.13a is larger than reported estimates for $MAPbI_3$[11], although such large widths are not strictly necessary and were chosen for demonstration purposes. We will return to the issue of determining the minimal required values for these widths later in the analysis of Fig. 2.16. The potential dropping across the ionic space charge layers remains approximately constant with applied voltage due to a high carrier density, explaining the relatively slow (non-exponential) growth in recombination with voltage visible in Fig. 2.13a. Since the ions enhance the internal drift field over the remainder of the perovskite bulk (i.e. outside the ionic layers), recombination through other channels is suppressed, leading to the slight increases in open-circuit voltage in Fig. 2.13a, despite the increased recombination at lower voltages. This prediction of a variation in instantaneous V_{oc} with the pre-biasing voltage was discussed previously [43] (sec. 2.4.3) is visible in the measurements of Fig. 2.5. Since band bending plays a key role in this mechanism we find that the recombination is highly sensitive to band offsets, as demonstrated in Fig 2.13a, which includes simulations for two values of the band offset that was adjusted by varying the perovskite electron affinity.

2.5.2 Role of Band Alignment

The finding that the current loss depends sensitively on the interfacial band offsets provides a potential point of contact with the hypothesis put forward in the first report of inverted hysteresis [34], namely that inverted hysteresis results from an extraction barrier, or unfavourable band offset, at the perovskite/ETL interface. The influence of band offsets is also highly relevant given

the recent finding that the electron affinity of $MAPbI_3$ can vary widely depending on details of the preparation method [40]. Based on this finding, we will carefully consider variations in χ_{MAPbI_3} as being one among many candidates to explain the different hysteresis behaviour observed in our one and two step cells (Fig. 2.12). Curiously, the prediction of the doping layer model points in the opposite direction to the hypothesis in Tress et al. [34], since as shown in Fig. 2.13a the current loss becomes larger in these models with increasing $\chi_{TiO_2} - \chi_{MAPbI_3}$, due to the band bending effect, whereas it was previously said that the effect grows with $-(\chi_{TiO_2} - \chi_{MAPbI_3})$, due to reduced charge extraction. To address this conflict it must be noted that the DLM takes ion accumulation to occur independently of the band offsets. This may be a good approximation when the perovskite bands are in an approximately symmetrical position with respect to the ETL and HTL (as depicted in Fig. 2.13b), but cannot be expected to hold in highly asymmetrical situations such as when the perovskite bands are positioned at energies so low as to create an extraction barrier at the ETL interface. Under these conditions the accumulation of free carriers would be expected to have an effect on the ion accumulation which is not accounted for in the standard DLM.

To investigate how asymmetrical band alignments could possibly affect ion accumulation we have developed semiconductor models using a drift-diffusion equation for the motion of ions, as reported previously in the literature [10, 11]. In this way the effects of carrier accumulation, caused by unfavourable band offsets and high forward biasing, are included through the contribution of accumulated carriers to the electric field. It is not clear yet whether the drift-diffusion equation represents a highly accurate description of ion motion in $MAPbI_3$, which appears to occur along localized pathways at the grain boundaries [8], and may be influenced by interactions with the contact layers [35], but it likely represents an approximation that improves on the static DLM. The picture that emerges upon accounting for the effect of band offsets on ion accumulation is summarized in Figs. 2.14(a-c), and subsumes the previous understanding provided by the DLM. When the perovskite bands are placed symmetrically with respect to E_c^{ETL} and E_v^{HTL}, there are two narrow regions of built-up ionic charge as depicted in Fig. 2.14a, one consisting of the accumulated ionic species and the other being an ionic depletion zone that exposes the compensating charge. The size of these two regions depends inversely on the ion density and they will not be equal in general [11], but otherwise the situation resembles that depicted in Fig. 2.13b for the DLM. On the other hand the predicted ion distributions under highly asymmetrical band placement represent a significant departure from the DLM assumptions. As in the DLM simulations the band alignment was varied by changing the value of χ_{MAPbI_3} keeping χ_{TiO_2} fixed. Focusing on the case of low-lying perovskite bands (high electron affinity) for definiteness (Figs. 2.14(b,c)) the increased electron density at forward bias caused by a reduced extraction rate at the ETL introduces significant contributions to the internal electric field. The result is

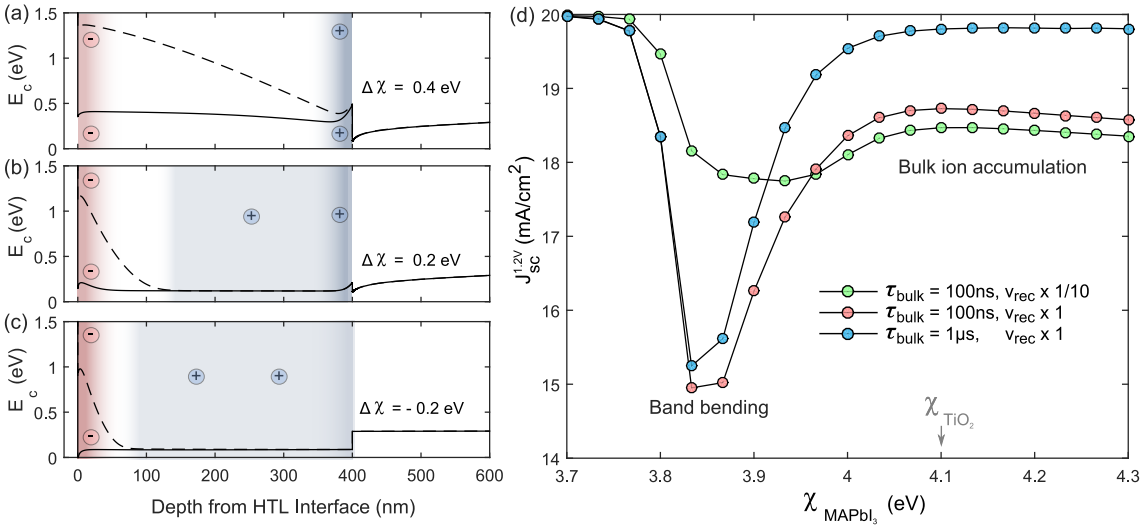

Figure 2.14: Predictions of the drift-diffusion model for ion accumulation. (a-c) Conduction band diagrams showing the effect of band offsets at the ETL interface on the resulting ion accumulation (depicted schematically here in color, exact distributions are given in Fig. 2.15) at forward bias (1.2 V as in the measurements of Fig. 2.12). The conduction bands are shown at two voltages (1 V: solid lines and 0 V: dashed lines) on a fast scan (10 V s^{-1}) from a starting voltage of 1.2 V. A dramatic difference results in terms where applied potentials appear following forward baising due to ionic accumulation in the bulk in (b) and (c). (d) Simulated reverse-scan J_{sc} (10 V s^{-1}) after forward biasing at 1.2 V using an illuminating photocurrent J_{ph} of 20 mAcm^{-2} for different values of the perovskite electron affinity. The calculations were repeated for three recombination models defined by their bulk lifetime and surface recombination velocities (detail in table 2.6). In models with significant surface recombination the dip at around $\chi_{MAPbI_3} = 3.85$ eV is larger due to the contribution of band bending to the current loss. The competing effect of an effective n-doping induced by forward biasing grows with χ_{MAPbI_3} and becomes more pronounced in models with smaller bulk lifetimes, which suffer more from the diffusion-limited transport.

that ionic charge is exchanged not between the two interfaces, but between a narrow layer near the HTL and the perovskite bulk (the exact ion distributions corresponding to Fig. 2.14 are provided in Fig. 2.15). This build-up of ionic charge in the bulk leaves most of the initially intrinsic perovskite effectively n-type following the forward biasing, and is the first prediction of its kind to our knowledge. Any subsequently applied potential therefore appears over the HTL/Perovskite p-n junction, leaving the electric field in a large portion of the cell unaffected by the applied voltage (until full depletion of the perovskite occurs at reverse bias).

Using the drift-diffusion model, the manner in which applied potentials appear across the perovskite layer immediately following forward biasing is predicted to differ according to the internal band alignments, as illustrated in Fig. 2.14(a-c). Here the conduction bands are shown

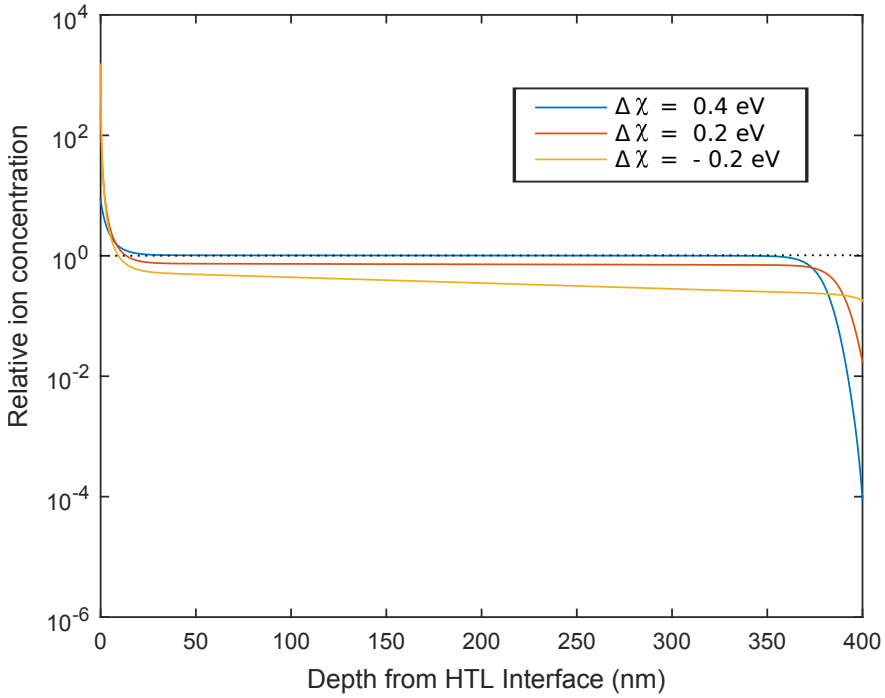

Figure 2.15: Distributions of the mobile ionic species corresponding to the band diagrams in Fig. 2.14a, obtained by biasing at 1.2 V until equilibrium was reached. The values shown are relative to the density of compensating defects, so that a concentration of 1 is perfectly compensated (zero net charge). The dashed line at 1 shows that only the cell with approximately symmetric band offsets ($\Delta\chi = 0.4\,\text{eV}$) has no net ionic charge in the bulk after biasing at 1.2V, whereas the buildup of bulk charge is significant in the other two cells. Since the mobile defect here was chosen to have a charge of -1, the net charge in the bulk is positive after forward biasing, corresponding to net n-doping. This phenomenon remains using mobile species with the opposite charge of +1, a change which primarily affects the accumulation widths.

at two representative applied potentials (1V in solid lines and 0 V in dotted lines) focusing on the perovskite/ETL interface. Perovskite cells with low-lying bands (Fig. 2.14(b,c)) responded to forward biasing by becoming temporarily n-type, forcing charges generated over most of the cell to exit via diffusion. In shifting from field-assisted to diffusion-limited charge collection the cell suffers from increased recombination in the perovskite bulk and/or through surface levels. We find that the region over which the drift field is screened can be much larger (as in Fig. 2.14c) than the interfacial regions of reversed drift field (unfavourable band bending) predicted by the DLM, which are limited in extent to the ionic space charge layers. As the electron extraction rate diminishes, the accumulation of ions in the bulk increases, causing larger regions of the cell to become diffusion-limited after forward biasing. In effect this predicts a growth of the current loss

with $-(\chi_{TiO_2} - \chi_{MAPbI_3})$, which is opposite to the DLM prediction and more in line with Tress et al. [34]. However, the effect of band-bending is still evident in the drift-diffusion calculations, and we find that it can also dramatically increase recombination at the perovskite/ETL interface as in the DLM. With respect to band alignments there are therefore two opposing contributions to the forward biasing current loss in the drift-diffusion model, one from band bending and the other from the effect of charge accumulation on the ion distributions.

As discussed with reference to the DLM model, the widths of the ionic space charge regions have a crucial effect on the recombination due to band bending depicted in Fig. 2.13b. In the drift-diffusion models these widths are determined primarily by the ion density, and the ionic depletion zone can be much wider than the accumulation or Debye length [11]. To include a significant band bending effect the simulations of Fig. 2.14a were performed with a positive mobile species (density $\approx 1 \cdot 10^{17}\,\mathrm{cm}^{-3}$, see table 2.6 for full details of the simulation) such that a wide ionic depletion zone occurs at the ETL interface under forward bias. These models allow us to investigate the competition between band bending and bulk ion accumulation, as done in the calculations of Fig. 2.14d. Here we have calculated the reverse scan ($10\,\mathrm{V\,s}^{-1}$) short-circuit current over a range of perovskite electron affinities, using different recombination models for the cell. The salient trend in Fig. 2.14d is a steady decrease in the forward-biased J_{sc} with increasing electron affinity, overlaid by a dip at intermediate values ($\chi_{MAPbI_3} \approx \chi_{TiO_2} - 0.2\,\mathrm{eV} = 3.9\,\mathrm{eV}$). The dip represents the contribution of band bending at the ETL interface as can be seen in the band diagram of Fig. 2.14b. The band bending diminishes with increasing χ_{MAPbI_3} and is also less evident when the recombination velocity at the TiO_2 interface is reduced. Apart from this contribution the current loss increases with χ_{MAPbI_3} due to the bulk ion accumulation (Fig. 2.14c), and the importance of this contribution grows with the amount of bulk recombination in the cell. The models of Fig. 2.14d are also used to simulate the J-V measurements in Fig. 2.12 and show good agreement with the DLM models at $10\,\mathrm{V\,s}^{-1}$ (Fig. 2.18), as well as faithfully reproducing the qualitative evolution with scan rate seen in Fig. 2.12(a,b).

2.5.3 Wavelength Dependence

Having developed an understanding of two potentially important factors in the appearance of inverted hysteresis, namely band bending and bulk ionic accumulation, we now return to interpreting the different behaviours exhibited by our one and two-step cells in Fig. 2.12. A common prediction across all models considered above is that the current loss following forward biasing originates from diffusion-limited regions localized on one side of the cell. In the DLM the size of these regions is pre-set, whereas in the drift-diffusion model the size and shape are determined by many factors including the ion density, the charge of the mobile species, band offsets, contact layer doping and relative dielectric constants. Nonetheless both models

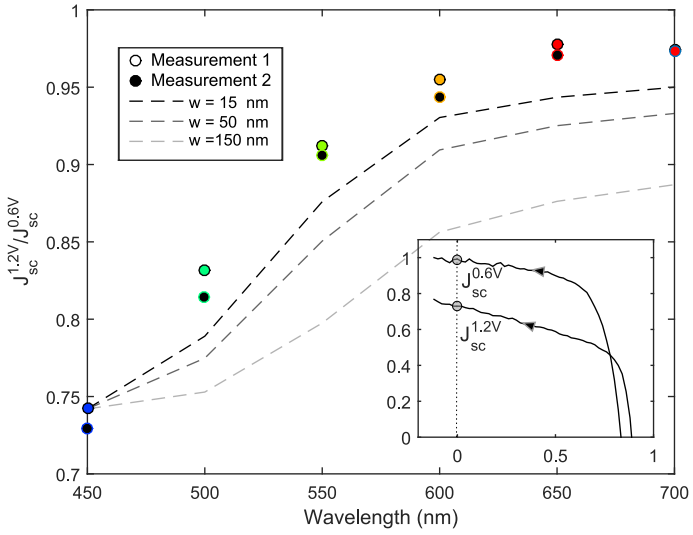

Figure 2.16: Measurements showing the effect of the illuminating wavelength on the current loss in a two-step cell. Cells illuminated with shorter wavelengths experience a larger J_{sc} loss after forward-biasing at 1.2 V expressed as a fraction of J_{sc} following biasing at 0.6 V instead. Both J_{sc} values were measured using rapid 10 V s^{-1} reverse scans starting at 1.2 V as shown in the inset. Filled and empty circles correspond to separate repeats of the same measurement (taken in different order) demonstrating that the effect is essentially reproducible. We note that expressing the current as a fraction limits the possible influence of variable light intensity, which was in any case observed to have little to no effect on the relative current loss (Fig. S5 in [33]).

predict that the current loss should increase when generation is concentrated in any one of these regions, such as when shorter wavelength light with a smaller absorption depth is used to probe the region near either interface. We have tested this prediction on our two-step $MAPbI_3$ cells using varying wavelength illumination shining in from the TiO_2 front-side. The results in Fig. 2.16 show that the recombination losses following forward-biasing increase dramatically with shorter-wavelength illumination. This is compelling evidence that there is indeed a region of high recombination forming at the $MAPbI_3$-TiO_2 interface after forward biasing. In Fig. 2.16 the J_{sc} measured on a rapid reverse scan following 1.2 V pre-biasing is expressed as a ratio of J_{sc} measured in the same manner after biasing the cell at a smaller forward voltage of 0.6 V. The ratio of these two currents $J_{sc}^{1.2V}/J_{sc}^{0.6V}$ cancels out the main factors related to external quantum efficiency and light intensity and therefore expresses differences due only to the pre-biasing voltage (including the effects of ion accumulation). A simple attempt at predicting this ratio is to assume that the $J_{sc}^{0.6V}$ value is close to the illuminating photocurrent, and that $J_{sc}^{1.2V}$ is reduced by an amount proportional to the quantity of generation occurring inside the diffusion-limited zones. The quantity $1 - J_{sc}^{1.2V}/J_{sc}^{0.6V}$ should therefore be proportional (by an unknown factor

depending on recombination probabilities within the diffusion-limited zone) to the fraction of generation occurring within the diffusion-limited zones at short-circuit. Denoting the width of the the $MAPbI_3$-TiO_2 zone at 0 V by w and absorption depth at the illuminating wavelength λ by δ_p, one then expects the following rough scaling of the current loss

$$\frac{1 - J_{sc}^{1.2V}/J_{sc}^{0.6V}|_{\lambda_1}}{1 - J_{sc}^{1.2V}/J_{sc}^{0.6V}|_{\lambda_2}} = \frac{1 - \exp(-w/\delta_{p1})}{1 - \exp(-w/\delta_{p2})} \, . \tag{2.1}$$

Predictions of this simplified model for different values of w have been added to the data of Fig. 2.16 by adjusting to the value of the measured current loss at 450 nm, and using absorption depths calculated from published optical data for $MAPbI_3$ [44]. Although the fit is not highly accurate, it can clearly be seen that smaller values of w predict a larger variation with wavelength. A minimum value of $w = 15$ nm is used since smaller widths would require a recombination probability greater than one within the diffusion-limited zone to account for the $\approx 25\%$ current loss measured at 450 nm. The measurements of Fig. 2.16 are therefore apparently more in favour of small regions (with a minimum width of 15 nm) having high recombination probability, possibly corresponding to regions of reversed electric field and high surface recombination as depicted in Fig. 2.13b and 2.14a, than the generically larger diffusion-limited regions of Figs. 2.14(b,c) predicted by bulk ion accumulation. We note that the minimum width of 15 nm should be interpreted as an effective width in a planar approximation of our mesoporous cells, and that the actual width could be significantly smaller due to the high surface area of the mesoporous scaffold. The application of these measurements to a planar cell archicture could be used to obtain a genuine lower bound on the widths of the ionic space charge layer, complementary to the upper bounds derived recently [42].

Band-bending of the kind shown in Fig. 2.13b seems to be the most likely explanation for the large wavelength-variation of $J_{sc}^{1.2V}$ in our two-step cells. Given this, we consider variations in the degree of band-bending as being a likely candidate to explain the difference between our one and two step cells (Fig. 2.12). As the band bending changes with the interfacial band offset, in the sense of diminishing with larger electron affinity, a slightly larger electron affinity in the one-step perovskite could be responsible for a smaller current loss (the simulations of Fig. 2.16 indicate that required variations would be less than 1 eV). Whilst the electronic band gap of $MAPbI_3$ is consistently reported in the range of 1.5 eV-1.6 eV, a wide variety of values have been assigned to the electron affinity, with reported values ranging from 3.6 eV to 4.8 eV [45, 46, 40]. Although ambiguity in determining the absolute values of these quantities from UV and X-ray photoelectron spectroscopy (XPS) measurements may explain some of this variability, a similarly large range of values has been recently obtained using a single protocol by varying the perovskite precursor stoichiometry and film deposition method [40]. In that work

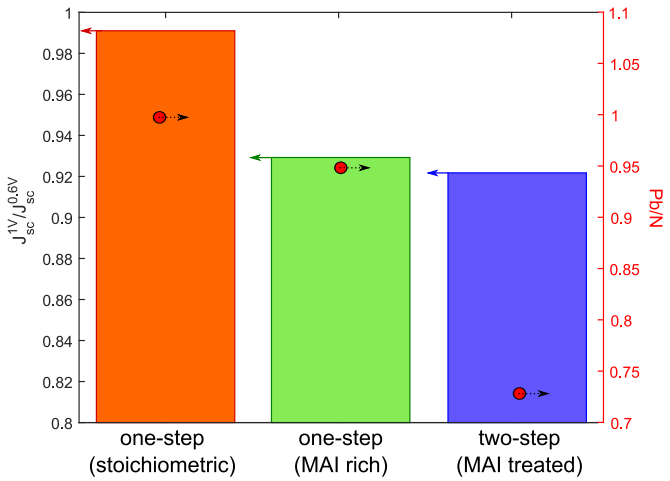

Figure 2.17: Measurements of J_{sc} after forward-biasing at 1 V showing a dependence on the film preparation. Values are expressed as a fraction of their values after biasing at a lower voltage (0.6 V). One-step cells prepared with a 5% MAI-rich precursor ratio were found to exhibit a large current loss after forward biasing ($\approx$ 7%), at a level comparable to the two-step cells ($\approx$ 8%), whose preparation includes a post-treatement step with a highly concentrated MAI. In this case the one-step cell exhibited an almost negligible J_{sc} loss of $\approx$ 1%. Composition (right axis) expresses the Pb4f to N1s ratio measured via XPS in the case of the two-step cell and the precursor ratios in the case of the one-step cells, which was independently verified to closely match the XPS result.

a correlation was found between the precursor ratio and the resulting film's binding energies, with MAI rich precursors tending to produce films of generally lower electron affinity. As the two-step procedure employed here for depositing perovksite films included a post-treatment with a highly concentrated solution of MAI, the perovskite layer in those cells is expected to be relatively MAI rich relative to that in the one-step cells. Consequently, the two-step cells are expected to feature lower values of χ_{MAPbI_3}, and therefore a greater interfacial band offset in the sense of $\chi_{TiO_2} - \chi_{MAPbI_3}$ being larger. This increased offset, and the concomitant increase in band-bending following forward biasing, plausibly explains the appearance of strongly inverted hysteresis in our two step cells.

2.5.4 XPS Measurements

XPS measurements were conducted on stoichiometric one-step and two-step films to verify the proposed variation in electron affinity (supplementary Fig. S2 in [33]). These measurements obtain the valence-band to Fermi-level separation, and therefore cannot immediately distinguish between changes in the valence band position relative to the vacuum level (electron affinity) and changes in Fermi-level position within the bands due to doping. However, our finding that the

valence-band to Fermi-level separation is higher in the MAI-rich two-step films contradicts an immediate interpretation based on doping, which would predict a lower separation due to the films becoming more p-type based on reported trends [47]. For this reason the proposed variation in the electron affinity seems to be a better explanation of the XPS measurements. As a final check on our hypothesis that stoichiometry dictates the appearance of inverted hysteresis in our chosen test structure, one-step cells were prepared with varying precursor ratios. The results shown in Fig. 2.17 depict the same normalized rapid reverse scan short-circuit current as in the wavelength test of Fig. 2.16. Here a drop in current after pre-biasing at $1V$ is again indicative of inverted hysteresis. Indeed, we find that both the two-step cells and the MAI-rich one-step cells exhibit similar behaviour in terms of the current loss after forward biasing, supporting the idea that the two-step cell's behaviour can be attributed to the MAI post-treatment. A correlation with composition was found (Fig. 2.17, right axis), as measured by the ratio of Pb4f to N1s XPS peaks, which again follows the trend predicted by our hypothesis.

2.5.5 Relation to Tress et al. 2016

Finally, we end our discussion of inverted hysteresis with some brief remarks about the relationship between ours and the preceding study by Tress et al. [34]. In that work the appearance of inverted hysteresis in mixed (MA-FA and I-Br) perovskite cells was attributed to the presence of an extraction barrier at the titania interface, due to the perovskite mixture's large electron affinity. Inverted hysteresis was also observed in $MAPbI_3$ cells prepared with a thin Al_2O_3 blocking layer on the mesoporous titania scaffold designed to artificially reduce the rate of electron extraction. Both of these observations are consistent with the understanding developed here, where we have shown that reduced electron extraction can lead to bulk ionic accumulation at forward bias, resulting in increased recombination. The mechanism of band bending also readily explains why the recombination after forward biasing should be more severe under short-wavelength illumination, whereas the previous explanation based on electron extraction rates does not. Indeed, the authors also suggested a localized increase in recombination near the titania interface following forward biasing, but the mechanism was attributed either to an additional interaction between band offsets and electron trapping, or due to recombination through levels introduced by the ionic defects themselves. The modelling was not by itself able to explain the increase in recombination after forward biasing, since it did not explicitly include the presence of ions. By including the presence of ions directly we have arrived at purely electrostatic explanations, in the sense that we only invoke the charge of the ions, and do not require that they act as significant recombination centres (although this remains a possibility). Nonetheless these models are able to explain the localized increase in recombination as well as a rich variety of hysteresis behaviours (Fig. 2.18), many of which strongly resemble both our observations and

some of the more exotic curves seen previously [34].

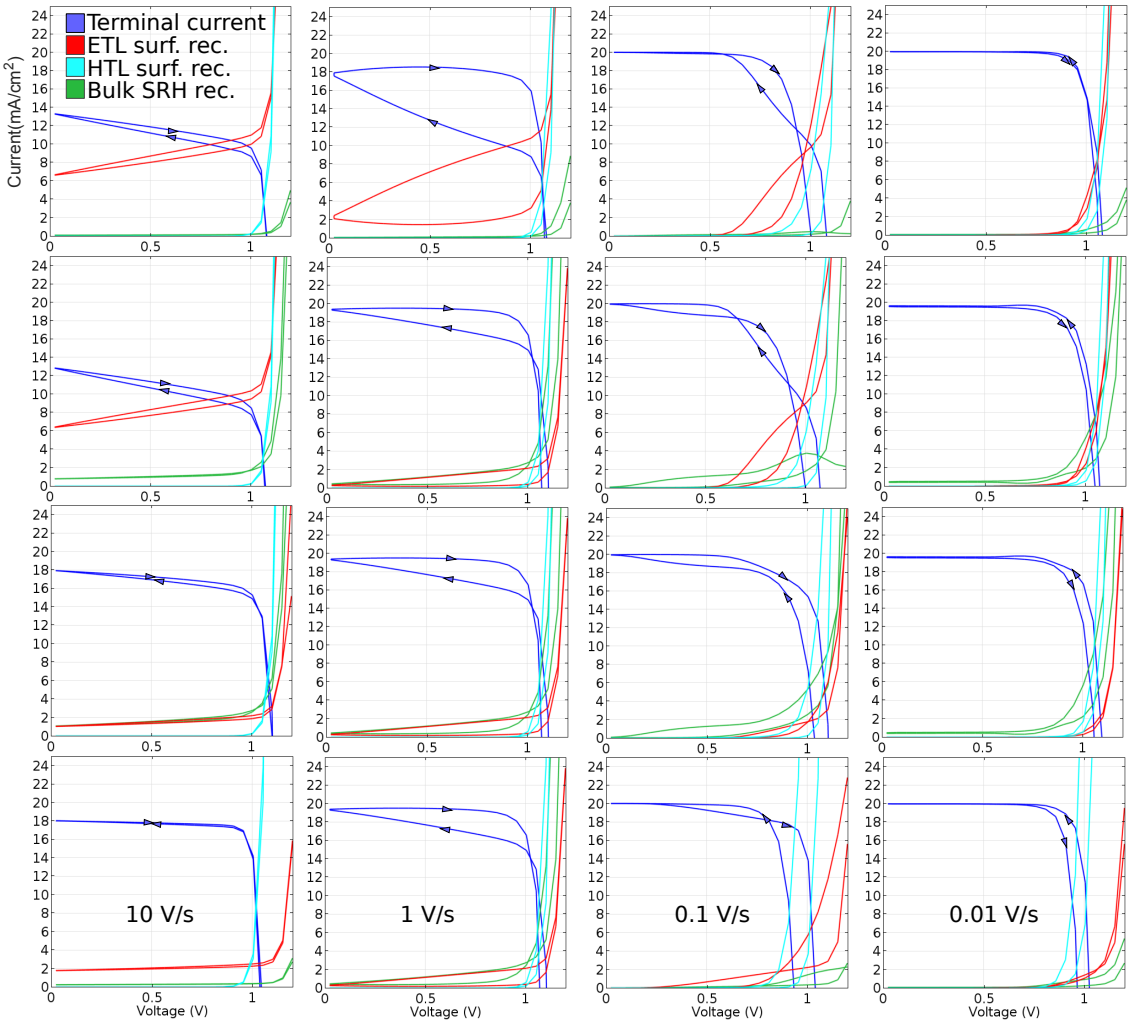

Figure 2.18: J-V scans calculated with our dynamic COMSOL model. Each row represents a separate simulation with modifications on the standard parameters in table 2.6 as listed below. Each column represents a particular scan rate (10V/s, 1V/s, 0.1V/s and 0.01V/s from left to right). The colours correspond to terminal currents in blue, with recombination currents in red, green and cyan as specified in the top left figure. Scans were performed starting from the 1.2V pre-biasing voltage, sweeping to 0V and finally back to 1.2V, closely mimicking the protocol used for the measurements of Fig. 2.1. The row parameters were as in table 2.6 with the following modifications: Row 1: standard parameters (table 2.6), which reproduce the observed trend in Fig. 2.12 of inverted hysteresis at high scan rates and normal ordering at slower speeds. Row 2: bulk lifetime to 0.1 µs. Row 3: bulk lifetime to 0.1 µs and ETL surface rec. times 1/10. Row 4: Absorber χ to 3.95 eV.

2.6 Summary and Conclusions

In this chapter we developed numerical device models to demonstrate that the ionic theory is viable as an inclusive account for hysteresis phenomena in PSCs, and not just the basic observations about rate-dependent I-V sweeps. Rapid-scan I-V characterization was used as a tool to unveil a number of unexpected behaviours relating to I-V hysteresis. This scanning protocol may not have a direct bearing on stabilized cell efficiency, but provides a window into the physical processes going on within the cell and can provide useful clues to fuel more specific investigations. We have given a new account for the importance of surface recombination in interfacting with ion accumulation to properly account for observed trends in the open-circuit voltage of cells subject to negative ionic accumulation. The observation of S-shaped rapid I-V scans provides strong evidence that significant interfacial recombination can occur at both the TiO_2/$MAPbI_3$ and $MAPbI_3$/Spiro-OMeTAD interfaces. The occurrence of "inverted hysteresis" was explained in terms of the ionic accumulation caused by biasing cells above their built-in potential. We propose that such "positive accumulation" may be responsible for enhancing the stabilized open-circuit voltage of some perovskite solar cells, although the effect of ions on stabilized efficiency remains unclear. The importance of surface recombination in explaining voltage trends, S-shaped curves and the inverted hysteresis effect clarifies the previously suggested link between interfacial trap states and hysteresis, and represents one reason to expect suppressed signatures of hysteresis in high performing cells.

Finally, non-monotonic transient behaviour in open-circuit voltage and dark current was also reproduced in a transient version of our numerical model, providing compelling evidence that these phenomena are also caused by ionic accumulation. The rate of these processes is however not well predicted by the ionic drift-diffusion theory, pointing to contributions from additional charging processes occurring at the interfaces, disordered conduction or perhaps to the existence of multiple mobile species. Nonetheless, given the number of explanatory successes this theory now enjoys, it seems likely that any microscopically distinct hypothesis for the origin of hysteresis in perovskite cells (such as that of ferroelectric behaviour) will have to resemble its device-level implications very closely. The unintuitive nature of many of the results presented here suggests that the possible contributions of mobile ions to exotic behaviour in PSCs should be carefully considered before invoking new physical phenomena.

We extended our initial investigation with a detailed study of inverted hysteresis in pure $MAPbI_3$ perovskite cells, and associated this behaviour with the detrimental effects of ion accumulation caused by biasing cells above their built-in potential. In cells with an extraction barrier at either charge-collection interface, drift-diffusion models for ionic motion predict that the effect can occur due to an accumulation of net ionic charge in the perovskite bulk, causing

carrier transport to become temporarily diffusion-limited. In cells without an extraction barrier inverted hysteresis can still occur, this time due primarily to detrimental band bending in the narrow ionic accumulation layers. We argue that the wavelength-dependence of our observations is more in favor of the band-bending contribution for our cells, and use this to explain variations in the severity of hysteresis inversions across different cell types defined by their precursor ratios. The transient semiconductor models used to analyze the inverted hysteresis correctly predict the observed variation in this effect with scan rate. Finally, our observation of a large (25%) loss in current at the wavelength of 450 nm suggests a new method for obtaining a lower bound on the ionic accumulation widths, since these would have to be of a reasonable size to generate such a large quantity of recombination.

Parameter	Layer	Value(s)	Figures	Description
ϵ_r	ABS	18 [48]	2.3-2.13	Perimittivity
E_g (eV)	ABS	1.55 [49], 1.6	2.3-2.11, 2.13	Band gap
χ (eV)	ABS	3.9, 3.8-4.3	2.3-2.11, 2.13	Electron affinity
N_c (cm^{-3})	ABS	$8 \cdot 10^{18}$, $5 \cdot 10^{18}$	2.3-2.11, 2.13	Density of states
N_v (cm^{-3})	ABS	$6 \cdot 10^{18}$, $5 \cdot 10^{18}$	2.3-2.11, 2.13	Density of states
t (nm)	ABS	320, 350	2.3-2.11, 2.13	Mobility
μ_n ($cm^2\,V^{-1}\,s$)	ABS	2	2.3-2.13	Mobility
μ_p ($cm^2\,V^{-1}\,s$)	ABS	2	2.3-2.13	Mobility
σ_n (cm^{-2})	ABS	$1 \cdot 10^{-15}$	All	Bulk SRH Cross-section
σ_p (cm^{-2})	ABS	$1 \cdot 10^{-15}$	All	Bulk SRH Cross-section
N_{td} (cm^{-3})	ABS	0, $1 \cdot 10^{16}$, $2 \cdot 10^{16}$	2.6, 2.3-2.5, 2.7	Bulk SRH Density (Neutral)
E_t	ABS	mid-gap	All	SRH Energy
W (nm)	ABS	10 , 30	2.3-2.4, All others	Ionic Accu. Width
N_D (cm^{-3})	ETL	$1 \cdot 10^{18}$, $5 \cdot 10^{17}$, $1 \cdot 10^{16}$	2.3-2.5 & 2.13, 2.6, 2.7	Donor doping
ϵ_r	ETL	31 [50]	All	Perimittivity
E_g (eV)	ETL	3.0	All	Band gap
χ (eV)	ETL	4.0-4.15	All	Electron affinity
N_c, N_v (cm^{-3})	ETL	$1 \cdot 10^{20}$, $1 \cdot 10^{20}$	All	Density of states
t (nm)	ETL	50	All	Thickness
μ_n ($cm^2\,V^{-1}\,s$)	ETL	0.1	All	Mobility
μ_p ($cm^2\,V^{-1}\,s$)	ETL	0.1	All	Mobility
N_A (cm^{-3})	HTL	$1 \cdot 10^{18}$, $5 \cdot 10^{17}$, $1.5 \cdot 10^{18}$	2.3-2.5 & 2.13, 2.6, 2.7	Net doping
ϵ_r	HTL	3 [51]	All	Perimittivity
E_g (eV)	HTL	3.0	All	Band gap
χ (eV)	HTL	1.9 [51], 2.2	2.13, All others	Electron affinity
N_c, N_v (cm^{-3})	ABS	$1 \cdot 10^{20}$, $1 \cdot 10^{20}$	All	Density of states
t (nm)	HTL	50	All	Thickness
μ_n ($cm^2\,V^{-1}\,s$)	HTL	0.1	All	Mobility
μ_p ($cm^2\,V^{-1}\,s$)	HTL	0.1	All	Mobility
D_{it} (cm^{-2})	ABS-ETL	0, $1 \cdot 10^{7}$, $1 \cdot 10^{8}$, $1 \cdot 10^{9}$, $1 \cdot 10^{10}$	2.6, 2.3, 2.7 & 2.13, 2.4, 2.3 & 2.5	Trap density
σ_p (cm^2)	ABS-ETL	$1 \cdot 10^{-15}$	All	IF SRH Cross-section
σ_n (cm^2)	ABS-ETL	$1 \cdot 10^{-15}$, $1 \cdot 10^{-13}$	2.6, 2.3, 2.7, 2.4, 2.3 & 2.5	IF SRH Cross-section
D_{it} (cm^{-2})	HTL-ABS	$1 \cdot 10^{7}$, $1 \cdot 10^{8}$, $1 \cdot 10^{9}$, $1 \cdot 10^{10}$, $5 \cdot 10^{10}$	2.3, 2.4 & 2.6, 2.13, 2.3 & 2.5, 2.7	Trap density
σ_n (cm^2)	HTL-ABS	$1 \cdot 10^{-15}$	All	IF SRH Cross-section
σ_p (cm^2)	HTL-ABS	$1 \cdot 10^{-15}$, $1 \cdot 10^{-13}$	2.3 & 2.5-2.7, 2.4	IF SRH Cross-section
ϕ_m	metal(ETL)	Flat-band	All	Work function
ϕ_m	metal(HTL)	Flat-band	All	Work function

Table 2.1: SCAPS Model parameters, chosen to emulate "normal-structure" TiO_2/$MAPbI_3$/Spiro-OMeTAD cells. These apply to our SCAPS simulations only, a separate value table is given for the COMSOL models. Values without references are estimates, with ranges chosen for illustrative purposes.

	HTL (Spiro-OMeTAD)	ABS ($MAPbI_3$)	ETL (TiO_2)
Thickness (nm)	100	400	100
Mobility ($cm^2\,V^{-1}\,s$)	$1 \cdot 10^{-3}$	2	$1 \cdot 10^{-3}$
N_c (cm^{-3})	$1 \cdot 10^{20}$	$5 \cdot 10^{18}$	$1 \cdot 10^{20}$
N_v (cm^{-3})	$1 \cdot 10^{20}$	$5 \cdot 10^{18}$	$1 \cdot 10^{20}$
N_D-N_A (cm^{-3})	-$1 \cdot 10^{17}$	0	$1 \cdot 10^{17}$
E_g (eV)	3.2	1.6	3.0
χ (eV)	1.9	3.85	4.1
ϵ_r	3	18	31

Table 2.2: COMSOL Model parameters used in Figs. 2.14, 2.15, and 2.12. Values without references are estimates, chosen for illustrative purposes.

Illuminating Photocurrent ($mA\,cm^{-2}$)	20
Optical penetration depth (nm)	50
Ion density (cm^{-3})	$7 \cdot 10^{17}$
Ion compensation (cm^{-3})	$7 \cdot 10^{17}$
Ion diffusion constant ($cm^2\,s^{-1}$)	$1 \cdot 10^{-11}$*
Charge of mobile species	-1
HTL surface rec. velocity S_n ($cm\,s^{-1}$)	1
HTL surface rec. velocity S_n ($cm\,s^{-1}$)	1
ETL surface rec. velocity S_n ($cm\,s^{-1}$)	1
ETL surface rec. velocity S_n ($cm\,s^{-1}$)	1
Bulk SRH lifetime ($\tau_n = \tau_p$) (µs)	1

Table 2.3: COMSOL Model parameters used in Figs. 2.14, 2.15, and 2.12. These values are estimates, chosen for illustrative purposes. * Intermediate between published estimates for iodine vacancy diffusion [52, 53].

Bibliography

[1] Yang, X.; Yanagida, M.; Han, L. Reliable evaluation of dye-sensitized solar cells. *Energy & Environmental Science* **2013**.

[2] Koide, N.; Chiba, Y.; Han, L. Methods of measuring energy conversion efficiency in dye-sensitized solar cells. *Japanese journal of applied physics* **2005**.

[3] Snaith, H. J.; Abate, A.; Ball, J. M.; Eperon, G. E.; Leijtens, T.; Noel, N. K.; Stranks, S. D.; Wang, J.; Wojciechowski, K.; Zhang, W. Anomalous Hysteresis in Perovskite Solar Cells. *The journal of ...* **2014**, *5*, 1511–1515.

[4] Kim, H.; Ivan, M.; Victoria, G.; Francisco, F.; J, J. E.; Park, N.; Bisquert, J. Mechanism of carrier accumulation in perovskite thin-absorber solar cells. *Nat Commun* **2013**, *4*, 2242.

[5] Li, C.; Tscheuschner, S.; Paulus, F.; Hopkinson, P. E.; Kießling, J.; Köhler, A.; Vaynzof, Y.; Huettner, S. Iodine Migration and its Effect on Hysteresis in Perovskite Solar Cells. *Advanced Materials* **2016**, *28*, 2446–2454.

[6] Yuan, Y.; Chae, J.; Shao, Y.; Wang, Q.; Xiao, Z.; Centrone, A.; Huang, J. Photovoltaic Switching Mechanism in Lateral Structure Hybrid Perovskite Solar Cells. *Advanced Energy Materials* **2015**, *5*, 1–7.

[7] W, d. D.; Zhang, W.; Burlakov, V. M.; Graham, D. J.; Leijtens, T.; Osherov, A.; Bulović, V.; Snaith, H. J.; Ginger, D. S.; Stranks, S. D. Photo-induced halide redistribution in organic-inorganic perovskite films. *Nat Commun* **2016**, *7*, 11683.

[8] Shao, Y.; Fang, Y.; Li, T.; Wang, Q.; Dong, Q.; Deng, Y.; Yuan, Y.; Wei, H.; Wang, M.; Gruverman, A.; et al. Grain boundary dominated ion migration in polycrystalline organic-inorganic halide perovskite films. *Energy & Environmental Science* **2016**, *9*, 1752–1759.

[9] Domanski, K.; Roose, B.; Matsui, T.; Saliba, M.; Turren-Cruz, S.-H.; Correa-Baena, J.-P.; Carmona, C. R.; Richardson, G.; Foster, J. M.; De Angelis, F.; et al. Migration of cations induces reversible performance losses over day/night cycling in perovskite solar cells. *Energy & Environmental Science* **2017**, *10*, 604–613.

[10] Van Reenen, S.; Kemerink, M.; Snaith, H. J. Modeling Anomalous Hysteresis in Perovskite Solar Cells. *Journal of Physical Chemistry Letters* **2015**, *6*, 3808–3814.

[11] Richardson, G.; O'Kane, S.; Niemann, R. G.; Peltola, T.; Foster, J. M.; Cameron, P. J.; Walker, A. Can slow-moving ions explain hysteresis in the current-voltage curves of perovskite solar cells? *Energy Environ. Sci.* **2016**, *9*, 1476–1485.

[12] Jüngel, A. Transport equations for semiconductors, volume 773. Springer **2009**.

[13] Zhao, T.; Shi, W.; Xi, J.; Wang, D.; Shuai, Z. Intrinsic and extrinsic charge transport in CH 3 NH 3 PbI 3 perovskites predicted from first-principles. *Scientific reports* **2016**, *6*, 19968.

[14] Frost, J. M. Calculating polaron mobility in halide perovskites. *Physical Review B* **2017**, *96*, 195202.

[15] Baccarani, G.; Jacoboni, C.; Mazzone, A. Current transport in narrow-base transistors. *Solid-State Electronics* **1977**, *20*, 5–10.

[16] Sze, S. M.; Ng, K. K. Physics of semiconductor devices. John wiley & sons **2006**.

[17] Hegedus, S. S.; Shafarman, W. N. Thin-film solar cells: device measurements and analysis. *Prog. Photovoltaics* **2004**, *12*, 155–176.

[18] Fonash, S. Solar cell device physics. Elsevier **2012**.

[19] Burgelman, M.; Nollet, P.; Degrave, S. Modelling polycrystalline semiconductor solar cells. *Thin Solid Films* **2000**, *361*, 527–532.

[20] Fonash, S. J. Band structure and photocurrent collection in crystalline and polycrystalline pn heterojunction solar cells. *Solid-State Electronics* **1979**, *22*, 907–910.

[21] Habasaki, J.; Leon, C.; Ngai, K. Dynamics of glassy, crystalline and liquid ionic conductors. *Top Appl Phys* **2017**, *132*.

[22] Shao, Y.; Fang, Y.; Li, T.; Wang, Q.; Dong, Q.; Deng, Y.; Yuan, Y.; Wei, H.; Wang, M.; Gruverman, A.; et al. Grain boundary dominated ion migration in polycrystalline organic–inorganic halide perovskite films. *Energy Environ Sci* **2016**, *9*, 1752–1759.

[23] Kröger, F.; Vink, H. Relations between the concentrations of imperfections in solids. *Journal of Physics and Chemistry of Solids* **1958**, *5*, 208–223.

[24] Walsh, A.; Scanlon, D.; Chen, S.; Gong, X. Self-Regulation Mechanism for Charged Point Defects in Hybrid Halide Perovskites. *Angewandte ...* **2015**.

[25] Mrowec, S. Defects and diffusion in solids: an introduction, Volume 5. Elsevier Scientific Pub. Co., 1980 **1980**.

[26] Tress, W.; Marinova, N.; Moehl, T.; Zakeeruddin, S. M.; Mohammad K., N.; Grätzel, M.; Nazeeruddin, M. K.; Grätzel, M. Understanding the rate-dependent J–V hysteresis, slow time component, and aging in CH 3 NH 3 PbI 3 perovskite solar cells: the role of a compensated electric field. *Energy Environ. Sci.* **2015**, *8*, 995–1004.

[27] Snaith, H. J.; Abate, A.; Ball, J. M.; Eperon, G. E.; Leijtens, T.; Noel, N. K.; Stranks, S. D.; Wang, J. T. W.; Wojciechowski, K.; Zhang, W. Anomalous hysteresis in perovskite solar cells. *Journal of Physical Chemistry Letters* **2014**, *5*, 1511–1515.

[28] Unger, E. L.; Hoke, E. T.; Bailie, C. D.; Nguyen, W. H.; Bowring, A. R.; Heumüller, T.; Christoforo, M. G.; McGehee, M. D. Hysteresis and transient behavior in current–voltage measurements of hybrid-perovskite absorber solar cells. *Energy & Environmental Science* **2014**, *7*, 3690–3698.

[29] Kim, H. S.; Park, N. G. Parameters affecting I-V hysteresis of CH3NH3PbI3 perovskite solar cells: Effects of perovskite crystal size and mesoporous TiO2 layer. *Journal of Physical Chemistry Letters* **2014**, *5*, 2927–2934.

[30] Sanchez, R. S.; Mas-Marza, E. Light-induced effects on Spiro-OMeTAD films and hybrid lead halide perovskite solar cells. *Solar Energy Materials and Solar Cells* **2016**.

[31] Almora, O.; Aranda, C.; Zarazúa, I.; Guerrero, A.; Garcia-Belmonte, G. Non-capacitive Hysteresis in Perovskite Solar Cells at Room Temperature. *ACS Energy Letters* **2016**, *1*, 209–215.

[32] Wu, Y.; Shen, H.; Walter, D.; Jacobs, D.; Duong, T.; Peng, J.; Jiang, L.; Cheng, Y.-B.; Weber, K. On the Origin of Hysteresis in Perovskite Solar Cells. *Advanced Functional Materials* **2016**.

[33] Shen, H.; Jacobs, D. A.; Wu, Y.; Duong, T.; Peng, J.; Wen, X.; Fu, X.; Karuturi, S. K.; White, T. P.; Weber, K.; et al. Inverted Hysteresis in CH3NH3PbI3 Solar Cells: Role of Stoichiometry and Band Alignment. *The journal of physical chemistry letters* **2017**, *8*, 2672–2680.

[34] Tress, W.; Correa Baena, J. P.; Saliba, M.; Abate, A.; Graetzel, M. Inverted Current–Voltage Hysteresis in Mixed Perovskite Solar Cells: Polarization, Energy Barriers, and Defect Recombination. *Advanced Energy Materials* **2016**, 1600396.

[35] Levine, I.; Nayak, P. K.; Tse, J.; Wang, W.; Sakai, N.; Van Reenen, S.; Brenner, T. M.; Mukhopadhyay, S.; Snaith, H. J.; Hodes, G.; et al. Interface-Dependent Ion Migration/Accumulation Controls Hysteresis in MAPbI 3 Solar Cells. *J. Phys. Chem. C* **2016**, *120*, 16399–16411.

[36] Wu, B.; Fu, K.; Yantara, N.; Xing, G.; Sun, S.; Sum, T. C.; Mathews, N. Charge Accumulation and Hysteresis in Perovskite-Based Solar Cells: An Electro-Optical Analysis. *Advanced Energy Materials* **2015**.

[37] Calado, P.; Telford, A. M.; Bryant, D.; Li, X.; Nelson, J.; Brian, C.; Regan, O.; Barnes, P. R. F. Evidence for ion migration in hybrid perovskite solar cells with minimal hysteresis. *arXiv:cond-mat.mat-sci/1606.00818* .

[38] Unger, E.; Hoke, E.; Bailie, C.; Nguyen, W.; Bowring, A.; Heumüller, T.; Christoforo, M.; MD, M. Hysteresis and transient behavior in current–voltage measurements of hybrid-perovskite absorber solar cells. *Energy Environ Sci* **2014**, *7*, 3690–3698.

[39] Lindblad, R.; Bi, D.; Park, B.-w.; Oscarsson, J.; Gorgoi, M.; Siegbahn, H.; Odelius, M.; Johansson, E.; Rensmo, H. Electronic Structure of TiO2/CH3NH3PbI3 Perovskite Solar Cell Interfaces. *J Phys Chem Lett* **2014**, *5*, 648–653.

[40] Emara, J.; Schnier, T.; Pourdavoud, N.; Riedl, T.; Meerholz, K.; Olthof, S. Impact of Film Stoichiometry on the Ionization Energy and Electronic Structure of CH3NH3PbI3 Perovskites. *Advanced Materials* **2016**, *28*, 553–559.

[41] Yang, T.; Gregori, G.; Pellet, N.; Grätzel, M.; Maier, J. The Significance of Ion Conduction in a Hybrid Organic-Inorganic Lead-Iodide-Based Perovskite Photosensitizer. *Angew. Chem. Int. Ed.* **2015**, *127*, 8016–8021.

[42] Belisle, R.; Nguyen, W.; Bowring, A. Interpretation of Inverted Photocurrent Transients in Organic Lead Halide Perovskite Solar Cells: Proof of the Field Screening by Mobile Ions and Determination of the Space Charge Layer Widths. *Energy Environ. Sci.* **2017**, *10*, 192–204.

[43] Jacobs, D. A.; Wu, Y.; Shen, H.; Barugkin, C.; Beck, F. J.; White, T. P.; Weber, K.; Catchpole, K. R. Hysteresis phenomena in perovskite solar cells: the many and varied effects of ionic accumulation. *Physical Chemistry Chemical Physics* **2017**, *19*, 3094–3103.

[44] Löper, P.; Stuckelberger, M.; Niesen, B.; Werner, J. Complex Refractive Index Spectra of $CH_3NH_3PbI_3$ Perovskite Thin Films Determined by Spectroscopic Ellipsometry and Spectrophotometry. *J. Phys. Chem. Lett.* **2015**, *6*, 66–71.

[45] Olthof, S. Research Update: The Electronic Structure of Hybrid Perovskite Layers and Their Energetic Alignment in Devices. *APL Mater.* **2016**, *4*, 091502.

[46] Endres, J.; Egger, D. A.; Kulbak, M.; Kerner, R. A.; Zhao, L.; Silver, S. H.; Hodes, G.; Rand, B. P.; Cahen, D.; Kronik, L.; et al. Valence and Conduction Band Densities of States of Metal Halide Perovskites: A Combined Experimental-Theoretical Study. *J. Phys. Chem. Lett.* **2016**, *7*, 2722–2729.

[47] Wang, Q.; Shao, Y.; Xie, H.; Lyu, L.; Liu, X.; Gao, Y.; Huang, J. Qualifying Composition Dependent P And N Self-Doping in $CH_3NH_3PbI_3$. *Appl. Phys. Lett.* **2014**, *105*, 163508.

[48] Samiee, M.; Konduri, S.; Ganapathy, B.; Kottokkaran, R.; Abbas, H. A.; Kitahara, A.; Joshi, P.; Zhang, L.; Noack, M.; Dalal, V. Defect density and dielectric constant in perovskite solar cells. *Applied Physics Letters* **2014**, *105*, 153502.

[49] Lee, M. M.; Teuscher, J.; Miyasaka, T.; Murakami, T. N.; Snaith, H. J. Efficient Hybrid Solar Cells Based on Meso-Superstructured Organometal Halide Perovskites. *Science* **2012**, *338*, 643–647.

[50] Tang, H.; Prasad, K.; Sanjines, R.; Schmid, P.; Levy, F. Electrical and optical properties of TiO2 anatase thin films. *Journal of applied physics* **1994**, *75*, 2042–2047.

[51] Poplavskyy, D.; Nelson, J. Nondispersive hole transport in amorphous films of methoxy-spirofluorene-arylamine organic compound. *Journal of Applied Physics* **2003**, *93*, 341–346.

[52] Eames, C.; Frost, J. M.; Barnes, P. R.; O'regan, B. C.; Walsh, A.; Islam, M. S. Ionic transport in hybrid lead iodide perovskite solar cells. *Nature communications* **2015**, *6*, 7497.

[53] Yang, T.-Y.; Gregori, G.; Pellet, N.; Grätzel, M.; Maier, J. The significance of ion conduction in a hybrid organic–inorganic lead-iodide-based perovskite photosensitizer. *Angewandte Chemie* **2015**, *127*, 8016–8021.

Chapter 3

Electrical Impedance Spectroscopy

3.1 Introduction

In the previous chapter we demonstrated the efficacy of ionic device models in accounting for the varied manifestations of I-V hysteresis in PSCs. However, rate-dependent I-V measurements leave much to be desired in terms of providing quantitative information. Various arbitrary choices in the scanning protocol (such as scan direction and pre-biasing conditions), as well as in the process of extracting information from the resulting curves (which are clearly too complex and varied to be parametrized by any small number of variables), render the technique mostly of use for qualitative comparisons. An effective solution to this problem is to instead study "local" behaviour around a single biasing point (V, J_{ph}) (applied voltage and illumination) in a small-signal measurement. This firstly solves the protocol ambiguity since the device should clearly be stabilized at (V, J_{ph}) prior to the measurement – no other choice presents itself. Second, it is far easier to completely quantify a small-signal response since at most two real variables are required (amplitude and phase for example). The small-signal counterpart of an I-V measurement is known as Electrical Impedance Spectroscopy (EIS), and entails measuring the current (or voltage) response of a device with respect to small perturbations in the applied voltage (or current, resp.). The behaviour of the linear response function can then be quantitatively studied as a function of frequency, at one or more biasing points (V, J_{ph}), to develop a detailed picture of the (linear) transient response.

Several additional reasons can be given for studying the application of EIS to PSCs. One is that although I-V curves are a mainstay of PV characterization, the most relevant aspect of a solar cell's current-voltage response is its behaviour around the maximum power point. Hysteresis will only be relevant in real-world applications to the extent that it influences maximum-power-point tracking, which occurs in the vicinity of V_{mpp}. The relevant transient behaviour can thereby be studied in detail by performing EIS measurements at V_{mpp} and 1-sun intensity (sec. 3.8). Another advantage is that the detailed frequency-dependent information afforded by EIS makes it easier to distinguish capacitive currents (i.e. those due to charging of the electrodes) from other transient processes in the cell. This is not readily done in I-V measurements, and we had to gloss over these contributions somewhat in our treatment of the rapid-scan measurements

in Chapter 2 (this approach is however justified in the final analysis by noting the small size of the high-frequency capacitive response at the scan rates considered – see sec. 3.8).

Finally, EIS provides an approachable testing-ground for further evaluating the models of Chapter 2. Indeed, there are several studies in the perovskite literature that contradict our current approach of describing hysteresis in terms of the ionic effect on charge collection (recombination more generally), suggesting instead that the effect is essentially capacitive (see e.g. [1, 2, 3, 4]). Others have pushed back against these claims (e.g. [5, 6, 7]), but have not explicitly demonstrated models or theories that are equally adequate in the domains of I-V hysteresis and EIS measurements. Prior to the work of this chapter, we are not aware of any attempt to simulate EIS measurements, by contrast with the many modelling studies on time-domain phenomena [8, 9, 10, 11, 12]. Instead, papers employing EIS generally rely on the use of equivalent circuits. Unfortunately, fitted parameters are rather useless if they cannot be confidently assigned to meaningful material and device properties, and there is no way to confidently assign these on the basis of circuit elements alone (whose choice is often highly non-unique). In this chapter we therefore give little time to considering appropriate equivalent circuits, and focus instead on obtaining correct physical interpretations for EIS measurements.

3.2 Outline

A brief summary of some of the questions to which EIS has been applied is given in sec. 3.3 (more detailed and critical discussion of the relevant literature is given in secs. 3.5.2 and 3.6). We begin by establishing a rigorous basis for interpreting measurements of capacitance by distinguishing charge-storage from other components of the capacitance in section 3.4.5. Common terminology relating to the charge-storage capacitance is defined in sec. 3.4.6. The theory of section 3.4.5 is then applied to establishing sound explanations for several observations of interest in secs. 3.5.2 (light-induced capacitance), 3.5.3 (loop features), and 3.5.4 (negative capacitance at low-frequencies). Having covered the main roles played by delayed recombination in capacitance measurements, we return to the familiar notions of charge storage to discuss high-frequency C-V measurements in sec. 3.6, and the ionic capacitance in 3.7. Finally, we discuss a simple application of EIS measurements to quantify hysteresis in sec. 3.8 and their advantages over the conventional I-V hysteresis indices.

3.3 A Conflicted Literature

EIS measurements have been called to give evidence on almost all major aspects of perovskite device physics, from built-in voltages and doping densities [13, 14], to interface couplings [15, 16],

defect densities [17, 18], recombination mechanisms [19, 20, 21] and density of states [22]. Unfortunately, the relative ease of performing these measurements, as compared with the difficulty of verifying a given interpretation, is such that there are now a great number of conflicting claims in the literature. A related issue is that discrepant interpretations have arisen for frequency-domain measurements on the one hand, and for time-domain measurements including I-V hysteresis on the other, which should be related via the Fourier transform and not by a change in physical picture. Here we give a brief overview of the conflicted state of the current literature on EIS as applied to perovskite cells in order to motivate the remainder of this chapter, which aims at clarifying these issues.

Early papers on this topic were largely attempts to better understand the working principles of PSCs using EIS coupled with a set of interpretations developed for organic and dye-sensitized cells (DSCs). One of the earliest [23] explicitly used an equivalent circuit developed for DSCs to fit the spectra of a $MAPbI_3$ cell under illumination, employing a transmission line element to fit the low-frequency feature. Ion migration was not recognized at this time, so the low-frequency feature was mistakenly attributed to carrier diffusion and the fitting used to obtain a carrier diffusion length. In relation to this suggestion we note that the timescale for carrier diffusion, $L^2/\mu_{n,p}$, with L the device thickness, is of order 0.1 ns (assuming $\mu_{n,p} \approx 10\,\mathrm{cm^2\,V^{-1}\,s}$), and therefore far too short to have anything to do with the low-frequency feature at $\approx$1 Hz. In another study, dielectric relaxation (i.e. local rearrangement of microscopic dipoles, rather than long-ranged ionic transport) was also considered a possibility for explaining the low-frequency feature [24]. To the contrary, a recent detailed study of the dielectric response puts the timescale for dielectric relaxation in the gigahertz range [25]. The importance of ions for the low-frequency response was perhaps first recognized in another DSC-based study [26], but not given much consideration in the equivalent-circuit fitting therein. In particular, the coupling between ion dynamics and collection efficiency and/or charge injection was not considered.

The ionic origin of the low-frequency feature was first discussed extensively by Bag et al. [27]. Once again however, the arguments in ref. [27] effectively presume that the electronic and ionic contributions are decoupled. This lead to the conclusion that an enhanced ionic feature under illumination must stem from light-activated ion migration, rather than the physically simpler explanation that ions affect the collected photocurrent, and therefore yield a response that scales proportionally with the light intensity (sec. 3.5.2). The neglect of coupling between ionic and electronic dynamics is a common mistake in the older EIS studies, and completely unwarranted given the strong effect of ion accumulation on internal fields (Chapter 2). Without such coupling the capacitive currents induced by ion accumulation would be far too small to account for I-V hysteresis (see for example the arguments in ref. [5]). More credible evidence for light-enhanced ion accumulation has been obtained in a recent study by examining the high-field poling of a

lateral structure under different illumination intensities [28]. However in these measurements it is hard to distinguish the effect of light-induced structural changes (degradation) from light-enhanced mobility. Our own measurements on $MAPb_3$ and mixed perovskite cells have failed to show clear evidence of light-enhanced mobility (Fig. 3.15 suggests that no such effect is present in mixed cation cells, at least under 620 nm LED illumination) but the possibility remains.

Another contentious issue concerns the high-frequency feature in EIS measurements, from which several authors have attempted to extract an effective lifetime [29, 30, 31, 32, 33] (more often the technique of photo-voltage decay was used for this purpose, but the physics involved is identical). To the contrary, our own simulations of the high-frequency feature fail to indicate any contribution related to the lifetime except at high forward bias (sec. 3.6). Instead the admittance at high frequencies is dominated by simple parallel-plate type charging of the selective contacts (sec. 3.4.6).[1] This is supported by observations that the magnitude of the high-frequency capacitances scales with the perovskite thickness in the expected "parallel-plate" manner [3] (see also Fig. 3.10 for the effect of the titania thickness). A more direct counterargument against using the lifetime interpretation is that there seems to be little correlation between PL intensity/lifetimes and the high-frequency time-constant [34, 35]. In general, lifetime features are only expected to emerge under conditions of high injection, as discussed in sec. 3.4.6.

In section 3.4.5 we mostly address the confusion surrounding the low-frequency feature and its associated capacitance. The high-frequency feature is covered in section 3.6. Overall, the simulations reported in this chapter provide considerable new insight into previously controversial observations regarding light-induced and negative capacitance, providing an apparently comprehensive set of interpretations for EIS measurements that are fully consistent with the theory of ion-induced I-V hysteresis developed in Chapter 2. The following section establishes some basic concepts and terminology needed for the ensuing discussion.

3.4 EIS: Basic Theory

In an EIS measurement one is tasked with accounting for features in the linear response function, usually the impedance $Z(\omega) = \mathcal{F}[V(t)]/\mathcal{F}[I(t)]$ with $\mathcal{F}$ denoting the fourier transform, or equivalently the admittance $Y = 1/Z$. The response function describes the system's behaviour with respect to small-amplitude sinusoidal purturbations in some control variable, e.g. the current response to a sinusoidal variation in applied voltage ΔV with angular frequency ω is $\Delta V \times Y(\omega)$ in phasor representation. Both Y and Z are generally complex valued with real and imaginary parts related via the Kramers-Kronig relations [36]. As usual the real part describes the system's

[1] We note that in the studies just cited no attempt was made to subtract the charging contribution or otherwise account for its absence.

in-phase and the imaginary part its out-of-phase (quadrature or antiphase) response. Due to linearity, knowledge of the frequency-domain response functions over a sufficient frequency range is equivalent to knowledge about the time-domain response to small-amplitude perturbations. This makes it clear that EIS is a very general technique, no different in theory from measuring transient time-domain responses (in practice the difference has mostly to do with the measuring equipment and methods of analysis). We will see that the classic exponential responses of many physical systems in the time domain have counterparts known as Debye relaxation responses, which tend to manifest as the iconic semi-circular arcs in Nyquist plots (the complex-plane representation of Z or Y data). To illustrate these basic concepts we will briefly describe the AC electrical response of some elementary seiconductor devices below.

3.4.1 Displacement current

First we establish the meaning of a useful concept in AC device anaylsis: that of displacement current. This can be viewed simply as a convenience or book-keeping device which stems from the equation of continuity for electric charge

$$\frac{\partial \rho}{\partial t} = -\sum_i \frac{\partial j_i}{\partial x} \tag{3.1}$$

where the electric current on the RHS is expressed as a sum of contributions from multiple species i, e.g. electrons, holes and/or mobile ions. Employing Gauss's law in 1 dimension, $\partial E/\partial x = \rho/\epsilon\epsilon_0$, this can be equivalently expressed as

$$\frac{\partial}{\partial x}\left(\epsilon\epsilon_0 \frac{\partial E}{\partial t} + \sum_i j_i\right) = 0 \tag{3.2}$$

implying that the bracketed term is a constant in space (across the device). The first term inside the brackets is denoted the displacement current, and its utility is that it renders the total current (sum of displacement and charge currents) a conserved quantity in space (not time!).

3.4.2 Impedance of a uniform semiconductor

To show off the displacement current in action, we consider a uniform slab of semiconducting material (n-type crystalline Si, say) of thickness d between two ideal ohmic contacts. In the steady state ($\omega = 0$) this basic device behaves simply as a resistor, but at non-zero frequency one anticipates capacitive behaviour as well. Locally the semiconductor's response is given by Ohm's law, $j_n = \sigma_n E$. Combining this with the equation of total current continuity:

$$\epsilon\epsilon_0 \frac{\partial E}{\partial t} + \sigma_n E = const. \tag{3.3}$$

Since the total current is conserved right into the metal contacts, the right-hand side of the above equation must be the electrical current carried by the metal contacts, since essentially no displacement current can flow in a metal ($E \approx 0$). Therefore, identifying *const.* as the electrical current (density) J flowing through the external circuit, and relating E to the applied voltage as $V = Ed$, we obtain the current-voltage relation

$$J = \frac{\epsilon\epsilon_0}{d}\frac{dV}{dt} + \frac{\sigma_n}{d}V \tag{3.4}$$

i.e. a charging component plus the steady-state resistive current. We move to the frequency domain by taking $V = v_0 + \delta v e^{i\omega t}$, $J = j_0 + \delta j e^{i\omega t}$. The linear response function Y is independent of the applied voltage and simply given by $\delta j/\delta v$, so

$$Y = \frac{1}{d}\left(i\omega\epsilon\epsilon_0 + \sigma_n\right). \tag{3.5}$$

Real and imaginary parts are described by the conductivity $G = \mathrm{Re}[Y] = \sigma_n/d$, and the capacitance $C = \omega^{-1}\,\mathrm{Im}[Y] = \epsilon\epsilon_0/d$, of which the latter can be recognized as simply the parallel plate capacitance. The impedance $Z = 1/Y$ is

$$Z = \frac{d\rho_n}{i\omega\epsilon\epsilon_0\rho_n + 1} \tag{3.6}$$

which takes the form of the basic Debye relaxation. As mentioned, this response is the frequency-domain counterpart of an exponential relaxation in the time domain (the two are a commonly encountered fourier-transform pair [37]), and yields a single semi-circular arc in the complex plane (a plot of $\mathrm{Im}[Z]$ against $\mathrm{Re}[Z]$) emanating from $Z = 0$ in the $\omega \to \infty$ limit and terminating at $Z = d\rho_n$ in the DC limit.

3.4.3 Carrier relaxation

It is worth recognizing that according to 3.5 current flows primarily as electronic current at low frequencies, and as displacement at high frequencies. This is quite a generic phenomenon, and useful to bear in mind when analyzing more complex devices. The selective contacts in a perovskite cell for example (ETL and HTL) are approximately uniform semiconductors which can be expected to conduct electronic current at low frequencies and displacement current at higher frequencies, just as in the above example. The switch-over between these two regimes

occurs approximately when the two current contributions balance (in magnitude), i.e. when

$$\omega \approx \frac{\sigma_{n,p}}{\epsilon\epsilon_0} \tag{3.7}$$

which defines a characteristic time $\epsilon_0\epsilon/\sigma_{n,p}$, often known as the dielectric relaxation time. This happens to also be the timescale at which local perturbations to the charge density inside a conductor are screened by the majority species. To see this, consider again a uniform segment of conductor or semiconductor, intially at equilibrium with conductivity σ. Suppose a small amount of charge $\rho(x)$ is then added to the system. Gauss' equation and the equation of continuity for holes (supposing these are the majority carrier for definiteness) read

$$\frac{\partial E}{\partial x} = \frac{1}{\epsilon\epsilon_0}(\rho(x) + \delta p(x)) \tag{3.8}$$

$$\frac{\partial}{\partial t}\delta p(x) = -\mu_p \frac{\partial}{\partial x}\left[(p_0 + \delta p(x))E\right] - D_p \frac{\partial^2}{\partial x^2}\delta p(x) \tag{3.9}$$

assuming the perturbation is small, the term $-\mu_p p_0 \partial E/\partial x$ will dominate the RHS of the second equation (note that E is of order $\rho(x)$), allowing us to eliminate E from the first equation as

$$\frac{\partial \delta p}{\partial t} = -\frac{\mu_p p_0}{\epsilon\epsilon_0}(\rho(x) + \delta p(x)) \tag{3.10}$$

which describes exponential relaxation (screening of the added charge by holes) on a timescale $\epsilon_0\epsilon/\sigma_p$, i.e. the dielectric relaxation time once again.[2] We note that the relaxation time described above, with ions in place of holes as the majority carrier, is key to the analysis of loop features in the impedance spectrum as discussed in sec. 3.5.3.

3.4.4 Heuristic model of a diode with mobile ions

The uniform semiconductor model above was a useful way to introduce some basic terminology and concepts, but is still somewhat far removed from the complexity of a perovskite solar cell. To move one step closer we next consider in a heuristic fashion a semiconductor device with slow mobile charge in the form of ions (heuristic since the drift-diffusion equations for ions coupled to electrons and holes are not exactly solvable analytically, and we shall not attempt to do so). The device in question is imagined to resemble a p-i-n heterojunction diode, such as a standard perovskite cell, with mobile ions in the i-layer that cannot penetrate into the p or n layers.

[2]The term "dielectric relaxation time" is unfortunate, because clearly this is a timescale associated with carrier motion, and has little to do with fundamental atomic relaxations or molecular rearrangements which also go by the name of dielectric relaxation.

As in Chapter 2, we further imagine that only a single ionic species is mobile, and is balanced by a homogeneous background of compensating charge. As discussed and seen previously, this tends to result in an essentially intrinsic region within the bulk semiconductor capped by ionic accumulation and depletion zones at the two ionically blocking contacts whose equilibrium state is dependent on the applied (and built-in) voltage. We suppose as in the fixed-layer models of Chapter 2 that the state of these ions is uniquely describable by a single variable quantifying the amount of accumulated (or depleted) charge in the interfacial layers. Instead of directly using the charge as this variable, it is more convenient to use the electrical potential difference across the two layers (the two being related by a capacitance as $Q_{ion} = CV_{ion}$). Finally, the equivalent variables Q_{ion}, V_{ion} are assumed to evolve in time according to the amount of ionic current flowing in the perovskite bulk

$$\frac{dQ_{ion}}{dt} = \sigma_{ion} E_{bulk} = \sigma_{ion} d^{-1}(V - V_{bi} - V_{ion}) \tag{3.11}$$

where d is the width of the perovskite, or in terms of V_{ion}

$$\frac{dV_{ion}}{dt} = \frac{1}{R_{ion} C_{ion}}(V - V_{bi} - V_{ion}) \tag{3.12}$$

with $R_{ion} = d\sigma_{ion}^{-1}$. It can be seen that this captures the behaviour of ions that move to screen the internal electric field away from the perovskite bulk on an ionic RC timescale. In anticipation of studying the small-signal response, the above determines the ionic behaviour (replacing $V = v_0 + \delta v e^{i\omega t}$ and $V_{ion} = v_{ion,0} + \delta v_{ion} e^{i\omega t}$ etc. as before) as

$$\delta v_{ion} = \frac{1}{(i\omega R_{ion} C_{ion} + 1)} \delta v \tag{3.13}$$

i.e. another Debye-type relaxation.

For the current-voltage response of our notional device we assume that the instantaneous diode current depends both on the applied voltage V and on the state of the ions described by V_{ion}, so that the electron/hole current is expressed as $J(V, V_{ion})$. We neglect electron/hole relaxation (which is often significantly faster than typical frequencies in an EIS measurement). In addition, the bulk perovskite also carries an ionic current dQ_{ion}/dt to the interfaces. The current or admittance therefore comprises four components, the first two relating to derivatives of the electron/hole current J with respect to its two voltage arguments, a third component from the ionic charging current dQ_{ion}/dt and a final contribution from displacement in the perovskite bulk $\epsilon\epsilon_0 \partial E_{bulk}/\partial t$ (note that we can apply continuity to evaluate the total current in the bulk perovskite). Thus for the admittance $Y = \delta j/\delta v$:

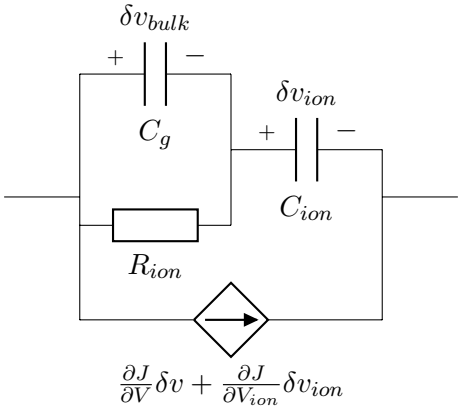

Figure 3.1: Equivalent circuit for a notional semiconductor device with a mobile ionic component. Note the dependent current source at the bottom which is determined by the state of the two internal capacitors. Here $C_g = \epsilon\epsilon_0 d^{-1}$ is the geometric capacitance of the perovskite layer and $\delta v = \delta v_{bulk} + \delta v_{ion}$ is the applied voltage perturbation.

$$Y = \frac{\partial J}{\partial V} + \frac{\partial J}{\partial V_{ion}}\frac{\partial v_{ion}}{\partial v} + i\omega \overbrace{C_{ion}\frac{\partial v_{ion}}{\partial v}}^{\delta Q_{ion}/\delta v} + i\omega\epsilon\epsilon_0 \overbrace{d^{-1}(1 - \frac{\partial v_{ion}}{\partial v})}^{\delta E_{bulk}/\delta v}. \tag{3.14}$$

Inserting 3.13 above for v_{ion} leaves

$$Y = \frac{\partial J}{\partial V} + \frac{\partial J}{\partial V_{ion}}\frac{1}{i\omega R_{ion}C_{ion}+1} + \frac{i\omega C_{ion}}{i\omega R_{ion}C_{ion}+1} + i\omega\epsilon\epsilon_0 d^{-1}\left(\frac{i\omega R_{ion}C_{ion}}{i\omega R_{ion}C_{ion}+1}\right). \tag{3.15}$$

Although somewhat formidable in appearance, this expression can be simply represented as the equivalent circuit depicted in Fig. 3.1. Its behaviour is governed by nothing other than the four current contributions named above. To illustrate the behaviour of this prototypical circuit some representative Nyquist plots are shown in Fig. 3.2. It can be seen that the impedance spectrum is generically composed of two arcs, one at high frequencies tending to $Z = 0$ corresponding to competition between displacement current in the bulk perovskite and the diode current (as in equation 3.6), and another arc at lower frequencies due to the ionic response. The interpretation of the low-frequency arc depends on which current contribution dominates: in Fig. 3.1(left) the spectra were calculated assuming that the ions have no effect on the electron/hole current, i.e. $\partial J/\partial V_{ion} = 0$. Furthermore we set the conductivity to a low value of $\partial J/\partial V_{ion} = 1\,\mu S$ to roughly emulate a perovskite cell measured at $0V$ in darkness (remaining parameters are given in the figure caption). This leaves only the ionic charging current dQ_{ion}/dt to produce the low-frequency feature, so the low-frequency arc can be properly labelled as capacitive. By contrast

in the other Nyquist plot included in Fig. 3.1(right) the ionic charging component is completely overwhelmed by the inclusion of non-zero ion-carrier coupling, or "electrode polarization" term $\partial J/\partial V_{ion}$, and by setting the conductivity significantly higher at $\partial J/\partial V_{ion} = 1\,\mathrm{mS}$ (imagining the cell at large forward bias or under illumination). A current-blocking effect is simulated by setting $\partial J/\partial V_{ion} = \alpha \partial J/\partial V$ with $-1 < \alpha < 0$ the blocking fraction. This describes the situation in which the transfer of the potential drop V from the bulk to the interfaces via ionic screening results in reduced current. It can be seen that a more negative blocking fraction (red series) is associated with a larger low-frequency arc relative to a less negative blocking fraction (blue series). We have also shown the effect of ion accumulation which affects the current oppositely, that is by amplification ($\alpha > 0$), which results in an arc extending below the real axis in the Nyquist plot (yellow series). Somewhat surprisingly perhaps, this is associated with negative values of the measured capacitance $C = \omega^{-1}\,1/\mathrm{Z}$ (this will be discussed further in sec. 3.5.4 and in the section below).

The heuristic model represented by equation 3.15 and the equivalent circuit in Fig. 3.1 illustrate the importance of accounting for the coupling between ionic and carrier dynamics. Using them, we have indicated that this coupling can overwhelm the contribution from simple ionic charging at low frequencies (the origin of I-V hysteresis), and that under certain circumstances one might even observe exotic effects such as negative capacitances. Whilst useful aids to thinking, these toy models give no quantitative information about the behaviour of real devices, and rely on a number of simplifying assumptions. In the following we establish the general concepts necessary to carry these insights over into more realistic simulations of an ionic solar cell.

3.4.5 Capacitance from Continuity

In the above we suggested that certain systems may be prone to exhibit a negative capacitance. To the extent that this is surprising we must re-examine what we mean by the term. With reference to frequency-domain measurements the word "capacitance" is generally used to denote the AC or parallel capacitance $C_p = \mathrm{Im}\,[Y]\,\omega^{-1}$. Unless otherwise stated, this is the measured quantity that is usually reported simply as capacitance. From its definition it is clear that the AC capacitance constitutes an inclusive measure of out-of-phase (hereafter antiphase) current oscillation, which may stem from genuine charge-storage – as in the intuitive notion of capacitance – but also from sustained currents which flow at a delay with respect to the applied voltage [38]. Acknowledgment of this fact was essential to the proper interpretation of negative capacitance measurements in a wide range of conventional semiconductor devices [39]. As we argue here, delayed recombination plays an outsize role in capacitance measurements of perovskite cells due to slow structural responses, such as the rearrangement of mobile ions.

In theory the distinction between intuitive charge-storage capacitance and the general AC

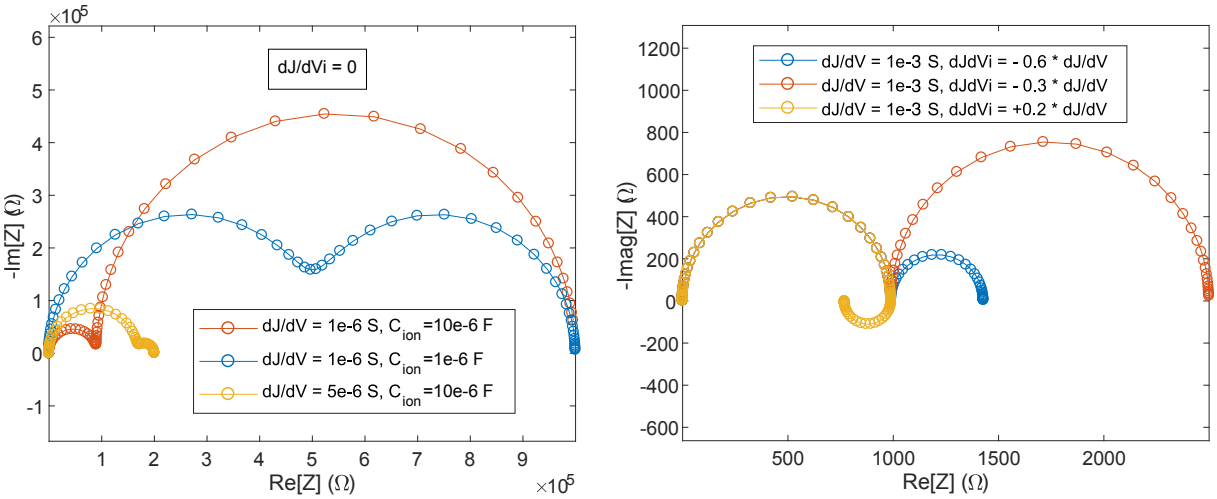

Figure 3.2: Some representative Nyquist plots using the model admittance/impedance specified by equation 3.15. The parameters chosen here were $R_{ion}C_{ion} = 1\,\mathrm{s}$, $C_{ion} = 10\,\mu\mathrm{F}$, $C_g = 100\,\mathrm{nF}$ with other parameters set according to the legends.

capacitance can be made very clear via considerations of current continuity [40], although experimentally these definitions are less accessible. A useful example to consider is the following continuity equation for electrons, with only generation and direct recombination included as source-sink terms for simplicity:

$$e\frac{\partial n}{\partial t} = \frac{\mathrm{d}}{\mathrm{d}x}j_n + e\,g - eR \tag{3.16}$$

where g and R are the generation and recombination rates respectively, j_n is the electron current, and e the electron charge. Considering just the first-order response to a sinusoidal voltage perturbation, this becomes (assuming constant generation)

$$i\omega\, e\,\hat{n} = \frac{\mathrm{d}}{\mathrm{d}x}\hat{j}_n - e\hat{R} \tag{3.17}$$

in which a hat is used to denote the frequency-domain derivative (e.g. $n = n_0 + \hat{n}\,e^{i\omega t}\mathrm{d}\,V$). In a device with carrier-selective contacts at both metallic terminals the above can be integrated to yield an expression for the admittance

$$Y \;= \underbrace{i\omega \int e\,\hat{n}\;\mathrm{dx}}_{Y_Q} + \underbrace{\int e\,\hat{R}\;\mathrm{dx}}_{Y_R} \tag{3.18}$$

in which each integral extends over the whole structure up to the metallic contacts (contribu-

tions from surface recombination being implicitly included as delta sources). Further discussion and details regarding this decomposition are included in appendix A (see also ref. [40] for an analogous treatment in the context of p-n junctions). Clearly the two terms labelled as Y_Q and Y_R relate to charge-storage and recombination respectively, and constitute the imaginary and real parts of Y precisely when the carrier densities respond perfectly in-phase with the applied potential. In this case the conductivity $G = \mathrm{Re}\,[Y]$ relates strictly to the recombination current and the AC-capacitance $\mathrm{Im}\,[Y]\,\omega^{-1}$ to stored charge, as intuition or experience might suggest. In general however carrier densities may not respond perfectly in-phase, meaning that Y_R and Y_Q are generically complex valued. This entails the possibility of non-zero contributions to the conductivity by Y_Q and perhaps more importantly to the AC-capacitance by Y_R. Accordingly the AC capacitance under general circumstances is given by

$$\begin{aligned} C_p &= C_Q + A_R \\ &= \int \mathrm{Re}\,[e\,\hat{n}]\ \mathrm{dx} + \frac{1}{\omega}\int \mathrm{Im}\left[e\,\hat{R}\right]\ \mathrm{dx} \end{aligned} \tag{3.19}$$

i.e. as a sum of the conventional storage capacitance C_Q and a contribution from antiphase recombination A_R. Before moving to the antiphase recombination, it may prove helpful to review some of the more familiar forms of capacitance associated with the charging component C_Q (equation 3.19) of the measured capacitance. This is done in the subsection below, and is mostly a matter of establishing terminology for the ensuing discussion.

3.4.6 C_Q: Geometric, Accumulation and Chemical Capacitances

Geometric Capacitance

The geometric capacitance of a device corresponds to the charge stored in its electrodes, usually with the assumption of an applied voltage that is developed uniformly across the internal layers (uniform displacement), as in a p-i-n cell or parallel-plate capacitor. The capacitance is referred to as "geometric" due to its dependence on the dielectric thickness d (in 1D) as

$$C_g = \epsilon\epsilon_0/d. \tag{3.20}$$

With reference to perovskite cells the geometric capacitance generally refers to charge stored on the selective contacts, usually conductive enough to be considered electrodes in the above sense,[3] and a field developed across the absorber layer (making d the perovskite thickness).

[3]Following our discussion of the uniform semiconductor impedance in sec. 3.4.3, this applies only as long as the measuring frequency is below the relaxation time of each contact – a condition which can fail at high frequencies for contacts with large permitivitty but poor conductivity. When it occurs this generally manifests as an extra

The geometric capacitance can only be measured in perovskite cells under certain conditions, as the amount of charge stored on the electrodes is readily overwhelmed by other contributions to the capacitance. Suitable conditions for measuring C_g are that the probe frequency is high enough to freeze out ionic contributions, and that the injected carrier density is low (entailing low applied bias and illumination). The geometric capacitance is expected to exhibit little to no voltage dependence, and have a magnitude in the range of $\approx 30 - 250\text{nF/cm}^2$ assuming a relative permittivity in the range of $24 - 60$ and planar thicknesses between $200 - 700\text{nm}$. A question arises as to how this quantity is determined in a two-electrode system when one or more of the electrodes is non-uniform, as for example the mesoporous titania scaffold in a normal-structure perovskite cell. This is conveniently discussed in terms of the effective thickness $d_{eff} = \epsilon\epsilon_0/C_g$ derived from a measurement of C_g assuming that the dielectric constant is known. Previously it was claimed that roughness can enhance the geometric capacitances, (equivalently reduce the effective thickness) by factors as large as 6 [41, 42]. Here we briefly correct this misunderstanding by simulating a mesoporous electrode system, and by an analytic argument showing that the effective thickness falls neatly between the capping layer thickness and the full extent of the perovskite layer. Roughness is therefore not a legitimate reason for observing abnormally large high-frequency capacitances, although it is very likely to affect the low-frequency ionic capacitance. Large high-frequency capacitance (larger than $\approx$260 nF cm^{-2}, corresponding to a small cell thickness of 200 nm with $\epsilon \approx 60$) may instead be an indication of small capping-layer thicknesses or non-negligible carrier densities in the perovskite layer (i.e. net doping).

Simulations of the geometric capacitance in a 2-d geometry designed to emulate a mesoporous cell are shown in Fig. 3.3. In the model of Fig. 3.3 (left) the capacitance calculated in the absence of mobile ions clearly corresponds to an electric field developed over the bulk of the perovskite layer. Concentration of charge density near the tips of the mesoporous scaffold result in an effective thickness which approximates the "capping layer" thickness of the perovskite layer (Fig. 3.3 left). Including mobile ions results in an electric field that is concentrated at the selective contact interfaces, and apparently mostly conforms to the rough mesoporous scaffold (Fig. 3.3 middle). Roughness can therefore be expected to enhance the ionic capacitance despite having little effect on the geometric one. Whether this effect is important for mesoporous cells will depend on the relative capacitance at the ETL and HTL interfaces, as these two contributions add in series.

A simple analytic argument confirming the insensitivity of the geometric capacitance to surface roughness is as follows. Consider a two-electrode system with one flat electrode at $y = -d$ and another rough electrode at $y = h(x) > 0$ with $\min(h(x)) = 0$. The capacitance is

arc or deviation in the high-frequency portion of the Nyquist plot.

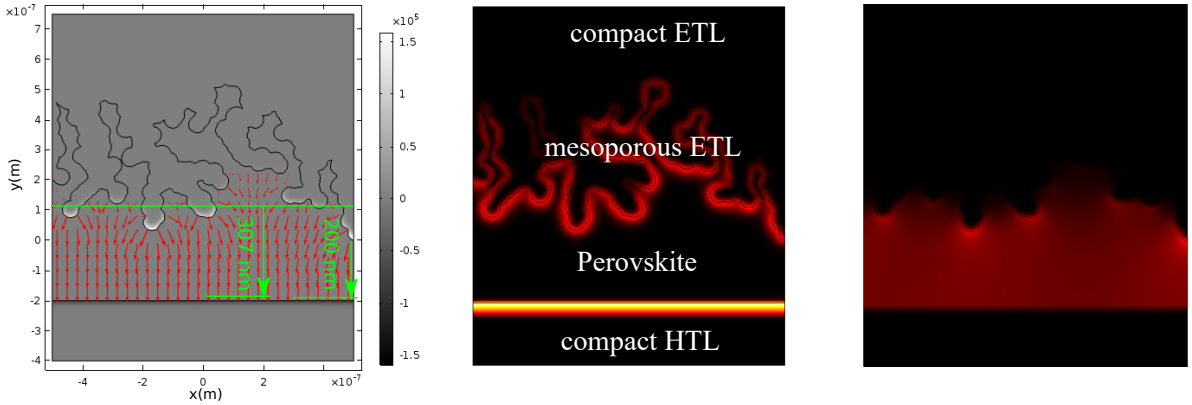

Figure 3.3: (Left) Capacitance calculations in a 2-D semiconductor model with a mesoporous ETL (no mobile ions). Greyscale coloration indicates the charge density, red arrows the electric field and the green line indicates the effective geometric thickness for the calculated value of capacitance. The effective separation is found to closely approximate what would normally be regarded as the capping layer thickness. (Middle, Right) Electric field strength with and without accumulated mobile ions, respectively.

determined by solving the Laplace equation for the potential subject to the boundary conditions $V(x,0) = 0$ and $V(x,h(x)) = \Delta V$ (the size of ΔV is insignificant due to linearity). Equivalently it is determined via minimization of the energy equation

$$E = \frac{1}{2}C(\Delta V)^2 = \frac{1}{2\epsilon\epsilon_0}\int |\nabla V|^2 \mathrm{d}^2\mathrm{x} \tag{3.21}$$

(note that in 2D C refers to a capacitance per unit length in orthogonal direction). The minimization principle implies that any trial function $\hat{V}$ satisfying the boundary conditions, but not necessarily the Laplace equation, entails a higher energy and therefore

$$C < \hat{C} = \frac{1}{\epsilon\epsilon_0(\Delta V)^2}\int |\nabla \hat{V}|^2 \mathrm{d}^2\mathrm{x}. \tag{3.22}$$

Taking the trial function

(3.23)

$$\hat{V}_1 = \begin{cases} \Delta V\left(\frac{y+d}{d}\right) & y < 0 \\ \Delta V & y \geq 0 \end{cases} \tag{3.24}$$

gives

$$C < \frac{1}{\epsilon\epsilon_0 d} \tag{3.25}$$

i.e. the true capacitance is bounded by the parallel-plate capacitance with separation equal to the minimum distance between the two electrodes d. This proves that no roughness, however extreme, can act to increase the geometric capacitance. We note that the argument above assumes perfectly conducting electrodes; the true capacitance in a cell with semiconducting selective contacts will generally be lower due to the additional depletion widths.

Chemical & Accumulation Capacitance

Although we make only passing mention of these concepts in the ensuing discussion, it is worth defining the accumulation and chemical capacitance since both appear at various points in the relevant literature concerning EIS. As the name suggests, accumulation capacitance is associated with the development of electrical potential in semiconductor regions under accumulation, defined here as the situation where uncompensated carrier densities are too large to be ignored in Poisson's equation. Under strong accumulation the capacitance grows exponentially with the voltage across the accumulated region [43]. The accumulation capacitance is only expected to manifest in perovskite cells at large forward bias ($V > V_{bi}$). The chemical capacitance is somewhat more subtle since it is associated in the first instance with changes in the chemical potential of carriers (related to their concentration), rather than the electrical potential. To understand the proper place of the chemical capacitance in EIS it is helpful to consider the small-signal equations for drift-diffusive transport of electrons and holes, which can be rendered in the form of a transmission line as in Fig. 3.4 [44]. The symbols in the figure are defined as follows:

$$r_n = (e\,\mu_n n)^{-1}, \quad r_p = (e\,\mu_p p)^{-1} \tag{3.26}$$

$$r_{rec} = \tau \frac{V_T}{e}\left(\frac{1}{n} + \frac{1}{p}\right)^{-1} \tag{3.27}$$

$$c_g = \epsilon\epsilon_0 \tag{3.28}$$

$$c_n^{\mu} = \frac{e}{V_T} n, \quad c_p^{\mu} = \frac{e}{V_T} p \tag{3.29}$$

where e is the electron charge, V_T the thermal voltage, and τ the direct-recombination lifetime. We note that the given expressions for c^{μ} assume the relation between chemical potential and carrier density implied by Boltzmann statistics [45]. By inspecting Fig. 3.4 it is clear that the relative charge state of the chemical capacitors c_{μ} is responsible for diffusion currents (a diffusion

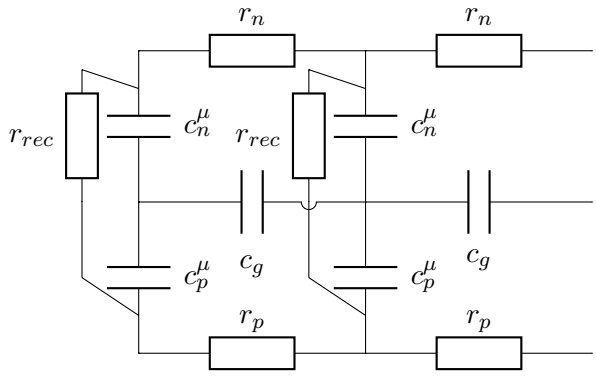

Figure 3.4: Equivalent transmission line for the small-signal drift-diffusion equations, adapted from ref. [44]. The top rail represents conduction-band electrons and the bottom rail valence-band holes. The middle rail carries the displacement current. Here we show a simplified version appropriate for direct recombination only, and assuming zero steady-state current. Depicted is a finite section (twice the fundamental "unit cell") of the infinite transmission line. Symbols are defined below.

current will flow between neighbouring capacitors when there is a difference their charge state, i.e. a gradient in chemical potential) whereas the drift currents are locally driven by voltage across c_g (gradients in electrical potential). Chemical capacitance is frequently mentioned in the older EIS literature on PSCs preceding the recognition of ion migration, where it was incorrectly invoked in place of the low-frequency ionic capacitance. To estimate the typical size of the chemical capacitance we must first note that the quantities in equations 3.29 are microscopic with macroscopic counterparts obtained via integration over the whole device (and using the appropriate composition law for the circuit element in question). The macroscopic chemical capacitance of a semiconductor film (e.g. perovskite layer) is obtained by combining the parallel microscopic capacitors in the transmission line of Fig. 3.4, that is via simple integration of the c^μ, and can therefore be estimated as $C_\mu \sim e/V_T N d$, with N a typical carrier density and d the absorber thickness. We note that this assumes balanced accumulation of electrons and holes in the absorber. To estimate the carrier density we consider a cell at open-circuit under illumination, for which generation balances recombination and hence $N \sim G/\tau$. Lifetimes in the range of 10-1000 ns and a generation of $20\,\mathrm{mA\,cm^{-2}}$ correspond then to carrier densities of $1 \cdot 10^{13}$-$1 \cdot 10^{15}\,\mathrm{cm^{-3}}$ in a 300 nm absorber, and capacitances of $C_\mu \sim$ 8-800 $\mathrm{nF\,cm^{-2}}$. This value is considerable, being comparable to the geometric capacitance, but is likely to be substantially smaller at lower bias voltages. In an ordinary p-i-n solar cell the carrier density and hence chemical capacitance scales with the applied voltage as $C^\mu \propto N \propto e^{V/\gamma V_T}$ [46], with γ the ideality factor. Once ionic screening of the internal field is included this scaling becomes questionable, and one expects a much weaker dependence of the carrier density on applied voltage (under

illumination), possibly leading to significant charge storage in the chemical capacitance at lower bias voltages. This possibility has failed to materialize in our exploratory simulations, in which charge stored in the perovskite generally contributes less than $\approx 10\,\mathrm{nF\,cm^{-2}}$ under 1-sun illumination for $V < V_{bi}$. Features which act to inflate carrier densities in the absorber layer such as a low mobility value could increase this contribution.

Any of the sub-circuits in Fig. 3.4 consisting of just the two chemical capacitors at a single location and the accompanying recombination resistance define an *RC* element with time-constant equal to the carrier lifetime τ. It is therefore not unreasonable to expect that the lifetime may feature directly as a characteristic timescale in an EIS measurement. Unfortunately, the decay of the recombination sub-circuit on the timescale τ contributes to the measured capacitance, and its contribution is therefore quantified by the chemical capacitance. As argued above this is unlikely to be a significant fraction of the measured capacitance except under circumstances (large forward bias) when other contributions to the total capacitance are liable to overwhelm it. It therefore seems unlikely that EIS can will be useful for measuring effective lifetimes in perovskite cells. We note in closing this discussion that "recombination resistance" is often used somewhat carelessly to denote the intermediate-frequency resistance extracted from equivalent circuit fitting [47, 48, 49, 50]. This labelling is only strictly correct under the assumption that the r_{rec} in equations 3.29 dominates the transport contributions $r_{n,p}$ (this may be a carryover from studies on DSCs where transport in the absorber is short-ranged).

Together the geometric, accumulation, depletion (see e.g. [51]) and chemical capacitance define the most commonly encountered contributions to C_Q as defined by equation 3.19. Each has distinct properties such as their particular dependence on applied voltage (possibly illumination), but all are ultimately forms of capacitance associated with conventional charge storage, i.e. contributions to C_Q. Below we consider a different class of contributions to the measured capacitance which instead arise from the A_R term in equation 3.19.

3.5 Antiphase Recombination in Capacitance Measurements

We now return to our discussion of the capacitance decomposition 3.19 to address the second component A_R. Although it has the dimensions of a capacitance, this designation will be avoided for A_R in order to emphasize its distinct origin. To obtain a better handle on A_R we consider a system whose total recombination current responds with delay to changes in the applied potential (due to unspecified mechanisms) on a unique exponential timescale τ, i.e.

$$R(t) = R_0 + [(R_\infty - R_0) + R_\tau \exp(-t/\tau)]\, H(t)\mathrm{d}V \tag{3.30}$$

where $(R_\infty - R_0)$ quantifies the steady-state and R_τ the transient response to a step-change in the applied potential $V(t) = V_0 + H(t)\mathrm{d}V$, with $H(t)$ the unit step function. Direct evaluation of the Fourier transform $\hat{R} = \mathcal{F}[R(t)]/\mathcal{F}[V(t)]$ applied in equation (3.19) yields a Debye-type expression for A_R:

$$A_R = \frac{\tau\, R_\tau}{1 + (\omega\tau)^2}\,. \tag{3.31}$$

A positive contribution to the AC capacitance will therefore result when recombination is initially large but decreased by the process causing delay ($R_\tau > 0$), and negatively to the capacitance when recombination increases over time ($R_\tau < 0$). This provides a particularly natural way for negative capacitance to arise in circumstances where the recombination current is significant compared to the charging current measured by C_Q (see ref. [39] for an extensive list of examples).

Apart from its ready flexibility in sign, the antiphase recombination A_R is also distinguished from the charge-storage capacitance by its explicit frequency dependence. In equation (3.31) this results in a low-frequency limit that is linearly proportional to the timescale of relaxation τ. Since there is in principle no limit to these timescales when slow agents such as migrating ions are present, the antiphase recombination can be arbitrarily large. The presence of highly visible slow transient responses in perovskite cells therefore makes consideration of the antiphase recombination essential in EIS and other small-signal measurements, particularly at low frequencies. It is important to note that even if these transient processes are rate-determined by a charging processes, such as the interfacial accumulation of ions, charging will often have a transient effect on the recombination current in a way which may dominate C_p. On the topic of timescales, we remark that replacing the Debye relaxation above with a Cole-Cole response, commonly used to model a broadened distribution of timescales parameterized by a factor $0 < \alpha < 1$ ($\alpha = 1$ being the un-broadened case) [36], leads to A_R capacitances which diverge as $\omega^{\alpha-1}$ at low frequencies.

EIS measurements of perovskite cells typically exhibit a high frequency response, associated with capacitive charging, and a low-frequency response due to interfacial ion accumulation, otherwise referred to as electrode polarization. Occasionally, distinct features appear in small-signal measurements at intermediate frequencies (1-100 Hz) as well [52, 6]. In sections 3.5.2, 3.5.3 and 3.5.4 we consider the role of antiphase capacitance with reference to each of these features, starting with the low and high frequency capacitance under illumination, before moving to intermediate features and other manifestations of negative capacitance. We follow with a study of the high-frequency capacitance under dark conditions (i.e. conventional C-V measurements) in sec. 3.6 to provide some experimental verification for our ionic drift-diffusion (IDD) models in a simpler setting.

3.5.1 Experimental Methods

The cells fabricated for this study included those based on $MAPbI_3$ and multi-cation perovskites, and were fabricated according to previously reported processes that generally result in high performing devices [53, 54]. The compact TiO_2 layer, of primary relevance to the C-V study of sec. 3.6, was made by spin-coating the TiO_2 precursor containing a titanium isopropoxide (TTIP) IPA solution and a diluted HCl IPA solution at a speed of 5000 rpm. The film thickness was controlled by varying the spin-coating times, and followed by annealing at 115° C. Each spinning cycle resulted in a TiO_2 film with thickness of 30±5 nm, and was repeated for the experiment reported in Fig. to obtain the thicker compact layers. After completing all spin-coating cycles, the film was subsequently annealed at 500° with a high oxygen pressure for 5 mins and in air for another 25 mins. For the mesoporous structure, a 70-80 nm-thick mesoporous titania layer was deposited on top of the cp-TiO_2 film by spin-coating diluted TiO_2 paste (30 NR-D) solution in ethanol (weight ratio of 1:12) at 5000 rpm for 25 s with an acceleration rate of 5000 rpm/s. The films were then sintered at 500° for 30 min in air and then left to cool.

EIS measurements were conducted on a Keysight B1500A Semiconductor Parameter Analyzer using the WGFMU unit and in-house software. High-frequency C-V measurements were conducted using the unit's dedicated capacitance meter.

3.5.2 Photo-induced Capacitance

First we consider EIS measurements under illumination. An experimental C-f spectra of a standard $MAPbI_3$ cell is shown in Figure 3.5a, taken with and without illumination provided by a 630 nm LED array at approximately 1 sun intensity. In the low-frequency part a single feature is apparent below 1 kHz under illumination and at somewhat lower frequencies in the dark. The low-frequency feature has a characteristic frequency of ≈ 0.1 Hz under illumination as determined from the Bode plot, which is similar to timescales of I-V hysteresis. A now considerable body of evidence points very strongly towards ion migration being the root cause of I-V hysteresis (see refs. [55, 56] for reviews), with I^- vacancies being the most likely culprit in $MAPbI_3$ [57, 58]. Given that a low-frequency EIS measurement is, in essence at least, an I-V measurement with a smaller amplitude and smoother waveform, the broad low-frequency feature can be confidently attributed to ion migration. The observed difference in timescales under dark and light conditions (the onset of the dark and illuminated features in Figure 3.5a) may be an indication of light-enhanced ion mobility [28], which we will not consider further. Our primary concern is to address the dramatic enhancement of low-frequency capacitance observed when the cell is measured under illumination. Considering the discussion above this would follow naturally if ion migration is acting to delay the recombination, or equivalently the collected

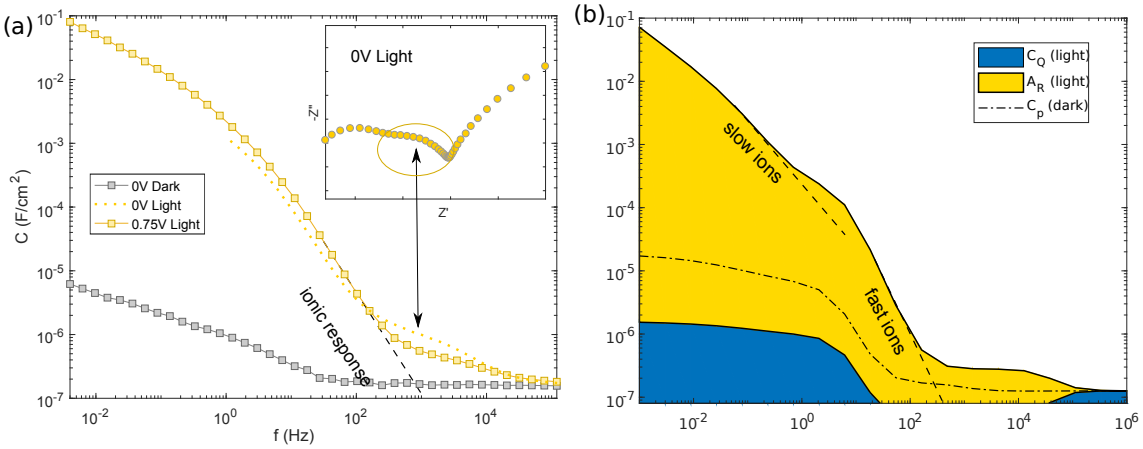

Figure 3.5: (a) Experimental C-f measurements of a "standard" FTO/cp-TiO_2/mp-TiO_2/$MAPbI_3$/Spiro-OMeTAD/Au cell in darkness (grey) and under illumination (yellow). The dashed line indicates an extrapolation of the ionic contribution towards high frequencies. (a, inset) Nyquist plot at 0 V under illumination, zoomed in on the high-frequency region (circled data corresponds to frequencies in the indicated portion of the C-f spectrum). (b) Area plot of a simulated C-f spectrum under illumination showing the relative contributions of antiphase recombination (A_R, yellow) and the more familiar charge-storage capacitance (C_Q, blue). Here two ionic species with diffusion constants $1 \cdot 10^{-10}\,\mathrm{cm}^2\,\mathrm{s}^{-1}$ and $1 \cdot 10^{-13}\,\mathrm{cm}^2\,\mathrm{s}^{-1}$ were used to emulate the broad spectrum observed experimentally.

photocurrent [5]. As a check on this theory we have performed simulations of this experiment, shown in Figure 3.5b. To roughly emulate the extreme broadening of the experimental low-frequency feature (which extends over 4 decades) we have included two ionic species (fast and slow) in the simulation of Figure 3.5b, although it is not clear how many distinct species are actually relevant in the device physics of $MAPbI_3$. Broadening of the experimental specturm could alternatively result from lateral variations in the RC constant of a single ionic species, or from diffusion along irregular pathways (e.g. grain boundaries) with varying activation energies between jumps. Indeed, inclusion of a slower species in the simulation results in enormous values of the low-frequency capacitance of order $1 \cdot 10^{-1}\,\mathrm{F\,cm}^{-2}$ due almost solely to the contribution from A_R, which are similar to those seen in our measurement. The massive contribution from A_R is found to occur generically (that is for almost all parameter choices that include a slow-moving ionic species) with slower ions leading to a larger low-frequency limit in accordance with the scaling in equation (3.31).

In the simulation of Figure 3.5b a positive A_R follows from $R_\tau > 0$, or a decreased rate of recombination due to ionic redistribution, which may appear counter-intuitive. This is resolved by recognizing that R_τ is defined by equation (3.30), and therefore refers to the transient

increment in recombination following a positive step-change in potential. Physically this step to forward bias is initially exerted over the entire perovskite bulk, hindering charge extraction, whereas after ionic redistribution it is felt only near the contact interfaces where it exerts a lesser influence. Experimentally $R_\tau > 0$ is the trend observed in step-transient measurements [59], wherein moving to forward bias is found to result in temporarily reduced photocurrent that rises over time (suggesting a recombination rate that decreases over time). Conceivably the opposite case of $R_\tau < 0$ could also occur, leading to negative capacitance under illumination, depending on the recombination model (see later discussion). However for the vast majority of the simulations carried out in this study $R_\tau > 0$ was observed at low-frequencies under illumination. As with I-V hysteresis [8, 9], recombination rates have an important effect on A_R, with higher rates straightforwardly leading to larger values. Several studies have observed a correlation between large values of the low-frequency capacitance (interpreted here as A_R) and the degree of hysteresis [60, 61], which is entirely natural when seen in this light.

In our opinion there can be little doubt that the experimentally observed capacitance at low frequencies stems from A_R, since the only mechanism required is a slow-moving agent acting on carrier densities and thereby recombination rates. Studies of I-V hysteresis have already amply demonstrated that mobile ions play just such a role in the halide perovskites, and our models constitute a further demonstration that the theory works quantitatively in the frequency-domain. However, given that similar measurements have been the subject of considerable interest and controversy in the literature, we feel it is important to spend some time in the following to consider alternative explanations.

The observation of a large increase in low-frequency capacitance under illumination was first reported in the guise of a giant ac-dielectric constant (an experimentally derived quantity simply proportional to C_p) [2]. Initially this observation was considered as evidence of light-induced changes to the fundamental dielectric constant, i.e. to the electronic or ionic polarizability, a notion that was greeted with both widespread interest [62, 63, 64, 65] and skepticism [66, 5, 7, 67]. A closely related observation is the commonly reported growth of AC conductivity with light intensity [68, 41, 20, 6], which manifests as a shrinking of the impedance in Nyquist plots. We remark that in other fields of material science observations of a giant dielectric constant are apparently not uncommon, but mostly arise due to extrinsic effects [69]. Without invoking changes to the fundamental dielectric constant, increases in the AC capacitance and conductivity can be simply understood as a consequence of larger recombination rates occurring under illumination [7, 67], which in turn contribute to both the real and imaginary parts of the admittance as in equation (3.18). Increased recombination primarily affects the real part (conductivity), with contributions to the imaginary part (capacitance) also appearing at lower frequencies due to ion-induced delay. A similar explanation was offered soon after the first

report of this phenomenon [7], but before the widespread recognition that ionic responses are fundamental in the transient response of perovskite cells. Disordered conduction pathways incorporating capacitive gaps were therefore proposed as a mechanism responsible for causing delay, the importance of which remains unestablished.

Quantitatively any theory of the photo-induced low-frequency capacitance in terms of accumulated carriers [70, 4] or ions (i.e. any theory invoking C_Q in the language of this paper) is problematic, as capacitances of order $10^{-1}\,\mathrm{F\,cm^{-2}}$ (Figure 3.5a), would imply an average separation ($d = \epsilon\epsilon_0/C$) less than 1 pm between compensating charges. This is clearly unphysical as a length-scale for quantum confinement, being vastly smaller than a typical electron de Broglie wavelength or orbital size. Such considerations apply whether or not there is charge transfer across the interface (pseudocapacitance [71]), as long as no chemical bonds are formed. A realistic treatment of accumulation capacitance must also take account of Fermi-Dirac statistics in order to reach the relevant limit of strong accumulation (Fermi level deep in the valence band) [70], the neglect of which leads to inflated estimates. Including just the former correction in the form of a generous 0.3 nm distance of closest approach already limits the accumulation capacitance to being less than $2 \cdot 10^{-4}\,\mathrm{\mu F\,cm^{-2}}$. The raw accumulation of carriers or ions must therefore be deemed an insufficient mechanism for explaining the photo-induced low-frequency capacitance. The reported evidence in favor of this fairly widespread theory [72, 73, 74] was an approximate linear scaling in the capacitance with light-intensity, and increasing values with larger perovskite thickness [70]. These features also follow naturally if the capacitance stems from antiphase recombination currents: both increasing the light intensity and film thickness (assuming incomplete absorption) will enlarge the total recombination current, and thereby its antiphase component as measured by A_R. The exponential dependence on open-circuit voltage with a logarithmic slope of $1/2k_BT$, touted as a unique characteristic of the accumulation capacitance, is simply indicative of the usual relation between the light intensity and open-circuit voltage $I_L \sim \exp(V_{oc}/\gamma k_B T)$ (with an ideality factor $\gamma = 2$), and therefore follows if the recombination current is proportional to the light intensity (a consequence of imperfect internal quantum efficiency) [75].

Photo-enhancement of the capacitance can also be observed in the high-frequency region. In the C-f plot of Figure 3.5a, an excess of approximately $300\,\mathrm{nF\,cm^{-2}}$ manifests between 1 kHz and 10 kHz under illumination compared to the dark measurement. Simultaneously, an additional intermediate arc appears in the Nyquist plot (Figure 3.5a inset). This feature was seen in several batches of cells, and appeared variously as either a distinguished arc in the Nyquist plot or simply as a broadening of the high-frequency feature. A similar feature has been reported previously in cells with a (poorly performing) Nb_2O_5 ETL [52]. The question arises as to whether the light-induced capacitance in this frequency range is attributable to C_Q, due to the

accumulation of poorly extracted carriers or perhaps a photo-doping effect, or alternatively to A_R. Although far from being conclusive confirmation, such a feature is already present in the simulation of Figure 3.5b (note the excess A_R capacitance above 1 kHz which exceeds C_p in the dark, denoted by dotted lines). In these simulations the onset of the light-induced high-frequency feature signals an accumulation of carriers at the perovskite/titania interface. Despite contributing only a small amount of stored charge, the delay induced by the charging process causes part of the recombination current to fall out of phase, resulting in significant contributions to the AC capacitance through A_R. Alternative theories for the light-induced high-frequency capacitance seen in Figure 3.5a can also be imagined, and may justify further study. However, the resemblance in these simulations is an important indication that antiphase recombination currents can also be significant beyond the ionic cutoff (extrapolated to approximately 1 kHz in Figure 3.5a) where purely carrier dynamics are at play.

In the absence of illumination recombination currents are smaller and the measured capacitance has a better chance of retaining its usual meaning in terms of charge storage. For this reason the un-illuminated measurements in Fig 1a, which feature a low-frequency capacitance of $1\,\mu F\,cm^{-2}$ to $10\,\mu F\,cm^{-2}$ at zero bias between 10 mHz to 100 mHz, are almost certainly a reflection of the C_Q capacitance associated with interfacial ion accumulation. For our analysis of ionic timescales in the next section it is necessary to note that the ionic capacitance is more properly referred to as an "ion-electrode" capacitance, since it is strongly influenced by the distribution of compensating charges in the contact layers. In the IDD model ions accumulated in the diffuse layers [71] are compensated on the contact side by either an excess of majority carriers, or else by depletion-layer space charges, which incur their own series contribution to the total ion-electrode capacitance. In theory it is this quantity (denoted C_{IE} in the following) that should determine the timescale of electrode polarization (i.e. the rate at which bulk electric fields are screened by interfacial ion accumulation), naively as $R \cdot C_{IE}$ with R the bulk ionic resistance. The implied dependence on electrode properties such as doping, dielectric constant and thickness may explain many of the observed differences between normal and inverted structure cells [60, 61, 76]. However, this also implies that the presence of depletion layers at either interface, in the absence of other effects, has a drastically limiting effect on the ion-electrode capacitance. For this reason, corrections to the standard IDD model were necessary to achieve dark capacitances above $1\mu F\,cm^{-2}$ in the simulation of Figure 3.5b. These were made via the inclusion of surface states at the perovskite/contact-layer interfaces as discussed in sec. 3.7, although we emphasize that such corrections are in no way crucial to the effect of giant illuminated capacitance discussed above.

3.5.3 Loop Features and Ion Diffusion

Distinct features occasionally appear in small-signal measurements of perovskite cells at intermediate frequencies (1-100 Hz), in addition to the usual high and low frequency responses [6]. Above we dealt with one intermediate feature above in the form of the light-induced high-frequency capacitance seen in normal-structure $MAPbI_3$ cells. Another kind of intermediate-frequency feature manifests in EIS measurements as a loop in the complex impedance plot [52], sometimes extending below the real axis, signifying a negative value of the AC capacitance. Suggestions for the meaning of these features include the interplay of an unidentified intermediate state [52], an interfacial charge transfer resistance [77], and genuine inductance (i.e. energy storage in magnetic fields) associated with the ionic conduction current [78]. Whilst the former two remain plausible, if vague, the use of inductors in equivalent circuits should not be conflated with physical inductance [79] and is simply a mechanism for modelling negative capacitances (actual negative capacitor elements would be no less physical). Instead, our IDD simulations suggest that loop features and negative capacitance in the intermediate frequency range are related to A_R on the timescale of ionic relaxation:

$$\tau_r = \frac{\epsilon\epsilon_0}{\sigma_{ion}}. \tag{3.32}$$

where ϵ is the perovskite's relative permitivitty and σ_{ion} is the ionic conductivity. In the theory of conventional semiconductors this quantity (expressed instead in terms of the carrier conductivity) is the timescale at which charge density perturbations are screened by the majority carrier [80]. The relaxation time τ_r is therefore expected to play some role whenever changes in the applied potential induce charge density variations at times $t < \tau_r$ in the bulk perovskite. The most natural way for this to occur is if sizeable carrier densities are present in the bulk of the perovskite layer. In that case, carrier screening of the applied potential will result in bulk charge density variations at short times that will be screened by ions on the timescale τ_r. Since the standard IDD models with perfectly compensated ions are essentially free of bulk carriers for low to moderate bias voltages, some modification is needed to introduce a significant carrier density and thereby make the relaxation time manifest.

We note in advance of the following that if the above theory is correct loop features should allow identification of the ionic conductivity through (3.32). In principle this can then be used to estimate the ion density, although presently a large range of ionic diffusion constants ($1 \cdot 10^{-8}\,\mathrm{cm^2\,s^{-1}}$ to $1 \cdot 10^{-12}\,\mathrm{cm^2\,s^{-1}}$ for the iodide vacancy in $MAPbI_3$) [81, 82] hinders the accuracy of this step. Observations of a loop feature at approximately 1 kHz [52] in this sense suggest ion densities between $1 \cdot 10^{17}\,\mathrm{cm^{-3}}$ to $1 \cdot 10^{21}\,\mathrm{cm^{-3}}$, which is at least in approximately the expected range [83].

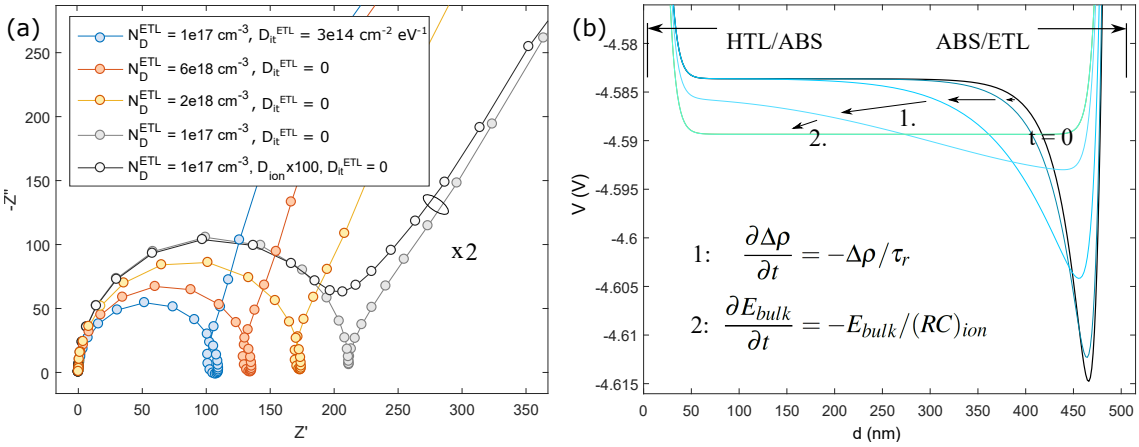

Figure 3.6: (a) Simulations exhibiting a loop feature at 0.6V under illumination. The data appearing in grey and black data have been scaled down by a factor of 2 for visibility. ETL properties that affect the high-frequency capacitance are found to have an important impact on the loop feature (here the doping N_D and interfacial defect density D_{it}). Loops can also be obscured by the high frequency feature if the ions are sufficiently fast (black circles). (b) Time domain simulation of the model in (a) (with $\mathrm{N_D^{ETL}} = 6 \cdot 10^{18}\,\mathrm{cm}^{-3}$) showing the evolution of the bulk potential (vacuum potential minus the grounded metal contact's workfunction = 4.4 eV) in response to a step change in applied potential (0.6 V→0.8 V). Contact layers (HTL and ETL) are located at $x = 0$ and $x = 500$ nm respectively. Ionic relaxation occurs on the timescale τ_r (step 1) and interfacial charging on the ionic RC timescale (step 2) according to the labelled equations.

Fig. 3.6 shows a simulated impedance spectrum featuring an "inductive loop" at intermediate frequencies, produced by including a net acceptor doping density at a significant fraction of the mean ion density ($N_A = 4 \cdot 10^{17}\,\mathrm{cm}^{-3}$ with $N_{ion} = 1 \cdot 10^{18}\,\mathrm{cm}^{-3}$). Figure 3.6a also shows a few variations of the base model with respect to the contact layers properties that will be discussed further below. By using a slightly lower ion density than the default of $1 \cdot 10^{19}\,\mathrm{cm}^{-3}$ we ensure that the doping density is not fully compensated by ion migration from the interfaces, and therefore results in a substantial bulk carrier density (see Fig. 3.7). Since the primary requirement is a large bulk carrier density, an alternative method of engineering the loop feature is to include an unfavorable band offset at one of the contact layers, such that photo-generated carriers are accumulated in the absorber. Regardless of the exact mechanism, the loop in such models results from a negative contribution to the total capacitance by A_R, and extends below the real axis only when this contribution overwhelms the remaining positive capacitance in C_Q.

The reason why ionic screening at the relaxation time manifests as negative capacitance is best understood in the time domain. Figure 3.6b plots the electrical potential across the bulk of the perovskite, showing the time evolution following a step change in applied potential. It is

seen that the system responds at short times ($t < 1\,\mu s$) with the development of an electric field at the perovskite/titania p-n junction ($t = 0$ in the figure). This initially localized potential drop is caused by a rearrangement of the majority holes within the depletion region, which entails a change in the bulk charge density. This perturbation is therefore screened away to the interfaces by ionic relaxation on the timescale τ_r (labelled as step 1 in the figure), leaving an approximately uniform electric field (linear potential drop) across the bulk. Eventually this uniform electric field is fully screened from the bulk by an exchange of ionic charge between the interfaces on the slower (RC) timescale of electrode polarization (step 2). The intermediate process of screening an inhomogeneous field into a uniform one temporarily increases recombination (i.e. results in a transient characterized by $R_\tau < 0$, see equation 3.30), in this model of the minority electrons at the HTL interface. We do not claim surface recombination plays a unique role however, as other recombination models could plausibly behave in a similar fashion. Increased recombination on the timescale τ_r results in a negative contribution to the capacitance as per equations 3.19 and 3.31, with positive capacitance taking over again at low frequencies (the timescale of electrode polarization) as previously.

Intermediate loop features have been reported by a few groups in the literature [52, 84, 78], but were not encountered in any of the cells handled for this study. In simulations the phenomenon is found to be somewhat delicate, being easily obscured by the standard low and high-frequency features. We infer from numerical experiments that a distance of some 1-2 decades between τ_r and the other high and low-frequency RC time-constants may be necessary for loop features to emerge. The intermediate relaxation time τ_r expressed as a fraction of the low frequency RC time-constant (assuming $R = \rho_{ion} L$) is simply C_{geo}/C_{IE}, the ratio of the geometric to ion-electrode capacitance. Simulations with a small ion-electrode capacitance consistently fail to produce loop features, likely because the ratio C_{geo}/C_{IE} is not small enough to ensure separation from the low-frequency feature. In IDD models the ion-electrode capacitance is determined by the ion density (which contributes a diffuse Debye-layer capacitance) and electrode properties depending on how the ions are compensated (e.g. doping density if by exposed dopants, or surface state density if by trapped carriers). This results in a strong dependency of the loop features on electrode properties as seen in Figure 3.6a. Loops can also be obscured if the ions are fast enough for τ_r to run into the high frequency feature (Fig 3.6a, black markers). These considerations may explain some of the observed sensitivity on properties of the titania layer [52, 85]. Another consideration is that the contribution of A_R will only be appreciable if a significant portion of the applied potential is dropped within the perovskite layer. For models with depleted, thick titania layers and no surface states this requirement is not met (since most of the potential drops within the titania) explaining why no loops appear in these simulations (Fig 3.6a, grey markers). Enlarging the doping density (red and yellow markers)

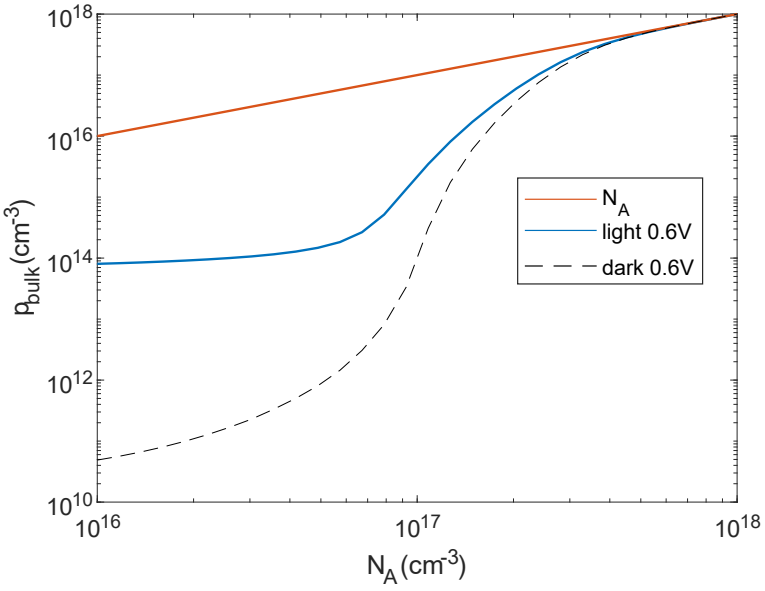

Figure 3.7: Simulated majority carrier density at a mid-point in the absorber layer, versus the homogeneous density of bulk acceptors under illumination (blue solid) and darkness (black dashed). The carrier density is seen to fall significantly below the density of dopants for doping concentrations much less than the ion density (here $1 \cdot 10^{19}\,\mathrm{cm}^{-3}$). Spatial variation of carrier densities in the bulk is minimal due to the screening effect of mobile ions.

or adding surface states (blue markers) serves the dual purposes of increasing the ion-electrode capacitance and also increasing the amount of applied potential dropped within the perovskite layer, both of which lead to more significant loops in simulation. Almost all cell parameters have an effect on A_R however, so isolating the experimentally relevant factors wherever loops appear will remain a challenging task.

Ionic Compensation of Dopants

In the discussion of loop features (Fig. 3.6) it was stated that a doping density comparable to the mean ion concentration was necessary to induce a significant bulk carrier density. In Fig. 3.7 this is justified by showing calculations of the bulk carrier density using our models under varying doping concentration, for a fixed (high) ion density. It can be seen that the majority carrier density falls significantly below the doping density whenever the doping is small compared to the ion density. Therefore, in simulating the loop feature we chose slightly lower ion densities ($N_A = 4 \cdot 10^{17}\,\mathrm{cm}^{-3}$ with $N_{ion} = 1 \cdot 10^{18}\,\mathrm{cm}^{-3}$) so that a significant carrier concentration could be obtained without a drastically large doping concentration.

3.5.4 Negative Capacitance

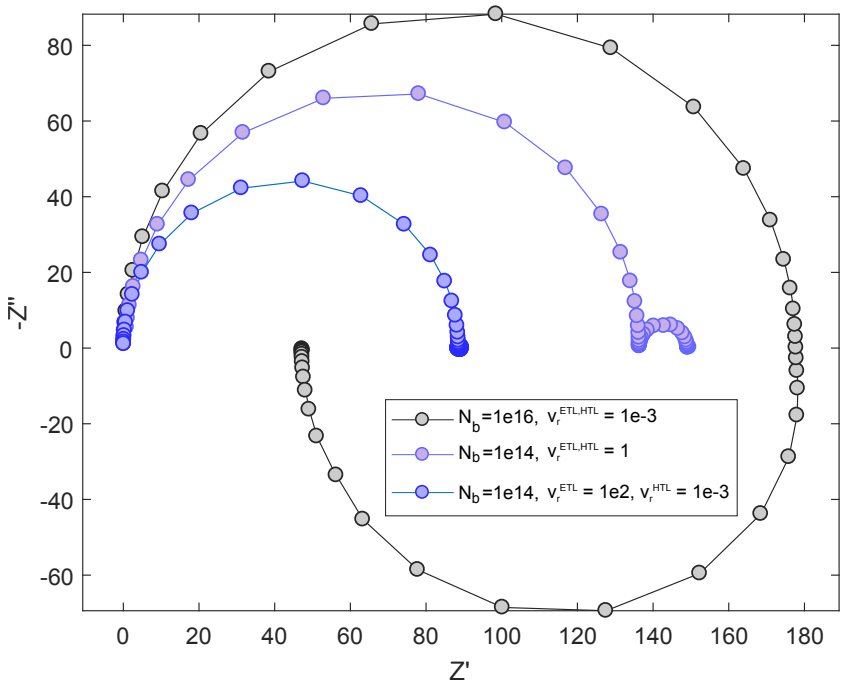

Figure 3.8: Simulated Nyquist plots (1 mHz to 1 MHz) under dark conditions and 1V forward bias for differing recombination models characterized by a single bulk SRH defect (density N_b) and surface recombination (velocity v_r) at each perovskite interface (see table 3.9 for further details). Here a negative low-frequency capacitance is observed in a model with a high density of bulk recombination centres (black series).

Negative capacitance in the low-frequency spectrum has also been reported several times, both under illumination [86, 85, 87] and in darkness [88, 86, 89]. In either case its physical origin has not been conclusively identified. Often, the low-frequency negative capacitance emerges under conditions where injected current is either dominant (under dark conditions) or a significant contributor (at large forward bias under illumination) to the total current. This raises the possibility that modulation of the injected current (rather than of the collected photocurrent as for the intermediate loops and giant capacitance) could be responsible for negative capacitance contributions through A_R. It has been shown previously that whilst ion accumulation below the built-in voltage generally increases the recombination of photo-generated carriers, it also acts to retard carrier injection, thereby reducing the dark current recombination [90]. Said otherwise, ionic redistribution in IDD models frequently has opposite effects on the recombination rate of photo-generated carriers ($R_\tau > 0$, see discussion above) and that of injected charge carriers ($R_\tau < 0$). Negative contributions to the capacitance from A_R may therefore be anticipated

whenever the injected current is a significant fraction of the total current. According to our numerical experiments, some of which are shown in Figure 3.8, this should not be regarded as a rule but simply as a possibility, as the magnitude and sign of the low-frequency capacitance is found to depend on the recombination model. In the simulations of Figure 3.8 a bulk recombination model resulted in negative capacitance (black markers), whereas surface recombination models showed positive capacitance with less overall sensitivity to the electrode polarization at low frequencies (blue markers). Similar behaviour can be expected under illumination if the bias voltage is large enough to produce a significant injected current. The suggestion that negative low-frequency capacitance is a detrimental indication for cell performance [87] may then be justified if these cells are "leaky", i.e. have a particularly high dark current (comparable to the collected photocurrent under illumination and forward bias). Alternatively, we note that in time-domain I-V measurements the unusual situation $R_\tau < 0$ (corresponding to negative capacitance) is referred to as "inverted-hysteresis" [91], and is interpreted in terms of ion-modulated collection efficiency (equivalently recombination). Typically inverted hysteresis is also only observed at forward bias voltages above the cell's built-in voltage, and is likely explained by ion-enhanced surface recombination [92] .

3.6 C-V Measurements

In the above we have shown that the antiphase recombination A_R plays a significant role in measurements under illumination, and also in darkness at low-frequencies and high bias (both conditions where the recombination current is significant compared to the charging current). By contrast, high-frequency C-V measurements taken under dark conditions provide a case where the charging current, and therefore C_Q, can be expected to dominate. Given the success of the IDD models in accounting for the ionic influence on recombination currents, it is of interest to know whether these models adequately represent the charging of perovskite cells as well. In the following we evaluate our EIS simulations against high-frequency C-V measurements taken on TiO_2/$MAPbI_3$/Spiro-OMeTAD cells.

In common with current-voltage measurements of normal structure $MAPbI_3$ cells, there is often clear rate-dependent hysteresis in capacitance-voltage sweeps. For simplicity here we focus on slow scans approximating a steady-state measurement, although the amount of hysteresis observed at rates as low as 0.1mV/s was still considerable. In the measurement of Figure 3.9a a slow scan rate of 0.7mV/s was used (plots of the hysteresis are included in Fig. 3.10a-b). At each voltage step a frequency scan was performed in the range of 1kHz-1MHz, revealing a plateau with a small degree of dispersion (dotted lines in Figure 3.9a, possibly caused by microscopic inhomogeneities [7]). After some exploration, simulations of this measurement were

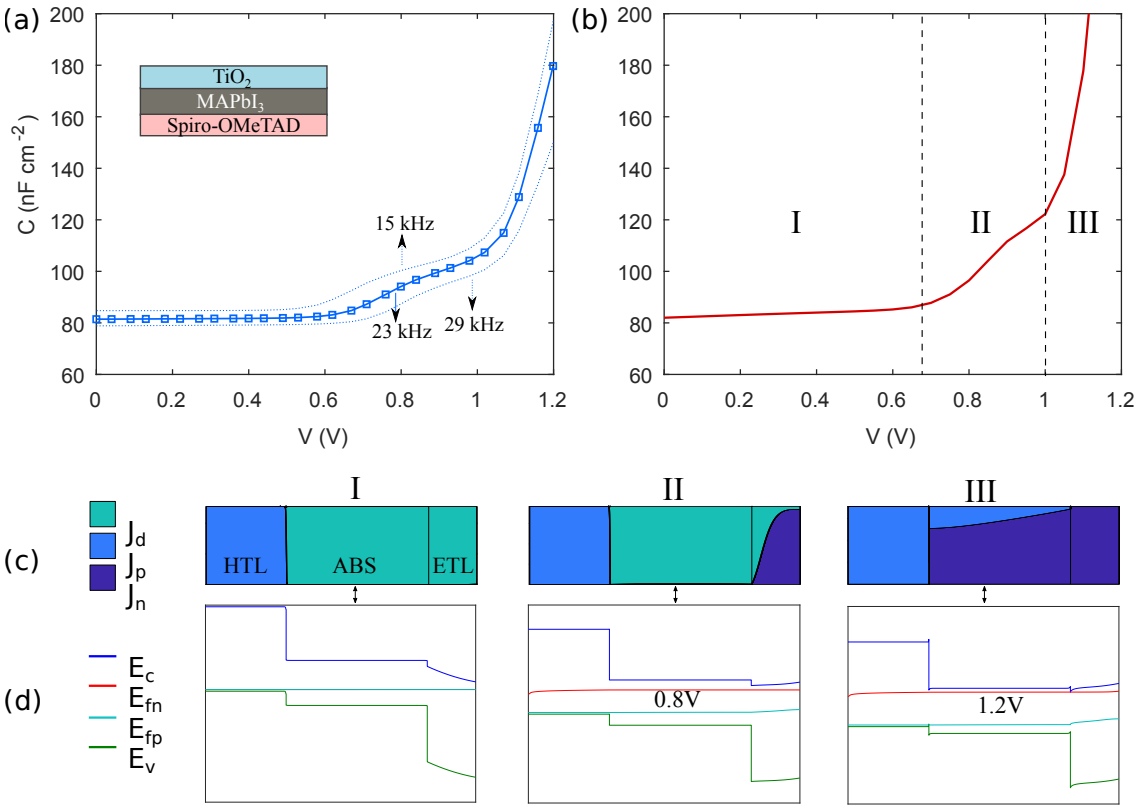

Figure 3.9: (a) Slow-scan measurements of the un-illuminated capacitance versus voltage taken on a standard $MAPbI_3$ perovskite cell. (b) Simulations of the same measurement (parameters in table S1). (c) Area plots of the AC current taken from the simulation in (b) showing spatially resolved contributions from electron and hole conduction (J_n, J_p), as well as displacement (J_d). (d) Band diagrams corresponding to (c), illustrating depletion in the ETL in region I and accumulation in region III.

found which strongly resemble the measurement (Figure 3.9b, the adjusted but physically reasonable parameters are listed in table 3.9. Furthermore, these models qualitatively reproduce the hysteresis behaviour observed in forward-reverse scan measurements (Figures. 3.10a,b,d). In the calculation of Figure 3.9b the system was relaxed for more than 1000s at each bias point to approximate steady-state. We will first provide an interpretation of the simulation results before assessing their physical relevance. Both the measured and simulated data can be split into three voltage regions according to qualitative behaviour as done in Figure 3.9b. Plots of the total ac-current, resolved into components of electron current, hole current, and displacement in Figure 3.9c serve to illustrate the mechanisms at play in each region. Accordingly, region I is defined by current flowing as displacement through both the perovskite and titania layers,

making the capacitance in this voltage range relatively small (technically a serial combination of the individual geometric capacitances). In region II the application of forward bias replenishes the depleted titania layer, shorting out its serial contribution to the capacitance and leaving only the perovskite layer as dielectric spacer. Finally in region III the accumulation of carriers within the perovskite layer causes a rapid increase in the capacitance with voltage (a combination of accumulation and recombination components, the latter part of which can be negative).

The apparent agreement between measurement and simulation in Figure 3.9 is striking but requires further scrutiny. Full depletion of the titania layer (as seen in the band-diagrams of Figure 3.9d) occurs due to ionic redistribution, and accounts for the relatively constant capacitance in region I of the simulations. Mobile ions screen the built-in voltage associated with the two contact layers away from the bulk of the perovskite, causing it to drop both inside the contact layers and in the narrow diffuse ionic layers adjoining them (invisibly small in Figure 3.9d). The specific parameters used in the simulation of Figure 3.9b include contact layer dopings of $1 \cdot 10^{19}\,\mathrm{cm}^{-3}$ for Spiro and $1 \cdot 10^{17}\,\mathrm{cm}^{-3}$ for titania, in addition to high ion densities $1 \cdot 10^{19}\,\mathrm{cm}^{-3}$ within the perovskite. These parameters cause most of the built-in voltage to drop within the titania, leaving it fully depleted at 0V (see Figure 3.9d). Our choice of a high doping density for the Spiro layer is motivated by KPFM studies which indicate that very little of the built-in and applied voltage drops within the Spiro layer [93, 94], suggestive of small depletion widths. However this could be a result of ion uptake from the perovskite layer instead of intentional doping, a process that has been clearly observed for several intrinsic and extrinsic species [95, 96, 97, 98]. Setting larger doping in the titania layer causes the extent of region II to reach downward to lower voltages, eventually entering the negative bias range. Examples of simulations with a larger titania doping are provided in Fig. 3.10e (these more closely resemble some previously reported C-V measurements) [99]. Since the doping of compact and mesoporous titania layers can vary widely with deposition and annealing methods, it is not surprising that previous reports have differed in their evaluation of whether the depletion width in titania is significant [94, 14, 13].Indeed, several studies have interpreted the capacitance seen in region II as being due to carrier accumulation in the perovskite layer (a result of p-type doping) [14], disregarding the effect of titania depletion by comparison [99].

To test the extent of depletion in the titania layer, otherwise identical $MAPbI_3$ cells were prepared on titania/FTO substrates with varying compact layer thicknesses (by spinning 2, 4 and 6 layers according to the procedures in sec. 3.5.1). It was found that the low-voltage capacitance (region I) scales inversely with the titania thickness (Fig. 3.10a-c), strongly indicating that the depletion width in titania extends over the full extent of the compact layer. No correlation was found between the capacitance in regions II or III and the titania thickness (see Figs. 3.10a-b). It therefore seems clear that the capacitance in region I of our measurements in Figure 3.9a

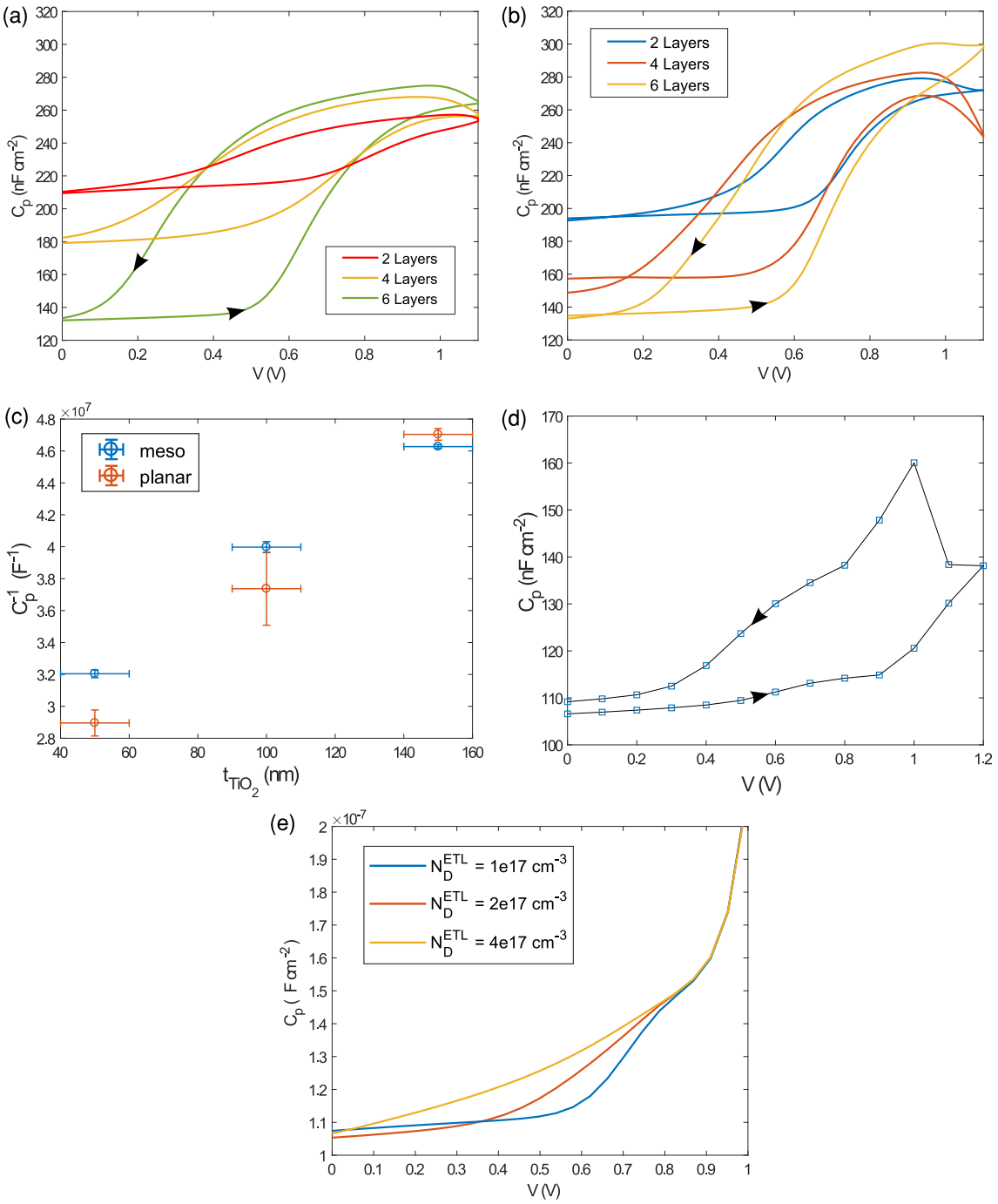

Figure 3.10: (a,b) C-V measurements at 10kHz of FTO/TiO_2/$MAPbI_3$/Spiro-OMeTAD/Au cells with varying compact layer thickness. Shown for (a) no mesoporous layer (planar cells) and (b) a ≈70 nm mesoporous layer, with one representative for each condition (a minimum of 2 devices for each were tested). Measurements were performed under dark conditions using a scan-rate of ≈ 20 mV s^{-1} (i.e. faster than the rate of 0.7 mV s^{-1} used in the measurements of Fig. 4a). The measurements of (a-c) were made on a separate batch of cells to the one given in Fig. 3.9, and apparently feature smaller absorber thicknesses as manifested by the larger capacitance values. (c) Average capacitance at 0V for all cells versus the compact layer thickness, estimated in the abscissa to within ±10 nm. (d) Simulated C-V at 10kHz using the model of Fig. 3.9b, this time with a significant scan-rate. These models qualitatively reproduce the hysteresis behaviour seen in measurements. (e) Simulations as in Fig. 3.9b with varying doping levels in the ETL (TiO_2) layer.

includes the geometric capacitance of a largely depleted titania layer. Whether the perovskite remains essentially free of carriers in region II as suggested by our simulations, or whether it also contributes to the depletion capacitance, is less certain. On this issue it must be noted that the concept of a macroscopically p-type (or n-type) perovskite layer becomes more complex in the IDD theory because ionized dopants can be compensated by mobile ions (which act themselves as a mobile doping density), instead of, or in addition to excess carriers [83]. As we show in Fig. 3.7, the IDD theory predicts that a large compensated ion density (order $1 \cdot 10^{19}\,\mathrm{cm}^{-3}$) will readily screen any excess charge away from the bulk up to a comparable density, bringing in far fewer than the expected number of carriers for compensation. For this reason the standard picture of a p-n type junction between perovskite and titania [94] is not comfortably compatible with the IDD model and a large density of compensated ions. This issue is entirely averted if the perovskite remains essentially intrinsic in terms of carrier density and depletion is located in the titania instead, where a static and approximately uniform doping profile of order $1 \cdot 10^{17}\,\mathrm{cm}^{-3}$ is within the expected range [100]. We conclude that the C-V measurements in Figure 1 can be understood using the IDD model if the depletion capacitance in region II is assigned to the titania layer instead of the perovskite. This does raise the problem of how to account for the negative space charge that appears in KPFM measurements as part of a p-n junction between the perovskite and titania, extending over as much as 300nm into the bulk [94, 93]. If these are an accurate representation of bulk electrical field profiles then ion densities must be much lower than DFT calculations would indicate [83], since the predicted densities yield Debye lengths on the order of a few nanometers. In any case, Mott-Schottky analysis applied to the perovskite layer is unlikely to yield reliable results as it assumes a static charge distribution compensated solely by carriers.

3.7 Ion-Electrode Capacitance

As discussed in reference to Fig. 3.5 above (see also Fig. 3.13 in sec. 3.8.1), the un-illuminated low-frequency capacitance of normal-structure cells reaches values of $1 - 10\mu\mathrm{F}\,\mathrm{cm}^{-2}$ at zero bias between $10 - 100\mathrm{mHz}$. Time-domain discharge measurements on the same cell type over 1000s charge-discharge cycles (effectively probing the 1 mHz range) yield integral capacitances as large as $80\mu\mathrm{F}\,\mathrm{cm}^{-2}$ (such discharge measurements are a more direct way of accessing the fundamental ion-electrode capacitance since there is no contribution from recombination currents when the discharge is measured at 0 V) [76]. In the IDD theory this capacitance is supposed to result from the accumulation of bulk ions in diffuse layers near the (ionically blocking) selective contact layers, as in the simplified Guoy-Chapmann theory of metal-electrolyte interfaces [9]. However, one of the many differences between metal-electrolyte interfaces and those in a perovskite cell is

that the carrier-selective contacts in the latter are doped semiconductors rather than metals. Ions accumulated in the diffuse layers should therefore be compensated on the contact side by either an excess of majority carriers, or else by depletion-layer space charges, which will incur their own series contribution to the total capacitance. Since depletion capacitance are typically less than $1\,\mu F\,cm^{-2}$, the large low-frequency capacitance is not compatible with ionic compensation by depletion-layer space charges unless the contact layers are doped at unrealistically high levels. To the contrary, as discussed in the final section on C-V measurements there is considerable evidence that the titania layer in our normal-structure cells is almost entirely depleted at $0V$, owing to modest doping densities coupled with the effect of ion accumulation. Since free electrons in the titania layer are primarily located beyond the edge of the depletion zone, some tens to hundreds of nanometers away from the interface, a large capacitance can only result if the charges compensating accumulated ions at the interface are not free carriers (i.e. they must be trapped). This is far from a surprising conclusion as anatase TiO_2 is famous for having a high density of reactive surface sites [101], and surface treatments have a clear effect on the low frequency capacitance as seen in measurements of passivated cells (Fig. 3.13). Based on the available evidence, the implicated surface states (or traps) could be intrinsic to the titania surface, the perovskite surface, hybridized orbitals, or bound states located on the ions themselves. Observations of bonding between iodine and atoms on the titania surface also suggest that a realistic picture should include a Helmholtz layer of adsorbed ions on the titania surface [96]. The Spiro interface is equally important for the ion-electrode capacitance since it contributes in series, but we are not aware of any comparable evidence in favour of surface states there. KPFM studies do indicate partial depletion however [73], so a comparable mechanism for accommodating charge is also required. A compelling possibility is provided by observations that the Spiro layer is highly permeable to extrinsic ions, including I^-, Li^+ and H^+ [96, 97, 98]. Any one of these ions, if capable of moving in both the perovskite and titania layers on the relevant timescales, would short out the depletion capacitance of the Spiro layer and so potentially explain the large ion-electrode capacitance. Instead of attempting to model ion permeation into the contact layers, the simulation of Fig. 3.5 includes surface states at both the titania and Spiro interfaces, which allow a large ion-electrode capacitance to develop given the high ion density ($1 \cdot 10^{19}\,cm^{-3}$).

3.8 Quantifying Hysteresis with EIS

Several attempts have been made at introducing a standard method for quantifying hysteresis in perovskite cells, generally on the basis of rate-dependent I-V measurements. Whilst straightforward to implement, the attempt to quantify hysteresis in terms of indices calculated from I-V

data can be problematic for the following reasons:

1. Uniqueness: The I-V sweeps of a cell with significant hysteresis are complex (c.f. Chapter 2), making it hard to settle on a well-motivated or unique quantifier.

2. Resolution: By sampling the I-V behavior at a few scan rates (as is standard practice) one obtains very limited information about the frequency/time-dependence of hysteresis, and incorrect conclusions can be drawn. In I-V measurement it is generally necessary to re-equilibriate the device between each sweep to avoid carry-over effects, which is time-consuming.

3. Relevance: For practical purposes only the transient behaviour near the operating point (maximum power point under illumination) is of interest, making most of the data in an I-V sweep redundant.

EIS measurements provide a natural alternative to the method of I-V indices. This addresses all three issues above in the following manner:

1. Uniqueness: EIS data is completely specified by only two real quantities at each frequency, making it far easier to settle on a unique quantifier. We argue below that the imaginary component of the admittance is a natural choice.

2. Resolution: In EIS it is efficient to gather data over a wide frequency range at high resolution.

3. Relevance: By measuring near the maximum power point under realistic conditions one obtains a measurement of hysteresis without redundancy.

The expression of hysteresis in an EIS measurement is best seen in the "Lissajous" figure traced by plotting the data as $(V(t), I(t))$ (Fig. 3.11 (left)). As long as linearity is observed (i.e. the voltage amplitude is not too large), the figure traced is an ellipse with area proportional to the imaginary component of the admittance. The area of the Lissajous ellipse (modulo the scaling factor ΔV^2) is a natural way to quantify hysteresis, and coincides with one commonly used I-V index which measures the area between forward and reverse scans [103], as depicted in Fig. 3.11 (left). Since the imaginary admittance is proportional to the AC-capacitance ($\mathrm{Im}\,[Y] = \omega C$), plots of $\mathrm{Im}\,[Y]$ also contain the high-frequency capacitance, which is of course another form of hysteresis (albeit a familiar and practically irrelevant one). This is the cause of the high-frequency blow-up ($\mathrm{Im}\,[Y] \propto \omega\, C_{hf}$). Ideally one would like to remove this high-frequency component to evaluate only the low-to-intermediate frequency hysteresis induced by ion migration, but this is hardly necessary provided that the features are sufficiently separated.

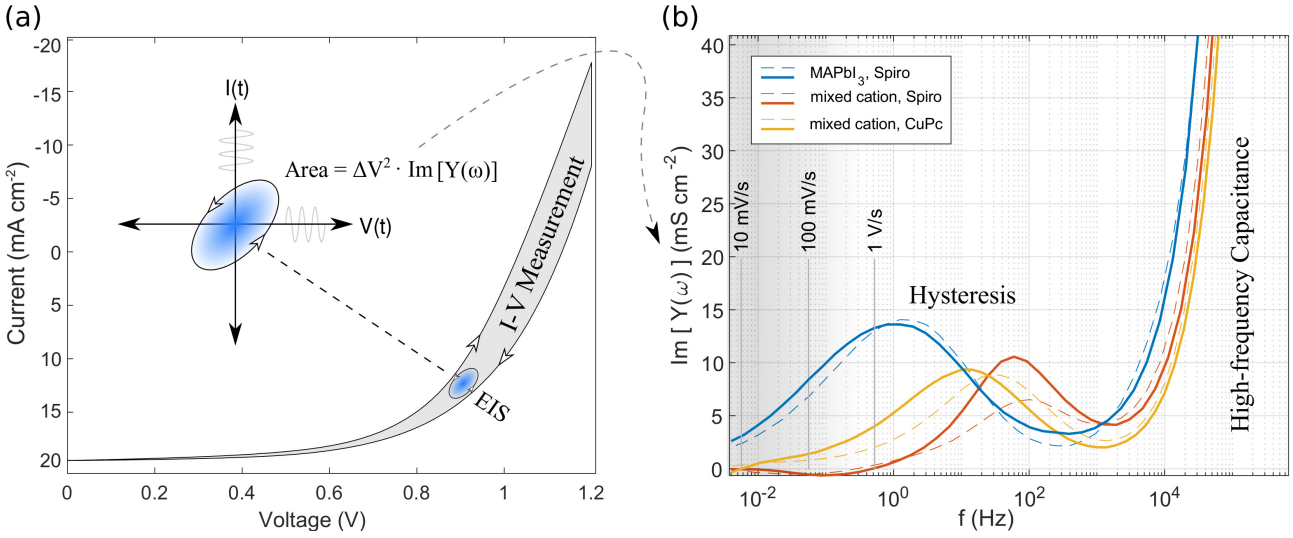

Figure 3.11: (a) Schematic of the comparison between an I-V sweep and EIS measurement, depicted for a perovskite cell under illumination. (b) EIS measurements of perovskite cells under illumination and biased near their maximum power-point. Plotted is the imaginary part of the admittance, which is simply related to the area of the Lissaffjous (current-voltage) ellipse as illustrated in (a). Measurements were taken for three cell types based on either the benchmark $MAPbI_3$ perovskite or a mixed cation perovskite, and with either Spiro-OMeTAD or CuPC as the hole-selective contact. Measurements on two distinct cells with each material combination are shown (solid and dotted lines) to indicate the processing variability. The limited frequency range accessed by typical I-V measurements, taken at 10-1000mV s^{-1}, is shaded in grey. The equivalent frequency for I-V measurements is determined via $f = r/\,2\,(V_f - V_i)$, with r the scan rate and $(V_f - V_i)$ the voltage sweep range.

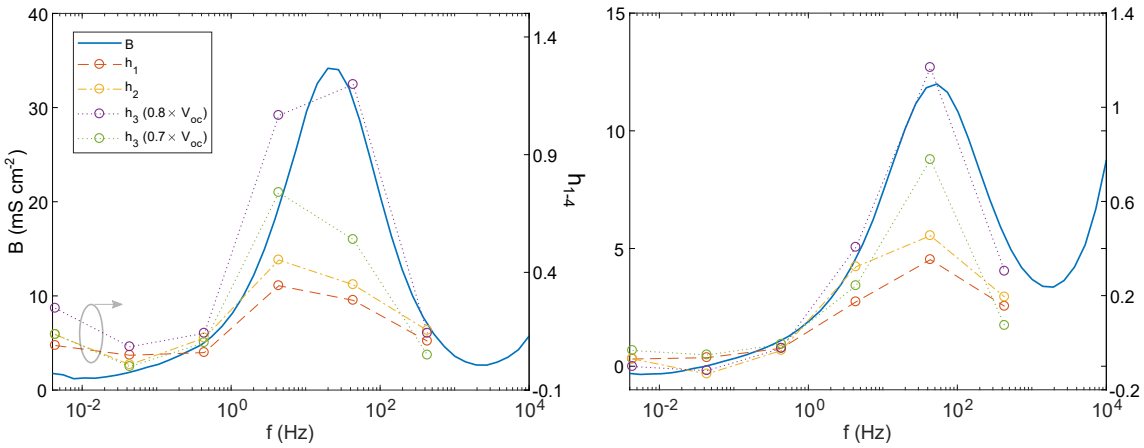

Figure 3.12: Comparison between the hysteresis indices h_1, h_2, h_3 and imaginary admittance ($B = \mathrm{Im}\, 1/Z$) measured on mixed cation cells with (right) and without (left) ETL-side fullerene passivation (made again according to ref. [102]). The I-V measurements were conducted as continuous reverse-forward sweeps starting at 1.15 V (pre-biasing for 10s per measurement) and ending at 0 V with variable scan rates r, converted to an effective frequency here as $f = r/\left(2 \times (1.15\,\mathrm{V} - 0\,\mathrm{V})\right)$. The EIS measurements were conducted close to the maximum power-point identified from the slowest ($10\,\mathrm{mV\,s^{-1}}$) I-V curve after 600 s stabilization.

An example of a "hysteresis plot", showing $\mathrm{Im}\,[Y]$ measured on 4 different cells is shown in Fig. 3.11(right). Here it is clear that the peaks, present at ≈ 1 Hz for $MAPbI_3$ and ≈ 100 Hz for the mixed cation cells, are quite distinct from the high-frequency capacitance (hysteresis) at > 10 kHz.

The relationship between the imaginary admittance and several hysteresis indices is indicated by the measurements of Fig. 3.12, conducted on two mixed-cation perovskite cells with and without ETL-side fullerene passivation. The indices h_{1-3} are three common choices encountered in the literature [104, 86, 103] defined as

$$h_1 = 1 - \frac{A_f}{A_r}$$
$$h_2 = 1 - \frac{\eta_f}{\eta_r}$$
$$h_3 = \frac{j_r(V^*) - j_f(V^*)}{j_r(V^*)}$$

where h_1 refers to the area A under the I-V curve, h_2 to the ratio of power maxima, h_3 to the ratio of currents at a specified voltage V^*, and in each case r and f stand for reverse and forward sweeps respectively. Qualitatively the agreement between these indices and the imaginary admittance ("susceptance") is good, and there seems to be no reason to favour one over any

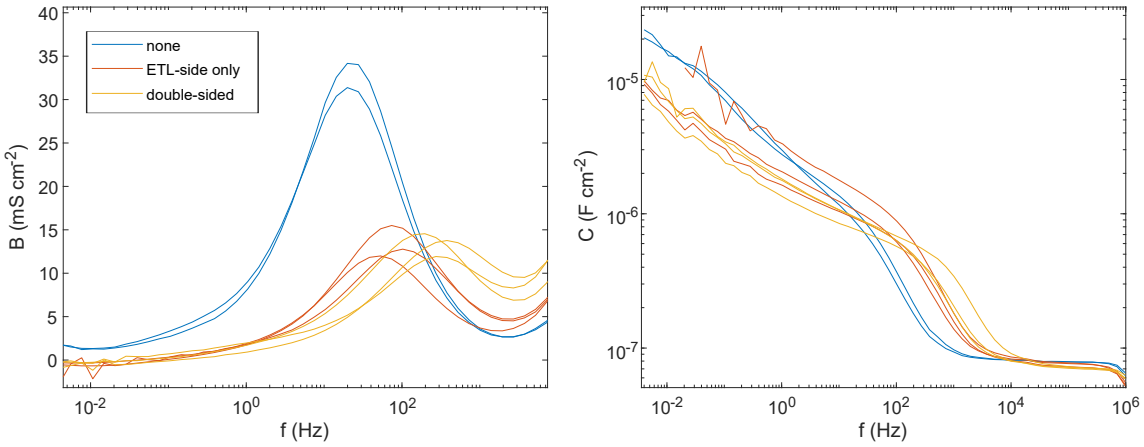

Figure 3.13: EIS measurements of mixed cation perovskite cells with varying passivation inclusions. (Left) Susceptance measured at the maxmimum power point (roughly identified by $100\,\mathrm{mV\,s^{-1}}$ scan) and (Right) dark capacitance measured at 0 V. Measurements were performed on two or three distinct cells per condition.

another. There is considerable variance between the absolute values however, which shows that the choice of index is not without consequence. It can be seen that both the susceptance and hysteresis are capable of taking on negative values – a sign of inverted hysteresis. In Fig. 3.12 the passivated cell (right panels) exhibits inverted hysteresis at low frequencies, as confirmed by the I-V scans (not shown). For the measurement of Fig. 3.12 we have performed I-V scans up to rates of $1000\,\mathrm{V\,s^{-1}}$, which is well outside the range that is usually investigated when reporting hysteresis indices (see e.g. [105, 106, 107, 108]). Usually scan-rates in the vicinity of $100\,\mathrm{mV\,s^{-1}}$ are employed and varied over approximately 1 order of magnitude. Clearly this would not be sufficient to capture the significant hysteresis peak in the mixed cation cells (Fig. 3.12(right)) at 100 Hz, and yet such measurements are frequently used as a basis for labelling cells as "hysteresis-free". Whilst true enough in the sense that these cells exhibit minimal hysteresis at normal scan rates, this paints a misleading picture about what is physically different in these cells, suggesting for instance that the mobile ions have been eliminated when in reality their response is simply quicker.

Having established the utility of EIS for quantifying hysteresis, we next apply this approach to a few cases of interest.

3.8.1 The effect of passivation

Interface passivation targeted at the perovskite/ETL interface in particular has been shown to dramatically reduce the appearance of I-V hysteresis, and lead to overall performance gains

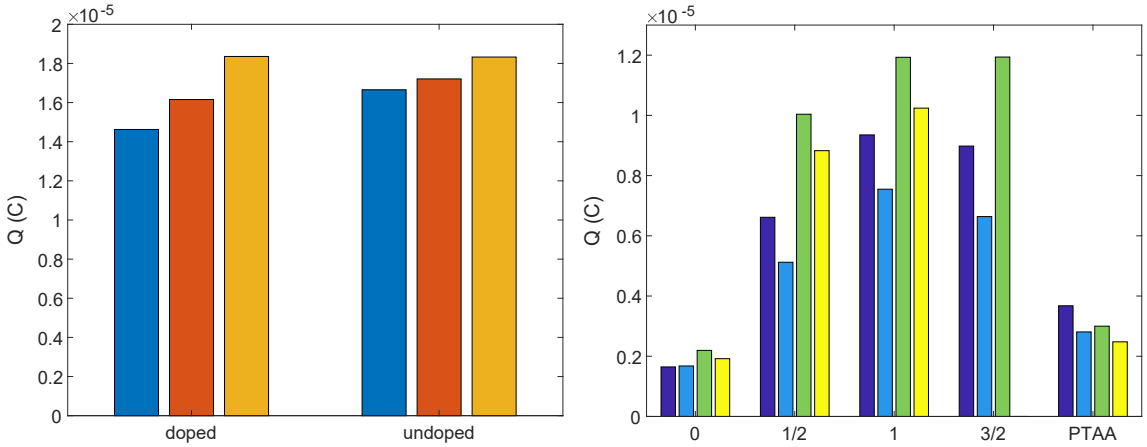

Figure 3.14: Effect of ETL (left) and HTL (right) doping on the amount of charge stored at 1 V, as measured by charging the cells for 600 s before discharging at 0 V for an equal time. Each bar represents a measurement on a distinct cell. The charge indicated is the integrated current over the discharge period. Indium was added as the dopant in the ETL experiment [109], whereas the fractions in the abscissca of the HTL figure refer to fractions of the usual Li-TFSI dopant amount added to the Spiro.

[19, 102]. Since the severity of hysteresis is known to scale with recombination rates (Chapter 2), it is not clear whether the hysteresis reduction in these cell types is simply a by-product of removing non-radiative recombination centres, or whether there is a more direct interaction with the mobile ions. In Fig. 3.13 we show EIS measurements (susceptance at the maximum power point under illumination, and capacitance at 0 V under dark conditions) of mixed cation cells with varying passivation levels: double-sided, ETL-side only and no passivation. The addition of ETL-side passivation is seen to reduce the magnitude of hysteresis considerably over the entire frequency range (Fig. 3.13(left)), and produces a slight shift in the peak position towards higher frequencies (≈ 70 Hz versus ≈ 20 Hz for the un-passivated cells). The magnitude reduction could readily result from a removal of non-radiative recombination centres, as suggested by the higher open-circuit voltages and increased photoluminescence observed in ETL-passivated cells [102]. On the other hand the frequency shift suggests a more direct interaction between the passivation layer and the mechanisms of ion accumulation, most likely through the ion-electrode capacitance (sec. 3.7). The introduction of a thin polymer layer between the perovskite and contact layers would be expected to change circumstances of ion accumulation, such as the availability of surface sites (sec. 3.7), resulting in smaller overall capacitance and therefore faster RC time-constants. Reduced capacitance is confirmed by the dark capacitance measurements in Fig. 3.13(right) except for one anomalous sample which exhibited large low-frequency noise.

Compared to the single (ETL) sided passivation, double-sided passivation in this experiment

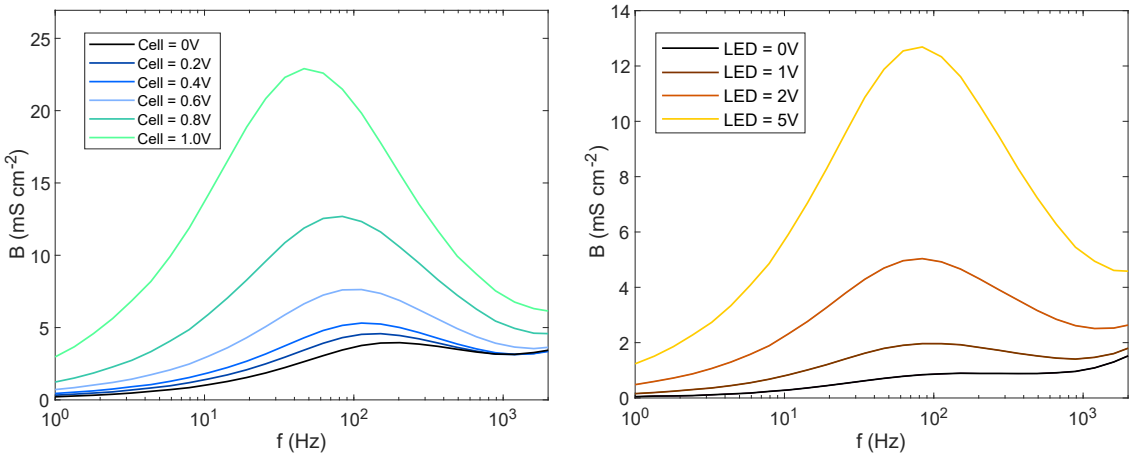

Figure 3.15: Effect of applied voltage (left) and illumination intensity (right) on the susceptance of a mixed cation perovskite cell. In the voltage measurement (left) illumination was fixed at approximately 1-sun intensity (LED=5 V), and in the illumination measurement (right) the cell was held at 0.8 V (here the legend refers to the LED driver voltage, approximately linearly related to the light intensity).

was only found to shift the peak frequency of hysteresis slightly, and had little effect on its magnitude. This is perhaps not surprising given our hypothesis that capacitance at the perovskite/HTL layer is facilitated by the penetration of a mobile species into the Spiro-OMeTAD HTL such as iodine or lithium (sec. 3.7). The role of Li in this capacity is jointly implicated by a previous study [98] and our own measurements of the stored charge as a function of Li-TFSI doping in the Spiro layer (Fig. 3.14). Returning to the capacitance measurements in Fig. 3.13(right), since the Spiro-OMeTAD HTL is already composed of large organic molecules, the addition of a thin PCBM layer (i.e. more large organic molecules) would not be expected to effectively block the mobile species (Li or otherwise). A weak blocking effect may be implicated by a slight reduction in the dark capacitance, but this observation may not be statistically significant given the observed spread.

3.8.2 Susceptance versus Voltage and Illumination

Since EIS gives only local information about hysteresis, one may wonder how the results vary with the applied voltage, and also with other conditions such as the illumination intensity. We find that voltage has a strong effect on hysteresis as measured by the susceptance, shown in Fig. 3.15(left). Moving to larger forward bias both increases the magnitude of hysteresis and reduces the characteristic timescale. Both trends are expected: on the one hand, it is natural for cells to exhibit higher sensitivity to voltage perturbations at large forward bias, as the injected current

increases near-exponentially with forward bias and the collection efficiency is also expected to drop rapidly beyond the built-in voltage. A decrease in the characteristic timescale indicates that the differential ion-electrode capacitance is an increasing function of voltage (making the RC time-constant grow and hence the characteristic frequency diminish). This is also unsurprising as one would expect the (differential) capacitance associated with ionic accumulation to increase towards the device's built-in voltage, since the width of the accumulation layers is an increasing function of $V - V_{bi}$. It is not clear from the measurements of Fig. 3.15 whether these trends continue beyond the built-in voltage.

The trend with illumination in Fig. 3.15 is basically another manifestation of the light-induced capacitance discussed in sec. 3.5.2. To re-iterate the basic idea: higher carrier densities under illumination lead to an increase in recombination, whose sensitivity to voltage contributes to both the conductivity and the susceptance. We remark that the implied dependence of recombination on applied voltage indicates a breakdown of the superposition principle, which is well-known to occur in many p-i-n type photovoltaic devices [75]. Indeed, the entire theory of hysteresis developed in Chapter 2 can be summarized as a collection efficiency which is non-ideal (i.e. less than unity), and a function of ion accumulation. The effect of ion accumulation on the dark current must also be considered but is of secondary importance in illuminated I-V measurements due to the relatively small magnitude of injected currents (except at large forward bias).

3.8.3 Temperature dependence

Since hysteresis apparently stems from ion migration, a thermally activated process, it is natural to investigate the effect of temperature on susceptance measurements. This was done on mixed cation cells as part of this investigation with the results shown in Fig. 3.16. It is observed that the characteristic (peak) frequency shifts to higher frequencies at elevated temperatures, as expected. However, it is also clear that some other change occurs simultaneously because the curves fail to coincide on bringing the temperature back down to the starting point. This could either be indicative of an irreversible form of degradation (perhaps involving the production of excess ions, explaining the faster response) or of a very slow process (such as the migration of a very slow species) over the timescale of measurement. We therefore did not attempt to extract an activation energy from these measurements. The increase in peak height indicates more extensive recombination loss at higher temperatures, consistent with the detrimental effect of heat on cell performance.

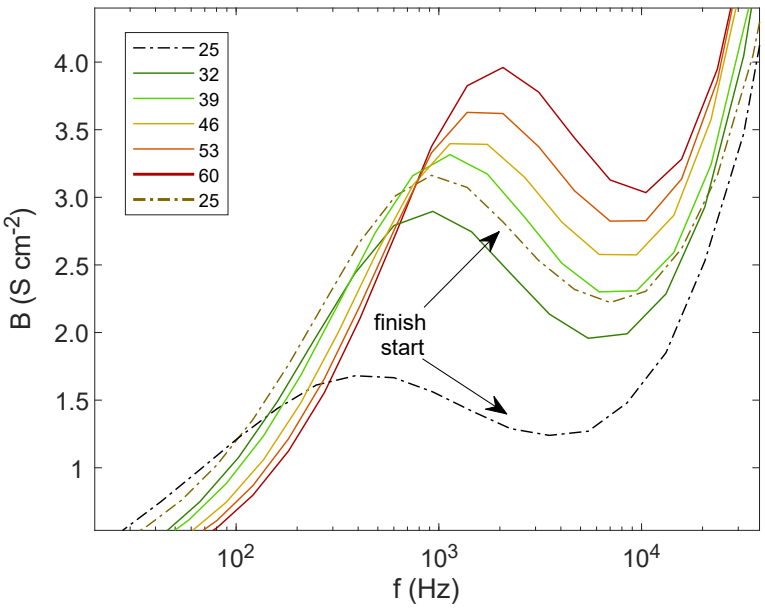

Figure 3.16: Effect of temperature on the susceptance peak of a mixed cation cell measured at max power point under illumination. This cell failed to return to its initial condition on lowering the temperature again (note that as previously the cell was stabilized for at least 600 s at each temperature prior to the EIS measurement).

3.9 Summary and Conclusions

In this chapter we have extended the theory and models developed in Chapter 2 for addressing I-V measurements to cover EIS measurements as well. Indeed, the simulations referred to here are the same drift-diffusion COMSOL Multiphysics® models applied in sec. 2.5, modified only to simulate EIS instead of I-V measurements. We have used these models to interpret the most common features seen in EIS measurements of standard perovskite solar cells, and found that they are successful in providing sound explanations for these with little modification.

A natural consequence of ion-induced hysteresis is that delayed recombination contributes significantly to capacitance measurements, which ultimately measure the delayed electrical response and therefore do not discriminate between charging currents and other sources of delay. We have described in detail how the AC capacitance obtained from measurements of a solar cell can be considered as a sum of two components, one from conventional charging currents and the other from phase-delayed recombination. In $MAPbI_3$ delayed recombination occurs due to ion migration, but many physical mechanisms could have a similar effect, including dielectric relaxation, slow carrier trapping and carrier accumulation. Indeed, we presented simulated evidence that a small but noticeable light-induced high-frequency capacitance can result purely

from carrier dynamics, with a mechanism that is similar to the ones responsible for producing negative capacitance in conventional diodes [39]. At low frequencies, we have argued that antiphase recombination is almost certainly responsible for observations of giant photo-induced capacitance. Inductive loop features and measurements of low-frequency negative capacitance can also be explained simply with recombination currents in mind, but further studies will be required for experimental confirmation.

One of the most common applications for EIS in cell characterization is the determination of doping densities via capacitance-voltage profiling. On this topic we have presented experimental C-V measurements, interpretively backed by simulations, which indicate significant depletion in the titania layer below forward bias voltages of $\approx$ 0.6V. This depletion implies that Mott-Schottky analysis should be undertaken with great care to avoid confusing the titania doping with that of the perovskite layer, which appears essentially un-doped in the cells fabricated for this study.

Despite uncertainties concerning the mechanism by which a large ionic charge is accommodated at the contact layer interfaces, it is still reasonable to expect that many important features in EIS measurements are properly identified by ionic drift-diffusion models. This is because the mechanisms described in this work result from generic processes, such as the qualitative effect of ion migration on internal electric fields, and ionic relaxation, that are not expected to depend sensitively on the proper description of adsorption processes.

The success of the models presented here in explaining several major features of interest, such as giant photo-induced capacitance, inductive loop features and capacitance-voltage curves, builds on their earlier achievements in the domain of I-V hysteresis [8, 9, 11, 90, 92]. The interpretations that follow from these models therefore fit into a unified understanding of transient behaviour, which should enable more integrated usage of EIS as a tool to supplement standard I-V measurements. On this topic we have shown that measurements of the imaginary admittance provide a straightforward and relatively unambiguous quantifier of hysteresis, with several advantages over the conventional hysteresis indices. The adoption of EIS as a method to quantify hysteresis would resolve the ambiguity in commonly encountered statements such as that certain cells are “hysteresis-free”, and better distinguish between genuinely suppressed hysteresis and mere changes in its characteristic timescale.

Parameter	Layer	Value(s)	Figures	Description
$N_A - N_D$ (cm^{-3})	ABS	0, $4 \cdot 10^{17}$, 0	3.5, 3.6, 3.8-3.9	Net doping
ϵ_r	ABS	62[25]	All	Perimittivity
E_g (eV)	ABS	1.6	All	Band gap
χ (eV)	ABS	3.9	All	Electron affinity
N_c, N_v (cm^{-3})	ABS	$8 \cdot 10^{18}$, $6 \cdot 10^{18}$	All	Density of states
t (nm)	ABS	300, 500, 500, 350	3.5, 3.6, 3.8, 3.9	Mobility
μ_n ($cm^2\,V^{-1}\,s$)	ABS	1	All	Mobility
μ_p ($cm^2\,V^{-1}\,s$)	ABS	1	All	Mobility
σ_n (cm^{-2})	ABS	$1 \cdot 10^{-15}$	All	SRH Cross-section
σ_p (cm^{-2})	ABS	$1 \cdot 10^{-17}$	All	SRH Cross-section
N_{td} (cm^{-3})	ABS	$1 \cdot 10^{14}$, $1 \cdot 10^{14}$, $1 \cdot 10^{14}$ to $1 \cdot 10^{16}$, $1 \cdot 10^{15}$	3.5, 3.6, 3.8, 3.9	Defect Density (Donor type)
E_t	ABS	mid-gap	All	SRH Energy
N_{ion} (cm^{-3})	ABS	$1 \cdot 10^{19}$, $2 \cdot 10^{18}$, $1 \cdot 10^{18}$, $1 \cdot 10^{19}$	3.5, 3.6, 3.8, 3.9	SRH Energy
D_1 ($cm^2\,s^{-1}$)	ABS	$1 \cdot 10^{-10}$,$1 \cdot 10^{-9}$, to $1 \cdot 10^{-11}$, $1 \cdot 10^{-11}$	3.5, 3.6, 3.8, 3.9	Ionic Diff. Const. (fast)
D_2 ($cm^2\,s^{-1}$)	ABS	$1 \cdot 10^{-13}$, 0, 0, 0	3.5, 3.6, 3.8, 3.9	Ionic Diff. Const. (slow)
N_D (cm^{-3})	ETL	$1 \cdot 10^{17}$, $1 \cdot 10^{17}$ to $6 \cdot 10^{18}$,$1 \cdot 10^{17}$	3.5-3.6, 3.8, 3.9	Net doping
ϵ_r	ETL	55,[110] 24[111]	3.5-3.8, 3.9	Perimittivity
E_g (eV)	ETL	3.39	All	Band gap
χ (eV)	ETL	4.1	All	Electron affinity
N_c, N_v (cm^{-3})	ETL	$8 \cdot 10^{18}$, $6 \cdot 10^{18}$	All	Density of states
t (nm)	ETL	120	All	Thickness
μ_n ($cm^2\,V^{-1}\,s$)	ETL	0.1	All	Mobility
μ_p ($cm^2\,V^{-1}\,s$)	ETL	0.1	All	Mobility
N_A (cm^{-3})	HTL	$1 \cdot 10^{19}$	All	Net doping
ϵ_r	HTL	3	All	Perimittivity
E_g (eV)	HTL	3.0	All	Band gap
χ (eV)	HTL	2.1	All	Electron affinity
N_c, N_v (cm^{-3})	HTL	$8 \cdot 10^{18}$, $6 \cdot 10^{18}$	All	Density of states
t (nm)	HTL	200	All	Thickness
μ_n ($cm^2\,V^{-1}\,s$)	HTL	0.1	All	Mobility
μ_p ($cm^2\,V^{-1}\,s$)	HTL	0.1	All	Mobility
v_n ($cm\,s^{-1}$)	ABS-ETL	$1 \cdot 10^4$, 10, $1 \cdot 10^{-3}$ to $1 \cdot 10^2$, $1 \cdot 10^4$	3.5, 3.6, 3.8, 3.9	Recombination velocity
v_p ($cm\,s^{-1}$)	ABS-ETL	$1 \cdot 10^4$, 10, $1 \cdot 10^{-3}$ to $1 \cdot 10^2$, $1 \cdot 10^4$	3.5, 3.6, 3.8, 3.9	Recombination velocity
E_t	ABS-ETL	mid-gap	All	SRH energy
D_{it} ($cm^{-2}\,eV^{-1}$)	ABS-ETL	$3 \cdot 10^{14}$, 0 to $3 \cdot 10^{14}$, 0	3.5, 3.6, 3.8-3.9	Trap density
v_n ($cm\,s^{-1}$)	HTL-ABS	$1 \cdot 10^4$, 10, $1 \cdot 10^{-3}$ to 1, $1 \cdot 10^4$	3.5, 3.6, 3.8, 3.9	Recombination velocity
v_p ($cm\,s^{-1}$)	HTL-ABS	$1 \cdot 10^4$, 10, $1 \cdot 10^{-3}$ to 1, $1 \cdot 10^4$	3.5, 3.6, 3.8, 3.9	Recombination velocity
E_t	HTL-ABS	mid-gap	All	SRH energy
D_{it} ($cm^{-2}\,eV^{-1}$)	HTL-ABS	$3 \cdot 10^{14}$,0	3.5, 3.6-3.9	Trap density
ϕ_m (eV)	metal(ETL)	4.4	All	Work function
ϕ_m (eV)	metal(HTL)	5	All	Work function

Table 3.1: Device parameters used in our EIS simulations, chosen to emulate a "normal-structure" TiO_2/$MAPbI_3$/Spiro-OMeTAD cell. Values without references are estimates, with ranges chosen for illustrative purposes.

Bibliography

[1] Germà, G.; Bisquert, J. Distinction between Capacitive and Noncapacitive Hysteretic Currents in Operation and Degradation of Perovskite Solar Cells. *ACS Energy Lett.* **2016**, 683–688.

[2] Juarez-Perez, E. J.; Sanchez, R. S.; Badia, L.; Garcia-Belmonte, G.; Kang, Y. S.; Mora-Sero, I.; Bisquert, J. Photoinduced Giant Dielectric Constant in Lead Halide Perovskite Solar Cells. *J. Phys. Chem. Lett.* **2014**, *5*, 2390–2394.

[3] Almora, O.; Zarazua, I.; Mas-Marza, E.; Mora-Sero, I.; Bisquert, J.; Garcia-Belmonte, G. Capacitive Dark Currents, Hysteresis, and Electrode Polarization in Lead Halide Perovskite Solar Cells **2015**, *6*, 1645–1652.

[4] Almora, O.; Aranda, C.; Germà, G. Do Capacitance Measurements Reveal Light-Induced Bulk Dielectric Changes in Photovoltaic Perovskites? *J. Phys. Chem. Lett.* **2018**.

[5] Tress, W.; Marinova, N.; Moehl, T.; Zakeeruddin; Nazeeruddin, M.; Grätzel, M. Understanding the rate-dependent J - V hysteresis, slow time component, and aging in $CH_3NH_3PbI_3$ perovskite solar cells: the role of a compensated electric field. *Energy Environ. Sci.* **2015**, *8*, 995–1004.

[6] Pockett, A.; Eperon, G. E.; Sakai, N.; Snaith, H. J.; Peter, L. M.; Cameron, P. J. Microseconds, milliseconds and seconds: deconvoluting the dynamic behaviour of planar perovskite solar cells. *Phys Chem Chem Phys* **2017**, *19*, 5959–5970.

[7] Almond, D. P.; Bowen, C. R. An Explanation of the Photoinduced Giant Dielectric Constant of Lead Halide Perovskite Solar Cells. *J. Phys. Chem. Lett.* **2015**, *6*, 1736–1740.

[8] van Reenen, S.; Kemerink, M.; Snaith, H. J. Modeling Anomalous Hysteresis in Perovskite Solar Cells. *J. Phys. Chem. Lett.* **2015**, *6*, 3808–14.

[9] Richardson, G.; EJ, O. S.; Niemann, R. G.; Peltola, T. A.; Foster, J. M.; Cameron, P. J.; Walker, A. B. Can slow-moving ions explain hysteresis in the current-voltage curves of perovskite solar cells? *Energy Environ. Sci.* **2016**, *9*, 1476–1485.

[10] O'Kane, S. E.; Richardson, G.; Pockett, A.; Niemann, R. G.; Cave, J. M.; Sakai, N.; Eperon, G. E.; Snaith, H. J.; Foster, J. M.; Cameron, P. J.; et al. Measurement and modelling of dark current decay transients in perovskite solar cells. *Journal of Materials Chemistry C* **2017**, *5*, 452–462.

[11] Calado, P.; Telford, A. M.; Bryant, D.; Li, X.; Nelson, J.; C, O. B.; Barnes, P. Evidence for ion migration in hybrid perovskite solar cells with minimal hysteresis. *Nat. Commun.* **2016**, *7*, 13831.

[12] Domanski, K.; Roose, B.; Matsui, T.; Saliba, M.; Turren-Cruz, S.-H.; Correa-Baena, J.-P.; Carmona, C. R.; Richardson, G.; Foster, J. M.; De Angelis, F.; et al. Migration of cations induces reversible performance losses over day/night cycling in perovskite solar cells. *Energy & Environmental Science* **2017**, *10*, 604–613.

[13] Laban, W.; Etgar, L. Depleted hole conductor-free lead halide iodide heterojunction solar cells. *Energy Environ. Sci.* **2013**, *6*, 3249–3253.

[14] Liu, W.; Zhang, Y. Electrical characterization of $TiO_2/CH_3NH_3PbI_3$ heterojunction solar cells. *J. Mater. Chem. A* **2014**, *2*, 10244–10249.

[15] Xu, X.; Liu, Z.; Zuo, Z.; Zhang, M.; Zhao, Z.; Shen, Y.; Zhou, H.; Chen, Q.; Yang, Y.; Wang, M. Hole selective NiO contact for efficient perovskite solar cells with carbon electrode. *Nano* **2015**, *15*, 2402–2408.

[16] Chen, W.; Wu, Y.; Liu, J.; Qin, C.; Yang, X.; Islam, A. Hybrid interfacial layer leads to solid performance improvement of inverted perovskite solar cells. *Energy Environ. Sci.* **2015**, *8*, 629–640.

[17] Samiee, M.; Konduri, S.; Ganapathy, B.; Kottokkaran, R.; Abbas, H. A.; Kitahara, A.; Joshi, P.; Zhang, L.; Noack, M.; Dalal, V. Defect density and dielectric constant in perovskite solar cells. *Appl. Phys. Lett.* **2014**, *105*, 153502.

[18] Duan, H.; Zhou, H.; Chen, Q.; Sun, P.; Luo, S.; Song, T.; Bob, B.; Yang, Y. The identification and characterization of defect states in hybrid organic-inorganic perovskite photovoltaics. *Phys. Chem. Chem. Phys.* **2015**, *17*, 112–116.

[19] Shao, Y.; Xiao, Z.; Bi, C.; Yuan, Y.; Huang, J. Origin and elimination of photocurrent hysteresis by fullerene passivation in $CH_3NH_3PbI_3$ planar heterojunction solar cells. *Nat. Commun.* **2014**, *5*, 5784.

[20] Zarazúa, I.; Han, G.; Boix, P. P.; Mhaisalkar, S.; Francisco, F.; Ivan, M.; Bisquert, J.; Germà, G. Surface Recombination and Collection Efficiency in Perovskite Solar Cells from Impedance Analysis. *J. Phys. Chem. Lett.* **2016**, *7*, 5105–5113.

[21] Contreras-Bernal, L.; Salado, M.; Todinova, A.; Calio, L.; Ahmad, S.; Idígoras, J.; Anta, J. A. Origin and whereabouts of recombination in perovskite solar cells. *J. Phys. Chem. C* **2017**, *121*, 9705–9713.

[22] Kim, H.; Ivan, M.; Victoria, G.; Francisco, F.; J, J. E.; Park, N.; Bisquert, J. Mechanism of carrier accumulation in perovskite thin-absorber solar cells. *Nat. Commun.* **2013**, *4*, 2242.

[23] Gonzalez-Pedro, V.; Juarez-Perez, E. J.; Arsyad, W.-S.; Barea, E. M.; Fabregat-Santiago, F.; Mora-Sero, I.; Bisquert, J. General working principles of CH3NH3PbX3 perovskite solar cells. *Nano letters* **2014**, *14*, 888–893.

[24] Bisquert, J.; Bertoluzzi, L.; Mora-Sero, I.; Garcia-Belmonte, G. Theory of impedance and capacitance spectroscopy of solar cells with dielectric relaxation, drift-diffusion transport, and recombination. *The Journal of Physical Chemistry C* **2014**, *118*, 18983–18991.

[25] Anusca, I.; nas, S.; Gemeiner, P.; Svirskas, a.; Sanlialp, M.; Lackner, G.; Fettkenhauer, C.; Belovickis, J.; Samulionis, V.; Ivanov, M. Dielectric Response: Answer to Many Questions in the Methylammonium Lead Halide Solar Cell Absorbers. *Adv. Energy Mater.* **2017**, *7*.

[26] Dualeh, A.; Moehl, T.; Tétreault, N.; Teuscher, J.; Gao, P.; Nazeeruddin, M. K.; Gratzel, M. Impedance spectroscopic analysis of lead iodide perovskite-sensitized solid-state solar cells. *ACS nano* **2013**, *8*, 362–373.

[27] Bag, M.; Renna, L. A.; Adhikari, R. Y.; Karak, S.; Liu, F.; Lahti, P. M.; Russell, T. P.; Tuominen, M. T.; Venkataraman, D. Kinetics of ion transport in perovskite active layers and its implications for active layer stability. *Journal of the American Chemical Society* **2015**, *137*, 13130–13137.

[28] Zhao, Y.; Zhou, W.; Zhou, X.; Liu, K.; Yu, D.; Zhao, Q. Quantification of light-enhanced ionic transport in lead iodide perovskite thin films and its solar cell applications. *Light: Sci. Appl.* **2016**, *6*, 16243.

[29] Pockett, A.; Carnie, M. J. Ionic Influences on Recombination in Perovskite Solar Cells. *ACS Energy Letters* **2017**, *2*, 1683–1689.

[30] Bi, D.; Yang, L.; Boschloo, G.; Hagfeldt, A.; Johansson, E. M. Effect of different hole transport materials on recombination in CH3NH3PbI3 perovskite-sensitized mesoscopic solar cells. *The Journal of Physical Chemistry Letters* **2013**, *4*, 1532–1536.

[31] Zhao, Y.; Nardes, A. M.; Zhu, K. Solid-state mesostructured perovskite CH3NH3PbI3 solar cells: charge transport, recombination, and diffusion length. *The journal of physical chemistry letters* **2014**, *5*, 490–494.

[32] Roiati, V.; Colella, S.; Lerario, G.; De Marco, L.; Rizzo, A.; Listorti, A.; Gigli, G. Investigating charge dynamics in halide perovskite-sensitized mesostructured solar cells. *Energy & Environmental Science* **2014**, *7*, 1889–1894.

[33] Lee, J.-W.; Lee, T.-Y.; Yoo, P. J.; Grätzel, M.; Mhaisalkar, S.; Park, N.-G. Rutile TiO 2-based perovskite solar cells. *Journal of Materials Chemistry A* **2014**, *2*, 9251–9259.

[34] Sanchez, R. S.; Gonzalez-Pedro, V.; Lee, J.-W.; Park, N.-G.; Kang, Y. S.; Mora-Sero, I.; Bisquert, J. Slow dynamic processes in lead halide perovskite solar cells. Characteristic times and hysteresis. *The journal of physical chemistry letters* **2014**, *5*, 2357–2363.

[35] Pascoe, A. R.; Duffy, N. W.; Scully, A. D.; Huang, F.; Cheng, Y. Insights into Planar CH3NH3PbI3 Perovskite Solar Cells Using Impedance Spectroscopy. *J. Phys. Chem. C* **2015**, *119*, 4444–4453.

[36] Macdonald, J. R.; Barsoukov, E. Impedance spectroscopy : theory, experiment, and applications. Hoboken, N.J. : Wiley-Interscience, 2nd edition **2005**.

[37] Fourier Transform Table. Url: `https://www.astro.umd.edu/~lgm/ASTR410/ft_ref3.pdf`, Accessed May 2018.

[38] Jonscher, A. The physical origin of negative capacitance. *J. Chem. Soc., Faraday Trans. 2* **1986**, *82*, 75–81.

[39] Ershov, M.; Liu, H.; Li, L.; Buchanan, M.; Wasilewski, Z.; Jonscher, A. K. Negative capacitance effect in semiconductor devices. *IEEE Trans. Electron Devices* **1998**, *45*, 2196–2206.

[40] Laux, S. Revisiting the analytic theory of pn junction impedance: Improvements guided by computer simulation leading to a new equivalent circuit. *IEEE Trans. Electron Devices* **1999**, *46*, 396–412.

[41] Pockett, A.; Eperon, G. E.; Peltola, T.; Snaith, H. J.; Walker, A.; Peter, L. M.; Cameron, P. J. Characterization of Planar Lead Halide Perovskite Solar Cells by Impedance Spectroscopy, Open-Circuit Photovoltage Decay, and Intensity-Modulated Photovoltage/Photocurrent Spectroscopy. *J. Phys. Chem. C* **2015**, *119*, 3456–3465.

[42] Bisquert, J.; Garcia-Belmonte, G.; Mora-Sero, I. Characterization of capacitance, transport and recombination parameters in hybrid perovskite and organic solar cells. In Unconventional Thin Film Photovoltaics **2016**, 57–106.

[43] Sze, S. M.; Ng, K. K. Physics of semiconductor devices. John wiley & sons **2006**.

[44] Sah, C.-T. The equivalent circuit model in solid-state electronics—Part I: The single energy level defect centers. *Proceedings of the IEEE* **1967**.

[45] Da Como, E.; De Angelis, F.; Snaith, H.; Walker, A. Unconventional Thin Film Photovoltaics. Royal Society of Chemistry **2016**.

[46] Taretto, K.; Rau, U.; Werner, J. Closed-form expression for the current/voltage characteristics of pin solar cells. *Applied Physics A* **2003**, *77*, 865–871.

[47] Contreras-Bernal, L.; Salado, M.; Todinova, A.; Calio, L.; Ahmad, S.; Idígoras, J.; Anta, J. A. Origin and whereabouts of recombination in perovskite solar cells. *The Journal of Physical Chemistry C* **2017**, *121*, 9705–9713.

[48] Zarazua, I.; Han, G.; Boix, P. P.; Mhaisalkar, S.; Fabregat-Santiago, F.; Mora-Sero, I.; Bisquert, J.; Garcia-Belmonte, G. Surface Recombination and Collection Efficiency in Perovskite Solar Cells from Impedance Analysis. *The journal of physical chemistry letters* **2016**, *7*, 5105–5113.

[49] Guillen, E.; Ramos, F. J.; Anta, J. A.; Ahmad, S. Elucidating transport-recombination mechanisms in perovskite solar cells by small-perturbation techniques. *The Journal of Physical Chemistry C* **2014**, *118*, 22913–22922.

[50] Pockett, A.; Eperon, G. E.; Sakai, N.; Snaith, H. J.; Peter, L. M.; Cameron, P. J. Microseconds, milliseconds and seconds: deconvoluting the dynamic behaviour of planar perovskite solar cells. *Physical Chemistry Chemical Physics* **2017**, *19*, 5959–5970.

[51] Schroder, D. K.; of Electrical, I.; Engineers, E. Semiconductor material and device characterization. [Piscataway, NJ] : IEEE Press ; Hoboken, N.J. : Wiley, 3rd ed edition **2006**, "Wiley-Interscience.".

[52] Guerrero, A.; Garcia-Belmonte, G.; Mora-Sero, I.; Bisquert, J.; Kang, Y. S.; Jacobsson, T. J.; Correa-Baena, J.-P.; Hagfeldt, A. Properties of Contact and Bulk Impedances in Hybrid Lead Halide Perovskite Solar Cells Including Inductive Loop Elements. *J. Phys. Chem. C* **2016**, *120*, 8023–8032.

[53] Shen, H.; Wu, Y.; Peng, J.; Duong, T.; Fu, X.; Barugkin, C.; White, T. P.; Weber, K.; Catchpole, K. R. Improved reproducibility for perovskite solar cells with 1cm^2 active area by a modified two-step process. *ACS Appl. Mater. Interfaces* **2017**, *9*, 5974–5981.

[54] Peng, J.; Wu, Y.; Ye, W.; Jacobs, D. A.; Shen, H.; Fu, X.; Wan, Y.; Wu, N.; Barugkin, C.; Nguyen, H. T.; et al. Interface passivation using ultrathin polymer-fullerene films for high-efficiency perovskite solar cells with negligible hysteresis. *Energy Environ. Sci.* **2017**, *10*, 1792–1800.

[55] Yuan, Y.; Huang, J. Ion Migration in Organometal Trihalide Perovskite and Its Impact on Photovoltaic Efficiency and Stability. *Acc. Chem. Res.* **2016**, *49*, 286–93.

[56] Saliba, M.; Correa-Baena, J.-P.; Graetzel, M.; Hagfeldt, A.; Abate, A. Perovskite solar cells from the atomic to the film level. *Angewandte Chemie International Edition* **2017**.

[57] Li, C.; Tscheuschner, S.; Paulus, F.; Hopkinson, P. E.; Kießling, J.; Köhler, A.; Vaynzof, Y.; Huettner, S. Iodine Migration and its Effect on Hysteresis in Perovskite Solar Cells. *Adv. Mater.* **2016**, *28*, 2446–2454.

[58] Meloni, S.; Moehl, T.; Tress, W.; Franckevičius, M.; Saliba, M.; Lee, Y.; Gao, P.; Nazeeruddin, M.; Zakeeruddin, S.; Rothlisberger, U.; et al. Ionic polarization-induced current-voltage hysteresis in $CH_3NH_3PbX_3$ perovskite solar cells. *Nat. Commun.* **2016**, *7*, 10334.

[59] Unger, E.; Hoke, E.; Bailie, C.; Nguyen, W.; Bowring, A.; Heumüller, T.; Christoforo, M.; McGehee, M. Hysteresis and transient behavior in current-voltage measurements of hybrid-perovskite absorber solar cells. *Energy Environ. Sci.* **2014**, *7*, 3690–3698.

[60] Kim, H.; Jang, I.; Ahn, N.; Choi, M.; Guerrero, A.; Bisquert, J.; Park, N. Control of I-V Hysteresis in $CH_3NH_3PbI_3$ Perovskite Solar Cell. *J. Phys. Chem. Lett.* **2015**, *6*, 4633–9.

[61] Elumalai, N. K.; Mahmud, A.; Wang, D.; Wright, M.; Upama, M. B.; Chan, K. H.; Xu, C.; Uddin, A. Hysteresis and electrode polarization in normal and inverted hybrid perovskite solar cells. *IEEE Photovoltaic Spec. Conf., 43rd* **2016**.

[62] Grätzel, M. The light and shade of perovskite solar cells. *Nat. Mater.* **2014**, *13*, 838–842.

[63] Chen, H.-W.; Sakai, N.; Ikegami, M.; Miyasaka, T. Emergence of hysteresis and transient ferroelectric response in organo-lead halide perovskite solar cells. *J. Phys. Chem. Lett.* **2014**, *6*, 164–169.

[64] Yang, T.-Y.; Gregori, G.; Pellet, N.; Grätzel, M.; Maier, J. The significance of ion conduction in a hybrid organic–inorganic lead-iodide-based perovskite photosensitizer. *Angew. Chem.* **2015**, *127*, 8016–8021.

[65] Jung, H. S.; Park, N.-G. Perovskite solar cells: from materials to devices. *small* **2015**, *11*, 10–25.

[66] Zhang, Y.; Liu, M.; Eperon, G. E.; Leijtens, T. C.; McMeekin, D.; Saliba, M.; Zhang, W.; de Bastiani, M.; Petrozza, A.; Herz, L. M.; et al. Charge selective contacts, mobile ions and anomalous hysteresis in organic–inorganic perovskite solar cells .

[67] Frost, J. M.; Walsh, A. What Is Moving in Hybrid Halide Perovskite Solar Cells? *Acc. Chem. Res.* **2016**, *49*, 528–535.

[68] Miyano, K.; Yanagida, M.; Tripathi, N.; Shirai, Y. Simple characterization of electronic processes in perovskite photovoltaic cells. *Appl. Phys. Lett.* **2015**, *106*, 093903.

[69] Lunkenheimer, P.; Bobnar, V.; Pronin, A. V.; Ritus, A. I.; Volkov, A. A.; Loidl, A. Origin of apparent colossal dielectric constants. *Phys. Rev. B* **2002**, *66*, 052105.

[70] Zarazua, I.; Bisquert, J.; Garcia-Belmonte, G. Light-Induced Space-Charge Accumulation Zone as Photovoltaic Mechanism in Perovskite Solar Cells. *J. Phys. Chem. Lett.* **2016**, *7*, 525–8.

[71] Conway, B. E. Electrochemical Supercapacitors : Scientific Fundamentals and Technological Applications. Boston, MA : Springer US **1999**.

[72] Gottesman, R.; Lopez-Varo, P.; Gouda, L.; Jimenez-Tejada, J. A.; Hu, J.; Tirosh, S.; Zaban, A.; Bisquert, J. Dynamic phenomena at perovskite/electron-selective contact interface as interpreted from photovoltage decays. *Chem* **2016**, *1*, 776–789.

[73] Bergmann, V. W.; Guo, Y.; Tanaka, H.; Hermes, I. M.; Li, D.; Klasen, A.; Bretschneider, S. A.; Nakamura, E.; Berger, R.; Weber, S. A. Local Time-Dependent Charging in a Perovskite Solar Cell. *ACS Appl. Mater. Interfaces* **2016**, *8*, 19402–19409.

[74] Contreras, L.; Idígoras, J.; Todinova, A.; Salado, M.; Kazim, S.; Ahmad, S.; Anta, J. A. Specific cation interactions as the cause of slow dynamics and hysteresis in dye and perovskite solar cells: a small-perturbation study. *Phys. Chem. Chem. Phys.* **2016**, *18*, 31033–31042.

[75] Hegedus, S. S.; Shafarman, W. N. Thin-film solar cells: device measurements and analysis. *Prog. Photovoltaics* **2004**, *12*, 155–176.

[76] Liu, H.; Liang, C.; Zhang, H.; Sun, M.; Liang, J.; Zhang, X.; Ji, C.; Guo, Z.; Xu, Y.; He, Z. Effects of surface morphology on the ionic capacitance and performance of perovskite solar cells. *Jpn. J. Appl. Phys.* **2017**, *56*, 090305.

[77] Ghahremanirad, E.; Bou, A.; Olyaee, S. Inductive Loop in the Impedance Response of Perovskite Solar Cells Explained by Surface Polarization Model. *J. Phys. Chem. Lett.* **2017**, *8*, 1402–1406.

[78] Kovalenko, A.; Pospisil, J.; Zmeskal, O.; Krajcovic, J.; Weiter, M. Ionic origin of a negative capacitance in lead halide perovskites. *Phys. Status Solidi RRL* **2017**, *11*.

[79] Tada, K. Comment on "Simulation of current-voltage curves for inverted planar structure perovskite solar cells using equivalent circuit model with inductance". *Appl. Phys. Express* **2017**, *10*, 059101.

[80] Van Roosbroeck, W. Current-carrier transport with space charge in semiconductors. *Phys. Rev.* **1961**, *123*, 474.

[81] Yang, T.; Gregori, G.; Pellet, N.; Grätzel, M.; Maier, J. The Significance of Ion Conduction in a Hybrid Organic-Inorganic Lead-Iodide-Based Perovskite Photosensitizer. *Angew. Chem., Int. Ed.* **2015**, *54*, 7905–7910.

[82] Eames, C.; Frost, J. M.; Barnes, P. R.; C, O. B.; Walsh, A.; Islam, S. M. Ionic transport in hybrid lead iodide perovskite solar cells. *Nat. Commun.* **2015**, *6*, 7497.

[83] Walsh, A.; Scanlon, D.; Chen, S.; Gong, X. Self-Regulation Mechanism for Charged Point Defects in Hybrid Halide Perovskites. *Angew. Chem., Int. Ed.* **2015**, *54*, 1791–1794.

[84] Wang, P.; Shao, Z.; Ulfa, M.; Pauporte, T. Insights into the Hole Blocking Layer Effect on the Perovskite Solar Cell Performance and Impedance Response. *J. Phys. Chem. C* **2017**, *121*, 9131–9141.

[85] Anaya, M.; Zhang, W.; Hames, B.; Li, Y.; Francisco, F.; Calvo, M. E.; Snaith, H. J.; Míguez, H.; Iván, M. Electron injection and scaffold effects in perovskite solar cells. *J. Mater. Chem. C* **2016**, *5*, 634–644.

[86] Sanchez, R. S.; Victoria, G.; Lee, J.; Park, N.; Kang, Y.; Ivan, M.; Bisquert, J. Slow Dynamic Processes in Lead Halide Perovskite Solar Cells. Characteristic Times and Hysteresis. *J Phys Chem Lett* **2014**, *5*, 2357–63.

[87] Francisco, F.; Kulbak, M.; Zohar, A.; Marta, V.; Hodes, G.; Cahen, D.; Ivan, M. Deleterious effect of Negative Capacitance in the Performance of Halide Perovskite Solar Cells. *ACS Energy Lett.* **2017**, *2*, 2007–2013.

[88] Dualeh, A.; Moehl, T.; Tétreault, N.; Teuscher, J.; Gao, P.; Nazeeruddin, M. K.; Grätzel, M. Impedance spectroscopic analysis of lead iodide perovskite-sensitized solid-state solar cells. *ACS Nano* **2014**, *8*, 362–73.

[89] Zohar, A.; Kedem, N.; Levine, I.; Zohar, D.; Vilan, A.; Ehre, D.; Hodes, G.; Cahen, D. Impedance Spectroscopic Indication for Solid State Electrochemical Reaction in $CH_3NH_3PbI_3$ Films. *J. Phys. Chem. Lett.* **2016**, *7*, 191–197.

[90] Jacobs, D.; Wu, Y.; Shen, H.; Barugkin, C.; Beck, F.; White, T.; Weber, K.; Catchpole, K. Hysteresis phenomena in perovskite solar cells: the many and varied effects of ionic accumulation. *Phys. Chem. Chem. Phys.* **2017**, *19*, 3094–3103.

[91] Tress, W.; Baena, J.; Saliba, M.; Abate, A.; Graetzel, M. Inverted Current-Voltage Hysteresis in Mixed Perovskite Solar Cells: Polarization, Energy Barriers, and Defect Recombination. *Adv. Energy Mater.* **2016**, *6*, 1600396.

[92] Shen, H.; Jacobs, D. A.; Wu, Y.; Duong, T.; Peng, J.; Wen, X.; Fu, X.; Karuturi, S. K.; White, T. P.; Weber, K.; et al. Inverted Hysteresis in $CH_3NH_3PbI_3$ Solar Cells: Role of Stoichiometry and Band Alignment. *J. Phys. Chem. Lett.* **2017**, *8*, 2672–2680.

[93] Jiang, C.; Yang, M.; Zhou, Y.; To, B.; Nanayakkara, S. U.; Luther, J. M.; Zhou, W.; Berry, J. J.; van de Lagemaat, J.; Padture, N. P.; et al. Carrier separation and transport in perovskite solar cells studied by nanometre-scale profiling of electrical potential. *Nat. Commun.* **2015**, *6*, 8397.

[94] Guerrero, A.; J, J. E.; Bisquert, J.; Ivan, M.; Germà, G. Electrical field profile and doping in planar lead halide perovskite solar cells. *Appl. Phys. Lett.* **2014**, *105*, 133902.

[95] Zhao, Y.; Zhou, W.; Tan, H.; Fu, R.; Li, Q.; Lin, F.; Yu, D.; Walters, G.; Sargent, E. H.; Zhao, Q. Mobile-Ion-Induced Degradation of Organic Hole-Selective Layers in Perovskite Solar Cells. *J. Phys. Chem. C* **2017**, *121*, 14517–14523.

[96] Carrillo, J.; Guerrero, A.; Rahimnejad, S.; Almora, O.; Zarazua, I.; Elena, M.; Bisquert, J.; Germà, G. Ionic Reactivity at Contacts and Aging of Methylammonium Lead Triiodide Perovskite Solar Cells. *Adv. Energy Mater.* **2016**, *6*, 1502246.

[97] Ginting, R.; Jeon, M.; Lee, K.; Jin, W.; Kim, T.; Kang, J. Degradation mechanism of planar-perovskite solar cells: correlating evolution of iodine distribution and photocurrent hysteresis. *J. Mater. Chem.* **2017**, *5*, 4527–4534.

[98] Li, Z.; Xiao, C.; Yang, Y.; Harvey, S. P.; Kim, D.; Christians, J. A.; Yang, M.; Schulz, P.; Nanayakkara, S. U.; Jiang, C.; et al. Extrinsic ion migration in perovskite solar cells. *Energy Environ. Sci.* **2017**.

[99] Almora, O.; Aranda, C.; Elena, M.; Germà, G. On Mott-Schottky analysis interpretation of capacitance measurements in organometal perovskite solar cells. *Appl. Phys. Lett.* **2016**, *109*, 173903.

[100] O'Regan, B.; Moser, J.; Anderson, M.; Graetzel, M. Vectorial electron injection into transparent semiconductor membranes and electric field effects on the dynamics of light-induced charge separation. *J. Phys. Chem.* **1990**, *94*, 8720–8726.

[101] Diebold, U. The surface science of titanium dioxide. *Surf. Sci. Rep.* **2003**, *48*, 53–229.

[102] Peng, J.; Wu, Y.; Ye, W.; Jacobs, D. A.; Shen, H.; Fu, X.; Wan, Y.; Wu, N.; Barugkin, C.; Nguyen, H. T.; et al. Interface passivation using ultrathin polymer–fullerene films for high-efficiency perovskite solar cells with negligible hysteresis. *Energy & Environmental Science* **2017**, *10*, 1792–1800.

[103] Levine, I.; Nayak, P. K.; Wang, J.; Sakai, N.; Reenen, S.; Brenner, T. M.; Mukhopadhyay, S.; Snaith, H. J.; Hodes, G.; Cahen, D. Interface-Dependent Ion Migration/Accumulation Controls Hysteresis in MAPbI3 Solar Cells. *J Phys Chem C* **2016**, *120*, 16399–16411.

[104] Kim, H.; Park, N. Parameters Affecting I–V Hysteresis of CH3NH3PbI3 Perovskite Solar Cells: Effects of Perovskite Crystal Size and Mesoporous TiO2 Layer. *J Phys Chem Lett* **2014**, *5*, 2927–2934.

[105] Rong, Y.; Hu, Y.; Ravishankar, S.; Liu, H.; Hou, X.; Sheng, Y.; Mei, A.; Wang, Q.; Li, D.; Xu, M.; et al. Tunable hysteresis effect for perovskite solar cells. *Energy & Environmental Science* **2017**, *10*, 2383–2391.

[106] Tripathi, N.; Yanagida, M.; Shirai, Y.; Masuda, T.; Han, L.; Miyano, K. Hysteresis-free and highly stable perovskite solar cells produced via a chlorine-mediated interdiffusion method. *Journal of Materials Chemistry A* **2015**, *3*, 12081–12088.

[107] Yoon, H.; Kang, S. M.; Lee, J.-K.; Choi, M. Hysteresis-free low-temperature-processed planar perovskite solar cells with 19.1% efficiency. *Energy & Environmental Science* **2016**, *9*, 2262–2266.

[108] Tang, Z.; Bessho, T.; Awai, F.; Kinoshita, T.; Maitani, M. M.; Jono, R.; Murakami, T. N.; Wang, H.; Kubo, T.; Uchida, S.; et al. Hysteresis-free perovskite solar cells made of potassium-doped organometal halide perovskite. *Scientific Reports* **2017**, *7*, 12183.

[109] Peng, J.; Duong, T.; Zhou, X.; Shen, H.; Wu, Y.; Mulmudi, H. K.; Wan, Y.; Zhong, D.; Li, J.; Tsuzuki, T.; et al. Efficient Indium-Doped TiOx Electron Transport Layers for High-Performance Perovskite Solar Cells and Perovskite-Silicon Tandems. *Advanced Energy Materials* **2017**, *7*.

[110] Van de Krol, R.; Goossens, A.; Schoonman, J. Mott-Schottky Analysis of Nanometer-Scale Thin-Film Anatase TiO_2. *J. Electrochem. Soc.* **1997**, *144*, 1723–1727.

[111] Stamate, M. D. On the dielectric properties of dc magnetron TiO2 thin films. *Appl. Surf. Sci.* **2003**, *218*, 318–323.

Chapter 4

Tandem Cell Integration

Although no doubt the most important and interesting components, there is more to a solar cell than its active and selective contact layers; in particular there are the electrodes, at least one of which must be transparent. Transparent electrode performance therefore has an important role to play in single-junction devices and an even greater one in tandem cells. The conversion of a stand-alone cell to a tandem configuration requires one of two replacements: for a four-terminal (4-T) tandem the top cell must be made semi-transparent by substituting the (typically metallic) rear electrode with a transparent conductor, whereas in two-terminal (2-T) designs a series-connecting "interconnection" layer[1] must take its place between the two subcells. The following chapter addresses aspects of these basic needs in sequence: in sec. 4.1 we discuss the transparent conductor requirements for both stand-alone and 4-T tandems, and in sec. 4.2 we discuss the device physics which enables a novel type of 2-T design, one that operates without an extraneous interconnection layer.

Our reasons for pursuing the study of metallization and transparent conductor requirements that appears here in sec. 4.1 were two-fold. It should be stated that in terms of its bare essentials there is nothing in this section which has not in been considered before in some form in the photovoltaic literature, although our presentation and approach are original. Indeed, metallization in the form of fingers and bus-bars has been an essential component of many commercial PV technologies for decades, and the basic aspects of their design and performance are well known. However, at the time of embarking on this study several aspects of metallization and its application to thin-film cells seemed to be poorly recognized in two separate bodies of literature. On the one hand there was the literature concerned with transparent electrode materials as technologies in their own right, and whose aims are to discover new materials, deposition techniques and sometimes nano-structures with superior opto-electronic performance. In this body of literature, the needs of any particular application, including photovoltaics, are understandably (but not quite justifiably) simplified. The general perception seems to be that a transparent electrode for thin-film photovoltaics needs to posses a conductivity amounting to

[1] A note on terminology: in 4.1 the interconnection region refers to the dead space in thin-film modules necessary to isolate individual cells, whereas in 4.2 the interconnection layer is that which appears between the two subcells in 2-T tandem configuration.

10Ω/sq in sheet resistance, and a minimum transparency of 90% [9]. As an estimate this figure is acceptable, however, it is too crude to be used for blindly preferencing one technology over another as is routinely practiced. For that purpose one must recognize that the optimal balance between sheet resistance and transparency is quite sensitive to technological factors such as the minimal scribe-width (for thin-film modules) or metallization dimensions, wherever the latter can be included. In our opinion this has led to an over-emphasis on conductivity to the detriment of transparency, since scribe-widths and metallization have been continuously improving in terms of the minimum dimensions that can be achieved with scalable methods. This problem of over-valuing conductivity is exacerbated by the most commonly used figures-of-merit (discussed in sec. 4.1.2). Lastly, it has also encouraged research on metal nano-structure electrodes (including to the author for a time!) which attempt to exploit wave-optical effects to achieve superior (typically narrow-band) transparency, when in reality the techniques necessary to manufacture such electrodes would be far better employed in depositing narrow-width fingers on conventional transparent conductive oxides. For all of these reasons, we thought it necessary to clarify the impact of metallization and other assumptions on transparent electrode requirements for thin-film photovoltaics. Hopefully our chosen method of presenting these considerations will make them clear to the intended audience.

Early studies on perovskite cells, particularly those concerned with 4-T tandems, were quick to identify the importance of transparent electrode performance for the efficient functioning of these devices, but several of these nonetheless also repeated the 10Ω/sq requirement without qualification. This is especially inappropriate for the rear electrode of a 4-T top-cell, since this can be metallized without difficulty, making 10Ω/sq far in excess of what is optimal. This was an additional motivation to set the record straight on the 10Ω/sq requirement, and the main reason why this work was pursued in a project devoted primarily to perovskite cells. Much of the discussion below refers simply to thin-film solar cells however to retain maximum generality wherever possible.

4.1 Transparent Conductor Requirements

Transparent conductors are a crucial enabling technology for the future of thin-film solar cells. Contenders for this role range from the familiar transparent conducting oxides such as indium- and fluorine-doped tin oxide, to graphene, carbon nanotubes, metalic nanowires, nano-patterned metalic films, conducting polymers and a variety of composites [1, 2, 3]. Each technology reaches a different compromise between the two primary properties of any transparent conductor, that is its optical transparency and sheet resistance. Consequently, the required balance between transparency and sheet resistance can have a profound effect on which technologies and pro-

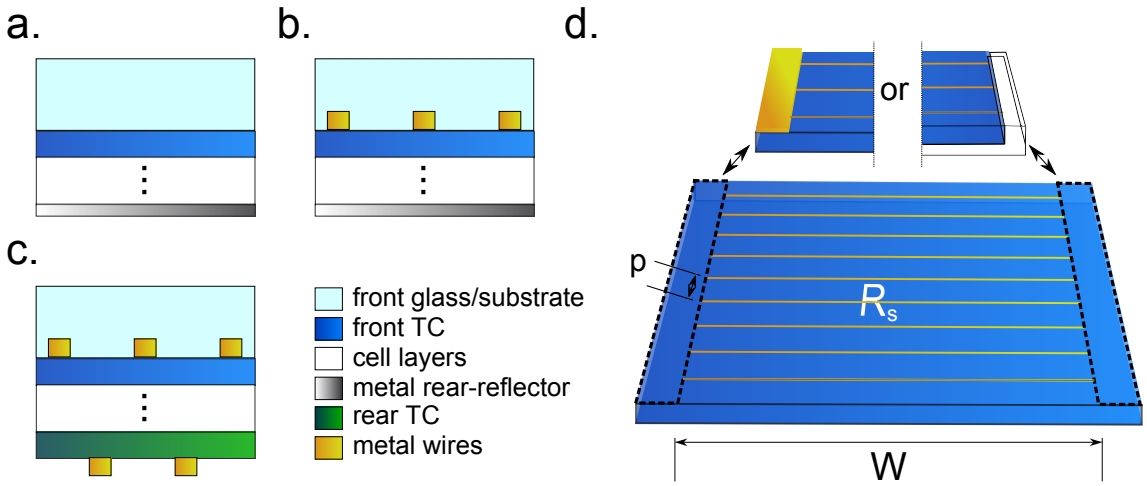

Figure 4.1: (a-c) Cross-sections of three basic cell types: (a) single cell with a bare front-side TC (b) single cell with metal wires inset into the front glass/substrate and (c) a semi-transparent cell with metallized front and rear TCs, such as might be used as the top-cell in a 4-T tandem device. (d) Schematic of a metallized TC in which the cell width W is defined as the distance between bus-bars (standard Si-type module), the scribed interconnect regions (monolithic thin-film module) or cell contacts (lab cell). Here p is the finger separation or pitch.]

cesses are declared relevant, and which receive the most attention. The issue of transparent conductor (TC) requirements has been the subject of a renewed focus recently with the advent of perovskite cells, which have attractive characteristics for use in a tandem arrangement with either conventional silicon cells or other perovskites [4, 5]. Tandem concepts such as the 4-T mechanical stack require as many as three transparent electrodes in total, putting a greater than usual pressure on electrode transparency [6]. The 2-T monolithically integrated tandem cell avoids the need for intermediate electrodes, but suffers losses of a different nature due to the necessity of current-matching between cells, making transparent electrode performance a key factor in the competition between these two designs. Finding a suitable transparent conductor for the rear of the perovskite top-cell is one of the major challenges that will need to be overcome before a viable 4-T tandem device can be demonstrated [7, 8]. In the absence of metallization, such a conductor should have a sheet resistance no greater than about 10Ω/sq [9], a challenging requirement to meet at high transparency. With metallization in the form of a conducting grid the required sheet resistances are considerably relaxed, allowing for the use of thinner layers which block less of the valuable light.

Transparent conductors are usually among the first or the last layers to be deposited in a thin-film solar cell. Electrodes which are deposited last, as in the window layer of a CIGS cell [10] or the rear electrode of a semitransparent perovskite cell [11], can be metallized with little

difficulty. Electrodes which are deposited first will affect the topography of all subsequent layers, so that any wires should be kept below a threshold height depending on the device structure to avoid producing shunt pathways or other undesirable features. Alternatively, wires may be embedded into the front-surface substrate so as to produce a relatively flat surface for subsequent layers, for example, by using metallic paste to fill grooves fashioned with an imprint [12, 13, 14] or laser scribing process. The wire sizes we consider lie in the range of $5 - 30\mu$m, whose upper limit falls within the present capability of industrially-relevant techniques such as screen [15], ink-jet [16, 17] and flexographic printing [18, 19]. Smaller metal wires with widths $< 20\mu$m can be fabricated using a wide variety of techniques including nano-imprint lithography [20], micro-contact printing [21] and nanotransfer printing [22], although it is beyond the scope of this paper to assess whether any of these techniques are viable candidates for low-cost mass-production in the near-future. Instead, we analyze the effects of metallization on transparent conductor requirements and performance, and in doing so provide impetus for the improvement of metallization technology.

We begin by reviewing the basic impact of ohmic and transparency loss on the efficiency of a solar cell. These loss mechanisms are tied together by introducing the efficiency factor, a measure of the TC's impact on its parent cell's efficiency, which we then use to perform a comparative study of TC technologies under different schemes of metallization. Finally, we give evidence that the standard figures of merit for transparent conductors may not be reliable indicators of performance in a solar cell, and suggest some simple alternatives based on the efficiency factor.

4.1.1 Transparent Conductor Requirements with Metallization

In a homogeneous conducting layer the trade-off between sheet resistance and transparency is largely unavoidable, as increasing the planar carrier density for the sake of conductivity will tend to reduce transparency (one can circumvent this by increasing the carrier mobility instead, but this provides only a limited scope for improvement). However, without the constraint of homogeneity, there is much to be gained in transparency by condensing carriers into a sparse network of dense filaments. In the limit of high concentration such networks become effectively metallic and opaque, with a transparency determined only by their covering fraction, and can therefore be made almost arbitrarily tall without affecting transparency. For example, a layer of silver 50nm thick has a transparency close to zero over the visible range, whereas the same volume of metal (having the same capacity to carry current over large distances) will produce an array of wires 1μm tall with a covering fraction of just 5%– or 95% transparency. Of course in heterogeneous conductors of this kind, such as arrays of regular or random metal wires, it becomes necessary to conduct current to the wires from all the intervening spaces, but as these distances are much smaller than the cell dimensions this task can be accomplished with only a

very thin or lightly doped layer. This explains why the combination of a homogeneous layer to collect current, and a network of metallic wires to transport it over macroscopic distances, is so effective at achieving efficient carrier transport with high transparency [23, 24, 25]. Different possibilities for incorporating metal wires into a typical thin-film cell structure are illustrated in Figs. 4.1(b,c).

Whether or not a transparent conductor is metallized, the optimal balance between its sheet resistance and transparency is determined by the joint effect of these properties on its cell's efficiency. To model this effect we will at first consider the top electrode on a stand-alone cell (Figs. 4.1(a,b)). To a good approximation [26] the sheet resistance of such an electrode affects the cell output voltage, whilst its transparency affects the current. Equation (4.1a) given below is for the reduction in voltage V_{mp}/V_{mp}^0 in a cell with an un-metallized or "bare" transparent conductor (Fig. 4.1a), normalized to its nominal value in an idealized cell without any ohmic loss. The second equation (4.1b) for the same factor is also standard [27] and applies instead to a layer with metal wires as in Figs. 4.1(b,d). It is derived by assuming that all the collected current flows directly through the TC to wires spaced at a period of p, before being conducted along the wires to the cell's contact, busbar or interconnect regions separated by a distance W (see Fig. 4.1d):

$$\frac{V_{mp}}{V_{mp}^0} = 1 - \frac{1}{3}\frac{J_{mp}^0 W^2}{V_{mp}^0} \times \begin{cases} R_s & (4.1a) \\ \frac{1}{4}(p/W)^2 R_s + R_M & (4.1b) \end{cases}$$

Here R_M is the metallization sheet resistance given by $R_M = \rho p/wh$, ρ is the metal resistivity (given the value $3 \cdot 10^{-6}\,\Omega\,\mathrm{cm}$ hereafter), w the wire width, h the wire height, J_{mp}^0 the collected current density assuming ideal transparency, and R_s is the bare TC sheet resistance. We note that in this expression the contribution of contact resistance between the TC and metal wires is neglected (see sec. 4.1.2 for justification). These expressions show that the effect of metallization is to replace the TC's sheet resistance R_s with an effective resistance $R_{eff} = \frac{1}{4}(p/W)^2 R_s + R_M$. In general this represents a significant improvement as the value R_M can be made very small at an almost negligible cost to transparency– for example, mesoscopic copper wires with $p/w = 100$ and $h = 1\mu m$ will shade just 1% of the incident radiation at $R_M \approx 2\Omega/\mathrm{sq}$. By comparison, a typical TC with comparable sheet resistance would block around 20% of the incoming light or more [2]. Within fabrication constraints the wires can be made taller to reduce R_M at no cost to transparency, which is therefore equivalent to reducing the metal's intrinsic resistivity ρ. Meanwhile, the factor $(p/W)^2$ in the effective sheet resistance can drastically reduce the impact of the TC's sheet resistance R_s in a metallized electrode when the wires are spaced close together, allowing for the use of highly transparent TCs with a larger sheet resistance than would

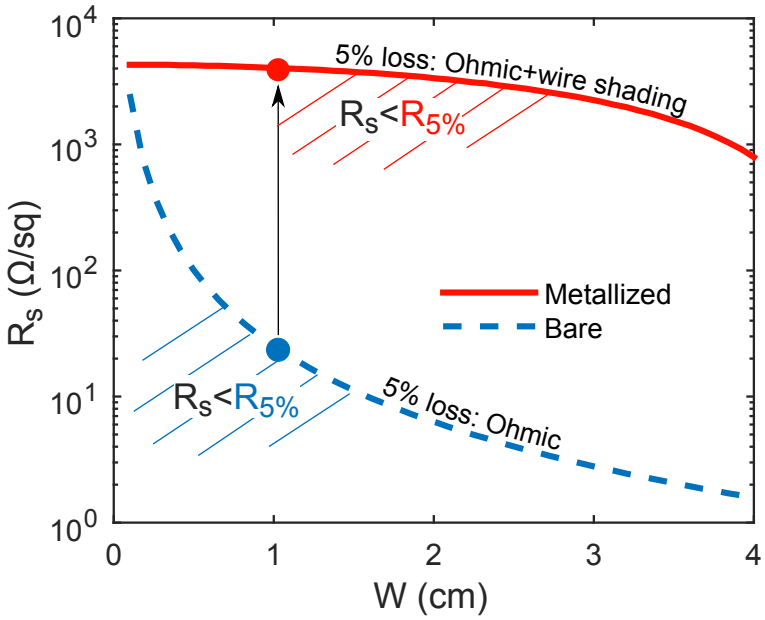

Figure 4.2: Sheet resistance requirements as a function of the contact/interconnect separation W for a bare TC (dotted, blue) and metallized TC (solid, red) assuming 5% efficiency loss in a cell with $J^0_{mp}/V^0_{mp} = 22\text{k}\Omega^{-1}\text{cm}^{-2}$. Losses were calculated assuming 100% TC transparency, and therefore include only Ohmic dissipation for the bare layer, and Ohmic dissipation plus wire shading for the metallized layer. The metal wires were assumed to have a width of 5 µm.

otherwise be optimal. For this purpose the wire width w must be made as small as possible so that the wires do not incur a large shading loss when closely spaced.

The W^2 scaling of ohmic loss with cell width makes this parameter an important determinant of sheet resistance requirements. In a monolithic thin-film module the tendency to make W smaller in order to reduce ohmic loss is countered by the necessary presence of interconnect regions, which represent undesirable dead space and should therefore be spaced far apart. Technological limits on the width of these interconnect regions set the balance at roughly $W \approx 1$cm, which leads to a required sheet resistance without metallization of about 10Ω/sq [9]. This well-known benchmark features in Fig. 4.2 where we have plotted the maximum allowable sheet resistance in order to keep losses under 5%, versus cell width, assuming a bare transparent conductor with perfect transparency (blue dotted line). The same quantity is also plotted for a metallized layer, but this time including the effect of wire shading in the 5% loss (red solid line). For longer cell widths metallization relaxes the required sheet resistances by a large amount, indeed by over two orders of magnitude at $W = 1$cm. Another important point regarding W is that whereas for a bare electrode the cell length affects the voltage loss through R_s, in a metallized electrode the variation in loss with length scales with R_M, tying the optimal value for

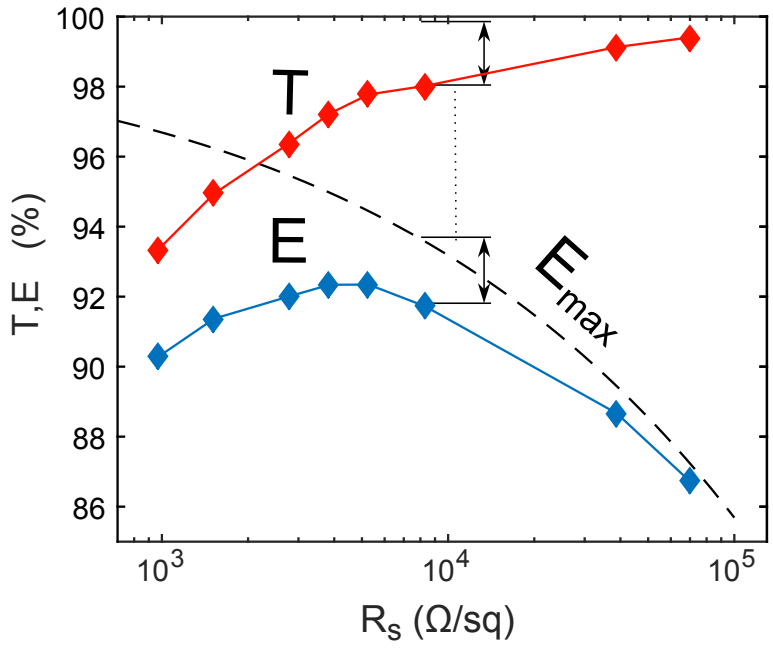

Figure 4.3: Experimental transparency and sheet resistance values for the carbon nanotube layers of ref. [28] (red upper series) and the corresponding efficiency factors (blue lower series) after including metallization with $w = 30\mu$m and $W = 1$cm. Each point lies below the maximal efficiency factor E_{max} (dotted) by a distance proportional to $(1 - T)$.

W to the wire height. Taller wires with their reduced R_M will allow for larger values of the cell width, which can reduce the negative impact of interconnect dead-space and thereby enhance module efficiency.

Just as the ohmic losses discussed above incur a reduction in cell voltage V_{mp}/V^0_{mp}, the effect of non-ideal transparency is to reduce the cell's nominal photocurrent J^0_{mp} by a factor $(1 - \frac{w}{p})$ from the wire shading, and further by a factor T due to the TC's transparency. At the module level, current is again reduced by a factor $(1 - \frac{s}{W})$ due to the interconnect space discussed above, where s is the interconnection width. Taken together the ohmic and current losses reduce power generation efficiency by a factor of $J_{mp}/J^0_{mp} \times V_{mp}/V^0_{mp}$, or

$$E(R_s, T) = \begin{cases} T\left(1 - \dfrac{s}{W^*}\right)\left(1 - \dfrac{1}{3}\dfrac{J^0_{mp}}{V^0_{mp}} W^{*2} R_s\right), & \text{(4.2a)} \\ T\left(1 - \dfrac{s}{W^*}\right)\left(1 - \dfrac{w}{p^*}\right) \times & \text{(4.2b)} \\ \left(1 - \dfrac{1}{3}\dfrac{J^0_{mp}}{V^0_{mp}}\left[W^{*2} R_M + \dfrac{1}{4} p^{*2} R_s\right]\right) \end{cases}$$

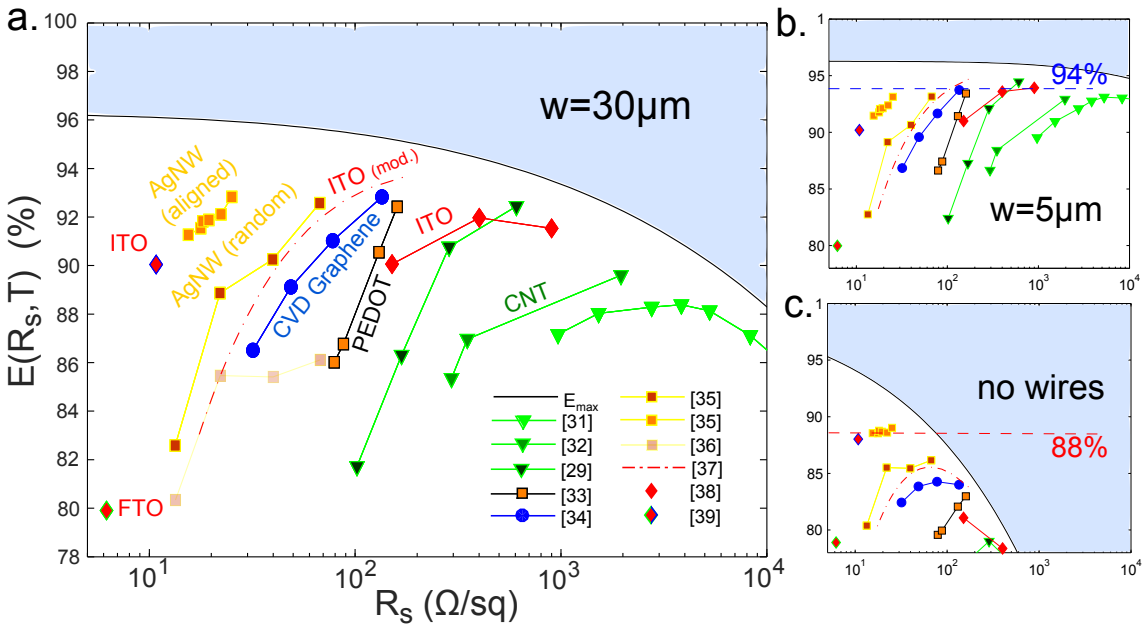

Figure 4.4: Plots of the efficiency factor E calculated using experimental (R_s, T) data from the literature. The wire widths are 30μm in (a), 5μm in (b), whereas (c) corresponds to a bare electrode. In each case the interconnect width is set to 200 µm and for (a) and (b) the wire height is 3μm.

which is defined as a fraction of the theoretical efficiency calculated in the absence of either loss mechanism, again for a bare and metallized TC respectively. The object of designing a transparent electrode is therefore to make this "efficiency factor" as close as possible to unity. The asterisks on p and W denote that the wire spacing and cell width should always be chosen so that E takes its maximum value, conditions which could in principle be used to eliminate these variables from the expressions for E. This is straightforward to accomplish by hand in the case of Eqn. (4.2a) (see section 3 below), but less so for Eqn. (4.2b), for which we resort to numerical optimization in the calculations to follow. As the transparency T is a common factor in Eqns. (2), E can be written in the form $E(R_s, T) = T \cdot E_{max}(R_s)$ which defines an envelope function $E_{max}(R_s)$ denoting the maximum fractional efficiency allowed by current and ohmic losses at a given sheet resistance. The shape of E_{max} is determined by the parameters J^0_{mp}/V^0_{mp} and s, and the metallization parameters R_M and w when they apply. In Fig. 4.3 we illustrate the role of E_{max} and demonstrate how the transformation from (R_s, T) data (red line) to (R_s, E) data (blue line) unambiguously reveals the optimal TC layer for a specific cell type.

In Fig. 4.4 we have used published R_s, T data [29, 30, 28, 31, 32, 33, 34, 35, 36, 37] to compute efficiency factors for a variety of TC technologies with and without a metal grid.[2]

[2]In all figures we have used transparency values reported at 550 nm, with the exception of the transparent

The cell parameters are taken to correspond roughly with a state-of-the-art perovskite cell, so that $J^0_{mp}/V^0_{mp} = 25\text{mA/cm}^2/1.1\text{V} = 22\text{k}\Omega^{-1}\text{cm}^{-2}$, and we use an interconnection width of $s = 200\,\mu\text{m}$ [9]. The shaded regions in Fig. 4.4 denote unphysical efficiency factors defined by $E > E_{max}$, and each data point is situated at the coordinates $(R_s, T \cdot E_{max})$. This comparison reveals that the wire width plays a deciding role in determining which TC technologies give acceptable performance in a solar device. For moderate wire widths of $w = 30\,\mu\text{m}$ (Fig. 4.4a), corresponding roughly to the capabilities of industrial screen printing, sheet resistances up to a few hundreds of Ohms per square remain competitive, and in that region the competition between technologies is fairly close. For smaller wires of width $w = 5\,\mu\text{m}$ the playing field is almost completely leveled, and high performance can be obtained with sheet resistances as large as several thousands of Ohms per square (Fig. 4.4b). By contrast, without metallization electrode performance drops off rapidly with increasing sheet resistance and the best candidates lie in the region of $10 - 50\Omega/\text{sq}$ (Fig. 4.4c). Comparing the best performers in each case we find that a relative efficiency improvement of approximately 5% can be expected in moving from bare to metallized electrodes. It is also clear that transparency becomes the primary measure of TC quality when smaller wire widths are available. This means that emerging TC technologies such as carbon-nanotubes, which are generally regarded as having unsuitably high sheet resistance for solar applications, can give competitive and even superior performance with the use of narrow-width metallization due to their ultra-high transparency [38]. Significantly, nearly all of the data in Fig. 4.4(a,b) trends steeply upwards with increasing sheet resistance, suggesting that in most cases the optimal transparency for these technologies (when augmented with a metal grid) has yet to be demonstrated.

The efficiency factors defined in (2) were introduced for the top electrode of a stand-alone cell, but a similar strategy can be pursued to model the performance of TCs in tandem cells with only slightly different equations. We include such an analysis in 4.1.3.

4.1.2 Figures of Merit for Solar Cells

To ease comparisons TCs are often ranked in terms of a figure of merit which is a simple function of sheet resistance and transparency. The most widely used is the DC to optical conductivity ratio [39]

$$\sigma_{d.c.}/\sigma_{opt} = \left[(T^{-\frac{1}{2}} - 1)\frac{2R_s}{Z_0}\right]^{-1} \tag{4.3}$$

oxide films (ITO and FTO) which generally exhibit a considerable variation in transmission with wavelength. For ITO and FTO each transmittance was weighted with the AM1.5g spectrum. For the other technologies full spectral data was not available.

in which $Z_0 = 377\,\Omega$. Although this relationship only strictly applies to a thin uniform layer when $\sigma_{d.c.}$ and σ_{opt} can be separately defined, it can nevertheless be used as an abstract figure of merit for any transparent conductor. An alternative to this is Haacke's function [40]

$$\Phi_H = T^q / R_s \tag{4.4}$$

in which q is arbitrary and can be chosen to suit the application, with typical values lying in the range $q = 20-100$. The test of a good figure of merit for solar applications is that electrodes with equal figures of merit should give roughly equal performance in a cell. Of course the efficiency factor satisfies this criterion by definition. To assess the others in Fig. 4.5 we have plotted level curves of the conductivity ratio and Haacke's function alongside level curves of the efficiency factor for a bare and metallized TC. Although with a hand-picked value for q Haacke's function can be made to follow the efficiency factor approximately (here we have chosen $q = 100$ to approximate the metallized curve), the more commonly used conductivity ratio has level curves which can be seen to bend distinctly in the wrong direction. As the normal to each level curve points in the direction of maximum change, the conductivity ratio suggests further decreasing the sheet resistance when it is lowest, and further increasing the transparency when it is already high. This is opposite to the common sense prediction, borne out by the efficiency factor, that these two properties must be balanced in a good electrode with diminishing returns applying as either property is improved. We conclude that the conductivity ratio cannot be relied upon to accurately reflect the performance of a transparent conductor in a solar cell (and indeed, is likely to be similarly unphysical for any application), although Haacke's figure may do a reasonable job if the parameter q is properly chosen.

For a bare electrode equation (4.2a) can readily be put in the form of a simple figure of merit as the optimization problem for W has a simple analytic solution. This is obtained by first setting the derivative of 4.2a with respect to W equal to zero, giving

$$2\frac{J^0_{mp}}{V^0_{mp}} R_s W^3 - \frac{J^0_{mp}}{V^0_{mp}} s R_s W^2 - 3s = 0 \tag{4.5}$$

and then noting that as the shading loss s/W should be no larger than a few percent for the optimal W (W^*), the second term can be safely neglected by comparison with the first, giving the expression

$$W^* = \left(\frac{3V^0_{mp} s}{2J^0_{mp} R_s} \right)^{1/3} \tag{4.6}$$

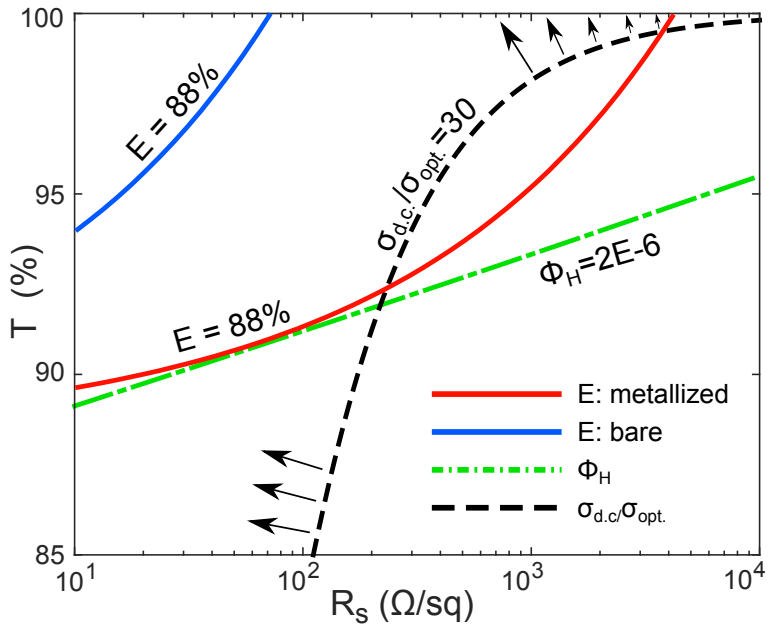

Figure 4.5: Level curves of the d.c. to optical conductivity ratio (black dashed) and Haacke's function (green dot-dash), as compared to contours of equal loss factor computed using equations (refbareFoM) (blue) and (4.9) (red). For the bare loss factor we have set $s = 200\mu$m, the wire width $w = 30\mu$m and in both cases $J^0_{mp}/V^0_{mp} = 22\text{k}\Omega^{-1}\text{cm}^{-2}$. Normally-oriented arrows on the conductivity ratio point in the direction of maximum "improvement".

This then yields a simple analytic expression for the optimal efficiency factor

$$E = T\left(1 - \frac{s}{W^*}\right)\left(1 - \frac{1}{3}\frac{J^0_{mp}}{V^0_{mp}}W^{*2}R_s\right), \tag{4.7}$$

$$W^* = \left(\frac{3V^0_{mp}s}{2J^0_{mp}R_s}\right)^{1/3} \tag{4.8}$$

However, with metallization included the problem of obtaining a simple expression for E_{max} is greatly complicated by the coupling between the optimal wire spacing p^* and cell width W^*. A limiting expression may be obtained by effectively taking the wire height $h \to \infty$ (or $R_M \to 0$),

and then following a similar procedure to the derivation above, giving

$$E(R_s, T) = T\left(1 - \frac{w}{p^*}\right)\left(1 - \frac{1}{12}p^{*2}\frac{J^0_{mp}}{V^0_{mp}}R_s\right), \tag{4.9}$$

$$p^* = \left(\frac{6V^0_{mp}w}{J^0_{mp}R_s}\right)^{1/3} \tag{4.10}$$

in which the dependence on cell width has completely vanished. As a brief aside, this approximate form of the optimal pitch p^* can be used to justify our neglect of contact resistance between the wires and underlying TC hitherto. Assuming that the contact is ohmic, these losses can be modelled with an additional term added to the voltage loss 4.1a:

$$\frac{\Delta V_c}{V^0_{mp}} = \frac{1}{3}\frac{J^0_{mp}}{V^0_{mp}}\frac{\rho_c}{w}p \tag{4.11}$$

in which ρ_c is the specific contact resistance. In order for the contact resistance to be negligible we require that this fraction be less than about 1%, which translates to $\rho_c \lessapprox 0.01\,\Omega\,\mathrm{cm}^2$ using typical numbers for the wire width and cell parameters. This condition is well satisfied for typical metallic contacts to conductive oxides and graphene [41], but may require attention in other cases such as carbon nanotubes [42].

Returning to the task of defining figures of merit, equations (4.8) and (4.9) are both approximate forms of the efficiency factor defined earlier (equations (4.2a,4.2b)), but do a good job of capturing the effects of a transparent conductor on solar cell performance. Although there appear to be quite a number of parameters in Eqns. (4.8) and (4.9), the cell is completely determined by the characteristic ratio J^0_{mp}/V^0_{mp} and interconnect width s in the unmetallized case , and in the metallized case by J^0_{mp}/V^0_{mp} together with the wire width w. Typically J^0_{mp}/V^0_{mp} lies in the range of $20 - 50\mathrm{k}\Omega^{-1}\mathrm{cm}^{-2}$ depending on the cell type [43, 44], the width s lies in the range of $100 - 1000\mu\mathrm{m}$ [9], and $w = 30\,\mu\mathrm{m}$ corresponds roughly to the current capabilities of industrial screen printing [15]. These expressions therefore represent simple alternatives to the standard TC figures of merit with a direct correspondence to actual solar cell performance.

4.1.3 4-T Tandem Electrodes

The efficiency factors defined by equations 4.2a, 4.2b were introduced for the top electrode on a stand-alone cell, but a similar strategy can be pursued to model the performance of TCs in tandem cells. If the (4-T) tandem efficiency is written as a sum of contributions from the top and bottom cells $\eta_{tandem} = \eta_{top} + \eta_{bottom}$ then the efficiency factor takes a corresponding two-part form. For the rear TC of a tandem top-cell, the electrode's sheet resistance only impacts

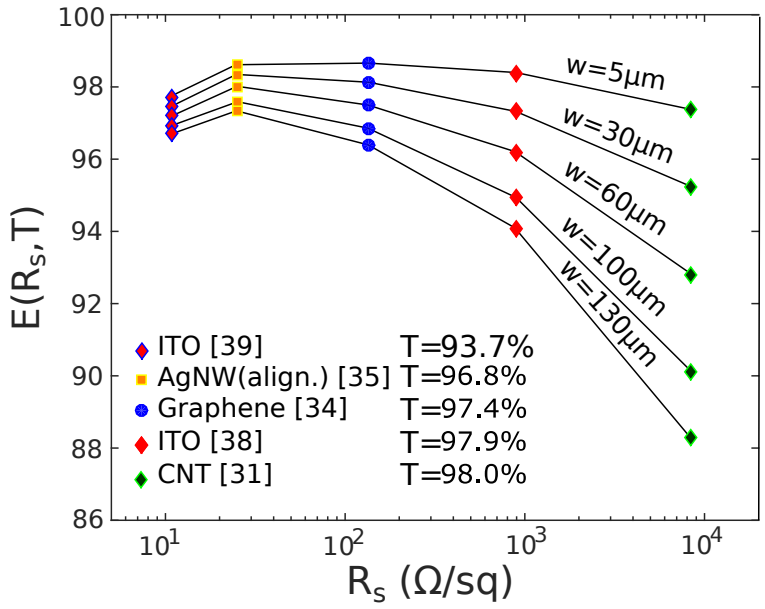

Figure 4.6: Plots of the tandem efficiency factor for the rear-electrode of a tandem top-cell, defined by equation 4.12 and calculated using experimental (R_s, T) data from the literature. Here $\phi = {}^{2}/_{3}$, ${}^{J^0_{mp}}/_{V^0_{mp}} = 19\,\mathrm{mS\,cm^{-2}}$, corresponding approximately to a perovskite-silicon 4-T tandem, and $W = 1\,\mathrm{cm}$. We note that the approach of using metallized monolayer graphene as a transparent electrode in a perovksite-silicon tandem was employed to good effect in ref. [45].

on the top cell's voltage, whilst the transparency only reduces the bottom cell's current, thus (neglecting interconnection losses here for simplicity). Similar considerations apply for the front top-cell and bottom-cell electrodes.

$$E(R,T) = T\left(1 - \frac{w}{p}\right)(1-\phi) + \left(1 - \frac{1}{3}\frac{J^0_{mp}}{V^0_{mp}}\right)\left(1 - \left[W^2 R_M + p^{*2} r_s\right]\right)\phi \qquad (4.12)$$

where $\phi = {}^{\eta_{top}}/_{\eta_{top}+\eta_{bottom}}$. This can be used as before to determine the optimal (R_s, T) combinations and wire spacings, with the minor caveat that T is no longer a common factor so that E_{max} cannot be defined as previously. In Fig. 4.6 we use this equation to again show the dramatic effect of wire width on the performance of high R_s electrodes by plotting the tandem efficiency factor above for technologies spanning a wide range of sheet resistances, using parameters appropriate to a perovskite-on-silicon combination.

4.2 Direct Integration of a Monolithic (2-T) Tandem

Design approaches for creating multi-junction cells can be categorized as either two-terminal (2-T) or four-terminal (4-T). The 2-T configuration allows for monolithic fabrication and obviates the need for additional front and rear electrodes, which incur parasitic electrical and optical losses as discussed in the previous section. The monolithic 2-T approach instead requires an interconnection layer that effectively facilitates, with minimal electrical and optical losses, the flow of photogenerated carriers from one subcell to the other and thence to the external circuit. Tunnel junctions consisting of a homojunction between two heavily doped p^+ and n^+ regions are commonly used to provide an interconnection layer [46]. Specifically, the first demonstration of a 2-T perovskite/Si tandem device used a partially crystallized, heavily doped n-type Si layer to form a tunnel junction on top of a crystalline p^+-Si emitter in the Si homojunction bottom cell, resulting in $\eta = 13.7\%$ [47]. Improved light management, combined with advances in perovskite photovoltaics, has yielded $\eta = 22.7\%$ by use of heavily-doped hydrogenated nanocrystalline Si (nc-Si:H) tunneling layers on a Si heterojunction (SHJ) bottom cell [48]. Tunnel junction designs require high-temperature processing, often in excess of 800 °C, for the thermal diffusion of dopants and/or recrystallization, and involve toxic gases for doping. Instead of a tunnel junction, the subcell interconnection in the majority of high-efficiency 2-T perovskite/Si tandem devices has therefore utilized a recombination layer formed with a transparent conductive oxide, such as indium-doped tin oxide (ITO) [49, 50, 51] or indium-doped zinc oxide (IZO) [52]. The present record efficiency of 23.6% for monolithic perovskite/Si tandems was accordingly obtained by incorporating an ITO intermediate layer to connect a SHJ bottom cell to a perovskite top cell [49]. Impediments to further efficiency improvements in such TCO-containing interconnection systems include substantial parasitic absorption due to free-carrier absorption at long wavelengths, suboptimal reflectance due to a mismatch between the refractive indexes of the TCO and Si, and the prevalence of shunt paths through the top cell, caused by surface roughness [53].

We demonstrate herein a distinct strategy for fabrication of efficient monolithic, 2-T perovskite/Si tandem solar cells. The approach does not utilize a conventional interconnection layer and instead places the perovskite top cell in direct contact with the Si homojunction bottom cell (Fig. 4.7A). Development of this unique approach was stimulated by the observation of a highly Ohmic contact between TiO_2 deposited by atomic-layer deposition (ALD) and p-type Si, in photoanodes that efficiently and stably evolve O_2(g) from water [54]. Despite the absence of an intentional recombination layer, we observe that under certain deposition conditions a conductive contact can be produced spontaneously between the two subcells in the monolithic tandem device. The observations are consistent with the formation of an atomic-scale recom-

bination layer due to a defective interphase region at the TiO_2/p^+-Si interface. The contact resistance between the top and bottom cells was strongly dependent on the band alignment at the TiO_2/p^+-Si interface and on the relative doping densities of the TiO_2 and p-Si, which are sensitive to the TiO_2 preparation method.

4.2.1 Interconnect-Free Tandem Design

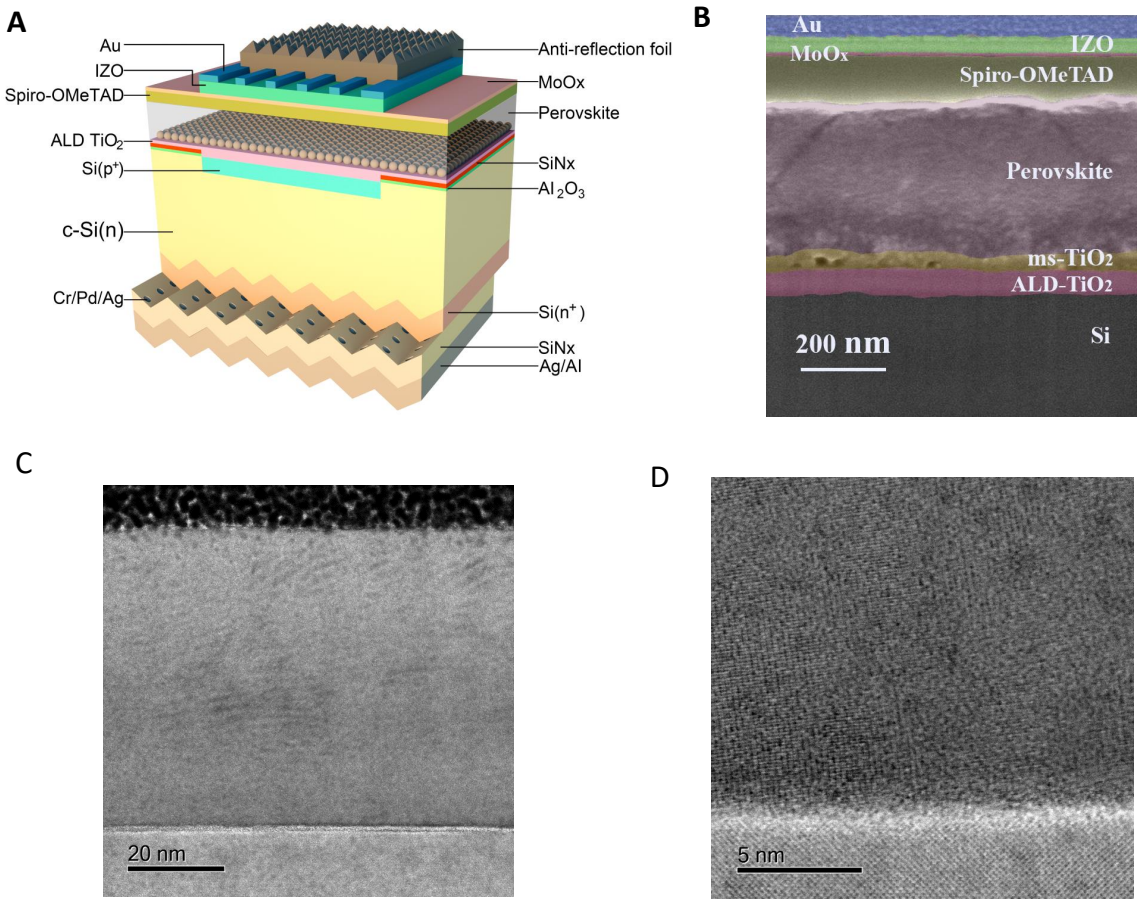

Figure 4.7: (A) Schematic of the interconnect-free monolithic tandem solar cell, (B) Cross-sectional scanning-electron microscope (SEM) image of the tandem device. (C) Scanning transmission-electron microscopy (STEM) bright field (BF) image and (D) high-resolution STEM BF image of the TiO_2/p^+-Si interface.

The perovskite top cell in the demonstration device consisted of a conventional n-i-p structure with a stack of cp-TiO_2 (compact TiO_2) / ms-TiO_2 (mesoporous-TiO_2) / perovskite / Spiro-OMeTAD / MoOx / IZO / Au grid, as illustrated in the cross-sectional SEM image in Fig. 4.7B. The ALD-deposited TiO_2 was uniform and conformal with a low surface roughness of

0.77 nm. Whilst largely amorphous in its initial state the compact layer became polycrystalline after annealing at 400 °C, as seen in the STEM images of Fig. 4.7D (annealed), as well as by XRD analysis. A 54 nm thickness was found to be optimal, covered by a $70-80$ nm ms-TiO_2 layer and an ultra-thin PCBM (Phenyl-C61-butyric acid methyl ester) /PMMA (Poly(methyl methacrylate)) passivation layer to improve the cell voltage and reduce hysteresis in the current density vs voltage (J-V) characteristics [55]. Multiple cation perovskites, which have consistently outperformed their single-cation originators [48], were used in the cell, and were fabricated using the anti-solvent one-step method [56]. A composition of $Cs_{0.05}Rb_{0.05}FA_{0.765}MA_{0.135}PbI_{2.55}Br_{0.45}$ yielded stable films with an appropriate bandgap (E_g= 1.63 eV) [57]. Current matching between the two subcells was obtained by deposition of a relatively thin ($\sim$ 300 nm) perovskite layer. To minimize the parasitic absorption of the Spiro-OMeTAD hole blocking layer while minimizing pinholes, the layer thickness was reduced to an optimum of 120 nm. Before sputtering a 40 nm IZO layer for the front contact, a 10 nm MoO_x layer was deposited to protect the Spiro-OMeTAD from sputtering damage. Optical losses on the front surface were minimized by the use of narrow Au grids having a width of $\sim$30 µm and a spacing of $\sim$ 1 mm, which resulted in 3% grid loss.

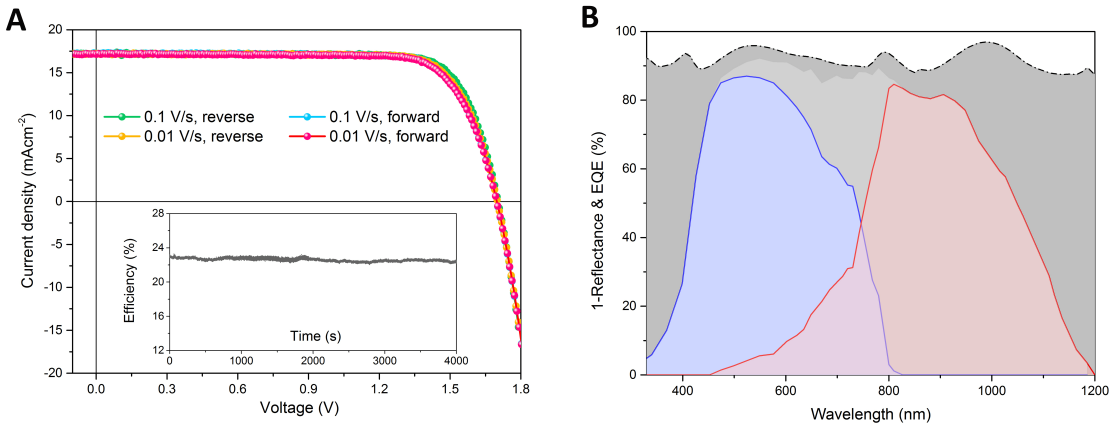

Figure 4.8: (A) J-V behavior of the proof-of-concept tandem device with both reverse and forward scanning at 0.1 V/s and 0.01 V/s, respectively. The inset shows the efficiency evolution of unencapsulated device under continuous illumination for $>$ 1h at the bias that yielded the maximum power point for the first J-V scan. (B) Absorbance (1-R, where R is the reflectance) of the tandem device (dashed dot line), external quantum efficiency (EQE) of the perovskite top cell (blue line), and EQE of the c-Si bottom subcell (red line).

Due to the large number of material interfaces, optical considerations are paramount in efficient multi-junction cell design. The tandem devices prepared herein had a low average reflection over the 400-1200 nm spectral region, partly due to the attachment of a textured foil

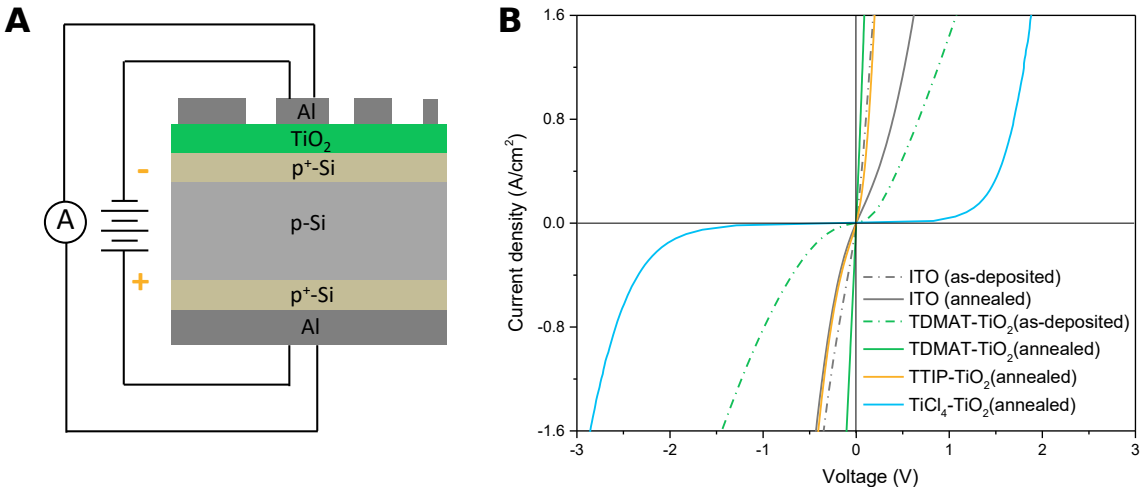

Figure 4.9: (A) Schematic of the structure used for measuring contact resistivity. (B) Comparison of the J-V behavior of ITO/p^+-Si and various TiO_2/p^+-Si structures before and after annealing at 400 °C in air.

to the front surface (Fig. 4.8B). Spectral response analysis revealed that the fabricated structure yielded nearly perfect current matching, with only a slightly larger integrated current density of 17.5 mA cm^{-2} for the perovskite top cell as compared with a current density of 17.2 mA cm^{-2} for the Si bottom cell. Better light management, via tuning of the perovskite composition [58] and removal of optical absorption and reflection from the Spiro-OMeTAD contact [59], should allow for higher short-circuit current densities. Minority-carrier lifetime measurements indicated that the TiO_2 only provided a weak passivation effect on the p^+-Si emitter, hence better passivation of the p^+-Si surface could lead to further improvements in the open-circuit voltage. Strategies including enhancement of the p^+-doping density to reduce the emitter thickness and hence absorption, or optimizing the p^+-Si and TiO_2 interface with respect to passivation, would also be beneficial. The likelihood of future improvements in the perovskite standalone efficiency, combined with the feasibility of improved light management and better design for the Si subcell, indicates that this system could plausibly be optimized to yield $\eta = 30\%$ [58, 60].

4.2.2 Characterization of the Titania-Silicon Contact

Efficient operation of this tandem device requires efficient charge transfer between the p+-Si emitter and TiO_2 layer. Specifically, photogenerated electrons collected in the TiO_2 layer must be able to recombine, while incurring minimal voltage loss, with corresponding holes from the Si emitter region. The n-type character of TiO_2 would be expected to produce a rectifying p-n heterojunction with p-type Si [61, 62]. However, the J-V characteristics of these tandem devices

did not exhibit S-shaped curves, nor fill-factor losses, that would be expected if a rectifying contact were present between the two sub-cells [63, 64]. To confirm the existence of facile electrical contact between TiO_2 and p^+-Si, the structure depicted in Fig. 4.9A was used to investigate the electrical properties of TiO_2/p^+-Si interface in our tandem device. Analogous devices were also fabricated using an ITO film instead of TiO_2 to emulate the recombination layer used in previous tandem designs [49, 50, 51]. The contact resistivity ρ_c of both films with respect to p^+-Si was determined via the method devised by Cox and Strack [65]. The contact resistivity so derived includes not only the desired metal oxide/p^+-Si contact resistivity, but also includes contributions from the bulk oxide as well as the oxide/Al contact. These measurements confirmed that the contact between TiO_2 and p^+-Si was highly Ohmic, characterized by a resistivity less than $30\,m\Omega\,cm^2$, surpassing that of the ITO/p^+-Si combination ($230\,m\Omega\,cm^2$). Post-deposition treatment in the form of annealing played a vital role in achieving the desired low resistance contact. Indeed, superior performance for the TiO_2/p^+-Si subsystem was only obtained after annealing the structure at 400 °C in ambient air, which produced more than a ten-fold reduction in the derived contact resistance. In contrast, annealing had a detrimental effect on the ITO/p^+-Si contact, and correlated with a reduction in the bulk conductivity after annealing of ITO deposited on quartz [50]. Tandem devices fabricated with ITO as a recombination layer exhibited inferior photovoltaic performance as determined by all device metrics, with V_{oc} = 1.510 V, $J_{sc} = 15.8\,mA\,cm^{-2}$ and FF = 0.637. The current loss in this device is likely a result of parasitic absorption in the ITO layer and reflection loss on the ITO/Si interface, and the reduced V_{oc} and FF are ascribable to inferior contact between the sub-cells (as supported by the J-V measurements of Fig. 4.9B), as well as shunting due to pinholes in sputtered ITO layers. The interconnect-free tandem cells thus have dual advantages of higher performance as well as more facile fabrication than the standard design that incorporates an ITO-based recombination layer.

TiO_2 layers prepared using different ALD precursors exhibited mutually different J-V characteristics (Fig. 4.9B). Ohmic, highly conductive behavior was observed after annealing the TiO_2 using tetrakisdimethylamidotitanium (TDMAT) as the ALD precursor (Fig. 4.9B, green solid line), however, very low conductivity ($> 10\,\Omega\,cm^2$) in the low-bias region was obtained when titanium tetrachloride (TiCl4) was used as the ALD precursor instead of TDMAT, despite nominally identical processing conditions (Fig. 4.9B, blue solid line). The use of titanium tetraisopropoxide (TTIP) resulted in intermediate performance, displaying conductive but distinctly non-linear J-V behavior (Fig. 4.9B, yellow solid line). The conductivity of the TiO_2/p^+-Si test structures was correlated well with the behavior of the tandem device, with η = 21% for TTIP as the precursor and $\eta = 3.6\%$ for TiCl4 as the precursor.

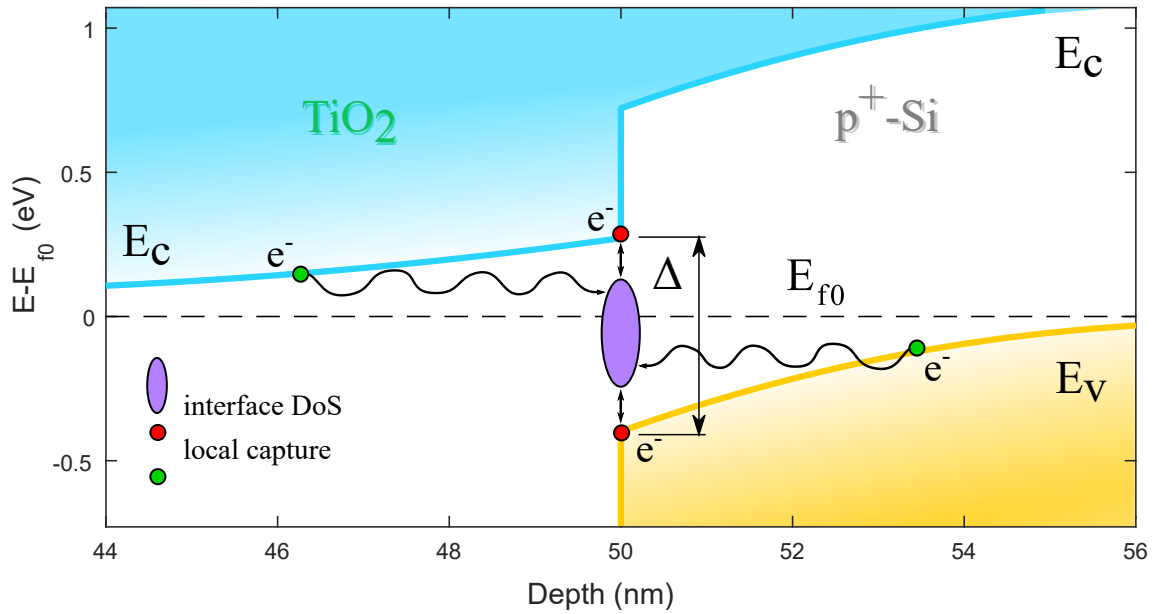

Figure 4.10: Simulated band diagram of the TiO_2/p^+-Si at equilibrium assuming n-type doping of $5 \cdot 10^{18}\,cm^{-3}$ on the TiO_2 and $1 \cdot 10^{19}\,cm^{-3}$ for p^+-Si (appropriate for our test structure with TDMAT TiO_2, see table S3. The unknown interfacial energy gap Δ is shown here for illustrative purposes as 600 meV, which falls within the range of reported measurements [66]). Both mechanisms of direct- and tunneling assisted capture by interfacial defects are shown.

4.2.3 Role of Defects & the Titania-Silicon Band-Offset

The interfacial band alignment is of prime importance for carrier transport between TiO_2 and p^+-Si. Based on X-ray photoelectron spectroscopic (XPS) measurements of the electron affinity (χ^{TiO_2}) for our TiO_2 samples ($4.35 - 4.7$ eV) and the ionization energy of Si (I.E.^{Si}), taken as 5.15 eV, neglecting any surface dipole contribution the band alignment at an idealized TiO_2/p^+-Si junction should result in an energy gap of $\Delta = E_c^{TiO_2} - E_v^{Si} = \chi^{TiO_2}$–I.E.$^{Si} \approx 0.45 - 0.8$ eV, between the top of the Si valence band and the bottom of the TiO_2 conduction band (Fig. 4.9). Experimental determinations of Δ that include the surface dipole require combining data from several techniques, and have only been reported rarely for TiO_2/p-Si interfaces [66, 67]. Values of Δ between 0.45 eV and 0.8 eV have been obtained depending on the 1-2 nm interlayer composition, supporting our observation of a strong sensitivity to processing. A non-vanishing gap at the TiO_2/p^+-Si interface prohibits at 0 V band-to-band tunneling between the TiO_2 conduction band and the Si valence band, due to a lack of overlap in the bulk density of states at equilibrium (see Fig. 4.9), as would occur in a standard tunnel diode. Sub-gap states in TiO_2 due to a band-tail or defect band may alter this situation, but the mechanism

is essentially the same as a defect-mediated pathway. The necessary band overlap between the TiO_2 conduction band and the Si valence band will occur at a threshold reverse voltage, but carriers must nevertheless tunnel through the sum of the depletion and interlayer widths, estimated to be 10's of nanometers for TiO_2 doping in the range of $1 \cdot 10^{17}\,cm^{-3}$ to $1 \cdot 10^{19}\,cm^{-3}$. This distance is at the upper limit of what is physically reasonable, and indicates that band-to-band tunneling at reverse bias is only likely to occur when both depletion regions are very small, corresponding to high doping [68]. At forward bias, the band overlap is decreased and band-to-band tunneling becomes prohibited. In this case, current could be carried via the thermionic emission of conduction-band electrons from TiO_2 over the barrier due to the conduction-band offset $E_g^{Si} - \Delta$, but this mechanism would predict a strong tradeoff between the forward and reverse current, contrary to the observed Ohmic behavior (i.e., large gaps Δ would provide a small barrier for the forward current while enlarging the threshold voltage for reverse current, and vice versa). compatible with the observed highly conductive contact between TiO_2 and p^+-Si. A more likely alternative is the presence of a substantial density of localized mid-gap states at the interface between Si and TiO_2. Such interfacial states can facilitate band-to-band tunneling at reverse bias and act as generation-recombination centers at all bias voltages [64, 69, 70, 71]. In such a scenario, electrons can move into and out of the defects states via local capture/emission as well as tunneling (Fig. 4.9). As generation-recombination centers, the interface states would have a substantial influence on charge transport by facilitating recombination of carriers at forward bias without requiring carriers to cross over the interfacial barrier. At reverse-bias, every recombination center could become a source of generation, and high conductivity can be obtained by thermally generated carriers. Conceptually this situation is similar to having a recombination-layer of atomic dimensions between the TiO_2 and p^+-Si created in situ and intrinsically via the native material contact, without the introduction of substantial optical losses.

Numerical drift-diffusion models based on SCAPS [72] were used to investigate the impact of interfacial generation-recombination centers on the junction current. These models were designed to compute the current across a TiO_2/p^+-Si heterojunction assuming Ohmic metal contacts on both sides, and therefore mainly addressed the junction current, with only minor contributions from bulk conduction through the small layers thicknesses (50 nm and 100 nm for TiO_2 and Si, respectively). Shockley-Read-Hall (SRH) recombination centers were added at the TiO_2/p^+-Si interface to physically correspond to localized states that are expected to form in the interfacial energy gap. Such defects are likely to occur at a high density, given the relatively low degree of lattice matching between TiO_2 and Si, the possibility of precursor remnants, Si dangling bonds, and the presence of a 1-2 nm amorphous alloy interlayer observed in our samples between the two bulk crystals (Figs. 4.9C, D). Interlayers are known to have

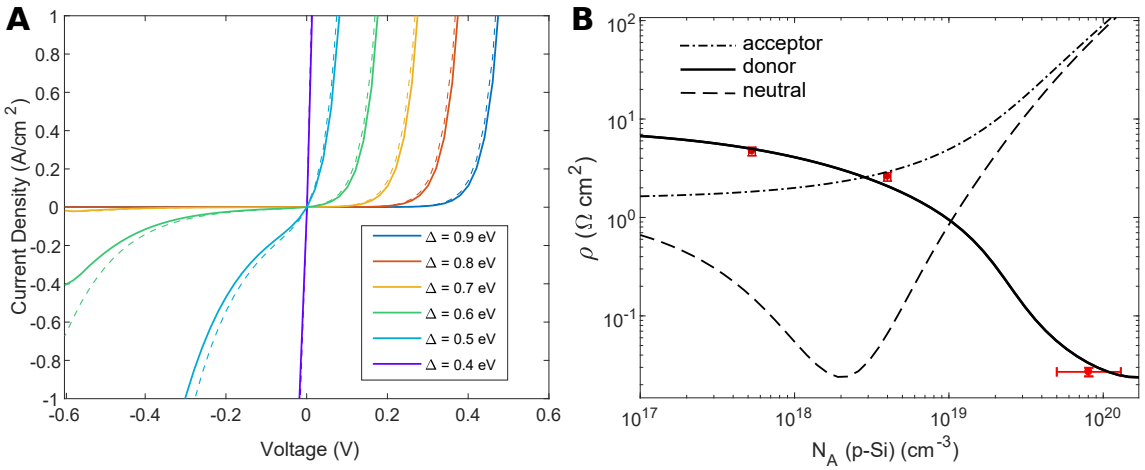

Figure 4.11: (A) Simulated I-V curves for varying interfacial gaps Δ. A single neutral mid-gap SRH defect was included with $S_n = S_p = 1 \cdot 10^5\,\mathrm{cm\,s^{-1}}$. The dashed curves are computed with tunneling to defects included. (B) Simulated small voltage resistivity ($\rho = \mathrm{d}V/\mathrm{d}I|_{V=0}$) with the TiO_2 donor density fixed at $1 \cdot 10^{18}\,\mathrm{cm^{-3}}$ and variable p-Si acceptor doping. Measurements are included as data points in red. Calculations for neutral (solid lines), acceptor-type (dotted lines) and donor-type (dot-dashed lines) are shown to demonstrate the important effect of defect charge on the interfacial carrier balance.

a profound effect on the interface dipole or band-alignment of semiconductor-semiconductor contacts [73], as well as on the mechanisms of charge transfer [74], and may therefore play a key role in our experimental system. For simplicity in our modeling, the contribution of the interlayer capacitance was neglected, while the defect density of the interlayer was captured in the interfacial SRH parameters. Tunneling due to defects was not accurately modeled due to a lack of detailed knowledge of the interface parameters, but calculations with tunneling processes included are presented in Fig. 4.11A to illustrate qualitatively the behavior that results from this effect.

Fig. 4.11A shows the computed J-V characteristics of a TiO_2/p^+-Si heterojunction with varying gaps Δ in the range of $0.4 - 0.9$ eV, and with a high density of neutral mid-gap defects (recombination velocities $S_n = S_p = 1 \cdot 10^5\,\mathrm{cm\,s^{-1}}$), all other parameters being equal. These J-V characteristics bear a striking resemblance to the experimental behavior of Fig. 4.9B in that they both exhibit the full range of qualitative characteristics seen experimentally, namely highly conductive Ohmic behavior (e.g. 0.4 eV), asymmetric exponential-type curves ($\Delta = 0.5, 0.6$ eV) and strong rectification (Δ = 0.7-0.9 eV). The detrimental effect of a large band offset can only be compensated by higher recombination velocities up to the physical limit of $S_{n,p} = v_{th} \approx 1 \cdot 10^7\,\mathrm{cm\,s^{-1}}$, likely ruling out high defect-mediated conductivity for band offsets greater than 0.7 eV. A somewhat less trivial prediction of the SRH model concerns the balance of

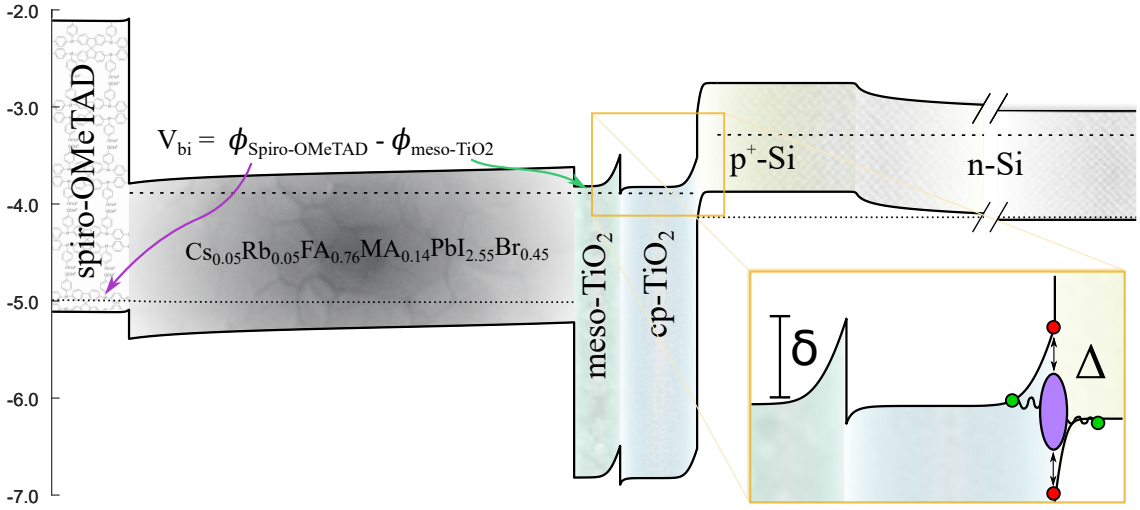

Figure 4.12: Simulated band diagram of the full tandem device at illuminated open-circuit. The inset depicts the two critical energetic offsets Δ and δ, respectively, defined as the valence-to-conduction band offset at the TiO_2-Si interface and the difference in work functions between our solution-processed mesoporous TiO_2 layer and that of the ALD compact layer.

carrier densities at the interface. According to equation B.3 (appendix B), the interfacial carrier densities must be balanced to achieve maximal conductivity (in particular $v_n n_0 \approx v_p p_0$ where n_0, p_0 are the equilibrium carrier densities at the interface and $v_{n,p}$ their quasi-recombination velocities). The interfacial conductivity benefited from a high substrate doping (Fig. 4.11B, red markers), which is consistent with donor type defects at the interface that act to deplete the hole density. Donor defects are frequently present at both TiO_2 and unpassivated-Si surfaces in the form of oxygen vacancies [75] and dangling bonds (P_b centers) [76], respectively. The SRH theory thus consistently accounts for the Ohmic conductivity between TiO_2/p^+-Si, in accord with the behavior observed previously for TiO_2-protected Si photoanodes [54, 77].

4.2.4 Role of Mesoporous Titania – Maintaining the Built-in Voltage

According to the SRH theory outlined above, the diverse behavior seen in Fig. 4.9B with respect to preparation conditions likely results from variations in the band offsets between the TiO_2 conduction-band edge and the Si valence band (Δ), the TiO_2 doping density, and the interfacial defect properties. Consistently, the highest-performing TDMAT-ALD TiO_2 samples exhibited relatively large electron affinities for anatase. The vacuum levels are only an approximate indicator of the actual band alignment, but the data suggest that a small Δ, in addition to a conductive TiO_2 layer, may be important to obtain a high-conductivity contact between p^+-Si and TDMAT-ALD TiO_2. The built-in voltage of a perovskite cell is determined in part by the

work function of the n-type TiO_2 selective contacts (corrected for surface dipole contributions), and thus has an important effect on the maximum open-circuit voltage. Larger n-type selective contact work functions reduce the built-in voltage and therefore the achievable quasi-Fermi level splitting, in contrast to the experimental observations that the perovskite cells on TDMAT-ALD TiO_2 function without substantial losses. The observed cell performance is thus indicative of an additional role for the mesoporous TiO_2 layer that is inserted in the standard cell architecture between the compact TiO_2 layer and the perovskite, to improve film quality and electron extraction. Single-junction perovskite cells fabricated without a mesoporous TiO_2 layer (i.e. directly on the TDMAT-ALD TiO_2 compact layer) exhibited drastically reduced open-circuit voltages (note that this does not indicate an intrinsic limit of planar cells, as solution-processed compact layers yielded uncompromised, high open-circuit voltages [78]), supporting our measurements which indicated that the conduction band in compact TDMAT-ALD TiO_2 is energetically lower-lying than in other TiO_2 preparations. Due to its smaller work function, inclusion of the solution-processed mesoporous layer therefore appears to maintain the built-in voltage of the cell [55]. A simulated band diagram of the complete tandem structure (Fig. 4.13) summarizes the key findings that contact between the high-work function cp-TiO_2 layer and p^+-Si is facilitated by interface defects, and that high cell voltages for the complete device rely crucially on the inclusion of the lower work function mesoporous TiO_2 to maintain the built-in voltage of the perovskite sub-cell. This latter point is substantiated by I-V simulations of a single-junction perovskite cell with and without a smaller work-function "mesoporous-titania" layer included between the perovskite and the "ALD-titania" layer with larger work-function (Fig. 4.13).

4.3 Summary and Conclusions

In this final chapter we have discussed the steps necessary to integrate perovskite and Si cells into a tandem arrangement, as motivated in Chapter 1. The requirements for integration hinge on whether the tandem is to be operated as two independent but stacked sub-cells (4-T), or as one monolithic (2-T) cell. In the former case no less than 3 transparent conductors are required to contact the two sub-cells, placing considerable weight on the properties of these. The use of metallization relieves the burden on a transparent conductor's sheet resistance, leveling the competition between technologies and allowing for other factors such as material compatibility or ease of processing to take precedence. We have shown that whenever it is possible to incorporate a narrow metallic grid ($w < 30\,\mu m$), the requirements for a transparent conductor shift dramatically towards achieving ultra-high transparency ($> 95\%$). Wire widths in the range of $20 - 30\mu m$ already relax the conventional sheet resistance requirement of 10Ω/sq by more than an order of magnitude, encompassing a wide range of emerging technologies, whilst widths

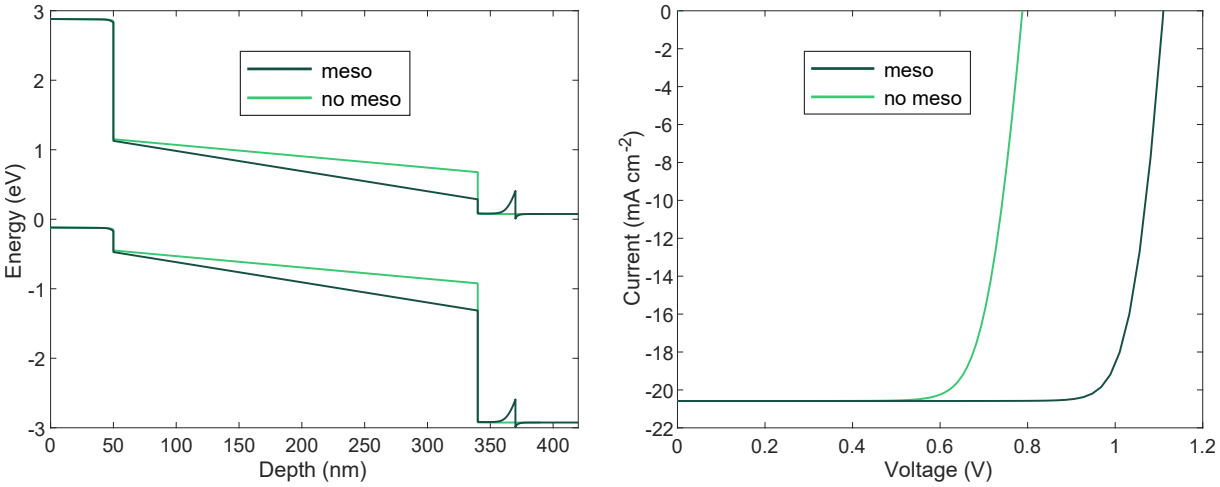

Figure 4.13: Simulated band diagram at 0V (left) and J-V behavior (right) of a single-junction perovskite solar cell with and without an additional "mesoporous" titania layer inserted between the perovskite and compact titania. This represents a 1D simplification of the complex 3-dimensional mesoporous structure present in our tandem cell design, but captures the qualitative effect of including titania layers with contrasting work functions. The mesoporous layer functions primarily to maintain the built-in voltage in the perovskite cell, as seen in the band diagram (left) and consequently discrepant open-circuit voltages (right). Here electron affinities of 4.1eV and 4.5 eV were used for the compact and mesoporous titania layers respectively.

approaching 5 µm will allow for several thousands of ohms per square in the transparent layer. Furthermore, we have shown that metallized transparent layers generally exceed the performance of the best bare transparent conductors due to a combined reduction of losses at the cell and module level. Narrow-width metallization therefore provides a clear route for approaching ideal electrode performance in thin-film solar cells. These findings demonstrate the potential for scalable methods of incorporating thin metal wires into cell substrates to disrupt the transparent conductor landscape.

For sensitive cell architectures embedding of the wires may be necessary to avoid drastic nonuniformities, and this is likely to be simpler for flexible polymer substrates than for glass. However even in the latter case one may look to the literature of microfluidics where the problem of structuring glass has received considerable attention [79, 80], or to well-established sol-gel techniques [12, 13] for imprinting patterns onto glass. Once embedded, these metal wires could be made very much taller than otherwise in order to accommodate larger cell widths, providing a reduction in module dead-space. Electrodes which are naturally exposed, such as the rear electrode in a perovskite 4-T tandem device, can be easily metallized and researchers should be aware that this obviates the widely quoted requirement of 10Ω/sq.

Monolithic 2-T tandems also require at least one transparent electrode, and for these the considerations above apply equally. Furthermore, regarding the interconnection of sub-cells, we have demonstrated a proof-of-concept 2-T perovskite-Si tandem device that functions without a conventional interlayer. An enabling feature of the device is the formation of an atomic-scale recombination layer between a compact TDMAT-ALD TiO_2 layer and the p^+-Si emitter region, which produces a highly conductive Ohmic contact between the two materials. The contact resistance, interfacial band offsets, defect densities, and doping densities are strongly dependent on processing, but therefore present several handles for tunability. The twin advantage of this design in reducing optical losses and in reducing processing steps brings the perovskite-Si pairing tandem structure one step closer to delivering its full potential.

Bibliography

[1] Hecht, D. S.; Hu, L.; Irvin, G. Emerging transparent electrodes based on thin films of carbon nanotubes, graphene, and metallic nanostructures. *Advanced Materials* **2011**, *23*, 1482–513.

[2] Ellmer, K. Past achievements and future challenges in the development of optically transparent electrodes. *Nature Photonics* **2012**, *6*, 809–817.

[3] Layani, M.; Kamyshny, A.; Magdassi, S. Transparent conductors composed of nanomaterials. *Nanoscale* **2014**, *6*, 5581–91.

[4] Snaith, H. J. Perovskites: The Emergence of a New Era for Low-Cost, High-Efficiency Solar Cells. *The Journal of Physical Chemistry Letters* **2013**, *4*, 3623–3630.

[5] Green, M. A.; Ho-Baillie, A.; Snaith, H. J. The emergence of perovskite solar cells. *Nature Photonics* **2014**, *8*, 506–514.

[6] Lal, N.; White, T.; Catchpole, K. Optics and Light Trapping for Tandem Solar Cells on Silicon. *IEEE J. Photovolt.* **2014**, *4*, 1380–1386.

[7] Bailie, C. D.; Christoforo, M. G.; Mailoa, J. P.; Bowring, A. R.; Unger, E. L.; Nguyen, W. H.; Burschka, J.; Pellet, N.; Lee, J. Z.; Gratzel, M.; et al. Semi-transparent perovskite solar cells for tandems with silicon and CIGS. *Energy Environ. Sci.* **2015**, *8*, 956–963.

[8] Löper, P.; Moon, S.-J.; Martín de Nicolas, S.; Niesen, B.; Ledinsky, M.; Nicolay, S.; Bailat, J.; Yum, J.-H.; De Wolf, S.; Ballif, C. Organic-inorganic halide perovskite/crystalline silicon four-terminal tandem solar cells. *Phys. Chem. Chem. Phys.* **2015**, *17*, 1619–1629.

[9] Rowell, M. W.; McGehee, M. D. Transparent electrode requirements for thin film solar cell modules. *Energy Environ. Sci.* **2011**, *4*, 131–134.

[10] Wennerberg, J.; Kessler, J.; Stolt, L. Design of grided Cu(In,Ga)Se-2 thin-film PV modules. *Solar Energy Materials and Solar Cells* **2001**, *67*, 59–65.

[11] Duong, T.; Lal, N.; Grant, D.; Jacobs, D.; Zheng, P.; Rahman, S.; Shen, H.; Stocks, M.; Blakers, A.; Weber, K.; et al. Semitransparent Perovskite Solar Cell With Sputtered Front and Rear Electrodes for a Four-Terminal Tandem. *IEEE Journal of Photovoltaics* **2016**, *PP*, 1–9.

[12] Marzolin, C.; Smith, S. P.; Prentiss, M.; Whitesides, G. M. Fabrication of glass microstructures by micro-molding of sol-gel precursors. *Advanced Materials* **1998**, *10*, 571–574.

[13] Schueller, O. J. A.; Whitesides, G. M.; Rogers, J. A.; Meier, M.; Dodabalapur, A. Fabrication of photonic crystal lasers by nanomolding of solgel glasses. *Appl. Opt.* **1999**, *38*, 5799–5802.

[14] Tvingstedt, K.; Inganäs, O. Electrode Grids for ITO Free Organic Photovoltaic Devices. *Advanced Materials* **2007**, *19*, 2893–2897.

[15] Ju, M.; Lee, Y.-J.; Lee, J.; Kim, B.; Ryu, K.; Choi, K.; Song, K.; Lee, K.; Han, C.; Jo, Y.; et al. Double screen printed metallization of crystalline silicon solar cells as low as 30 μm metal line width for mass production. *Solar Energy Materials and Solar Cells* **2012**, *100*, 204 – 208, photovoltaics, Solar Energy Materials, and Technologies: Cancun 2010.

[16] Sirringhaus, H.; Kawase, T.; Friend, R. H.; Shimoda, T.; Inbasekaran, M.; Wu, W.; Woo, E. P. High-Resolution Inkjet Printing of All-Polymer Transistor Circuits. *Science* **2000**, *290*, 2123–2126.

[17] Li, Z.; Hsiao, P.-C.; Zhang, W.; Chen, R.; Yao, Y.; Papet, P.; Lennon, A. Patterning for Plated Heterojunction Cells. *Energy Procedia* **2015**, *67*, 76 – 83, proceedings of the Fifth Workshop on Metallization for Crystalline Silicon Solar Cells.

[18] Lorenz, A.; Senne, A.; Rohde, J.; Kroh, S.; Wittenberg, M.; Kruger, K.; Clement, F.; Biro, D. Evaluation of Flexographic Printing Technology for Multi-busbar Solar Cells. *Energy Procedia* **2015**, *67*, 126 – 137.

[19] Thibert, S.; Chaussy, D.; Beneventi, D.; Reverdy-Bruas, N.; Jourdan, J.; Bechevet, B.; Mialon, S. Silver ink experiments for silicon solar cell metallization by flexographic process. In 38th Photovoltaic Specialists Conference, 2266–2270.

[20] Ahn, S. H.; Guo, L. J. High-Speed Roll-to-Roll Nanoimprint Lithography on Flexible Plastic Substrates. *Advanced Materials* **2008**, *20*, 2044–2049.

[21] Kumar, A.; Whitesides, G. M. Features of gold having micrometer to centimeter dimensions can be formed through a combination of stamping with an elastomeric stamp and an alkanethiol "ink" followed by chemical etching. *Applied Physics Letters* **1993**, *63*, 2002–2004.

[22] Loo, Y.-L.; Willett, R. L.; Baldwin, K. W.; Rogers, J. A. Additive, nanoscale patterning of metal films with a stamp and a surface chemistry mediated transfer process: Applications in plastic electronics. *Applied Physics Letters* **2002**, *81*, 562–564.

[23] Hsu, P.-C.; Wang, S.; Wu, H.; Narasimhan, V. K.; Kong, D.; Ryoung Lee, H.; Cui, Y. Performance enhancement of metal nanowire transparent conducting electrodes by mesoscale metal wires. *Nature Communications* **2013**, *4*, 2522.

[24] Zou, J.; Yip, H.-L.; Hau, S. K.; Jen, A. K.-Y. Metal grid/conducting polymer hybrid transparent electrode for inverted polymer solar cells. *Applied Physics Letters* **2010**, *96*, 203301.

[25] Zhu, Y.; Sun, Z.; Yan, Z.; Jin, Z.; Tour, J. M. Rational Design of Hybrid Graphene Films for High-Performance Transparent Electrodes. *ACS Nano* **2011**, *5*, 6472–6479, pMID: 21774533.

[26] Koishiyev, G. T.; Sites, J. R. Impact of sheet resistance on 2-D modeling of thin-film solar cells. *Solar Energy Materials and Solar Cells* **2009**, *93*, 350–354.

[27] Green, M. Silicon Solar Cells: Advanced Principles & Practice. Centre Photovoltaic Devices & Systems **1995**.

[28] Geng, H.-Z.; Kim, K. K.; So, K. P.; Lee, Y. S.; Chang, Y.; Lee, Y. H. Effect of Acid Treatment on Carbon Nanotube-Based Flexible Transparent Conducting Films. *J. Am. Chem. Soc.* **2007**, *129*, 7758–7759.

[29] Scardaci, V.; Coull, R.; Coleman, J. N. Very thin transparent, conductive carbon nanotube films on flexible substrates. *Applied Physics Letters* **2010**, *97*, 023114.

[30] Li, J.; Hu, L.; Wang, L.; Zhou, Y.; Grüner, G.; Marks, T. J. Organic light-emitting diodes having carbon nanotube anodes. *Nano Letters* **2006**, *6*, 2472–2477.

[31] McCarthy, J. E.; Hanley, C. a.; Brennan, L. J.; Lambertini, V. G.; Gun'ko, Y. K. Fabrication of highly transparent and conducting PEDOT:PSS films using a formic acid treatment. *J. Mater. Chem. C* **2014**, *2*, 764–770.

[32] Bae, S.; Kim, H.; Lee, Y.; Xu, X.; Park, J.-S.; Zheng, Y.; Balakrishnan, J.; Lei, T.; Kim, H. R.; Song, Y. I.; et al. Roll-to-roll production of 30-inch graphene films for transparent electrodes. *Nature Nanotechnology* **2010**, *5*, 574–578.

[33] Kang, S.; Kim, T.; Cho, S.; Lee, Y.; Choe, A.; Walker, B.; Ko, S.-J.; Kim, J. Y.; Ko, H. Capillary Printing of Highly Aligned Silver Nanowire Transparent Electrodes for High-Performance Optoelectronic Devices. *Nano Letters* **2015**, *15*, 7933–7942.

[34] Silver nanowire data [33] (random array) with the efficiency factor calculated without metallization (i.e. for a bare electrode), included for comparison.

[35] For this series we have modelled the transmission through ITO layers of varying thickness using the Beer-Lambert formula for absorption, taking the extinction coefficient from ref [81] and neglecting reflection.

[36] In-house measurements of RF-sputtered ITO deposited at room temperature (see ref. [11] for further details).

[37] In-house measurements of commercial samples of ITO (Sigma Aldrich 578274, $t \approx 120$nm on glass) and FTO (Dyesol TEC7, $t \approx 650$nm on glass). As the reflectance of these thin-films can vary widely we have elected to include only absorption in the transparency data, so that $T = 1 - A$, making these values an upper estimate.

[38] We note that a significant loss in voltage or collection efficiency may result if the mobility of the underlying active layer is not sufficient to ensure a smooth passage for carriers to the individual tubes (for CNT layers) or nanowires (AgNW electrodes), an issue which may arise in certain organic semiconductors.

[39] De, S.; Coleman, J. N. The effects of percolation in nanostructured transparent conductors. *MRS Bulletin* **2011**, *36*, 774–781.

[40] Haacke, G. New figure of merit for transparent conductors. *Journal of Applied Physics* **1976**, *47*, 4086–4089.

[41] Grosse, K. L.; Bae, M.-H.; Lian, F.; Pop, E.; King, W. P. Nanoscale Joule heating, Peltier cooling and current crowding at graphene–metal contacts. *Nature nanotechnology* **2011**, *6*, 287.

[42] Jackson, R.; Graham, S. Specific contact resistance at metal/carbon nanotube interfaces. *Applied Physics Letters* **2009**, *94*, 012109.

[43] Ramanathan, K.; Keane, J.; Noufi, R. Properties of high-efficiency CIGS thin-film solar cells. In Conference Record of the Thirty-first IEEE Photovoltaic Specialists Conference, 195–198.

[44] Wu, X.; Dhere, R. G.; Albin, D. S.; Gessert, T. A.; DeHart, C.; Keane, J. C.; Duda, A.; Coutts, T. J.; Asher, S.; Levi, D. H.; et al. High-Efficiency CTO/ZTO/CdS/CdTe Polycrystalline Thin-Film Solar Cells: Preprint **2001**.

[45] Lang, F.; Gluba, M. A.; Albrecht, S.; Rappich, J.; Korte, L.; Rech, B.; Nickel, N. H. Perovskite solar cells with large-area CVD-graphene for tandem solar cells. *The journal of physical chemistry letters* **2015**, *6*, 2745–2750.

[46] Amano, C.; Sugiura, H.; Yamamoto, A.; Yamaguchi, M. 20.2% efficiency Al0. 4Ga0. 6As/GaAs tandem solar cells grown by molecular beam epitaxy. *Applied physics letters* **1987**, *51*, 1998–2000.

[47] Mailoa, J. P.; Bailie, C. D.; Johlin, E. C.; Hoke, E. T.; Akey, A. J.; Nguyen, W. H.; McGehee, M. D.; Buonassisi, T. A 2-terminal perovskite/silicon multijunction solar cell enabled by a silicon tunnel junction. *Applied Physics Letters* **2015**, *106*, 121105.

[48] Sahli, F.; Kamino, B. A.; Werner, J.; Bräuninger, M.; Paviet-Salomon, B.; Barraud, L.; Monnard, R.; Seif, J. P.; Tomasi, A.; Jeangros, Q.; et al. Improved optics in monolithic perovskite/silicon tandem solar cells with a nanocrystalline silicon recombination junction. *Advanced Energy Materials* **2018**, *8*, 1701609.

[49] Bush, K.; Palmstrom, A.; Yu, Z.; Boccard, M.; Cheacharoen, R.; Mailoa, J.; McMeekin, D.; Hoye, R.; Bailie, C.; Leijtens, T.; et al. a, D. Harwood, W. Ma, F. Moghadam, HJ Snaith, T. Buonassisi, ZC Holman, SF Bent and MD McGehee. *Nat. Energy* **2017**, *2*, 17009.

[50] Wu, Y.; Yan, D.; Peng, J.; Wan, Y.; Phang, S. P.; Shen, H.; Wu, N.; Barugkin, C.; Fu, X.; Surve, S.; et al. Monolithic perovskite/silicon-homojunction tandem solar cell with over 22% efficiency. *Energy & Environmental Science* **2017**, *10*, 2472–2479.

[51] Albrecht, S.; Saliba, M.; Baena, J. P. C.; Lang, F.; Kegelmann, L.; Mews, M.; Steier, L.; Abate, A.; Rappich, J.; Korte, L.; et al. Monolithic perovskite/silicon-heterojunction tandem solar cells processed at low temperature. *Energy & Environmental Science* **2016**, *9*, 81–88.

[52] Werner, J.; Weng, C.-H.; Walter, A.; Fesquet, L.; Seif, J. P.; De Wolf, S.; Niesen, B.; Ballif, C. Efficient monolithic perovskite/silicon tandem solar cell with cell area¿ 1 cm2. *The journal of physical chemistry letters* **2015**, *7*, 161–166.

[53] Saliba, M.; Matsui, T.; Domanski, K.; Seo, J.-Y.; Ummadisingu, A.; Zakeeruddin, S. M.; Correa-Baena, J.-P.; Tress, W. R.; Abate, A.; Hagfeldt, A.; et al. Incorporation of rubidium cations into perovskite solar cells improves photovoltaic performance. *Science* **2016**, *354*, 206–209.

[54] Hu, S.; Shaner, M. R.; Beardslee, J. A.; Lichterman, M.; Brunschwig, B. S.; Lewis, N. S. Amorphous TiO2 coatings stabilize Si, GaAs, and GaP photoanodes for efficient water oxidation. *Science* **2014**, *344*, 1005–1009.

[55] Peng, J.; Wu, Y.; Ye, W.; Jacobs, D. A.; Shen, H.; Fu, X.; Wan, Y.; Wu, N.; Barugkin, C.; Nguyen, H. T.; et al. Interface passivation using ultrathin polymer–fullerene films for high-efficiency perovskite solar cells with negligible hysteresis. *Energy & Environmental Science* **2017**, *10*, 1792–1800.

[56] Xiao, M.; Huang, F.; Huang, W.; Dkhissi, Y.; Zhu, Y.; Etheridge, J.; Gray-Weale, A.; Bach, U.; Cheng, Y.-B.; Spiccia, L. A fast deposition-crystallization procedure for highly efficient lead iodide perovskite thin-film solar cells. *Angewandte Chemie* **2014**, *126*, 10056–10061.

[57] Shen, H.; Peng, J.; Jacobs, D.; Wu, N.; Gong, J.; Wu, Y.; Karuturi, S. K.; Fu, X.; Weber, K.; Xiao, X.; et al. Mechanically-stacked Perovskite/CIGS Tandem Solar Cells with Efficiency of 23.9% and Reduced Oxygen Sensitivity. *Energy & Environmental Science* **2018**.

[58] Yu, Z.; Leilaeioun, M.; Holman, Z. Selecting tandem partners for silicon solar cells. *Nat. Energy* **2016**, *1*, 16137.

[59] Grant, D.; Catchpole, K.; Weber, K.; White, T. Design guidelines for perovskite/silicon 2-terminal tandem solar cells: an optical study. *Optics Express* **2016**, *24*, A1454–A1470.

[60] Todorov, T.; Gunawan, O.; Guha, S. A road towards 25% efficiency and beyond: perovskite tandem solar cells. *Molecular Systems Design & Engineering* **2016**, *1*, 370–376.

[61] Yan, J.; Gilmer, D.; Campbell, S.; Gladfelter, W.; Schmid, P. Structural and electrical characterization of TiO2 grown from titanium tetrakis-isopropoxide (TTIP) and TTIP/H2O ambients. *Journal of Vacuum Science & Technology B: Microelectronics and Nanometer Structures Processing, Measurement, and Phenomena* **1996**, *14*, 1706–1711.

[62] Jhaveri, J.; Avasthi, S.; Man, G.; McClain, W. E.; Nagamatsu, K.; Kahn, A.; Schwartz, J.; Sturm, J. C. Hole-blocking crystalline-silicon/titanium-oxide heterojunction with very low interface recombination velocity. *Photovoltaic Specialists Conference (PVSC), 2013 IEEE 39th* **2013**, 3292–3296.

[63] Schropp, R.; Von der Linden, M.; Wallinga, J.; Knoesen, D.; Hyvarinen, J.; Skarp, J.; Suntola, T.; Willemen, J.; Zeman, M.; Metselaar, J.; et al. Progress in inexpensive a-Si: H/a-Si: H tandem module technology. *Photovoltaic Energy Conversion, 1994., Conference Record of the Twenty Fourth. IEEE Photovoltaic Specialists Conference-1994, 1994 IEEE First World Conference on* **1994**, *1*, 626–629.

[64] Willemen, J. A. Ph.D. thesis, Delft University of Technology **1998**.

[65] Cox, R.; Strack, H. Ohmic contacts for GaAs devices. *Solid-State Electronics* **1967**, *10*, 1213–1218.

[66] Perego, M.; Seguini, G.; Scarel, G.; Fanciulli, M.; Wallrapp, F. Energy band alignment at Ti O 2/ Si interface with various interlayers. *Journal of Applied Physics* **2008**, *103*, 043509.

[67] Hu, S.; Richter, M. H.; Lichterman, M. F.; Beardslee, J.; Mayer, T.; Brunschwig, B. S.; Lewis, N. S. Electrical, photoelectrochemical, and photoelectron spectroscopic investigation of the interfacial transport and energetics of amorphous TiO2/Si heterojunctions. *The Journal of Physical Chemistry C* **2016**, *120*, 3117–3129.

[68] Mei, B.; Pedersen, T.; Malacrida, P.; Bae, D.; Frydendal, R.; Hansen, O.; Vesborg, P. C.; Seger, B.; Chorkendorff, I. Crystalline TiO2: a generic and effective electron-conducting protection layer for photoanodes and-cathodes. *The Journal of Physical Chemistry C* **2015**, *119*, 15019–15027.

[69] Okamoto, H.; Nitta, Y.; Hamakawa, Y. Design Parameters of a-Si: H High-Voltage Photovoltaic Cells. *Japanese Journal of Applied Physics* **1980**, *19*, 545.

[70] Ahmed, S.; Melloch, M.; Harmon, E.; McInturff, D.; Woodall, J. Use of nonstoichiometry to form GaAs tunnel junctions. *Applied physics letters* **1997**, *71*, 3667–3669.

[71] Zide, J.; Kleiman-Shwarsctein, A.; Strandwitz, N.; Zimmerman, J.; Steenblock-Smith, T.; Gossard, A.; Forman, A.; Ivanovskaya, A.; Stucky, G. Increased efficiency in multijunction solar cells through the incorporation of semimetallic ErAs nanoparticles into the tunnel junction. *Applied physics letters* **2006**, *88*, 162103.

[72] Burgelman, M.; Nollet, P.; Degrave, S. Modelling polycrystalline semiconductor solar cells. *Thin Solid Films* **2000**, *361*, 527–532.

[73] Tung, R. T. The physics and chemistry of the Schottky barrier height. *Applied Physics Reviews* **2014**, *1*, 011304.

[74] Kamohara, S.; Park, D.; Hu, C. Deep-trap SILC (stress induced leakage current) model for nominal and weak oxides. In Reliability Physics Symposium Proceedings, 1998. 36th Annual. 1998 IEEE International, IEEE, 57–61.

[75] Diebold, U. The surface science of titanium dioxide. *Surface science reports* **2003**, *48*, 53–229.

[76] Ragnarsson, L.-Å.; Lundgren, P. Electrical characterization of P b centers in (100) Si–SiO 2 structures: The influence of surface potential on passivation during post metallization anneal. *Journal of Applied Physics* **2000**, *88*, 938–942.

[77] Chen, Y. W.; Prange, J. D.; Dühnen, S.; Park, Y.; Gunji, M.; Chidsey, C. E.; McIntyre, P. C. Atomic layer-deposited tunnel oxide stabilizes silicon photoanodes for water oxidation. *Nature materials* **2011**, *10*, 539.

[78] Wu, Y.; Shen, H.; Walter, D.; Jacobs, D.; Duong, T.; Peng, J.; Jiang, L.; Cheng, Y.-B.; Weber, K. On the origin of hysteresis in perovskite solar cells. *Advanced Functional Materials* **2016**, *26*, 6807–6813.

[79] Stjernström, M.; Roeraade, J. Method for fabrication of microfluidic systems in glass. *Journal of Micromechanics and Microengineering* **1999**, *8*, 33–38.

[80] Iliescu, C.; Tay, F. E. H.; Miao, J. Strategies in deep wet etching of Pyrex glass. *Sensors and Actuators, A: Physical* **2007**, *133*, 395–400.

[81] Holman, Z. C.; Filipič, M.; Descoeudres, A.; De Wolf, S.; Smole, F.; Topič, M.; Ballif, C. Infrared light management in high-efficiency silicon heterojunction and rear-passivated solar cells. *Journal of Applied Physics* **2013**, *113*, 013107.

Chapter 5

Closing Remarks and Future Directions

In the period 2014-2016 I-V hysteresis was much discussed as being both a significant and perplexing issue with regard to perovskite cells. The material presented in Chapter 2 gives an indication of why: cells at this time exhibited highly rate-dependent I-V curves on top of a great number of other transient phenomena in current-voltage measurements, all of which begged for a coherent explanation. It seems that such an explanation has now been found in the consequences of ion migration, as first explained in the pioneering papers of refs. [1, 2, 3], and as elaborated in subsequent work including our own [4, 5]. In recent years the focus on hysteresis has diminished, perhaps partly due to the development of this understanding, but more likely for the simple reason that the best performing cells today exhibit minimal hysteresis, as many predicted on the basis of its correlation with excess recombination. This does not demonstrate that the first-cause of ion migration has been eliminated – as shown in sec. 3.8 one of the primary differences in the higher-performing mixed-perovskite and passivated cells is a shift to shorter timescales which masks the issue at typical scan rates. Therefore, since ion migration still persists in the best cells today, but has little impact on stabilized performance, it mostly remains to understand the impact of ionic conduction and accumulation on device stability. Because of this likely relevance to stability, and to a lesser extent to maximum-power-point tracking, the common practice of declaring cells to be "hysteresis-free" using only I-V measurements at relatively slow scan rates is misleading. In our opinion the community would be better served by the practice of reporting measurements such as the EIS metric of sec. 3.8, plus low-frequency capacitance measurements to properly capture the degree of ion migration and accumulation.

Part of the motivation for this work was a need to grasp the relevant physics at play in perovskite cells for the sake of their characterization and development. This could hardly be considered accomplished without an understanding of the large-scale transient variations dealt with in Chapter 2. Having achieved this understanding at a satisfactory level, a more detailed investigation of transient responses, this time including capacitive contributions and to shorter timescales, was carried out in Chapter 3. In total Chapters 2 and 3 provide the necessary background for attempts to apply more advanced characterization methods; deep-level transient

spectroscopy (DLTS) and admittance spectroscopy are two examples which have seen extensive usage in the past. Both of these techniques aim at obtaining important information about sub-gap defects through their induced (temperature-dependent) transient responses. Such defects are certainly present in perovskite cells, both in the bulk and at their interfaces, and likely play a contributing role to their transient responses, as well as being a performance-limiting factor. However, given the often overwhelming impact of ion migration on transient measurements, it will be challenging to successfully measure defects by their transient signature. Only by understanding the manifestations of ion migration in detail can the pitfall of mistaken attributions be avoided, and this applies to many of the methods of cell characterization which will see use in the years to come. Indeed, input from characterization will likely be increasingly important in driving further improvements in cell performance, and this remains a promising area for future input from theory and modelling.

Our final chapter tackled the higher-level problem of integrating perovskite cells into a tandem arrangement, chiefly with a Si partner cell. The work on transparent conductor requirements and metallization was partly spurred by an observation that the earliest perovskite-Si (4-T) tandems reported in the literature generally suffered from huge losses owing to poor transparency in the rear contact of the perovskite top-cell. In a few cases this was due to the use of transparent conductive oxides with low sheet resistance but high absorption, justified by an appeal to the figure of 10 Ohm/sq as the allowable upper limit for thin-film cells. Closer inspection revealed that the figure of 10 Ohm/sq results from specific assumptions about thin-film module design, including the absence of any fingers or bus-bars which are difficult to incorporate on the front-side surface without affecting subsequent processing. No such restriction applies to the rear side of a perovskite cell however, making the adherence to 10 Ohm/sq unnecessary and harmful due to the trade-off with transparency. The conclusions of this work also address the community working on new transparent conductor technologies, where the impression of 10 Ohm/sq as a benchmark figure is widespread. Instead of focusing on designing new transparent conductors with low sheet resistance, we have shown that the needs of thin-film solar cells would equally if not better served by developing scalable methods of patterning narrow-width metal fingers into front- and rear-side electrodes, whilst utilizing existing high-transparency TC technologies for the under-layer.

Whilst the 4T tandem has advantages in terms of ultimate theoretical efficiency, band-gap pairings and spectral robustness, these may be outweighed by the costs associated with running the sub-cells on independent circuits, and by losses induced in the additional transparent electrodes and encapsulation. Making monolithically integrated cells avoids these costs and losses, but introduces new challenges in terms of processing (depending on the integration strategy) and in dealing with current-matching. We have described one strategy for monolithic integra-

tion which is appealingly minimalistic, in that it places the perovskite cell in direct contact with its tandem partner. Whether this strategy can be generalized to other material combinations, and to what extent there is a trade-off between the interfacial defect-mediated conductivity and passivation of the bottom cell remain as open questions. Further questions arise regarding the standard method of assessing current-matching in monolithic perovskite-Si cells, given that the standard method of light-biased EQE measurement ignores the well-known voltage-dependence of collection efficiency in p-i-n type solar cells.

Bibliography

[1] Tress, W.; Marinova, N.; Moehl, T.; Zakeeruddin, S. M.; Mohammad K., N.; Grätzel, M.; Nazeeruddin, M. K.; Grätzel, M. Understanding the rate-dependent J–V hysteresis, slow time component, and aging in CH 3 NH 3 PbI 3 perovskite solar cells: the role of a compensated electric field. *Energy Environ. Sci.* **2015**, *8*, 995–1004.

[2] Richardson, G.; O'Kane, S.; Niemann, R. G.; Peltola, T.; Foster, J. M.; Cameron, P. J.; Walker, A. Can slow-moving ions explain hysteresis in the current-voltage curves of perovskite solar cells? *Energy Environ. Sci.* **2016**, *9*, 1476–1485.

[3] van Reenen, S.; Kemerink, M.; Snaith, H. J. Modeling Anomalous Hysteresis in Perovskite Solar Cells. *J. Phys. Chem. Lett.* **2015**, *6*, 3808–14.

[4] Jacobs, D. A.; Wu, Y.; Shen, H.; Barugkin, C.; Beck, F. J.; White, T. P.; Weber, K.; Catchpole, K. R. Hysteresis phenomena in perovskite solar cells: the many and varied effects of ionic accumulation. *Physical Chemistry Chemical Physics* **2017**, *19*, 3094–3103.

[5] Shen, H.; Jacobs, D. A.; Wu, Y.; Duong, T.; Peng, J.; Wen, X.; Fu, X.; Karuturi, S. K.; White, T. P.; Weber, K.; et al. Inverted Hysteresis in CH3NH3PbI3 Solar Cells: Role of Stoichiometry and Band Alignment. *The journal of physical chemistry letters* **2017**, *8*, 2672–2680.

Appendix A

Continuity and the Admittance

In sec. 3.4.5 we claimed that the AC admittance can generally be decomposed into two components relating separately to charge storage and recombination (equation 3.18). This section provides further detail and discussion concerning this decomposition. The starting point is the continuity equation for electrons (in the following it is understood that analogous expressions apply for holes), which in 1D and in the time-domain takes the form

$$e\,\frac{\partial n}{\partial t} = \frac{\mathrm{d}}{\mathrm{d}x} j_n - e\,U_n$$

where U_n is a term encompassing all sources and sinks including photo-generation, recombination, capture and emission. Linearizing, moving to the frequency domain ($n = n_0 + \hat{n}\,e^{i\omega t}\mathrm{d}V$) and rearranging

$$\frac{\mathrm{d}}{\mathrm{d}x}\hat{j}_n = i\omega\,e\,\hat{n} + e\,\hat{U}_n. \tag{A.1}$$

For a device with two metallic terminals located at $x = 0, L$, the terminal current $\hat{I} = Y$ will generally be expressed in terms of both carrier currents plus a displacement contribution (ionically blocking terminals are assumed), such that

$$Y = \hat{j}_n(0) + \hat{j}_p(0) + \hat{j}_d(0) = \hat{j}_n(L) + \hat{j}_p(L) + \hat{j}_d(L)\ .$$

In a device with ideal selective contact layers it is assured that only one of the carrier currents is non-negligible beyond the selective boundary. Suppose first of all that just a single electron-selective layer exists adjoining the terminal at $x = L$ (the $x = 0$ terminal being in contact with the absorber layer), then integration of (A.1) gives:

$$\begin{aligned} Y &= \hat{j}_n(L) + \hat{j}_d(L) + \cancelto{0}{\hat{j}_p(L)} \\ &= \hat{j}_n(0) + i\omega \int e\,\hat{n}\ \mathrm{dx} + \int e\,\hat{U}_n\ \mathrm{dx} + \hat{j}_d(L) \end{aligned} \tag{A.2}$$

In this case the first term relates to both the recombination of photogenerated electrons at the p-type contact, and to injection of electrons (mostly relevant at reverse bias). Either way this term conceptually belongs with the U_n since it represents a sustainable source of current. Alternatively if there is also a hole-selective layer adjoining the $x = 0$ terminal then $j_n(0)$ simply vanishes. Similar arguments apply to the case where there is only a selective contact on the n-side. The displacement term on the other hand can be related to the surface charge density (equivalently electron density) on the surface of the metallic terminal $\hat{n}_s$ via Gauss's law as

$$\hat{j}_d(L) = i\omega\,\epsilon\epsilon_0\,\hat{E}(L) = -i\omega\,e\,\hat{n}_s \tag{A.3}$$

and therefore conceptually belongs with the carrier density integral where it can be included as a delta source. Jointly these two simplifications leave only two terms in the admittance decomposition, one relating to accumulated charge and the other to sources of recombination (possibly including injection at metallic contacts) as in equation (1) of the main text.

When sub-gap defects are involved, one might consider it desirable to distinguish the component of U_n relating to capture and emission of electrons, which resembles a charge storage process, from some

suitably defined recombination rate. This soon runs into difficulty however, as can be seen by examining the most natural splitting of U_n^d (for a single defect level) which extracts the defect filling rate:

$$U_n^d = \frac{\partial f_n}{\partial t} N_t + \left(U_n^d - \frac{\partial f_n}{\partial t} N_t \right) \tag{A.4}$$

$$= \frac{\partial f_n}{\partial t} N_t + U_p^d \, . \tag{A.5}$$

where N_t is the density of defects with occupation f_n. The problem here is that although the first term has a definite interpretation in terms of the charge stored in the defect level, the hole capture rate could refer either to recombination or capture-release. Identifying U_p as the recombination rate R also breaks symmetry between carrier types. Conversely, attempting to split off a symmetric recombination rate from U_n leaves a remainder which has no physical interpretation in terms of stored charge. It is therefore unlikely that there exists a unique resolution to this conceptual issue of distinguishing recombination events from filling of the defect levels. This is mostly a problem for the rare case where a defect behaves simultaneously as a trap and a recombination centre; generally either one or the other behaviour tends to dominate making the interpretation of $U_{n,p}^d$ as either a charge-storage or recombination term clear. For example, a shallow electron trap implies $U_p^d \approx 0$ in which case the $\hat{U}_n$ in equation (3.18) contributes to Y_Q (the component of Y relating to charge storage) as

$$Y_Q = i\omega \int e \left(\hat{n} + N_t \hat{f}_n \right) \, \mathrm{dx} \tag{A.6}$$

On the other hand for a deep defect level steady-state conditions require $|\hat{U}_n| = |\hat{U}_p|$, and so the identification $R = U_p$ becomes less problematic, although there is still potential ambiguity in the phase. These ambiguities were not significant in any of the simulations considered in the main text, but may arise in other cases.

Appendix B

Analysis of SRH Contact Resistivity

Valuable insights can be gained into the SRH model of sec. 4.2.3 by imposing some simplifying assumptions on the TiO_2-p^+-Si interface. Assuming that a single SRH defect is present at the interface, the heterojunction current can then be expressed in terms of the SRH equation:

$$j = \frac{e\,(np - n_0 p_0)}{v_n^{-1}(p + p_t) + v_p^{-1}(n + n_t)} \tag{B.1}$$

where n, p are the carrier densities at the interface (electrons on the n-side and holes on the p-side respectively), n_0, p_0 are their respective equilibrium values, v_n, v_p are the quasi-recombination velocities, and n_t, p_t are related to the defect energy level. Assuming further that the carrier mobilities are high enough to result in essentially flat quasi-fermi levels throughout the interfacial region, this relationship can be further related to the applied voltage V as:

$$j = \frac{eN_cN_v \exp\left(-\frac{\Delta}{v_{th}}\right)\left(\exp\left(\frac{V}{v_{th}}\right) - 1\right)}{v_n^{-1}\left(N_A \exp\left(-\frac{V_p}{v_{th}}\right) + p_t\right) + v_p^{-1}(N_D \exp\left(-\frac{-V_n}{v_{th}}\right) + n_t)} \tag{B.2}$$

in which $v_{th} = k_B T/e$, $V_{p,n}$ denote the potential drops in the n and p-side depletion regions ($V_n + V_p = V_{bi} - V$), $N_{A,D}$ are the donor and acceptor doping densities on the n- and p-side respectively and $N_{c,v}$ the density of states. The expression simplifies somewhat for the small-signal conductivity to

$$\sigma = \frac{dj}{dV}|_{V=0} = \frac{\frac{e}{v_{th}} N_cN_v \exp\left(-\frac{\Delta}{v_{th}}\right)}{v_n^{-1}(p + p_t) + v_p^{-1}(n + n_t)} \tag{B.3}$$

An extremum occurs with respect to the placement of the equilibrium Fermi level E_{f0} within the interfacial band gap Δ (assuming V_{bi} is fixed) when $v_n n_0 = v_p p_0$, i.e. σ is maximized when the interfacial carrier densities are balanced in the stated sense. This conclusion applies regardless of whether the interface defects carry a substantial charge. Defects of donor type partially compensate the acceptor p-side doping, and therefore require larger acceptor doping to reach the optimum balance than if the defect charge were absent (c.f. the comparison between neutral and donor defects in Fig. 4.11 of the main text). Conversely, acceptor-type defects compensate the n-side donor doping and shift the balance towards requiring extra donors. The experimental data in Fig. 4.11 indicate that excess p-side acceptors are necessary to reach the optimum balance. This implies that a high density of compensating donors are present, whether in the form of interface defects, incompletely ionized sub-gap states in titania (e.g. a band-tail) or simply a high density of ionized bulk donors. The latter seems unlikely given our Hall effect measurements of the TTIP titania used in Fig. 4.11 which indicate only modest bulk n-type doping.